



**HAL**  
open science

# Modelling the propagation and bifurcation of plasticity induced cracks in Nickel base single crystal superalloys

Prajwal Sabnis

► **To cite this version:**

Prajwal Sabnis. Modelling the propagation and bifurcation of plasticity induced cracks in Nickel base single crystal superalloys. Other. Ecole Nationale Supérieure des Mines de Paris, 2012. English. NNT : 2012ENMP0074 . pastel-00819218

**HAL Id: pastel-00819218**

**<https://pastel.hal.science/pastel-00819218>**

Submitted on 30 Apr 2013

**HAL** is a multi-disciplinary open access archive for the deposit and dissemination of scientific research documents, whether they are published or not. The documents may come from teaching and research institutions in France or abroad, or from public or private research centers.

L'archive ouverte pluridisciplinaire **HAL**, est destinée au dépôt et à la diffusion de documents scientifiques de niveau recherche, publiés ou non, émanant des établissements d'enseignement et de recherche français ou étrangers, des laboratoires publics ou privés.

École doctorale n°432 : Sciences des Métiers de l'Ingénieur

**Doctorat ParisTech**

**T H È S E**

pour obtenir le grade de docteur délivré par

**l'École nationale supérieure des mines de Paris**

**Spécialité Mécanique**

*présentée et soutenue publiquement par*

**Prajwal Ajit SABNIS**

le 16 Novembre 2012

**Modélisation numérique de la propagation et de la bifurcation des fissures dans les superalliages monocristallins à base de nickel**

**Modelling the propagation and bifurcation of plasticity induced cracks in Nickel base single crystal superalloys**

Directeur de thèse : **Samuel FOREST**

**Jury**

**M. Nagaraj ARAKERE**, Professeur, MAE, University of Florida

**M. Eric CHARKALUK**, Chargé de Recherches, CNRS, LML, École Centrale de Lille

**M. Khemais SAANOUNI**, Professeur, LASMIS, Université de Technologie de Troyes

**M. Anthony BURTEAU**, Ingénieur de Recherche, SNECMA

**M. Jonathan CORMIER**, Maître de Conférences, Institut P', ENSMA

**M. Bernd MARKERT**, Professeur, MIB, Universität Stuttgart

**M. Samuel FOREST**, Professeur, CdM, Mines ParisTech

**M. Matthieu MAZIERE**, Chargé de Recherches, CdM, Mines ParisTech

Président & Examineur

Rapporteur

Rapporteur

Examineur

Examineur

Examineur

Directeur de Thèse

Invité

**T  
H  
È  
S  
E**

**MINES ParisTech**

**Centre des Matériaux**

CNRS UMR 7633, B.P. 87, 91003 EVRY Cedex, France



---

## Résumé

### Modélisation numérique de la propagation et de la bifurcation des fissures dans les superalliages monocristallins à base de nickel

Le but principal de cette thèse est de développer un modèle numérique pour modéliser les phénomènes de bifurcation et du branchement des fissures. Pour réaliser cet objectif, il était indispensable de posséder un modèle permettant un couplage fort entre le modèle de Plasticité cristalline et celui de l'Endommagement régularisé. Dans un premier temps, quelques outils de post-traitement ont été développés pour analyser les systèmes de glissement actifs. Ces outils ont été utilisés sur des simulations d'éprouvettes réelles, et comparés à des résultats expérimentaux. Par ces comparaisons, l'application du modèle de Plasticité cristalline aux superalliages monocristallins a été validée. Ce modèle a ensuite été couplé avec le modèle d'endommagement régularisé. Le couplage a été réalisé dans les deux sens, c'est-à-dire que l'évolution de la plasticité a une influence sur l'endommagement et vice-versa. Le nouveau modèle peut être implémenté simplement, avec la méthode traditionnelle des Éléments Finis. Des expériences étudiant la propagation de fissure sous des chargements de types différents ont été simulées à l'aide de ce nouveau modèle : éprouvettes CT, fissuration en Mode II et rupture en fluage. Une méthode pour l'identification des paramètres matériaux a également été proposée.

**Mots clés :** Nickel, Monocristal, Superalliages, Plasticité cristalline, Propagation de fissure, Bifurcation de fissure, Couplage, Régularisation, Évolution de l'endommagement, Micro-endommagement, Essais de fluage, Essais de cisaillement, Eprouvette CT, Méthode des Éléments Finis, Approche micromorphe

## Abstract

### Modelling the propagation and bifurcation of plasticity induced cracks in Nickel base single crystal superalloys

The main goal of this dissertation was to develop a model to simulate the processes of crack bifurcation and crack branching in anisotropic materials. To achieve this goal, a thorough coupling of crystal plasticity and regularised damage models was deemed necessary. Firstly, post-processing tools were developed to better analyse the results obtained from standard Crystal Plasticity simulations. These were then compared with experiments, thereby validating the use of Crystal Plasticity models for Nickel base single crystal superalloys. The validated Crystal plasticity model was then coupled with a regularised microdamage model such that the evolution of plasticity influenced damage and vice versa. The newly developed model allows for the simulation of cracks using the standard Finite Element Approach. Experiments studying crack propagation under different types of loads were simulated using the newly developed model, including CT, shear and creep specimens. A methodology was also proposed for the identification of the newly introduced material parameters.

**Keywords:** Nickel base, Single Crystal, Superalloys, Crystal Plasticity, Crack Propagation, Crack Bifurcation, Two-way Coupling, Damage Evolution, Microdamage, Regularisation, Creep tests, Shear tests, CT tests, Finite Element Method, Micromorphic approach



---

# Acknowledgement

The three years during which I researched the results presented in this work at Centre des Matériaux (CdM) are full of pleasant experiences. These are fond memories that I will cherish for the rest of my life, and for these I am grateful to many people.

First and foremost, I would like to offer my most sincere and my most heartfelt gratitude to my adviser Prof. Samuel Forest. He has been a most encouraging adviser and a very motivating mentor. His ceaseless enthusiasm, his impeccable attention to detail and his willingness to engage with his students have been instrumental in the completion of this thesis. His constant encouragement, and his seemingly tireless dedication to teaching is truly inspiring. It has been a great pleasure and an honour to work on this thesis with Prof. Forest.

I would like to thank the members of my PhD defence committee, who despite their hectic schedules accepted the positions of reviewers and examiners of my thesis. I would like to offer sincere thanks to Prof. Khemais Saanouni and Dr. Eric Charkaluk for being my reviewers. The discussions and observations they presented have allowed me a wholly new perspective on my work. I would like to offer special thanks to Prof. Nagaraj Arakere for the various discussions over the years, which have enabled me to appreciate and understand the industrial perspective of current research. I would like to thank Dr. Jonathan Cormier for being on the defence committee, and for all the discussions about the creep phenomenon. Our discussions have helped me understand better the importance of material mechanisms under varying temperature and loading regimes. I would like to thank Dr. -Ing Bernd Markert for his guidance over the years. In working with him, I began researching phase field models for fracture, which turned into an opportunity of working at CdM with Prof. Samuel Forest. I would also like to thank Anthony Burteau and Dr. Matthieu Mazière for the helpful discussions over the years.

I would like to acknowledge the support and the funding provided by SNECMA under the PRC DDV SC project. I would also like to thank my colleagues from the project, Dr. Farida Azzouz, Dr. Stephane Quillici, Dr. Vincent Maurel, Dr. Alain Koster, Flora Salgado, Pierre Sallot and Melanie Leroy, for helping me with my integration into the project group; especially in the first few project meetings, when I was absolutely unable to speak a word of French.

I am grateful to Djamel from the VAL team at the centre, who helped me enormously in implementing the developed model in Zebulon.

I would also like to thank the members of the football team (Fred, George, Greg, Mamadou, Lingtao and all the others) for making Wednesdays a very pleasant day to go to work. I would also like to thank Fatima, Felix, Guruprasad, Henry, Jarmila and Vladislav for their friendship.

I would like to thank Konaly Sar, Liliane Locicero, and Anne Piant for helping me

---

with the official procedures that were required during my stay in France. I would also like to thank Sarojinee Bonneville, Nicolas Cordero, Ozgur Aslan and Justin Dirrenberger who helped me immensely during my initial days in France. I would like to thank the computer administrators at the centre, Olivier Delhomme and Gregory Sainte-Luce for their extremely prompt responses to computer related issues and for some very nice computer hardware related discussions in the cafe. I would also like to thank Odile Adams for all the help regarding the literature.

I am indebted to my office colleagues Julian Durand, Michael Fischlschweiger, Anthony Marais, Guillaume Martin and Remi Martinez for providing a wonderful atmosphere to work in. In particular, words are utterly inadequate to describe how grateful I am to Guillaume and Julian, for their help and their friendship, which extended beyond life at Centre des Matériaux.

Finally I would like to thank my family for their constant support during the preparation of the thesis. I would like to thank my wife Ranjita for being patient with me during the preparation of the manuscript. More than anything else I would like to thank my parents, without whose guidance and support, I would never have pursued a PhD.

*If you do something and it turns out pretty good, then you should go do something else wonderful, not dwell on it for too long. Just figure out what's next.*

*Steve Jobs*

*La science, mon garçon, est faite d'erreurs, mais d'erreurs qu'il est bon de commettre, car elles mènent peu à peu à la vérité.*

*Jules Verne  
dans "Voyage au centre de la Terre"*



---

# Contents

<b>Acknowledgement</b>	<b>iv</b>
<b>Nomenclature</b>	<b>ix</b>
<b>Introduction</b>	<b>1</b>
<b>I Fundamentals</b>	<b>7</b>
<b>1 Nickel base single-crystal superalloys</b>	<b>9</b>
1.1 Introduction . . . . .	9
1.2 Composition and microstructure . . . . .	10
1.3 Mechanics of NBSX . . . . .	13
1.4 Conclusion . . . . .	21
<b>2 Essentials of material modelling</b>	<b>23</b>
2.1 Phenomenological concepts . . . . .	23
2.2 Constitutive modelling of materials . . . . .	29
<b>II Crystal Plasticity simulations of NBSX</b>	<b>33</b>
<b>3 Plasticity evolution in NBSX</b>	<b>35</b>
3.1 Crystal plasticity theory . . . . .	35
3.2 State and constitutive equations . . . . .	37
3.3 Post-processing procedures . . . . .	39
<b>4 Effect of secondary orientation on notch tip plasticity</b>	<b>47</b>
4.1 Introduction . . . . .	47
4.2 Experimental results . . . . .	50
4.3 Crystal plasticity finite element model and computational tools . . . . .	53
4.4 Results and comparison . . . . .	56
4.5 Discussion . . . . .	67
4.6 Conclusions . . . . .	70
	vii

<b>5</b>	<b>Crystal plasticity analysis of cylindrical indentation on Ni-base single crystal superalloy specimens</b>	<b>71</b>
5.1	Introduction . . . . .	71
5.2	Experimental study . . . . .	72
5.3	Computational analysis . . . . .	74
5.4	Results & discussion . . . . .	77
5.5	Conclusions . . . . .	85
<b>III</b>	<b>Damage Modelling</b>	<b>89</b>
<b>6</b>	<b>Gradient Based Damage Modelling</b>	<b>91</b>
6.1	Numerical models for cracks and damaged zones . . . . .	91
6.2	Microdamage model . . . . .	93
6.3	Regularisation approaches . . . . .	97
6.4	Conclusion . . . . .	100
<b>7</b>	<b>Coupled crystal plasticity and microdamage model</b>	<b>101</b>
7.1	Coupled crystal plasticity and microdamage model . . . . .	102
7.2	Analytical Solution for a simple case . . . . .	105
7.3	Characteristic response of the XMD model . . . . .	107
7.4	Conclusion . . . . .	117
<b>8</b>	<b>Numerical Experiments</b>	<b>121</b>
8.1	Element formulation and integration schemes . . . . .	122
8.2	Compact tension specimens . . . . .	123
8.3	Mode II test . . . . .	133
8.4	Creep tests . . . . .	139
8.5	Conclusion . . . . .	146
	<b>Conclusions and Perspectives</b>	<b>149</b>
	<b>A Material Parameters used in simulations</b>	<b>155</b>
	<b>B Numerical aspects</b>	<b>157</b>
	<b>C Polycrystal simulations</b>	<b>161</b>
	<b>References</b>	<b>178</b>

# Nomenclature

## Conventions

$(\cdot)$	Scalar
$(\underline{\cdot})$	Vector
$(\overset{\sim}{\cdot})$	Second-order tensor
$(\overset{\approx}{\cdot})$	Fourth-order tensor
$\nabla(\cdot)$	Gradient of $(\cdot)$ w.r.t. reference configuration
$\text{div}(\cdot)$	Divergence of $(\cdot)$ w.r.t. reference configuration
$\det(\cdot)$	Determinant of $(\cdot)$
$\dot{(\cdot)}$	Rate of change of quantity $(\cdot)$ w.r.t. time
$[hkl]$	Crystallographic direction
$(hkl)$	Normal to crystallographic slip/damage plane
$\{hkl\}$	Family of crystallographic planes
$(hkl)[pqr]$	Slip system defined in terms of normal to slip plane and slip direction
$\underline{\mathbf{A}}^T$	Transpose of second order tensor $\underline{\mathbf{A}}$

## Tensor operations

$\underline{\mathbf{a}} \cdot \underline{\mathbf{b}}$	Scalar product between vectors, $\underline{\mathbf{a}}$ and $\underline{\mathbf{b}}$
$\underline{\mathbf{a}} \otimes \underline{\mathbf{b}}$	Tensor product between vectors $\underline{\mathbf{a}}$ and $\underline{\mathbf{b}}$
$\underline{\mathbf{A}} \cdot \underline{\mathbf{B}}$	Single contraction between second order tensors, $\underline{\mathbf{A}}$ and $\underline{\mathbf{B}}$
$\underline{\mathbf{A}} : \underline{\mathbf{B}}$	Double contraction between second order tensors, $\underline{\mathbf{A}}$ and $\underline{\mathbf{B}}$
$\underline{\mathbf{A}} : \underline{\underline{\mathbf{B}}}$	Double contraction between second order tensor, $\underline{\mathbf{A}}$ and fourth order tensor $\underline{\underline{\mathbf{B}}}$
$\underline{\underline{\mathbf{A}}} : \underline{\mathbf{B}}$	Double contraction between fourth order tensor, $\underline{\underline{\mathbf{A}}}$ and second order tensor $\underline{\mathbf{B}}$

## Mechanical quantities

$\underline{\underline{\boldsymbol{\sigma}}}$	Cauchy stress tensor
---	----------------------

---

$\underline{\mathbf{b}}$	Generalised stress related to gradient of microdamage
$a$	Generalised stress related to microdamage
$\underline{\boldsymbol{\varepsilon}}$	Total strain tensor
$\underline{\boldsymbol{\varepsilon}}^e$	Elastic contribution to total strain tensor
$\underline{\boldsymbol{\varepsilon}}^p$	Plastic contribution to total strain tensor
$\underline{\boldsymbol{\varepsilon}}^d$	Damage contribution to total strain tensor
$\underline{\mathbf{l}}^s$	Slip direction in slip system $s$
$\underline{\mathbf{n}}^s$	Normal to slip plane for slip system $s$
$\underline{\mathbf{M}}^s$	Orientation tensor for slip system $s$ , $\underline{\mathbf{l}}^s \otimes \underline{\mathbf{n}}^s$
$\tau^s$	Resolved shear stress for slip system $s$
$r^s$	Plasticity threshold for slip system $s$
$\gamma^s$	Plastic slip on slip system $s$
$\gamma$	Total accumulated plastic slip
$Y^r$	Damage threshold for damage plane $r$
$d_\mu$	Microdamage
$\nabla d_\mu$	Gradient of microdamage
$\underline{\mathbf{n}}^r$	Normal to damage plane $r$
$\underline{\mathbf{N}}_d^r$	Normal tensor for damage plane $r$ , $\underline{\mathbf{n}}^r \otimes \underline{\mathbf{n}}^r$
$d_{open}^r$	Opening type damage on damage plane $r$
$d$	Total accumulated damage

## Material parameters

$r_0$	Initial plastic threshold
$h$	Strain hardening coefficient (for linear isotropic hardening only)
$Y_0$	Initial damage threshold
$H$	Softening parameter
$\beta$	Plasticity-damage coupling strength
$H_\mu$	Penalty parameter
$A$	Regularisation parameter

# Introduction

Les superalliages monocristallins à base Nickel sont principalement utilisés dans les moteurs d'avion. Ces matériaux conçus pour des applications à haute température sont très difficiles à fabriquer et à usiner. Dans les composants comme les aubes de turbine, les caractéristiques comme les trous et les canaux de refroidissement sont la source de l'amorçage de microfissures. Dans ce contexte de microfissuration, les outils de simulation numérique ont une grande importance, en vue de leur utilité dans la prévision des sites d'amorçages et des chemins de fissuration. Les simulations numériques sont aussi utilisées pour estimer la durée de vie des composants et ainsi certifier leur utilisation.

Pour les simulations de structures, les modèles matériaux utilisés qui prennent en compte des mécanismes différents dans la matière sont assez nombreux. Cette thèse présente le développement d'un tel modèle, qui introduit un couplage fort entre les mécanismes de la plasticité et de l'endommagement. La thèse se décompose en 3 parties : la première donne une introduction aux superalliages monocristallins, à la modélisation des milieux continus et aux concepts introduits dans le développement du modèle. La deuxième partie présente le modèle de plasticité cristalline et les outils des post-traitements utilisés. Enfin la troisième partie présente une brève revue de la modélisation d'endommagement, le développement d'un modèle couplé et son application sur des éprouvettes expérimentales. La conclusion et les annexes liées à ce travail de thèse se trouvent à la fin de manuscrit.

Present day gas turbine engines such as the M-88 (SNECMA) and the CFM-56 (SNECMA/GE) represent an accumulation of decades of technological advances in material and manufacturing sciences. The high performance materials obtained as products of such research activities enable aviation-power-plant manufacturers to meet the challenges set by the extreme operating environments in turbine engines. For example, the thermodynamic efficiency of a gas turbine engine is known to increase with an increase in the Turbine Inlet Temperature (TIT). A higher TIT results in lower fuel consumption and in less pollution. Such engines typically have lower operating costs in comparison to engines with a lower TIT. Such high performance engines demand that the materials used in turbine components (seen towards the right end of Figure 1) be able to withstand sustained cyclic loads with temperatures being in the vicinity of (at times in excess of) 1100° C. To address such requirements, many materials and manufacturing techniques have been developed. One such material is the Nickel Base Single Crystal (NBSX) superalloy.

Materials such as AM1, CMSX-4, PWA-1480 have been developed to have vastly improved performance characteristics as compared to their polycrystalline counterparts. A typical NBSX turbine blade is seen in Figure 2. Essential features such as cooling holes (seen in Figure 2) and cooling channels inside the blade (not seen in the figure) improve

\*Image source: [http://en.wikipedia.org/wiki/File:J85\\_ge\\_17a\\_turbojet\\_engine.jpg](http://en.wikipedia.org/wiki/File:J85_ge_17a_turbojet_engine.jpg)

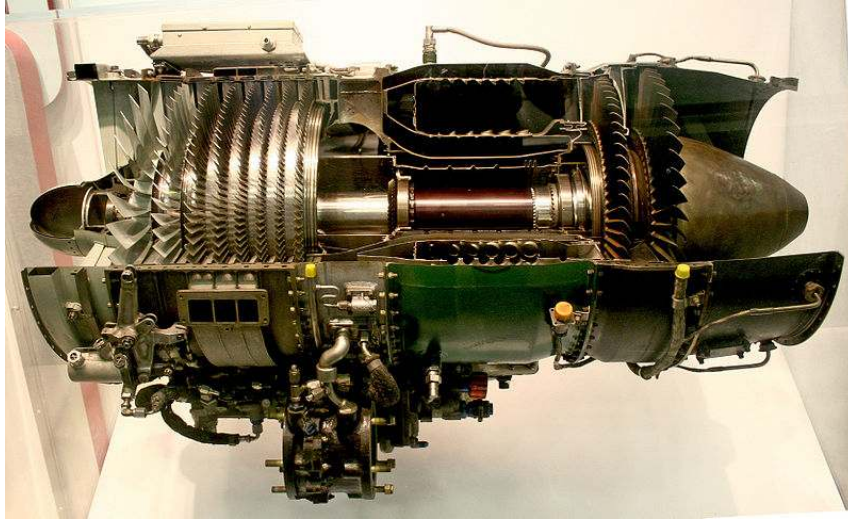


Figure 1: Section view of GE J85 engine. Turbines subject to high temperature operations are seen at the right end of the image.\*

the functional efficiency of the blade's performance. However, these features also induce stress concentration, and hence strain localisation. The effects of stress concentration are enhanced considerably in a standard flight profile, where both, the amplitude and frequency of the loads vary with the changing needs of the flight profile. This localisation of strain renders the material susceptible to damaging under continued loading. Such evolution of damage leads to microcrack propagation in the blade, eventually leading to macroscopic turbine blade failure. In extreme scenarios, a failed turbine blade can lead to a damaged turbine disc, or entire engine failures. In their article, [Sujata et al. \[2010\]](#) present an interesting study of an extreme scenario, where engine failure was caused by a failed turbine blade. While there exist non-destructive testing methods to analyse damaged zones in a structure, models that enable the detection of crack-initiation locations and crack-growth paths in complex geometries are of paramount importance in ensuring the continued and safe operation of in-service engines. Such predictive models can also be used for improving the designs of individual components at the industrial level.

Within this context, there are many different numerical models and numerical approaches that are available in literature. Of the popular approaches, the local approach to modelling failure in materials is interesting as it allows for the development of models based on micromechanics. Comprehensive discussions about the development of local models can be found in literature (see [Besson et al. \[2004\]](#), [Lemaitre and Desmorat \[2005\]](#) for example). However, when used in conjunction with finite element schemes, these models exhibit a localisation of results in the presence of softening phenomena (irrespective of whether the softening is induced by plasticity or damage). In damage models, for example, this localisation is observed by the damage variable being confined to the width of a single finite element. The final outcome of this mesh-dependency is that the crack paths predicted by such models tend to depend on patterns present in the mesh used for a simulation. Thus, the local approach to modelling failure is unsuitable for the development of predictive models for softening related phenomena. A solution to this problem, is to use non-local approaches or gradient approaches, which resolve the problem by introducing a regularisation of the variable that represents the evolution of material softening. A discussion regarding the fine differences between the two approaches can be found in [Peerlings et al. \[2001\]](#). Of the two regularisation approaches, the gradient

approach is preferred for the models discussed in this dissertation, as it allows for a systematic, thermodynamically consistent derivation of numerical models (for a more detailed discussion, see [Forest \[2009\]](#)).

Other methods such as eXtended Finite Element Method and Cohesive Zone Modelling do exist. Although the extended finite element approach is popular among numerical engineers, it is at the present, not sufficiently advanced to be considered for the development of a model that includes multiple inelastic phenomena such as plasticity and damage in the material. [Bouvard et al. \[2009\]](#) present a cohesive zone model for the simulation of ductile failure. However, such modelling requires a prescient knowledge of the crack path. This is impractical for predictive models, where neither the crack path nor the site of initiation are known.

Accounting for the points mentioned above, a micromechanically motivated model with a regularised damage variable was developed in [Aslan and Forest \[2009\]](#), [Aslan et al. \[2011a\]](#). In the models described in these works, a weak coupling with crystal plasticity was introduced. The coupling is referred to as a weak coupling since it considered only the influence of plasticity on the evolution of damage and not the reciprocal influence (A more general discussion of coupled problems, their solution methods and their applications can be found in [Markert \[2010\]](#)). Secondly, the form in which anisotropic damage was introduced required the integration of three new variables at each integration point. This in turn led to a numerical inefficiency of the model, in cases where both plasticity and damage were activated. The following dissertation represents an attempt to develop a coupled numerical continuum model that uses gradient-based damage concepts to capture macroscopic softening behaviour in the material, while attempting to address the above identified weak points of the earlier models. An attempt has been made to ensure that the variables introduced/retained in the model adhere as closely as possible to microscopic studies based on experiments. In that sense, the models discussed in this thesis can be considered to be motivated by material behaviour at the microscopic level.

Although the models developed in this work are of a coupled nature, no claim is made that they include all possible couplings or that they will work unconditionally under any test case. It is presumed that the reader is familiar with concepts of *Continuum Mechanics* and hence no explicit description of continuum mechanics and continuum thermodynamics is included. The uninformed reader is directed to better sources (see [Chadwick \[1999\]](#) for an introduction to continuum mechanics; [Lemaitre and Chaboche \[1994\]](#), [Besson et al. \[2010\]](#) for an introduction to non-linear material mechanics and related numerical treatments). The models presented are derived in the manner of rational thermodynamics (after [Truesdell \[1969\]](#)). The reader is also presumed to be familiar with basic numerical schemes such as integration schemes. Many good books are available for reference, e.g. see [Kreyszig \[2006\]](#), [Press et al. \[2007\]](#), [Arfken et al. \[2012\]](#). The following work focuses on different aspects of material model development and testing.

The thesis is divided into three parts. The first part presents a fundamental introduction to NBSX superalloys, with a brief review of the typical material composition and microstructure. Typical deformation and cracking mechanisms observed in the material are also revisited. The following chapter reviews concepts essential to the continuum modelling of materials in a generalised manner. Classical concepts of fracture mechanics are recalled briefly to enable a comparison in later chapters. The second part introduces the classical crystal plasticity model (as discussed in [Méric et al. \[1991\]](#) and [Mandel \[1973; 1974\]](#)). A post-processing tool for the determination of dominant slip systems is developed and is applied to crystal plasticity simulations of different sets of experiments. Comparisons between experiments, Anisotropic Elasticity (AE) and Crystal

---

Plasticity (CP) simulations are presented and discussed. The third part then introduces the motivations behind the gradient-based modelling of fracture. The *Microdamage model* (Aslan [2010]) is introduced as a basis for further model development. A comparison of similar models is presented and is followed by the development of a coupled elastic-viscoplastic-damage model. Different aspects of the model are explored using numerical tests. Finally, some real experimental observations are simulated to showcase the capabilities of the newly developed model. The thesis is concluded with the identification of avenues for further development.

The work presented in this thesis was carried out as part of the *Programme de Recherches Concertées Durées de Vie des Structures Chaudes* (PRC-SC) project, which is aimed at studying the various material and structural processes observed in high-temperature components used in aviation engines. The project addresses various aspects related to materials, such as oxidation of materials, crack growth in materials, fatigue failure at high temperatures, predictive models for failure etc. PRC-SC is a collaborative research project with multiple partners in France. The aviation engine industry is represented in the project by Onera, Snecma-SAFRAN group and Turbomeca-SAFRAN group. The CNRS research labs involved in the project are Centre des Matériaux- Mines ParisTech, Institut P<sup>2</sup>-ENSMA, LMT-Cachan, LMS-X, CIRIMAT ENSIACET and CEAT.

The main goal of the project is to review and analyse the present design methodology used for these crucial components. The analysis is also accompanied by the development of new tools to enable more reliable and more comprehensive design of components. One of the important tasks of the project is to develop further, practical numerical approaches that account for multiple phenomena that are active in the components. The project is divided into the following different themes:

- Material behaviour and damage in a volume element
- Surface effects and thin-walled structures
- Cracks
- Multi-scale methods and calibration
- Advanced numerical methods

The work presented and developed in this dissertation is categorised under the third theme, which is aimed at the development of efficient numerical models to simulate crack propagation. The theme also aims to validate the developed models on the basis of already available experimental data. I am grateful to Snecma-SAFRAN group for sponsoring this work.

---

<sup>†</sup>Image source (Figure 2):  
[http://ec.europa.eu/research/transport/projects/items/ultmat\\_en.htm](http://ec.europa.eu/research/transport/projects/items/ultmat_en.htm)



Figure 2: Typical turbine blade used in high-temperature high-pressure turbine stages<sup>†</sup>

---

---

Part I

Fundamentals



## Chapter 1

# Nickel base single-crystal superalloys

### Résumé

Dans ce premier chapitre, une brève description des superalliages monocristallins est présentée. La discussion se concentre sur les aspects physiques du matériau, tels que la microstructure et la composition. Les phénomènes de fatigue et de fluage (qui sont très importants dans ce genre de matériaux) et leurs effets sur la propagation des fissures sont également discutés. Ce chapitre contient les aspects fondamentaux qui sont nécessaires pour comprendre les méthodes suivies dans le développement du modèle XMD (présenté en chapitre 7). Certaines critères qui doivent être pris en compte par le modèle sont également identifiés. Ces critères sont :

- Elasticité anisotrope
- Plasticité cristalline
- L'endommagement cristallographique
- Couplage dans les deux sens entre la plasticité et l'endommagement

### 1.1 Introduction

The family of high performance materials known as “superalloys” have been in development since the early 1900s. The introduction of the turbojet engine in the late 1930s accelerated research of high temperature materials, the result of which was the introduction of superalloys into aircraft engine components. Although many superalloys with different base materials have been developed, the present work is focused on superalloys based on Nickel. A good overview of the historical development of superalloys can be found in [Durand-Charre \[1997\]](#).

Aircraft components made of superalloys in the earlier years (around the 1960s) were produced by metalworking/forging. These production methods were replaced by various casting and powder metallurgy processes, thereby enabling the production of hollow components, such as the present day turbine blade. Early superalloys produced by the casting process were poly-crystalline in nature. At higher temperatures, the components made of these materials were prone to failure due to accumulation of damage at the grain boundaries. With the advent of directional solidification, components with columnar grains provided vast performance improvements over their polycrystalline

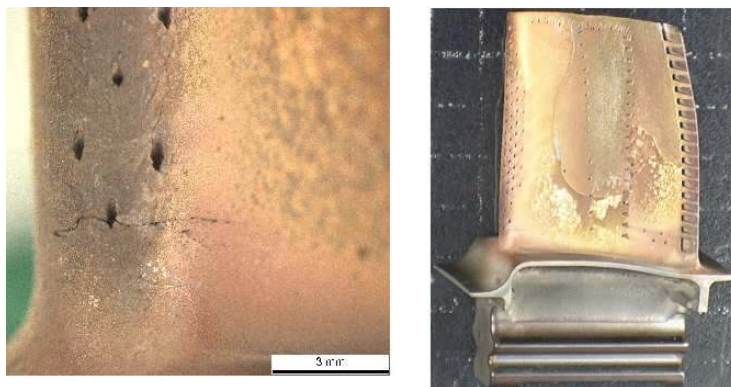


Figure 1.1: Crack initiation at a cooling hole. *Image courtesy: SNECMA*

counterparts. However, the issues related to the presence of grain boundaries persisted. Further technological advances allowed the production of superalloys with a single crystal structure, thereby eliminating the problems caused by damage initiation and accumulation at grain boundaries. Present day aero-engine components utilise all three families of superalloys, viz. polycrystalline, directionally solidified and single crystal superalloys. The choice of these materials are made based on a number of factors such as operating temperatures, operating loads, manufacturing cost, manufacturing difficulty etc. For example, Titanium superalloys are used in compressor components, Nickel-base and Cobalt-base polycrystalline alloys are used in the production of the engine combustion chamber, turbine discs etc. In what follows, work is concentrated on Nickel base superalloys such as the PWA148X series (Pratt & Whitney), AM1 (SNECMA) and the CMSX series (Cannon Muskegon), which are used in high-pressure turbine blades. A good overview of various aspects of superalloy manufacture can be found in [Reed \[2006\]](#).

In the 1960s, research in the fields of aerodynamics and material science led to the development of turbine blades with cooling features. These features included hollow blades with internal cooling pathways, cooling holes on the leading edge of the blade profile and the cooling slats on the trailing edge of the blade. Although these features enable the augmentation of operating temperatures, they also act as stress concentration features. Consequently, highly localised straining and damage initiation is often found in the vicinity of features such as cooling holes and notches. An example of such a crack is seen in Figure 1.1. Another example of crack initiation at a hole in a fatigue test specimen is shown in Figure 1.2 (from [Kaminski \[2007\]](#)). The mechanics of deformation that drive the development of cracks in the NBSX superalloys depend quite strongly on the type of loading imposed on the components. The mechanisms active under fatigue loading are quite different than those active under creep conditions. The following sections cover briefly the microstructure and the chemical composition of NBSX superalloys, following which, the different mechanisms that are active in the said family of materials are discussed.

## 1.2 Composition and microstructure

The element *Nickel* proves an attractive alternative as a base material for superalloys. Titanium for example, offers low oxidation resistance and hence, cannot be used in the high pressure turbine stages, where the extremely high temperature gases create a highly oxidising atmosphere. Nickel has an Face Centred Cubic (FCC) structure and is tough and ductile. Nickel retains microstructural stability up to very high temperatures due to

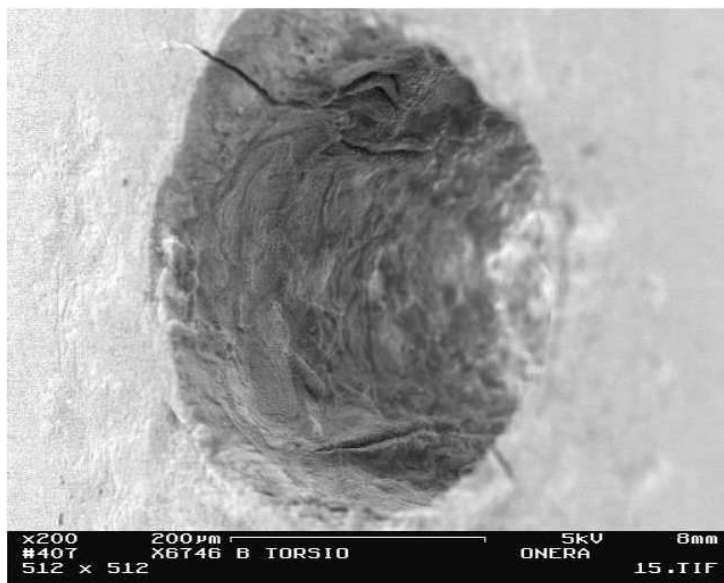


Figure 1.2: Crack initiation at a hole in a fatigue test specimen Kaminski [2007]

low diffusion rates. Lastly, Nickel does not exhibit phase changes in a temperature range extending from room temperature, up to the melting point. All these reasons make Nickel a very interesting material for use in high temperature applications.

The modern NBSX typically consists of two phases – the  $\gamma$  and the  $\gamma'$  phases. The latter phase consists of intermetallic precipitates (i.e. precipitates of compounds such as  $Ni_3Al$ ,  $Ni_3Al_2$  etc.), and are key to achieving the improved mechanical properties of an NBSX. This strengthening occurs in part due to the internal “Coherence Stresses”, which are present in the material due to the lattice misfit between the two phases. The misfit between the lattice parameters of the two phases is in between 0-1%. This misfit value is small enough to be accommodated by the localised elastic distortion of the material lattice. These localised strains, the so-called “coherence strains” cause hardening, thereby increasing material strength. To ensure high temperature stability, the size of the precipitates is controlled precisely to around  $0.5 \mu m$ . Coarser precipitates increase the lattice misfit and lead to high temperature instabilities of the microstructure. Early generations of NBSX were designed to contain about 25% volume fraction of  $\gamma'$  precipitates. But, present day methods such as vacuum induction refining allows for the production of alloys with up to 70%-80% volume fraction of the precipitate strengthening phase. Higher concentrations of precipitates lead to the drastic reduction of creep strength.

The solid solution matrix, i.e. the  $\gamma$  phase, consists mainly of elemental Nickel with up to 40% of other alloying elements. The alloying elements impart strength to the ductile Nickel matrix phase by solid solution strengthening. In addition to strengthening, they also enhance other material properties such as oxidation resistance, creep resistance etc. Table 1.1 provides a list of various alloying elements used in superalloys and their corresponding functions. Figure 1.3 shows the microstructure of fourth and fifth generation NBSX developed by NIMS, Japan. Examples of NBSX composition are provided in Table 1.2.

Some of the other phases that can be found in Nickel base superalloys include the  $\gamma''$  phase and the Topologically Close Packed (TCP) phases such as the  $\mu$ - and the  $\sigma$ - phases. The  $\gamma''$  phase, which has a tetragonal lattice structure, occurs in forms of precipitates and is found typically in superalloys containing Niobium. These precipitates provide additional mechanical strength by strain hardening. The TCP phases are brittle phases and are found

## 1.2. Composition and microstructure

Alloying Elements	Application
Co, Cr, Mo, W, Ta, Re	Solid Solution Strengthening
Al, Ti	Formation of $\gamma'$ phase ( $Ni_3Al, Ni_3Ti$ )
Co	Raises the solvus temperature of $\gamma'$ phase
Al, Cr	Oxidation resistance
Cr, Co	Sulfidation resistance
Re	Delays rafting in the $\gamma'$ phase
Co, Mo, W, Re, Cr	Formation of topologically closed packed structure

Table 1.1: Role of different elements in the alloy Durand-Charre [1997]

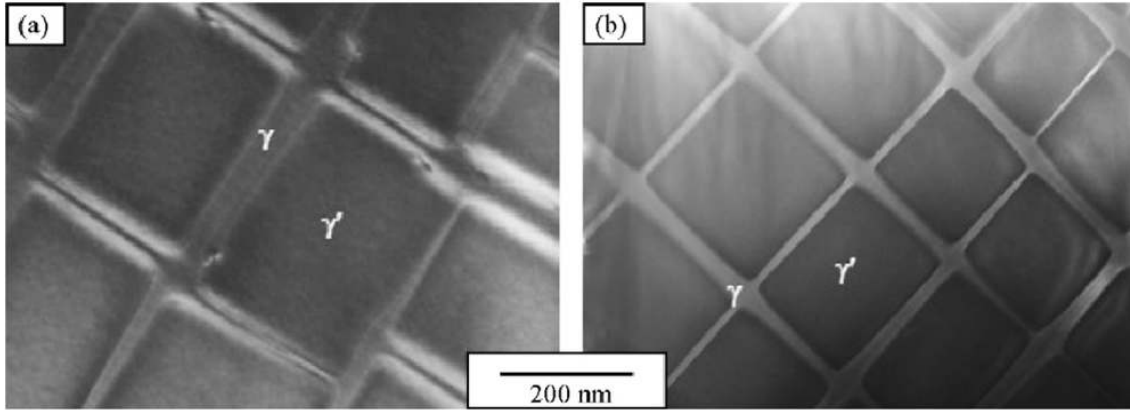


Figure 1.3: Post heat treatment microstructure of NBSX; (a) TMS-138A, a fourth generation superalloy, (b) TMS-168, a fifth generation superalloy. Yeh et al. [2008]

in alloys with high concentrations of Chromium, Molybdenum, Tungsten and Rhenium. The elements Cr, Mo, W and Re are important in alloy compositions as they enhance the creep resistance offered by the material. However, when the concentrations are too high, the formation of brittle TCP phases is promoted which in turn embrittles the material. Thus, the composition of the alloys should be carefully balanced to ensure that the desired properties are achieved. For a more detailed discussion of the various phases and the

Alloy	Generation	Composition (in %)											
		Ni	Cr	Co	Mo	W	Al	Ti	Ta	Re	Nb	Hf	Ru
PWA1480	1 <sup>st</sup>	62.5	10	5	-	4	5	1.5	12	-	-	-	-
CMSX-2	1 <sup>st</sup>	66.6	8	4.6	0.6	7.9	5.6	0.9	5.8	-	-	-	-
AM1	1 <sup>st</sup>	60.6	8	6	2	6	5.2	1.2	9	-	-	-	-
AM3	1 <sup>st</sup>	67.0	8	6	2	5	6	2	4	-	-	-	-
MC2	1 <sup>st</sup>	64.5	8	5	2	8	5	1.5	6	-	-	-	-
PWA1484	2 <sup>nd</sup>	59.4	5	10	2	6	5.6	-	9	3	-	-	-
CMSX-4	2 <sup>nd</sup>	61.8	6.5	9	0.6	6	5.6	1	6.5	3	-	0.1	-
CMSX-10	3 <sup>rd</sup>	69.6	2	3	0.4	5	5.7	0.2	8	6	0.1	0.03	-
TMS-75	3 <sup>rd</sup>	59.9	3	12	2	6	6	-	6	5	-	0.1	-
TMS-138	4 <sup>th</sup>	66.9	3	6	3	6	6	-	6	5	-	0.1	2
TMS-169	5 <sup>th</sup>	59.2	4.6	6.1	2.4	5	5.6	-	5.6	6.4	-	0.1	5

Table 1.2: Composition of different Ni-base superalloys Durand-Charre [1997]

different metallurgical aspects of superalloys, the reader is directed to [Reed \[2006\]](#), [Durand-Charre \[1997\]](#), [Donachie and Donachie \[2002\]](#) and [Sims et al. \[1987\]](#).

### 1.3 Mechanics of NBSX

The evolution of cracks in a given NBSX specimen is a combination of many different coupled processes. Over the decades, many experimental studies have been conducted to study these processes in an individual and in a coupled manner. Based on these studies, phenomenological models and empirical relations have been proposed. While irreversible plastic straining occurs due to the process of crystallographic slip, the deformation mechanisms that drive the evolution of cracks in NBSX are dependent on the type of loading acting upon the superalloy components. Mechanisms that are activated under fatigue differ significantly from the mechanisms that are activated under creep, and this plays an important role in the evolution of cracks in NBSX components. [Pineau and Antolovich \[2009\]](#) provide an overview of the various mechanisms active in an NBSX superalloy under fatigue loading. The following paragraphs present a discussion on the various mechanisms of deformation that are considered to be important for the models developed at a later stage in this thesis.

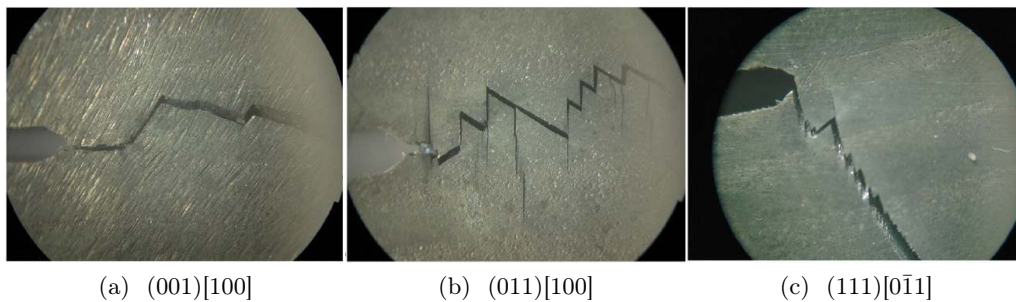


Figure 1.4: Crack growth at  $750^{\circ}C$  in compact tension specimens made of the DD3 superalloy under monotonic loading (from [Wen and Yue \[2007\]](#)). The influence of crystal orientation on the crack-paths is evident. The (...) indicates the normal to the initial notch-plane and the loading direction. The [...] term indicates the direction along which the initial notch is oriented.

#### Plasticity in Ni-base single crystal superalloys

Starting with the early observations of Ewing and Rosenhain in 1900, many years before the identification and documentation of the crystalline lattice structure of metals by Hull in 1919, the mechanics of inelastic deformation in crystalline material has been a subject of great interest. The pioneering experiments by Taylor and Elam in the 1920s not only provided experimental proof of the crystalline nature of metals, but also provided an identification and an analysis of the slip planes in Aluminium crystals, viz. the  $\{111\}$  family of slip planes. In the meantime, Schmid suggested in 1924, that the occurrence of plastic slip on any crystallographic slip plane commences only when the resolved shear stress on that particular plane reaches a critical value. Taylor and Elam also identified conditions for the activation of conjugate slip systems, in the presence of an active slip system experiencing “self-hardening”. These seminal observations laid the foundation for the development of most of today’s phenomenological models. In these early years, dislocations were also studied as being the reasons behind the phenomenological

observations of crystallographic slip. Proceeding from the linear dislocations theory of Volterra (1905), Taylor also identified hardening interactions between the dislocations. All these phenomenological observations from study of metals provide a sound base for the development of micromechanically motivated material models, such as the ones that will be discussed at a later stage. A more detailed discussion of the historical developments of crystallography can be found in the book by [Asaro and Lubarda \[2006\]](#).

NBSX alloys, like other monocrystalline materials, undergo plastic deformation by the movement of dislocations on select crystallographic planes. Since these materials have an Face Centred Cubic (FCC) lattice structure, the crystallographic slip occurs along the octahedral planes. Figure 1.5 shows the atomic structure typical of an NBSX lattice. The dark-red atoms represent Ni-atoms and the yellow atoms represent the atoms of the alloying elements such as Aluminium or Titanium. The figure also shows one of the octahedral slip planes with the three possible slip directions. It is clear that slip occurs along the planes with the most dense packing of atoms. Figure 1.7 shows the four possible octahedral slip planes that can be activated in an NBSX crystal. Since each plane consists of three slip directions, a total of twelve octahedral slip systems can be activated in an NBSX crystal.

In addition to the octahedral slip, evidence of crystallographic slip along macroscopic cubic planes have also been reported for certain orientations at higher temperatures (e.g. see [Antolovich et al. \[1992\]](#), [Copley and Kear \[1967\]](#), [Clément et al. \[1991a\]](#), [Clément et al. \[1991b\]](#)). The macroscopic slip planes are shown in the Figure 1.6. However, it was shown by [Bettge and Österle \[1999\]](#), that cubic slip is actually caused due to vast amounts of interacting octahedral slip. The observation made by [Bettge and Österle \[1999\]](#) has also been replicated numerically by the use of multi-scale modelling (see [Tinga et al. \[2010\]](#)). Proceeding with these latter observations, the plasticity models developed in this thesis consider only octahedral slip.

#### Damage and micro-macro crack propagation

NBSX components are typically subject to fatigue and creep loading conditions during their service life. Consequently, a good understanding of the creep and fatigue deformation mechanics is essential to the realistic simulation of crack growth in NBSX. Numerous studies aimed at understanding the various mechanisms active in the propagation of cracks under these kinds of loads have been conducted.

Crack development mechanism under fatigue loading occurs under significantly complex conditions. Crack initiation occurs due to a variety of reasons. One common occurrence of initiation is observed at the interface between the material matrix and Persistent Slip Bands (PSBs), at which location, very high strain gradients exist due to the discontinuous character of the interface. Other possible locations for crack initiation are offered by microvoids and precipitates. Once a crack is initiated, crack growth can be characterised into three regimes, a schematic representation of which is shown in Figure 1.8. The regime A in the figure corresponds to a regime where crack growth occurs at a rate that cannot be easily detected and is usually related to some sort of a threshold in fracture/damage models. The regime B corresponds to a more stable crack growth regime, where the now classical Paris law is applicable. The third regime C is characterised by unstable crack growth. The development of cracks under regime A, i.e. in the near-threshold is a mixture of mixed mode (Modes I and II) crack growth. At higher rates of crack growth in the near threshold regime, Mode I crack growth dominates (see [Suresh \[2003\]](#)). In the more stable crack growth regime development of cracks is almost entirely plasticity-induced, i.e. the propagation of the cracks is the result of vast amounts of localised inelastic straining.

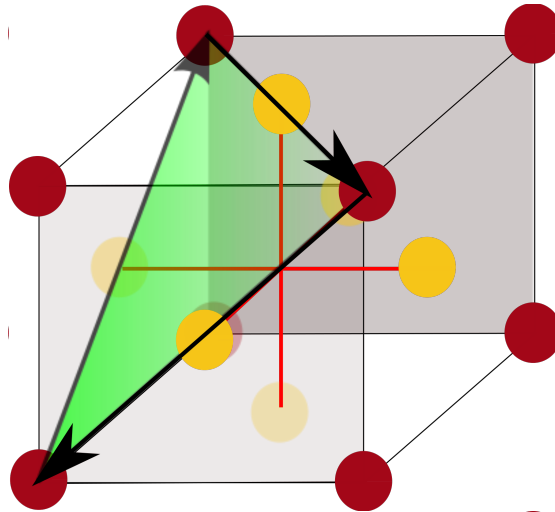


Figure 1.5: Positions of atoms in an FCC crystal. The slip directions are shown for one of the  $\{111\}$  family of slip planes

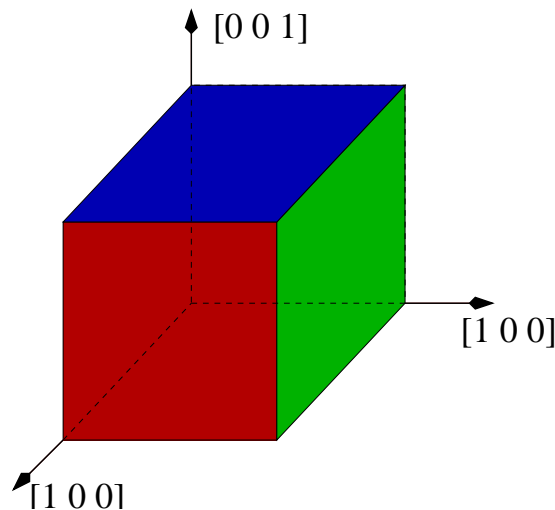


Figure 1.6: The three cubic slip planes in an FCC crystal

In the case of single crystals, this translates to crack growth due to the accumulation of plastic slip along the crystallographic slip planes. A very thorough discussion and analysis of the various possibilities that cause fatigue crack initiation and fatigue crack growth can be found in [Suresh \[1991\]](#).

Examples of fatigue tests on NBSX superalloys can be found in studies by [Arakere and Swanson \[2002\]](#), [Marchal et al. \[2006\]](#), [Fleury and Rémy \[1994\]](#), [Rémy and Defresne \[1990\]](#), [Antolovich et al. \[1981\]](#) etc. A good review of fatigue deformation mechanisms and fatigue crack growth in superalloys can be found in [Pineau and Antolovich \[2009\]](#). Experimental observations show that fatigue cracks propagate by accumulation of extensive plastic deformation that localises at concentration features such as notches and crack tips. Figure 1.9 shows the intense localisation of plastic slip at a crack tip in an NBSX specimen. Another experimental study concerning the observation of extensive slip traces at the crack tips in NBSX superalloys subject to fatigue loading can be found in [Chalant and Rémy \[1982\]](#). Such observations of localised plastic slip ahead of the crack tip indicate that

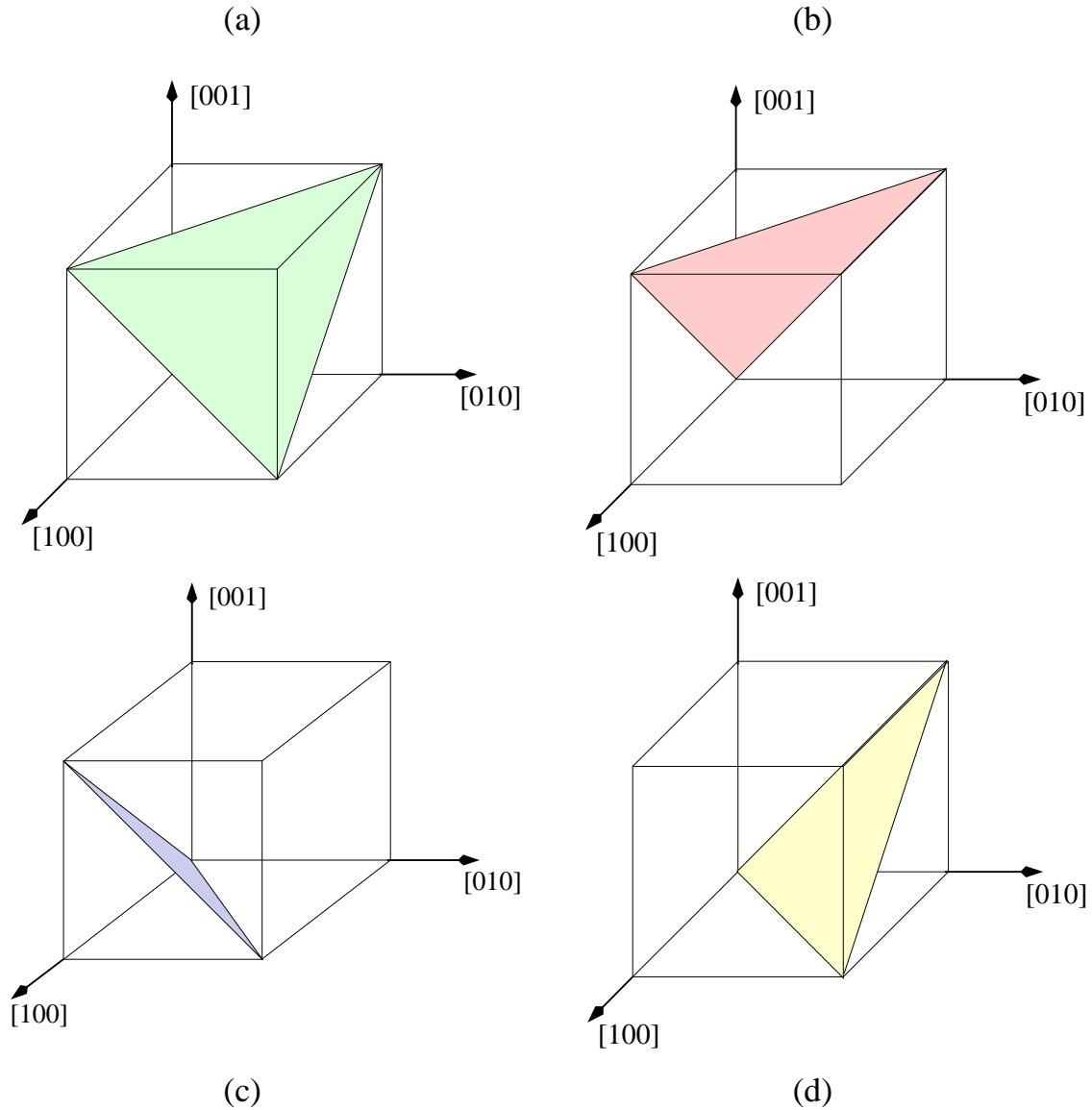


Figure 1.7: The four octahedral slip planes in an FCC crystal

plasticity precedes crack propagation in NBSX alloys. Hence, it is hypothesised that any numerical model capable of realistically simulating cracks in NBSX must include plasticity. The numerical modelling of crystal plasticity and some of its applications to the simulations of NBSX will be discussed in Part II. The various concepts involved in plasticity and the numerical modelling of plasticity can be found in literature (see Lubarda [2002], Asaro and Lubarda [2006], Besson et al. [2010], Dunne and Petrinic [2006]). Detailed discussion about the numerical modelling of crystal plasticity are reserved for later chapters.

Following the discussion of crack growth under fatigue conditions, mention must be made of crack-closure phenomena. Figure 1.10 shows some of the mechanisms that can cause crack closure in the context of NBSX superalloys. Other possibilities including crack shielding by micro-cracks, crack-shielding by dislocations, crack-bridging by particles and plasticity-induced crack closure etc. are discussed in Suresh [1991]. Irrespective of the root mechanism, the main outcome of the crack closure phenomena is that there is no further evolution of damage at that point, provided that there is no reversal of loading locally. In the models treated in this thesis, effects such as oxidation and obstacles-induced-deflection

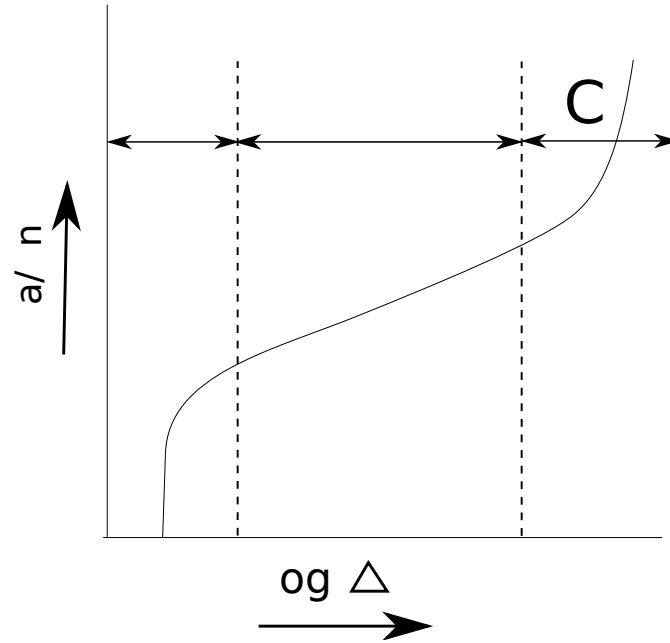


Figure 1.8: Schematic representation of fatigue crack growth; fatigue cracks are typically characterised by plotting the crack extension ( $da$ ) per number of cycles ( $dN$ ) against the logarithm of the SIF range  $\Delta K$  ( $\log \Delta K$  represents the cyclic loading imposed on the specimen).

are not treated. However, a mechanism to handle localised crack-closure, such as those that could occur in the case of roughness-induced-closure, is included.

Creep deformation in NBSX superalloys is typically characterised into three stages. The first stage usually consists of formation of deformation networks. This stage is dominated by a gradual decrease in strain-rate. The second stage is characterised by a more stable behaviour in which the strain-rate is stabilised and the dislocation density reaches a level of saturation. The tertiary creep stage is characterised by a marked increase in the strain rate, which in turn is caused by the formation of pores and cracks (Figure 1.13 shows examples of pores in an NBSX specimen). A more detailed description of creep deformation can be found in Wintrich [2004].

Focusing on the tertiary creep stage which is marked by development of pores and cracks, two broad categories can be recognised. In the first category, creep occurs under the conditions of relatively low temperatures (up to about  $750-800^\circ C$ ) and relatively high stresses ( $\approx 750MPa$ ). In this category, the cuboidal form of the precipitates is conserved and the distribution of precipitates in the network is also preserved. The principle cause of damage and crack propagation in this category is the formation of micro-cracks at pores in the material. The pores observed in this type of creep damage are usually present from the time of manufacturing. The growth of the crack occurs in a manner similar to ductile failure, with the coalescence of pores and voids up to failure. Deformation in this mode of failure is driven primarily by precipitate shear. Thus, the crack growth in this mode is principally driven by localised mode I fracture.

A second category that can be observed, is that of high temperature, low stress creep. In this category of creep deformation, sustained levels of low stress (as low as  $250MPa$ ) at extremely high temperatures ( $> 1100^\circ$ ) cause microstructural changes. The cuboidal precipitates morph into raft-like structures (the process of this change is called “rafting”). Following the formation of rafts, raft networks are formed based on the misfit between the  $\gamma$  and  $\gamma'$  phases. Due to the formation of these raft-like structures, dislocation climb is

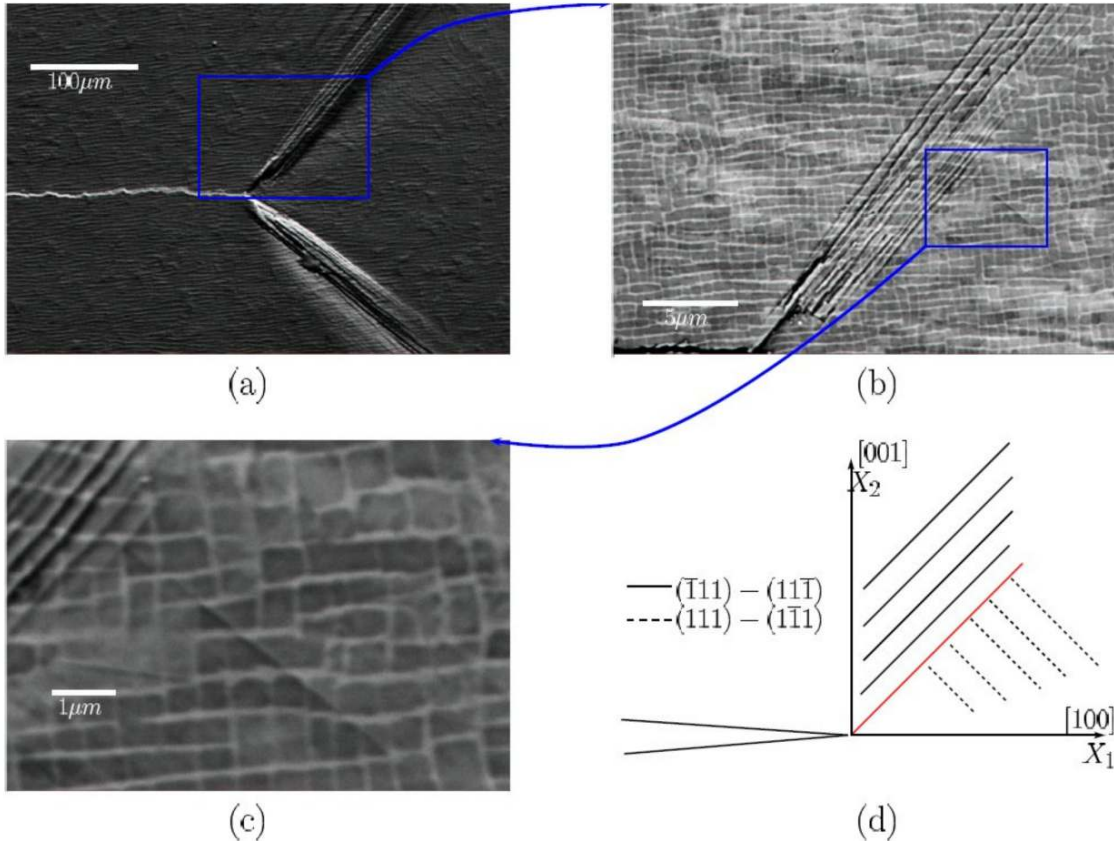


Figure 1.9: Slip localisation at crack tips and identification with theoretically expected slip traces  
Flouriot [2004]

no longer easily possible. This is the reason for the observation of tearing of rafts. After large amounts of localised plastic deformation, void nucleation due to dislocation climb is observed. The failure growth mechanism in this category is also characterised by ductile failure, i.e. by the growth and coalescence of voids. However, crack growth usually follows the orientation of the rafts and the failure process is shear driven. Figure 1.11 shows a schematic representation of the rafting process; Figures 1.12 and 1.14 show an example of rafting observed in high temperature creep tests.

Since material creep occurs at extremely high temperatures, other processes also influence deformation related response of NBSX superalloys. For instance, at temperatures higher than  $0.4\theta_m$  ( $\theta_m =$  melting temperature), diffusion creep becomes important. The consideration of these processes are outside the scope of the models discussed in this thesis. For a more comprehensive discussion of creep mechanisms, the reader is directed to sources in literature (e.g Wintrich [2004]). Examples of experimental studies on creep in Nickel-base superalloys can be found in Drew et al. [2004], Chatterjee et al. [2010], Zhang et al. [2004]. Shah et al. [2004] present a study of primary creep in Nickel base superalloys and Seetharaman and Cetel [2004] present a study of the effect of the thickness of the specimen on creep response. Most of the tests found in literature are concerned with carrying out isothermal creep in superalloys. An example of anisothermal creep testing has been published by Cormier et al. [2008].

It is clear from the above discussions that the failure of NBSX components is principally driven by mixed modes of fracture, depending on the type of loading imposed on the test piece. Particular attention was paid to revisiting the micromechanically observed

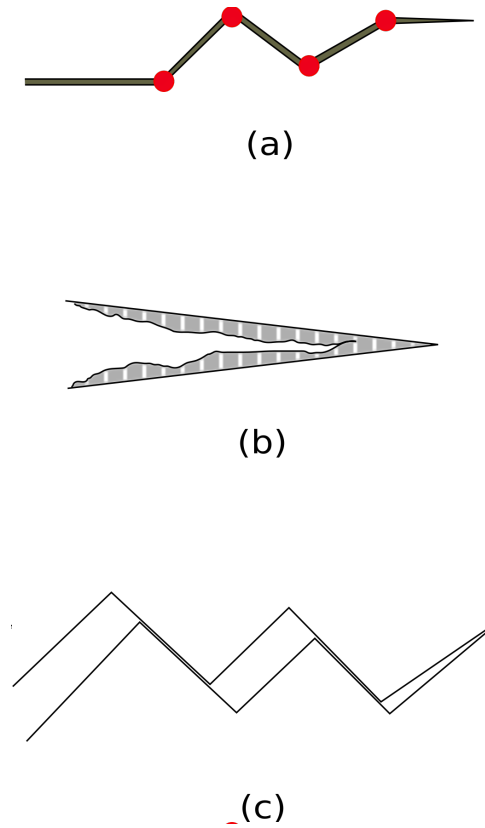


Figure 1.10: Different mechanisms that can lead to crack closure under fatigue conditions in an NBSX superalloy. (a) Crack deflection due to obstacles (shown in red) (b) Crack closure by oxide film formation (the patterned region shows a non-uniform oxide film)(c)Crack closure due to roughness of crack surfaces. All figures after the schematic descriptions in Suresh [1991]

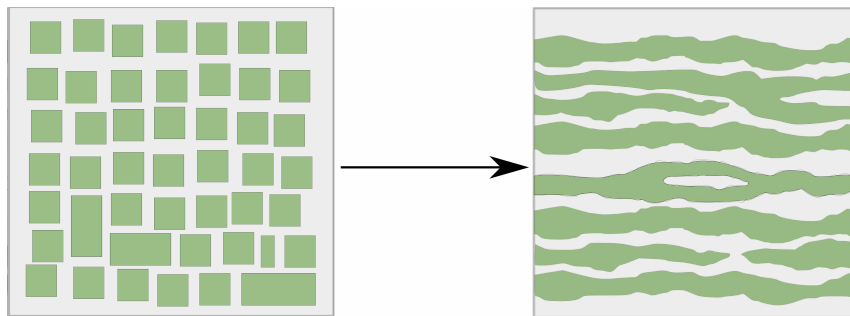


Figure 1.11: Schematic representation of rafting process

behaviours under creep and fatigue load experiments. From the points revisited so far, the presence of shear driven fracture propagation is accepted. Experimental studies such as Milligan and Antolovich [1987] have recorded opening type crack growth in NBSX specimens. Such observations highlight the importance of mixed-mode crack growth. This point has also been discussed at length in Suresh [1991] for the case of fatigue failure. Thus, any material model aimed at simulating crack growth phenomena in superalloys must be capable of handling mixed mode crack growth, which in turn manifests itself in the forms of crack-bifurcation and crack-branching.

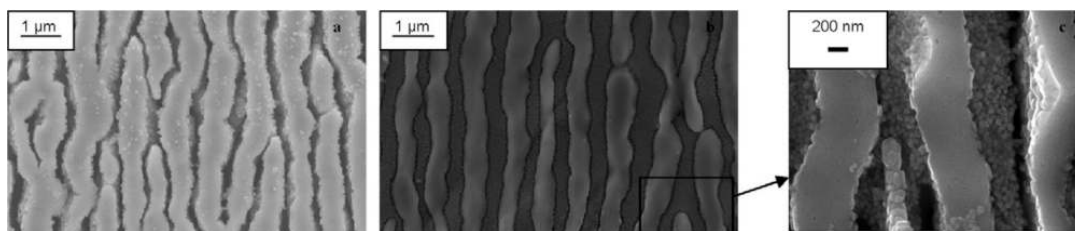
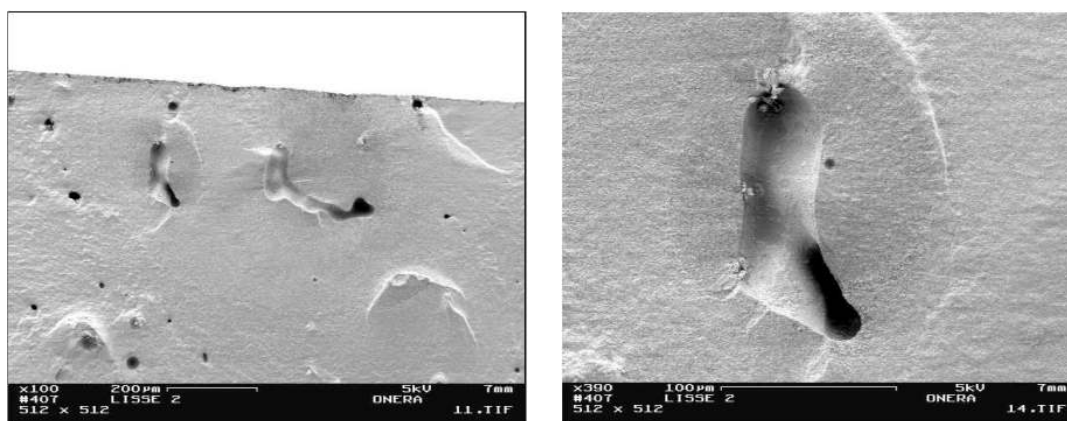


Figure 1.12: Examples of microstructural changes observed experimentally for anisothermal conditions in [Cormier et al. \[2008\]](#)



(a) Observed pores in the specimen

(b) Close-up view of one of the two major pores on the left

Figure 1.13: Experimentally observed pores in an AM1 specimen [Kaminski \[2007\]](#)

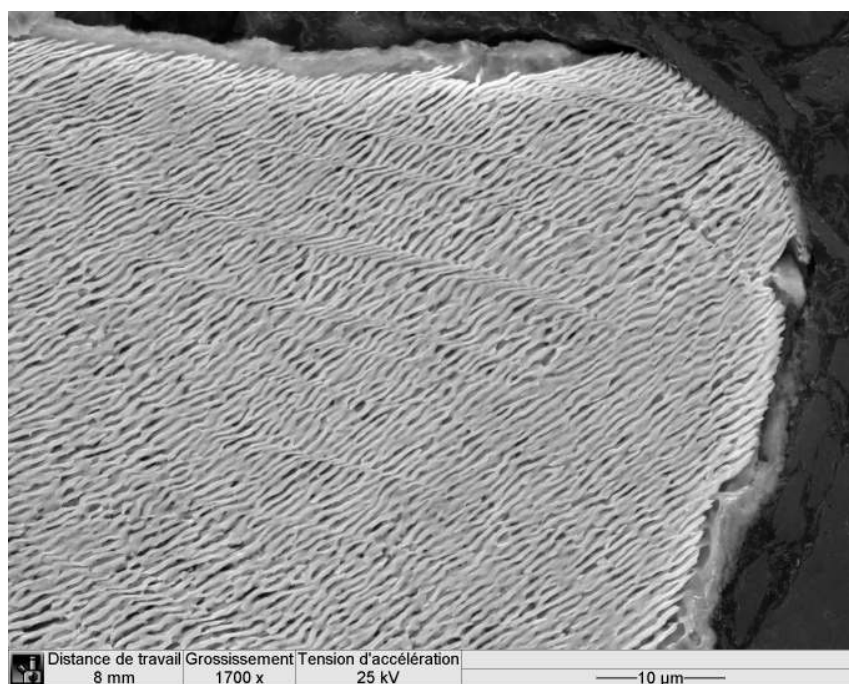


Figure 1.14: Microstructural changes near a crack bifurcation in a creep specimen; *Images courtesy: Institute P', ENSMA*

## 1.4 Conclusion

Following the discussions from earlier sections, a basic set of requirements for an effective generalised numerical model can be deduced. These are summarised as follows:

- **Anisotropic elasticity:** The FCC lattice structure of the NBSX crystals results in an anisotropic response in the form of cubic elasticity. Thus, a model used for NBSX superalloys must be capable of handling cubic elasticity to ensure the correct material response is obtained for loading under different orientations.
- **Anisotropic plasticity:** The occurrence of inelastic deformation by the motion of dislocations along the octahedral slip systems implies that the evolution of plastic slip is also anisotropic in nature. Various simulations and analyses have shown that plasticity models based on crystal plasticity theory are able to predict the material response in a reasonably accurate manner. Hence, a conclusion can be drawn that a model that incorporates crystal plasticity in some form is a must for inelastic simulations in NBSX superalloys.
- **Anisotropic damage:** Irrespective of the anisotropic (for example monocrystalline *or* directionally solidified alloys) or isotropic (polycrystalline alloys) nature of materials, the damaging process has been observed to be anisotropic. This would imply that a reasonably accurate description of damage would need to incorporate a direction/orientation dependent representation of damage. Consequently, this is considered an indispensable property for the models to be discussed in Part III of this thesis.

The discussions presented above recapitulate the micromechanics that drive the development of cracks in NBSX superalloys. So far, the effect of plasticity on damage has been discussed in a clear manner. It is clear that the development of cracks is strongly affected by the development of slip bands, kink bands, persistent slip bands etc. However, what has not been discussed explicitly is the effect on damage on the evolution of plasticity. Experiments on perforated specimens (see for example [Scheyvaerts and Pardoen \[2010\]](#)) show the localisation of slip bands in the regions between perforations intended to represent pores. Micrographs also show intense slip localisation between voids during the void coalescence phase of ductile fracture. These observations indicate that it is possible in real materials, that the accumulation of damage (voids, cavities etc.) in a particular region of a macroscopic specimen causes a localised weakening of the material. This means that in this locally weakened region, the material yields more readily as compared to a virgin material. Irrespective of the physical material mechanisms involved in such a localised weakening of material, it is hypothesised that such behaviour can be captured by the introduction of an additional coupling which leads to the evolution of the plasticity threshold along with the evolution of damage. To implement this hypothesis, the following additional requirement is imposed on the material model developed in this thesis:

- *Models are required to have a two-way coupling between the mechanisms of plasticity and damage.*

It is emphasised that in the above stated requirement, the reference to a “two-way” coupling implies that the evolution of damage must influence the development of plasticity and, likewise, the development of plasticity must influence the development of damage in the material. The rest of the chapters in this thesis describe the development of

## 1.4. Conclusion

---

a fully coupled elastic-viscoplastic-damage model that is aimed at fulfilling the four micromechanics motivated requirements identified in this chapter.

## Chapter 2

# Essentials of material modelling

### Résumé

Le deuxième chapitre présente les aspects qui sont utilisés dans la modélisation numérique des fissures. Le chapitre contient aussi une description générale de l'approche pour obtenir les équations constitutives qui sont thermo-mécaniquement cohérentes.

The complete modelling of all the mechanisms involved in the ductile fracture of metals leads to very complex numerical models which demand vast amounts of computational resources. Consequently, practical numerical modelling of material mechanisms demand the use of modelling concepts that are representative of the actual phenomena. In this context, phenomenological models that are partially based on micromechanical considerations present an ideal option for numerical implementation. The following sections present the phenomenological concepts used in the numerical models discussed in this thesis. While anisotropic elasticity has been identified as one of the requirements for a NBSX model, the reader is directed to the better sources in literature (see for example [Lubarda \[2002\]](#)) for detailed discussions of concepts related to modelling of elasticity. The chapter presents some concepts that are inherent to the crystal plasticity model used in the studies presented in the thesis. The plasticity related concepts are then followed by a discussion of certain essential concepts involved in the form of damage-modelling considered here. Lastly, the steps involved in the development of thermodynamically consistent material models are reviewed in brief.

## 2.1 Phenomenological concepts

### 2.1.1 Plasticity related concepts

#### Plastic yield criterion

Recalling the experimental observations that the plastic slip occurs along crystallographic planes with dense atomic packing, it is possible to define crystal plasticity models which model inelastic deformation confined to the crystallographic planes with the help of slip systems. A slip system  $s$  is defined in terms of slip plane normals  $\underline{m}^s$  and slip directions  $\underline{l}^s$ . The four octahedral slip planes and the three macroscopic cubic slip planes in an FCC single crystal are shown in Figures 1.7 and 1.6 respectively. Apart from the knowledge of

the slip planes, a yield criterion is needed to represent the activation of plasticity. Schmid [1924] proposed that plastic slip in crystalline material occurs when the Resolved Shear Stress (RSS) exceeds a Critical Resolved Shear Stress (CRSS) value. This concept can be understood by the simple example of a crystalline cylinder of area  $A$ , subject to a load  $F$  (see Figure 2.1a). Assuming that the plastic slip in the cylinder occurs in slip plane  $s$  (with slip normal  $\underline{m}^s$  and slip direction  $\underline{l}^s$ ), the RSS  $\tau^s$  in the glide plane is given by

$$\tau^s = \sigma \cos(\lambda) \cos(\phi) \quad (2.1)$$

Now, according to Schmid's law, inelastic glide on the plane would occur if

$$|\tau^s| \geq \tau_c \quad (2.2)$$

Although Schmid proposed this law on the basis of deformation in Zinc crystals, it has been found to be reasonably accurate for most crystalline deformation. A detailed discussion of the Schmid law can be found in Schmid [1924]. For our purposes, the Schmid criterion is implemented due to its simplicity and effectiveness.

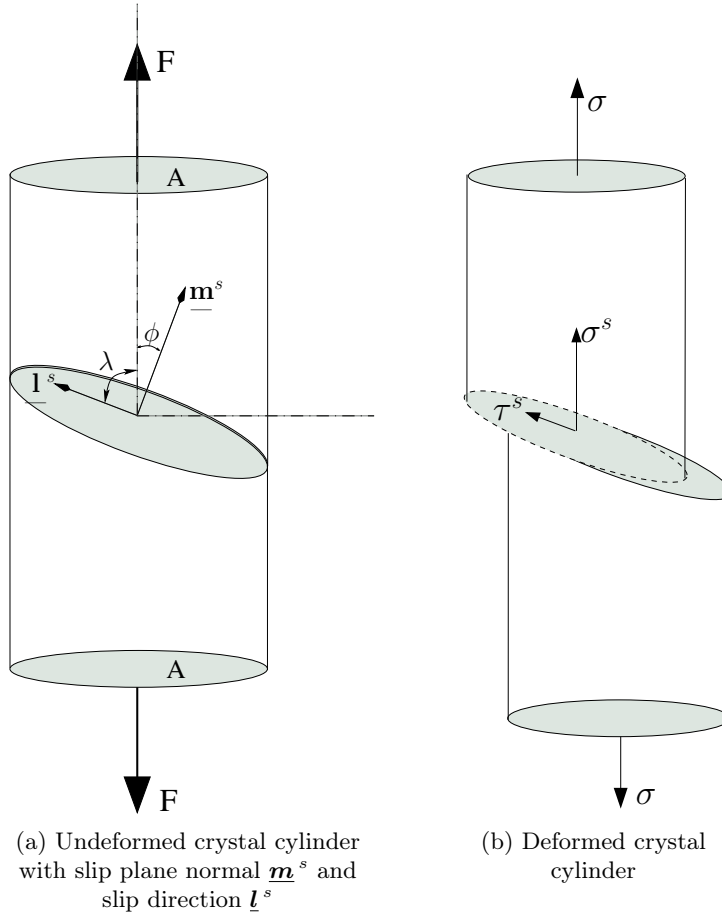


Figure 2.1: Simple illustration of Schmid's law;  
*Plastic deformation occurs when  $\tau^s$  exceeds  $\tau_c$ .*  
 (note: Here, Cauchy stress  $\sigma = \frac{F}{A}$ )

### Isotropic and kinematic hardening

In Chapter 1, it was indicated that the crystal plasticity models are based on the theory of dislocations. Experimental observations indicate that an increased amount of shear in a slip

plane leads to an increase in the shear-resistance of the plane. This mechanism is usually referred to as the “self-hardening” mechanism. The self-hardening mechanism however, does not account for the interaction between slip systems. The hardening caused by this interaction between different slip systems is also referred to as “latent-hardening”. To be more precise, latent hardening describes the process where the motion of a dislocation on a slip system  $s$  causes hardening in slip systems  $r \neq s$ . Other hardening effects can be found in superalloys due to the presence of solid solutes, precipitates etc. A convenient way of representing the hardening observed in crystals, is to use a hardening law in the form

$$\Delta\tau^s \propto \sum_r h^{sr} \Delta\gamma^r, \quad (2.3)$$

where  $h^{sr}$  is a matrix that represents latent hardening. In the case that no interaction between slip systems is considered,  $h^{sr}$  can be substituted by the identity matrix.  $\gamma^s$  represents the accumulated plastic strain on a slip system  $s$ . The process of strain-hardening, which relates to the self and latent hardening mechanisms, is usually modelled numerically by considering either a linear or non-linear increase in the plastic threshold  $r$ . Thus, a very common way of modelling material hardening is to use the relation

$$\tau_c^s = r^s = r_0 + Q \sum_r h^{sr} \gamma^r, \quad (2.4)$$

which represents an increase in the initial yield threshold for system  $r_0$ . The equation 2.4 represents a linear hardening relation for a slip system  $s$ , and represents the phenomenological concept of “isotropic hardening”, which relates to an expansion of the yield surface. A schematic representation of isotropic hardening is shown in Figure 2.2. It is pointed out that for a case where interaction between slip systems is isotropic ( $h^{sr} = 1$ ), the equation reduces to

$$r^s = r = r_0 + Q \sum_r \gamma^r \quad (2.5)$$

Thus, in the case that the matrix  $h^{sr}$  is the unity matrix, all the slip systems will have the same plastic yield threshold. In such a case, it is possible to use a single yield threshold for all the slip systems in a crystal.

It is also important to note that in many crystalline material, dislocation densities are known to saturate upon continued plastic yielding. Thus, from a micromechanical perspective, a hardening model based on saturation of dislocation densities is preferable. In many single crystal material models, this is achieved by the use of a non-linear hardening law. One such example of a non-linear hardening law as presented in [Méric et al. \[1991\]](#) is given as

$$r^s = r_0 + Q \sum_r h^{sr} (1 - e^{-bv^r}) \quad (2.6)$$

In the above relation, the term  $(1 - e^{-bv^r})$  is the representation of the exponential saturation of dislocation density, given in terms of the cumulative slip,  $v^s = |\dot{\gamma}^s|$ . For a more detailed description of the non-linear hardening, the reader is referred to [Besson et al. \[2010\]](#). However, a generalised method to obtain the evolution equations for the so-called “internal variables” ( $v^s$  in this case) is discussed towards the end of the present chapter.

The material phenomenon known today as the “Bauschinger Effect” was known to researchers as early as in the late 1800s. The phenomena is characterised by an increase in the plastic yield threshold for tensile loading, and a corresponding decrease in the plastic yield threshold in compression. Numerical modelling of the Bauschinger effect is achieved

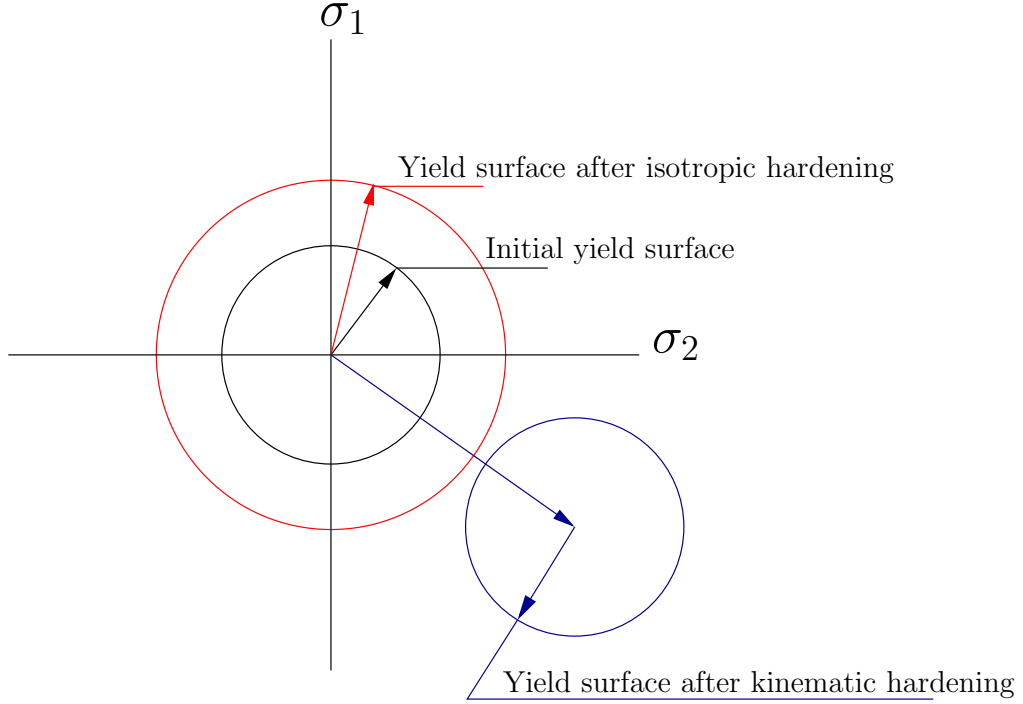


Figure 2.2: Schematic representation of numerical hardening concepts. (a) Red circle representing isotropic hardening by the expansion of the initial yield surface. (b) Blue circle representing kinematic hardening by a translation of the original yield surface. The yield surfaces are shown in a 2D principal stress space.

with use of the concept of kinematic hardening, where the size of the yield surface is not changed, but is just translated. Figure 2.2 shows in Blue, a schematic representation of kinematic hardening and schematic representation of isotropic hardening in Red.

One of the classical kinematic hardening laws used for single crystals is given as

$$x^s = C\alpha^s \quad (2.7)$$

$$\dot{\alpha}^s = \dot{\gamma}^s - D\dot{v}\alpha^s \quad (2.8)$$

where  $x^s$  represents the translation of the yield surface,  $\alpha$  is the state variable that represents the micromechanical processes that cause kinematic hardening in the material.  $C$  and  $D$  are material constants that are calibrated by experimental studies. The plasticity yield criteria  $f_p^s$  is then modified to include kinematic hardening as

$$f_p^s = |\tau^s - x^s| - r^s \quad (2.9)$$

Further details concerning the law can be found in [Besson et al. \[2010\]](#).

### 2.1.2 Fracture and damage related concepts

#### Classical modes of failure

The conventional study of what is today popular as “Fracture Mechanics” rose to prominence only in the aftermath of Griffith’s seminal work (see [Griffith \[1921\]](#)). In his article, Griffith introduced the idea of fracture as a balance between bulk and surface energies. Following this publication, many analytical solutions were developed. Some of

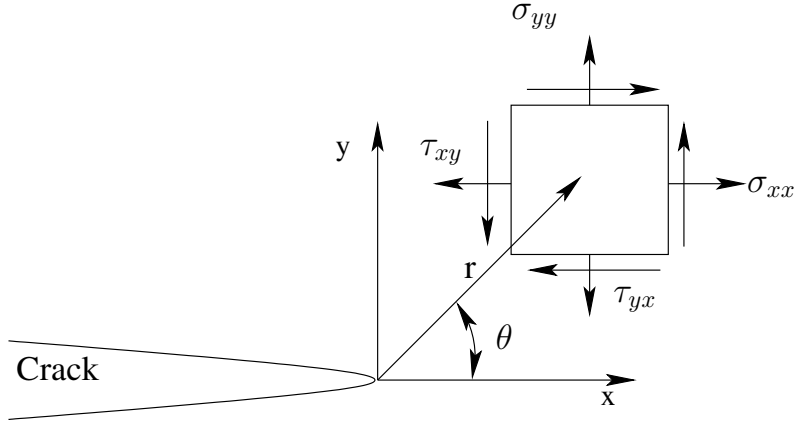


Figure 2.3: Local definition of cylindrical coordinate system at crack tip

the most prominent contributions such as the the Stress-Intensity-Factor (SIF) by [Irwin \[1957\]](#) belong to the school of Linear Elastic Fracture Mechanics (LEFM). A number of books describing the LEFM and the extension of LEFM concepts to plasticity by the inclusion of the plastic zones around a crack tip are available (see for example [Gross and Seelig \[2006\]](#), [Anderson \[2005\]](#)). The J-integral method introduced by [Rice \[1967\]](#) is another popular method, aimed originally at 2D cracks in materials with small scale yielding at the crack tip.

In classical LEFM, the fields ahead a crack tip are typically characterised by a SIF, first introduced by [Irwin \[1957\]](#). The use of the SIF, usually denoted by  $K$  can be given by the generalised relation

$$\sigma_{ij}(r, \theta) = \frac{K}{\sqrt{2\pi r}} f_{ij}(\theta) \quad (2.10)$$

where  $\sigma_{ij}$  denotes the stress field,  $r$  denotes the distance from the crack tip and  $f_{ij}$  is a dimensionless function that depends on the loading imposed on the specimen and on the geometry of the specimen. It is noted that all measurements in the given formula are made using a cylindrical coordinate system defined locally at the crack tip (see Figure 2.3). It is obvious that as  $r \rightarrow 0$ , the stress  $\sigma_{ij}$  tends to  $\infty$ .

A majority of these methods require a pre-existing crack and hence are not applicable in cases, where crack initiation is also to be predicted. Furthermore, the analytical solutions provided in fracture data handbooks are obtained often by analysis of simple experimental specimens. In addition to being empirical in nature, many such equations are often obtained from experiments on isotropic specimens and are hence inapplicable to materials such as NBSX. An indispensable outcome of classical fracture studies is the concept of *Modes of failure*. Failure is categorised into three modes of fracture, which are shown in Figure 2.4.

As is clear from the figure, the modes are classified on the type of loads driving the fracture. The three modes are identified as *Opening* (Mode I), *Sliding* (Mode II) and *Tearing* (Mode III). The concept of the three modes is an important one as it allows one to model complex features of failure such as crack branching and crack bifurcation. Consider for example, the popular G-criterion, which provides a relation between the resistance to fracture offered by a cracked specimen (the so-called ‘‘Fracture Toughness’’  $K_{IC}$ ) and the SIFs defined for each of the three modes of failure. The relation for  $K_{IC}$  is given by (after

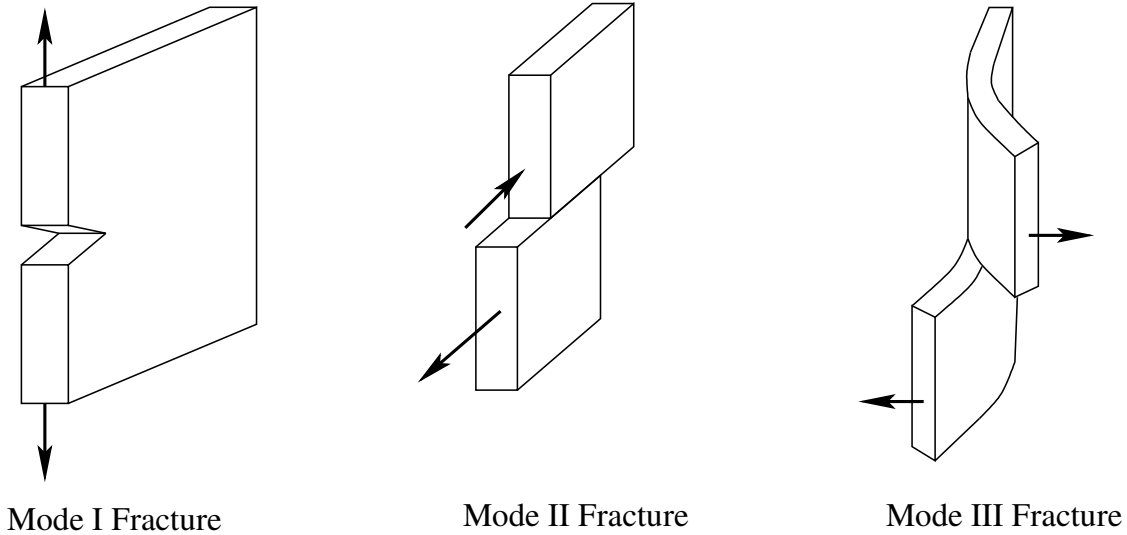


Figure 2.4: The three classical modes of fracture

Sih and MacDonald [1974]):

$$K_{Ic}^2 = K_I^2 + K_{II}^2 + \frac{E}{2\mu} K_{III}^2 \quad (2.11)$$

It is worth noting that the determination of SIF depends on the loading and on the geometry of the specimen considered. This makes the use of SIF complicated when anisotropic materials or components with complex geometry are subject to mixed mode loading conditions. Further discussions of fracture mechanics related concepts can be found in literature (Gross and Seelig [2006], Anderson [2005]). At this point we proceed with the notion that the modes of failure are an important concept that is to be accounted for in the model developed for NBSX superalloys.

### Anisotropic damage, opening and accommodation

The difficulties observed in classical fracture mechanics led to the development of the micromechanically based “local approach” to modelling failure. As the name suggests, the approach is based on the description of damage in a material at a local level. The method presents, very often, non-linear models that describe via constitutive equations, the evolution of damage in a material. For a detailed discussion of damage models, the reader is referred to works by Besson et al. [2004], Lemaitre and Desmorat [2005]. One of the biggest advantages of this method is the ease with which anisotropic damage can be accommodated. Examples of anisotropic damage can be found for both, brittle and ductile materials, in the articles by Qi and Bertram [1999], Lemaitre et al. [2000], Feng et al. [2002], Brünig [2003], Ekh et al. [2004], Bargellini et al. [2009], Badreddine et al. [2010] etc. Anisotropic damage is usually modelled by the consideration of a tensorial damage variable, which complicates the model in terms of numerical implementation. To address this complexity, the concept of “Opening and Accommodation systems” is introduced (see also Marchal [2006]).

Damage evolution in NBSX has been observed to occur along specific crystallographic planes. This observation can be leveraged to obtain a simplified representation of a crystallographic system of damage. Let us begin with an assumption that “damage” in

a material is defined as a strain-like dimensionless quantity, which represents in some abstract form, an opening in the crystallographic lattice, along a chosen plane. Now, from Figure 2.4, it is clear that for a complete description of the three modes of fracture, a set three damage variables corresponding to three mutually perpendicular directions are necessary. Let this set be denoted by

$$\mathcal{D}: = d_1, d_2, d_3 \quad (2.12)$$

Consider once again, a simple cylinder subject to tensile loading (Figure 2.5). Assuming that the damage evolution occurs on a particular plane, it is possible to obtain from the imposed load, the load acting normal to the damage plane. This load is referred to as  $\sigma_n = \underline{\mathbf{n}} \cdot \underline{\boldsymbol{\sigma}} \cdot \underline{\mathbf{n}}$ , with  $\underline{\mathbf{n}}$  as the unit vector normal to the damage plane. It is also clear that the shear loads in the directions  $\underline{\mathbf{a}}_1$  and  $\underline{\mathbf{a}}_2$  can also be obtained in a manner not dissimilar to that of obtaining the resolved shear stress for the Schmid criterion in plasticity. Following the identification of these three stress components acting on the chosen damage plane, it is possible to define a criterion that describes the activation of damage component that corresponds to a particular direction on the chosen damage plane. The criterion for the activation of each damage component is chosen in a form analogous to the Schmid criterion for plasticity. This is given by the equation

$$\sigma_n \geq \sigma_{n_{crit}} \quad (2.13)$$

for the opening mode corresponding to the damage component  $d_1$

$$\sigma_{ai} \geq \sigma_{ai_{crit}} \quad \text{for } i = 1, 2 \quad (2.14)$$

for the accommodation in directions  $\underline{\mathbf{a}}_1$  and  $\underline{\mathbf{a}}_2$ , corresponding to the damage components  $d_2$  and  $d_3$  respectively. Following the definition of such criteria, it is possible to describe the evolution of the damage components as a function of the yield criteria.

In the above presented mechanism of damage, the evolution of damage along the normal to the damage plane is called, and will henceforth be referred to as ‘‘Opening’’. The two in plane shear components corresponding to the direction vectors  $\underline{\mathbf{a}}_1$  and  $\underline{\mathbf{a}}_2$  will henceforth be referred to as ‘‘Accommodation’’. The details concerning the numerical implementation of these concepts will be discussed in Part III. It is worth noting that the definition of damage in this form allows for an easy incorporation of mixed modes of failure and of anisotropic damage models.

With the concept descriptions provided above it is possible to develop an effective material model to describe failure in a material. The following section presents in brief the methodology used to obtain thermodynamically consistent constitutive relations for the material models.

## 2.2 Constitutive modelling of materials

A continuum material model represents a black box that defines the mathematical relations between variables representing the active mechanisms in a material and their corresponding force conjugates. The use of the principle of virtual power allows for the derivation of some of the necessary constraints imposed on a specimen being simulated. More specifically, they allow for the derivation of balance relations, which provide a link between the bulk and surface forces. However, they do not provide any indication or information about the evolution of variables that cannot be externally controlled/measured (i.e. the so-called ‘‘Internal Variables’’) or their conjugate forces. The process of obtaining controlling

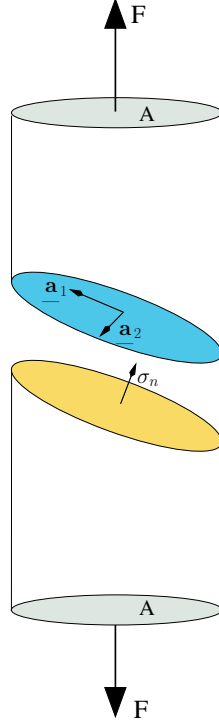


Figure 2.5: Simple representation of concepts of opening and accommodation.  $\underline{a}_1$  and  $\underline{a}_2$  represent the accommodation directions,  $\sigma_n$  represents the stress acting normal to the crystallographic damage plane.  $F$  is the force applied on the specimen.

relations for these internal variables/conjugate forces is called constitutive modelling. The following section reviews briefly the steps involved in a thermodynamically consistent modelling of material behaviour.

The starting point of any thermodynamically sound model must be the consideration of the energy and entropy balance relations, the local forms of which are given as

$$\rho \dot{\epsilon} = \underline{\sigma} : \underline{\dot{\xi}} + \rho r - \text{div } \underline{q} \quad (2.15)$$

$$\rho \dot{\eta} + \text{div } \left( \frac{\underline{q}}{T} \right) - \frac{\rho r}{T} \geq 0 \quad (2.16)$$

In the energy balance relation (Equation 2.15),  $\epsilon$  is the specific energy of the system,  $\underline{\sigma}$  denotes the Cauchy stress,  $\underline{\xi}$  represents the strain in the system,  $r$  is the heat supply and  $\underline{q}$  the heat flux in the system. The terms  $\eta$  and  $T$  in the entropy balance (Equation 2.16) denote specific entropy and temperature at the material point respectively.

The introduction of the energy balance into the entropy inequality leads to the Clausius-Duhem inequality (CDI), given as

$$-\rho(\dot{\epsilon} - T\dot{\eta}) + \underline{\sigma} : \underline{\dot{\xi}} - \frac{\underline{q}}{T} \cdot \text{grad } T \geq 0 \quad (2.17)$$

Introduction of the Legendre transform (Equation 2.19) allows the CDI to be rewritten in the form of Equation 2.18.

$$-\rho \dot{\psi} + \underline{\sigma} : \underline{\dot{\xi}} - \frac{\underline{q}}{T} \cdot \text{grad } T \geq 0 \quad (2.18)$$

$$\psi = \epsilon - T\eta \quad (2.19)$$

Equation 2.18 represents the dissipation in a system, and can be split into local and conductive parts. These are given by the relations

$$\rho \mathcal{D}_{loc}: = -\rho \dot{\psi} + \underline{\boldsymbol{\sigma}} : \underline{\dot{\boldsymbol{\varepsilon}}} \geq 0 \quad (2.20)$$

$$\rho \mathcal{D}_{cond}: = -\frac{\mathbf{q}}{T} \text{grad } T \geq 0 \quad (2.21)$$

In the models discussed in the following chapters, no thermal effects are considered. Consequently, the necessary constitutive relations can be obtained by the consideration of the local dissipation relation alone (Equation 2.20). It is noted that the local and conductive dissipation inequalities in Equations 2.20 and 2.21 are also referred to as the Clausius-Planck-Inequality (CPI) and the Fourier-Inequality (FI) respectively.

The main aim of deriving the thermodynamic dissipation inequality represented by the CPI, is to use the CPI to derive energy based relations that link the dissipative mechanisms in a material and their corresponding force conjugates. With the CPI in place, the next step is to define a Free Energy Functional (FEF) that depends on a desired set of variables. For pedagogic purposes, a simple FEF depending on elastic component of the strain tensor  $\underline{\boldsymbol{\varepsilon}}^e$  and internal variable  $\alpha$  is considered.

$$\Psi = \hat{\Psi}(\underline{\mathbf{x}}, \underline{\boldsymbol{\varepsilon}}^e, \alpha) \quad (2.22)$$

By the principle of equipresence, the thermodynamic conjugate forces of  $\underline{\boldsymbol{\varepsilon}}$  and  $\alpha$ ,  $\underline{\boldsymbol{\sigma}}$  and  $x$  respectively are given by

$$\underline{\boldsymbol{\sigma}} = \hat{\boldsymbol{\sigma}}(\underline{\mathbf{x}}, \underline{\boldsymbol{\varepsilon}}^e, \alpha) \quad (2.23)$$

$$x = \hat{x}(\underline{\mathbf{x}}, \underline{\boldsymbol{\varepsilon}}^e, \alpha) \quad (2.24)$$

Considering a simple additive split of the total strain tensor into reversible (elastic component  $\underline{\boldsymbol{\varepsilon}}^e$ ) and irreversible parts (plastic component  $\underline{\boldsymbol{\varepsilon}}^p$ ),

$$\underline{\boldsymbol{\varepsilon}} = \underline{\boldsymbol{\varepsilon}}^e + \underline{\boldsymbol{\varepsilon}}^p \quad (2.25)$$

The insertion of the FEF into the 2.20 yields

$$\rho \mathcal{D}_{loc}: = \left( \underline{\boldsymbol{\sigma}} - \rho \frac{\partial \Psi}{\partial \underline{\boldsymbol{\varepsilon}}^e} \right) : \underline{\dot{\boldsymbol{\varepsilon}}}^e + \underline{\boldsymbol{\sigma}} : \underline{\dot{\boldsymbol{\varepsilon}}}^p - \rho \frac{\partial \Psi}{\partial \alpha} \dot{\alpha} \geq 0 \quad (2.26)$$

The relation in Equation 2.26 must hold for arbitrary rates of strain and internal variable evolution. This implies that the terms included in the brackets must vanish to ensure non-trivial solutions. Thus, the final constitutive relations for the stress state is given as

$$\underline{\boldsymbol{\sigma}} = \rho \frac{\partial \Psi}{\partial \underline{\boldsymbol{\varepsilon}}^e} \quad (2.27)$$

and the residual dissipation is given by

$$\underline{\boldsymbol{\sigma}} : \underline{\dot{\boldsymbol{\varepsilon}}}^p - \rho \frac{\partial \Psi}{\partial \alpha} \dot{\alpha} \geq 0 \quad (2.28)$$

where,

$$x = \rho \frac{\partial \Psi}{\partial \alpha} \quad (2.29)$$

represents the thermodynamic conjugate of the internal variable  $\alpha$ . The above approach also known as Coleman's exploitation method, has been developed in the framework of

## 2.2. Constitutive modelling of materials

---

rational mechanics (see [Truesdell \[1969\]](#)). For a more detailed discussion of the approach, see [Coleman and Noll \[1963\]](#).

*Note: The models in the following chapters do not consider thermal aspects. Consequently the temperature and thermal gradients are excluded from the FEF dependency list.*

In addition to obtaining the constitutive relations for the state variables, equations that describe the evolution of the internal variables are necessary. Such relations are obtained by the consideration of a dissipation potential  $\Phi$ , which is defined by

$$\Phi = \hat{\Phi}(\boldsymbol{\sigma}, x) \quad (2.30)$$

From the relation for residual dissipation (Equation 2.28), it is clear that evolution equations are needed for the variables  $\alpha$  and  $\tilde{\boldsymbol{\varepsilon}}^p$ , which cannot be measured physically. The evolution equations are then obtained as

$$\dot{\alpha} = -\frac{\partial \Phi}{\partial x} \quad (2.31)$$

$$\dot{\tilde{\boldsymbol{\varepsilon}}}^p = \frac{\partial \Phi}{\partial \boldsymbol{\sigma}} \quad (2.32)$$

$$(2.33)$$

The generalised procedure described above is used in later chapters to obtain thermodynamically consistent coupled continuum model.



## Part II

# Crystal Plasticity simulations of NBSX



## Chapter 3

# Plasticity evolution in NBSX

### Résumé

Le troisième chapitre présente le modèle de plasticité cristalline pour le cas d'un monocristal. Les outils de post-traitement, ( $\gamma$ -maps et le visibility index) sont introduits. L'outil  $\gamma$ -maps permet d'identifier les systèmes de glissement les plus actifs dans une région d'intérêt. Le deuxième outil, le visibility index, permet d'identifier la visibilité des traces de glissement sur un plan d'observation choisi; dans le cas considéré, les indices pour trois orientations sont présentés. La combinaison de ces deux outils permet la comparaison entre les simulations et les expériences par l'examen visuel.

The following chapter presents the classical crystal plasticity material model as discussed in Mandel [1973; 1974], Méric et al. [1991]. Both, *Small-strain* and *Large-strain* formulations are considered. Following the discussion of the numerical model, a post-processing tool, the  $\gamma$ -maps, is introduced. Along with the post-processing tool, a complementary index called the *Visibility Index* is also introduced with a view to comparing simulation results with the experimental observation of slip line activity. Various application possibilities of the post-processing tool are then explored in the following chapters (Chapters 4 and 5). The studies presented in this part of the thesis showcase only a few of the possible applications of crystal plasticity. A more thorough overview is provided by Roters et al. [2010].

### 3.1 Crystal plasticity theory

#### Kinematics

Consider a body  $\mathcal{B}$  in its reference configuration that is enclosed by a collection of boundary points  $\mathcal{S}$ . Each material point  $\mathcal{P}$  has a unique placement function  $\chi(\mathcal{P}, t)$ , which allows the identification of position vectors  $\underline{\mathbf{X}}$  at time  $t \geq t_0$  (i.e. the reference configuration) and  $\underline{\mathbf{x}}$  at time  $t > t_0$  (i.e. the deformed/actual configuration). Using this definition of position vectors, it is possible to define a displacement vector  $\underline{\mathbf{u}}$  and its gradient (w.r.t. the reference configuration) as

$$\underline{\mathbf{x}} = \chi(\mathcal{P}, t) \quad ; \quad \underline{\mathbf{X}} = \chi(\mathcal{P}, t_0) \quad (3.1)$$

$$\underline{\mathbf{u}} = \underline{\mathbf{x}} - \underline{\mathbf{X}} \quad (3.2)$$

$$\underline{\mathbf{F}}: = \nabla \underline{\mathbf{x}} = \underline{\mathbf{1}} + \nabla \underline{\mathbf{u}} \quad (3.3)$$

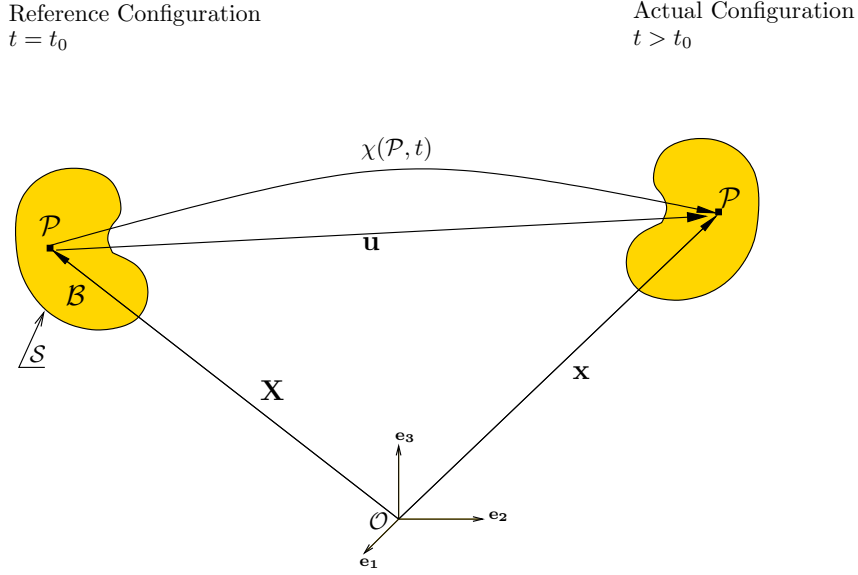


Figure 3.1: Definition of continuum transformations

The mapping of position vectors and displacement vectors is shown in Figure 3.1.

$$\tilde{\mathbf{F}}(\underline{\mathbf{X}}) = \underline{\mathbf{1}} + \nabla \underline{\mathbf{u}} = \underline{\mathbf{1}} + \frac{1}{2} (\nabla \underline{\mathbf{u}} + \nabla^T \underline{\mathbf{u}}) + \frac{1}{2} (\nabla \underline{\mathbf{u}} - \nabla^T \underline{\mathbf{u}}) \quad (3.4)$$

Introducing the strain and rotation tensors  $\underline{\varepsilon}$  and  $\underline{\omega}$  as the symmetric and skew symmetric parts of the deformation gradient, we have

$$\underline{\varepsilon} = \frac{1}{2} (\nabla \underline{\mathbf{u}} + \nabla^T \underline{\mathbf{u}}) \quad ; \quad \underline{\omega} = \frac{1}{2} (\nabla \underline{\mathbf{u}} - \nabla^T \underline{\mathbf{u}}) \quad (3.5)$$

Equation 3.4 can be rewritten as

$$\tilde{\mathbf{F}} = \underline{\mathbf{1}} + \underline{\varepsilon} + \underline{\omega} \quad (3.6)$$

For the numerical modelling of crystal plasticity, Mandel [1973] suggested a generalised formulation in which a multiplicative decomposition of the deformation gradient tensor  $\tilde{\mathbf{F}}$ , into elastic and plastic parts ( $\tilde{\mathbf{F}}_e$  and  $\tilde{\mathbf{F}}_p$  respectively) is introduced. This split is shown in Figure 3.2. The decomposition of the deformation gradient is based on the introduction of an intermediate isoclinic configuration,  $dV^*$ , having the same crystal orientation as in the initial configuration. The intermediate configuration contains all the accumulated inelastic deformation in the continuum. The final/actual configuration  $dV'$  is then obtained by the elastic part  $\tilde{\mathbf{F}}_e$  of the multiplicative split, which accounts for lattice distortion and rotations in the material. The multiplicative decomposition is given by the relation

$$\tilde{\mathbf{F}} = \tilde{\mathbf{F}}_e \cdot \tilde{\mathbf{F}}_p \quad (3.7)$$

The polar decompositions of the elastic and plastic parts are then introduced as

$$\tilde{\mathbf{F}}_e = \underline{\mathbf{R}}^e \cdot \underline{\mathbf{U}}^e \quad (3.8)$$

$$\tilde{\mathbf{F}}_p = \underline{\mathbf{R}}^p \cdot \underline{\mathbf{U}}^p \quad (3.9)$$

with the material stretch being represented by the tensors  $\underline{\mathbf{U}}^e$  and  $\underline{\mathbf{U}}^p$ , and the material rotations being represented by the tensors  $\underline{\mathbf{R}}^e$  and  $\underline{\mathbf{R}}^p$ . The superscripts  $e$  and  $p$  denote

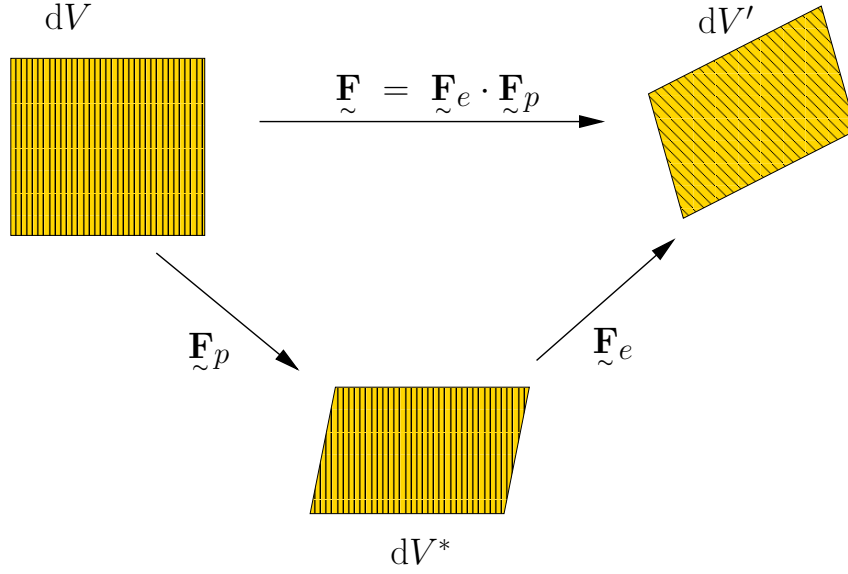


Figure 3.2: Multiplicative split of deformation gradient tensor,  $\tilde{\mathbf{F}}$  at the material point  $\mathcal{P}$

the elastic and plastic contributions respectively. These tensors can be further represented as

$$\tilde{\mathbf{U}}^e = \tilde{\mathbf{1}} + \tilde{\boldsymbol{\xi}}^e \quad (3.10)$$

$$\tilde{\mathbf{U}}^p = \tilde{\mathbf{1}} + \tilde{\boldsymbol{\xi}}^p \quad (3.11)$$

$$\tilde{\mathbf{R}}^e = \tilde{\mathbf{1}} + \tilde{\boldsymbol{\omega}}^e \quad (3.12)$$

$$\tilde{\mathbf{R}}^p = \tilde{\mathbf{1}} + \tilde{\boldsymbol{\omega}}^p \quad (3.13)$$

Thus, the deformation gradient tensor  $\tilde{\mathbf{F}}$  can be written down as

$$\tilde{\mathbf{F}} = (\tilde{\mathbf{1}} + \tilde{\boldsymbol{\omega}}^e) \cdot (\tilde{\mathbf{1}} + \tilde{\boldsymbol{\xi}}^e) \cdot (\tilde{\mathbf{1}} + \tilde{\boldsymbol{\omega}}^p) \cdot (\tilde{\mathbf{1}} + \tilde{\boldsymbol{\xi}}^p) \quad (3.14)$$

For metals, the elastic strain  $\boldsymbol{\xi}^e$  remains so small that the rotation matrix  $\tilde{\mathbf{R}}^e$  essentially gives the lattice rotation under deformation. When the plastic strain  $\boldsymbol{\xi}^p$  also is small, the decomposition provides the additive decomposition of the total strain which is frequently used in small strain formulations. I.e. for small elastic and plastic strains,

$$\|\tilde{\boldsymbol{\xi}}^e\| \ll 1; \|\tilde{\boldsymbol{\xi}}^p\| \ll 1; \|\tilde{\boldsymbol{\omega}}^e\| \ll 1; \|\tilde{\boldsymbol{\omega}}^p\| \ll 1 \quad (3.15)$$

Thus, Equation 3.14 reduces to

$$\tilde{\mathbf{F}} \approx \tilde{\mathbf{1}} + \tilde{\boldsymbol{\xi}}^e + \tilde{\boldsymbol{\xi}}^p + \tilde{\boldsymbol{\omega}}^e + \tilde{\boldsymbol{\omega}}^p \quad (3.16)$$

From Equations 3.16 and 3.6, we have

$$\tilde{\boldsymbol{\xi}} = \tilde{\boldsymbol{\xi}}^e + \tilde{\boldsymbol{\xi}}^p \quad (3.17)$$

$$\tilde{\boldsymbol{\omega}} = \tilde{\boldsymbol{\omega}}^e + \tilde{\boldsymbol{\omega}}^p \quad (3.18)$$

## 3.2 State and constitutive equations

Based on the multiplicative split of the deformation gradient tensor, the Green-Lagrange strain tensor can be introduced as

$$\tilde{\mathbf{E}} = \frac{1}{2} [\tilde{\mathbf{F}}_e^T \tilde{\mathbf{F}}_e - \tilde{\mathbf{1}}] \quad (3.19)$$

### 3.2. State and constitutive equations

Introducing the Piola Kirchhoff stress tensor  $\underline{\underline{\mathbf{\Pi}}}$  as

$$\underline{\underline{\mathbf{\Pi}}} = J_e \underline{\underline{\mathbf{F}}}_e^{-1} \underline{\underline{\boldsymbol{\sigma}}}_e \underline{\underline{\mathbf{F}}}_e^{-T} \quad (3.20)$$

and the Mandel stress tensor  $\underline{\underline{\mathbf{M}}}$  as

$$\underline{\underline{\mathbf{M}}} = J_e \underline{\underline{\mathbf{F}}}_e^T \underline{\underline{\boldsymbol{\sigma}}}_e \underline{\underline{\mathbf{F}}}_e^{-T} \quad (3.21)$$

the stress power can be rewritten as

$$J \underline{\underline{\boldsymbol{\sigma}}}_e : \dot{\underline{\underline{\mathbf{F}}}} \underline{\underline{\mathbf{F}}}_e^{-1} = \underline{\underline{\mathbf{\Pi}}} : \dot{\underline{\underline{\mathbf{E}}}} + \underline{\underline{\mathbf{M}}} : \dot{\underline{\underline{\mathbf{F}}}}_p \underline{\underline{\mathbf{F}}}_p^{-1} \quad (3.22)$$

It is noted that the  $J = \det(\underline{\underline{\mathbf{F}}})$ ,  $J_e = \det(\underline{\underline{\mathbf{F}}}_e)$ . In metals, plastic deformation is isochoric, thus  $J_p = \det(\underline{\underline{\mathbf{F}}}_p) = 1$ .

The introduction of the stress power into the generalised local dissipation relation yields the elasticity state law as

$$\underline{\underline{\mathbf{\Pi}}} : = \rho \frac{\partial \psi}{\partial \underline{\underline{\mathbf{E}}}} = \underline{\underline{\mathbf{C}}} : \underline{\underline{\mathbf{E}}} \quad (3.23)$$

where  $\underline{\underline{\mathbf{C}}}$  is a fourth order tensor representing the elastic moduli. It is pointed out the above relation is obtained upon the assumption of a quadratic potential w.r.t.  $\underline{\underline{\mathbf{E}}}$ . As mentioned earlier, the anisotropic nature of NBSX crystals is captured by the use of cubic crystal elasticity. Due to reasons of crystal symmetry,  $\underline{\underline{\mathbf{C}}}$  can be represented as a 6x6 matrix characterised by three material parameters; i.e.

$$\underline{\underline{\mathbf{C}}} = \begin{pmatrix} y_{1111} & y_{1122} & y_{1122} & 0 & 0 & 0 \\ y_{1122} & y_{1111} & y_{1212} & 0 & 0 & 0 \\ y_{1122} & y_{1122} & y_{1111} & 0 & 0 & 0 \\ 0 & 0 & 0 & y_{1212} & 0 & 0 \\ 0 & 0 & 0 & 0 & y_{1212} & 0 \\ 0 & 0 & 0 & 0 & 0 & y_{1212} \end{pmatrix} \quad (3.24)$$

The evolution of the plastic slip is modelled as a multimechanism problem with an internal variable  $\gamma^s$  being assigned to each slip system  $s$ . The evolution of  $\gamma^s$  is controlled by the implementation of the Schmid criterion, according to which plasticity commences only after the resolved shear stress  $\tau^s$  reaches a certain CRSS,  $\tau_c$ . The resolved shear stress which is given as

$$\tau^s = \underline{\underline{\mathbf{M}}} : (\underline{\underline{\mathbf{l}}}^s \otimes \underline{\underline{\mathbf{m}}}^s) \quad (3.25)$$

is introduced into the yield criteria, which is given by

$$f_p^s = |\tau^s| - \tau_c \quad (3.26)$$

$\underline{\underline{\mathbf{l}}}^s$  and  $\underline{\underline{\mathbf{m}}}^s$  are the slip direction and the normal to the slip plane respectively. The evolution of  $\gamma^s$  is controlled by a classical Norton type power law. In Equation 3.27, large values of  $n$  and low values of  $K$  lead to an almost ideal elastic-plastic behaviour in the usual range of strain rates.

$$\dot{\gamma}^s = \left\langle \frac{|\tau^s| - \tau_c}{K} \right\rangle^n \text{sign}(\tau^s) \quad (3.27)$$

The evolution of the plastic part of the deformation gradient  $\underline{\underline{\mathbf{F}}}_p$  is given by the relation

$$\underline{\underline{\mathbf{F}}}_p \underline{\underline{\mathbf{F}}}_p^{-1} = \sum_{s=1}^{12} \dot{\gamma}^s (\underline{\underline{\mathbf{l}}}^s \otimes \underline{\underline{\mathbf{m}}}^s) \quad (3.28)$$

In the simulations presented here, linear isotropic hardening is included and the interaction between slip systems is ignored, as recognised by [Nouailhas et al. \[1995\]](#) for Ni-base superalloys:

$$\tau_c = R_0 + Hv^s, \quad (3.29)$$

with

$$\dot{v}^s = |\dot{\gamma}^s| \quad (3.30)$$

where  $R_0$  is the initial critical resolved shear stress and  $H$  is the hardening modulus. It is worth noting that in small strain formulations with linearised strain tensors, the Mandel stress  $\underline{\mathbf{M}}$  in Equation 3.25 can be replaced by the Cauchy stress  $\underline{\boldsymbol{\sigma}}$  as the two become equivalent. Furthermore, in small-strain formulations, the multiplicative split of the deformation gradient tensor leads to an additive split of the total infinitesimal strain tensor ( $\underline{\boldsymbol{\varepsilon}}$ ) into elastic and plastic parts ( $\underline{\boldsymbol{\varepsilon}}^e$  and  $\underline{\boldsymbol{\varepsilon}}^p$  respectively). This split is recalled as

$$\underline{\boldsymbol{\varepsilon}} = \underline{\boldsymbol{\varepsilon}}^e + \underline{\boldsymbol{\varepsilon}}^p \quad (3.31)$$

For the infinitesimal case, the plastic strain rate is derived from equation 3.28 as

$$\dot{\underline{\boldsymbol{\varepsilon}}}^p = \sum_{s=1}^{12} \dot{\gamma}^s \left( \frac{1}{2} (\underline{\boldsymbol{l}}^s \otimes \underline{\boldsymbol{m}}^s + \underline{\boldsymbol{m}}^s \otimes \underline{\boldsymbol{l}}^s) \right) \quad (3.32)$$

### 3.2.1 Determination of slip system activity

A typical NBSX superalloy consists of an FCC lattice structure, which indicates the presence of 12 Octahedral slip systems on 4 slip planes. In addition to these principal slip systems, Nickel-base superalloys also exhibit macroscopic plastic slip along 6 cubic slip systems (see [Méric et al. \[1991\]](#)). The cubic slip systems are usually activated in the high-temperature operating regimes or for specific crystal orientations, like tension along [111] direction. In the case of loading along [001] directions considered in this work, the simulations presented in this paper incorporate only octahedral slip (i.e. slip along the 12 octahedral slip systems). The definitions of the slip systems used in the simulations are shown in Table 3.1. Various experimental results and corresponding modelling by [Nouailhas and Cailletaud \[1995\]](#) indicate that there is no interaction between the slip systems. Hence, no interaction matrix is introduced in the hardening law.

Similar to other metals with an FCC lattice structure, NBSX superalloys exhibit plastic slip evolution along the octahedral slip planes. In the simulations carried out in Chapters 4 and 5, only octahedral slip planes are considered. The slip systems are identified as shown in Table 3.1. The reasons for the non-inclusion of the cubic slip systems in the simulations has been discussed in Chapter 2.

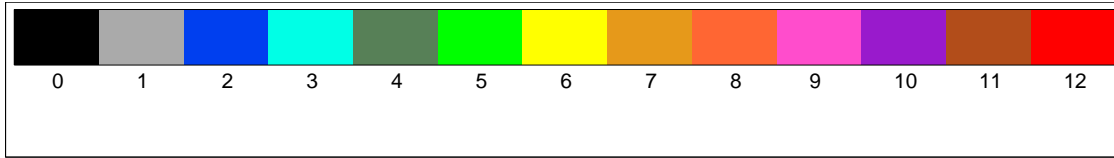
## 3.3 Post-processing procedures

### 3.3.1 Dominant slip system maps

The FE simulations provide the discretised fields of stress, strain, amounts of plastic slip  $\gamma^s$  and RSS  $\tau^s$  for all slip systems. The results presented in the following chapters show the maps of the dominant activated slip systems in the predicted plastic zone. The post-processing procedures used in the preparation of these maps are described in the following section.

Slip system number	Normal to slip plane	Slip direction
1	(1 1 1)	$[\bar{1} 0 1]$
2	(1 1 1)	$[0 \bar{1} 1]$
3	(1 1 1)	$[\bar{1} 1 0]$
4	(1 $\bar{1}$ 1)	$[\bar{1} 0 1]$
5	(1 $\bar{1}$ 1)	$[0 1 1]$
6	(1 $\bar{1}$ 1)	$[1 1 0]$
7	( $\bar{1}$ 1 1)	$[0 \bar{1} 1]$
8	( $\bar{1}$ 1 1)	$[1 1 0]$
9	( $\bar{1}$ 1 1)	$[1 0 1]$
10	(1 1 $\bar{1}$ )	$[\bar{1} 1 0]$
11	(1 1 $\bar{1}$ )	$[1 0 1]$
12	(1 1 $\bar{1}$ )	$[0 1 1]$

Table 3.1: Definition of slip systems used in the crystal plasticity model.


 Figure 3.3: Scale used for the dominant plastic slip maps ( $\gamma$ -maps). Each number corresponds to the respective slip system number as defined in Table 3.1. The number 0 indicates no plastic slip.

As a first step, the absolute values of the plastic slips at a given time step were computed at each integration point of the finite element mesh. The maximum among these values and the corresponding slip system number  $1 \leq n_{\max} \leq 12$  were stored. This field of  $n_{\max}$ , can be plotted as a contour map; these maps will henceforth be referred to as  $\gamma$ -maps. The scale used in the  $\gamma$ -maps is shown in Figure 3.3, unless otherwise indicated. Each number on the scale indicates the corresponding slip system as defined in Table 3.1. When, for symmetry reasons, several slip systems take the same highest slip value, the largest system number is retained for  $n_{\max}$  and a negative sign attached to this index, as a convention. The value  $n_{\max} = 0$  is attributed to material points undergoing purely elastic deformation. For the post processing procedures, a slip system is considered to be inactive when the absolute value of the plastic slip of that particular system is smaller than  $10^{-7}$ . This value is arbitrarily selected, but is essential in differentiating the regions of specimen undergoing purely elastic deformation from the regions exhibiting plastic slip.

### 3.3.2 Testing of the $\gamma$ -maps generated

To ensure that the post-processing procedure described above is able to handle cases of symmetry where two or more active slip systems attain identical highest slip values, the following tests were simulated. A single crystal specimen similar to a double edge notch specimen was considered. The dimensions were so chosen that the specimen was geometrically symmetric. This specimen was then modelled in 2- and 3-dimensions as a quarter piece symmetric and one-eighth piece symmetric specimen respectively. The

geometry definition and the crystal orientation considered for these test simulations are shown in Figure 3.4.

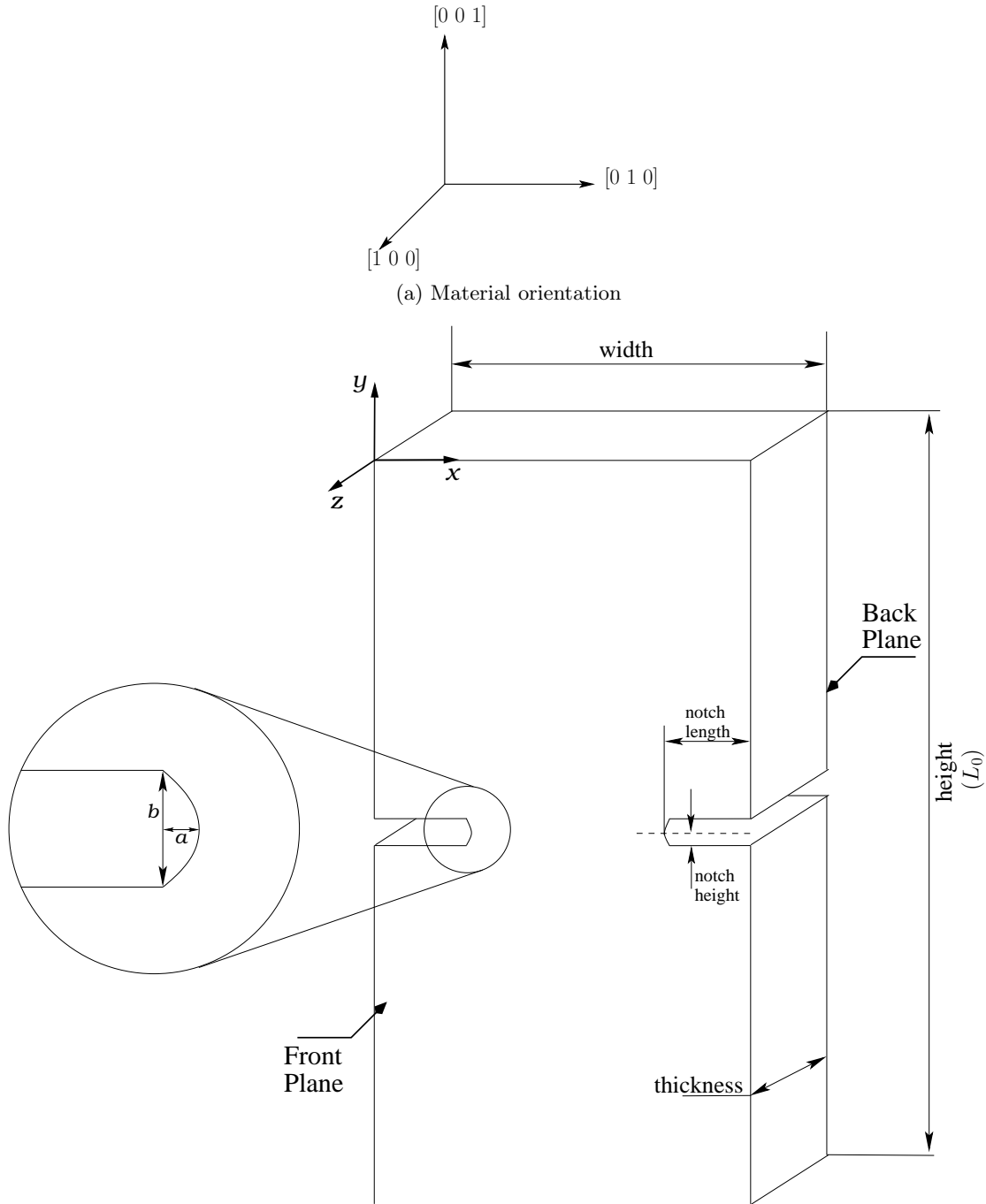


Figure 3.4: Specimen definition used for the testing of  $\gamma$ -maps

Displacement controlled loading was imposed on the top edge/face, along the [001] direction. The choice of specimen orientation was influenced by multiple factors. The imposition of loading on the [001] direction was chosen as this is the direction along which NBSX blades are grown. The four-fold symmetry of the (001)[010] orientation makes it the most suitable candidate to test the behaviour of the post-processing tool as it offers the greatest probability of multiple slip systems with an equal amount of plastic slip, and hence multiple dominant slip systems. Application of the post-processing procedure to

the results of the 2D simulations indicated multiple dominant slip systems (indicated by a negative index on the contour plot). The 2D model was then extruded to form a one-eighth symmetric 3D model of the same specimen. Symmetry boundary conditions were imposed on the 3D model and the monotonic tensile load was applied.

The application of the post-processing procedure to the results of the 3D computation resulted in unique dominant slip systems. The results of these two tests are shown in Figures 3.5 and 3.6. Considering a point of integration just ahead of the notch tip (second layer of elements from the notch tip along the horizontal axis), the 2D simulation indicates that there is indeed activation of multiple slip systems just ahead of the notch tip, such that there are multiple systems that have an equal amount of slip which is much greater than the other slip systems. Upon closer inspection, it is found that the systems 2, 5, 7 and 12 are most active, each with a  $\gamma$  of 0.0075. This is more than the other activated slip systems at the point which are systems 4 and 11, which show a  $\gamma = 0.003$ . The remaining slip systems show no plastic activity at this point. At the same location on the surface of the 3D test specimen, only slip system 4 is identified as the dominant system. This could possibly be attributed to the surface effect. At the symmetric core however, an activation of multiple slip systems is expected. The 3D simulations indicate otherwise. At the same location from the notch tip, the core shows slip system 2 as the dominant system with a  $\gamma$  located in between the values of 0.009 and 0.01. A close examination of each individual slip system indicates that the slip systems 5, 7 and 12 also exhibit very similar amounts of slip. Thus, the choice of only one particular slip system at the core can be attributed to differences arising from the numerics of the simulation. Such an observation also implies that 2D simulations could provide a good idea of the conditions at the core of a specimen, when the free surface is at sufficient distance from the core (sufficient enough that the surface effects do not influence the fields at the core).

The test simulations point at two aspects, (i) The numerical implementation of the post-processing procedure described in the earlier section is capable of handling cases of multiple dominant slip systems. (ii) The results indicating unique dominant slip systems near the free surface of the specimen (in the 3D case) originate from free surface and thickness effects. The unique dominant systems at the system core is attributed to numerical factors. This point will be discussed further in the following two chapters.

#### 3.3.3 Visibility index

The predicted  $\gamma$ -maps need not necessarily correspond to the slip lines visible on the surface of an experimental specimen. The “*Visibility Index*” (VI) is introduced as a complementary index to the  $\gamma$ -maps to help in the analysis of such cases. The visibility of the slip lines at the surface of the specimen depends on the Burgers vector’s component perpendicular to the  $z$ -axis. The VI here is defined as the absolute value of the scalar product between the normalised vector normal to the free surface as indicated for the different orientations in Figure 3.4 and the normalised slip direction of the slip system being considered (The slip direction vectors are defined in Table 3.1). In the following chapters, three main orientations are considered. These are shown in Figure 3.7. The VI of the slip systems for the different orientations are described in the Table 3.2.

In Table 3.2, a visibility index 0 indicates that the considered slip system does not have a slip/ displacement component perpendicular to the  $z$ -axis and hence does not create a step on the surface. Also, a greater value of the visibility index indicates a more prominent slip band.

In the following two chapters, experiments carried out on NBSX specimens are

presented for different secondary orientations. These tested orientations are shown in Figure 3.7. Figure 3.8 also shows the theoretically expected slip systems. The post-processing procedures described so far are applied to the simulations of the said experiments. The obtained  $\gamma$ -maps are then compared to the experimental observations.

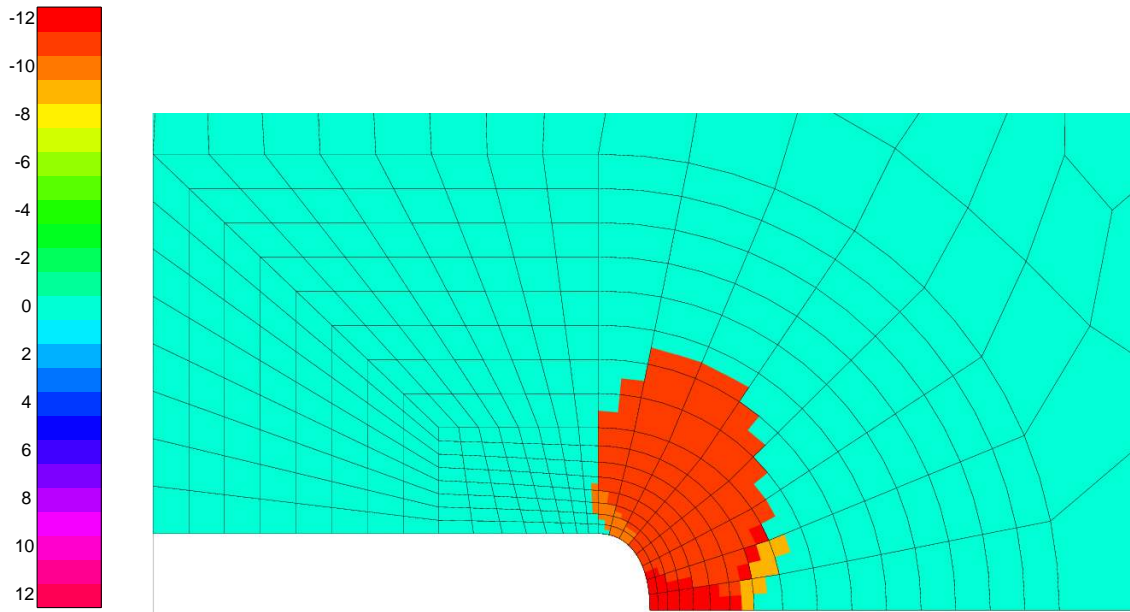


Figure 3.5: 2D simulations of a quarter piece symmetric model at an imposed displacement of 0.03 mm (943 N) on the top edge. Negative slip system numbers denote multiple dominant slip, the highest integer value being kept.

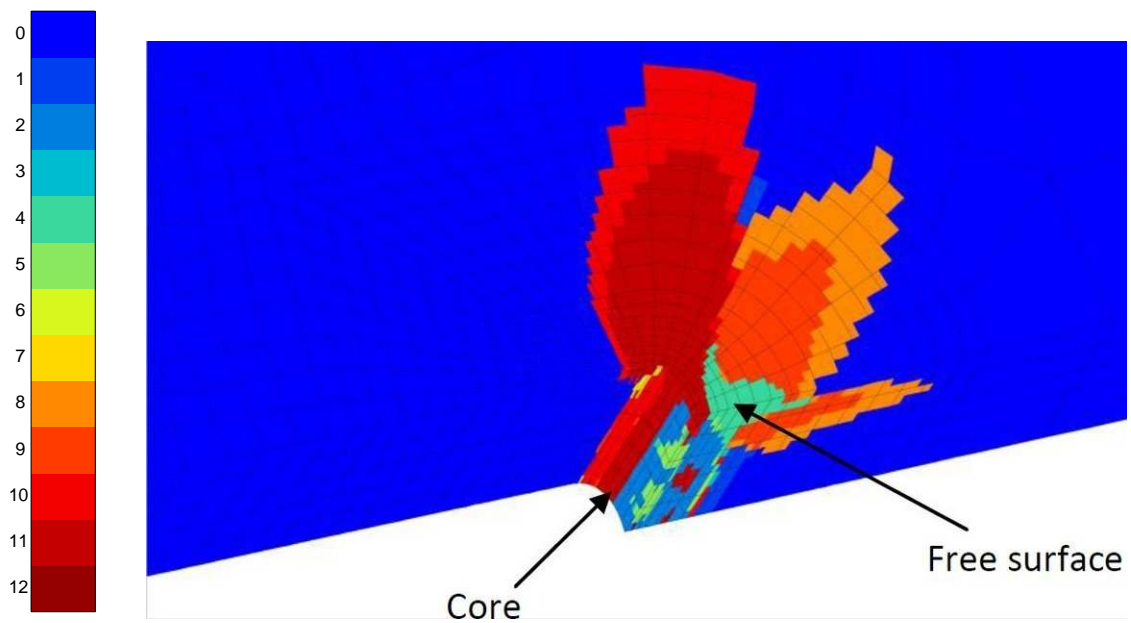


Figure 3.6: 3D simulations of a one-eighth symmetric model at an imposed displacement of 0.0299 mm (819 N) on the top edge. A drastic change in the plastic slip fields from the free surface to the core is apparent.

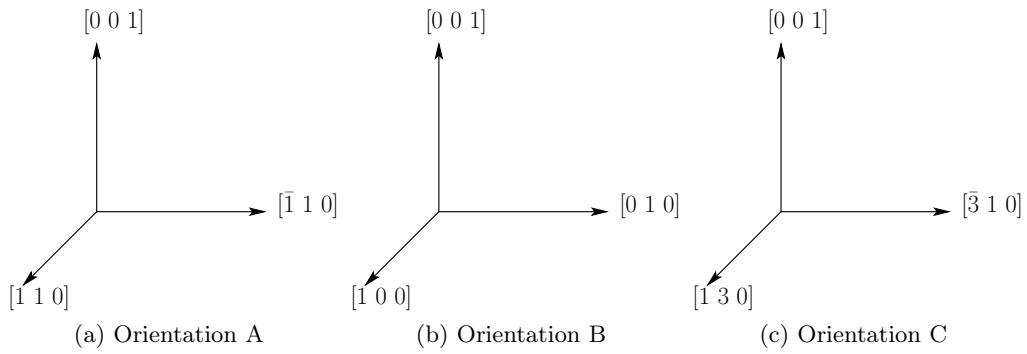


Figure 3.7: Orientations tested in the following chapters

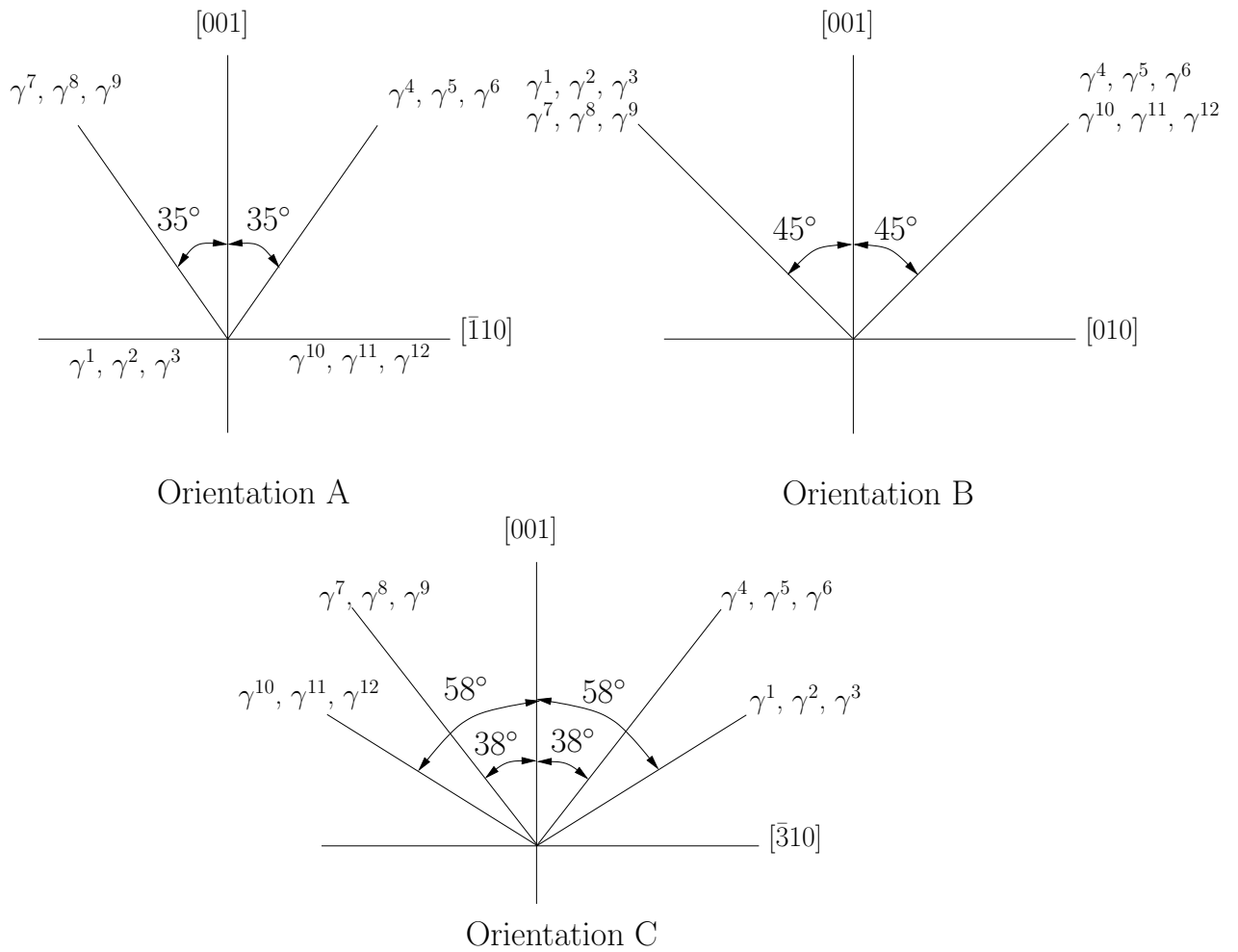


Figure 3.8: Theoretical slip traces expected on the free surface of a specimen

Slip System Number	Orientation A	Orientation B	Orientation C
1	0.5	0.707	0.223
2	0.5	0.0	0.670
3	0.0	0.707	0.447
4	0.5	0.707	0.223
5	0.5	0.0	0.670
6	1.0	0.707	0.894
7	0.5	0.0	0.670
8	1.0	0.707	0.894
9	0.5	0.707	0.223
10	0.0	0.707	0.447
11	0.5	0.707	0.223
12	0.5	0.0	0.670

Table 3.2: Visibility of the various slip systems on the surface of different orientations. 0 indicates that the slip lines will not be visible on the surface.

## Chapter 4

# Effect of secondary orientation on notch tip plasticity

### Résumé

Le chapitre suivant présente les résultats des simulations d'éprouvettes réelles en utilisant le modèle de plasticité cristalline. Les outils de post-traitement, qui étaient présentés dans le chapitre précédents sont appliqués à ces résultats. Puis, les simulations sont comparées aux études expérimentales.

Trois expériences sont étudiées. Les essais différents portent sur des éprouvettes de PWA1480 à double entaille, qui sont chargées en traction selon l'orientation principale [001]. L'orientation secondaire est variée pour les trois éprouvettes. Les expériences montrent clairement que l'orientation secondaire apporte un effet important sur l'évolution de plasticité dans les superalliages monocristallins.

La comparaison des simulations avec les résultats expérimentaux montre que les simulations en plasticité cristalline sont suffisamment fidèles à l'expérience. En analysant ces calculs 3D, une différence importante a été trouvée entre l'état de contrainte à l'intérieur de l'éprouvette et l'état de contrainte à la surface libre. Cette observation met en évidence la nécessité des calculs 3D.

*Note: The results presented in this chapter have been published in the International Journal of Plasticity. See Sabnis et al. [2012]*

## 4.1 Introduction

NBSX superalloy blades are being used increasingly in turbine engines due to their superior thermal resistance, thermomechanical fatigue, creep, stress rupture, and melt resistance capabilities over their polycrystalline counterparts. Directional solidification is used to produce a single crystal blade (VerSnyder and Guard [1960]) with the [001] low modulus orientation parallel to the growth direction. The secondary direction normal to the growth direction, which is typically referenced to a line parallel to the blade attachment, is random if a grain selector is used to form the single crystal. In most cases, grain selectors are used to produce the desired [001] growth direction in blade castings. Therefore the secondary orientations of the single crystal components are determined but not controlled, and hence every blade has a different secondary orientation that can vary from  $0^\circ$  to  $90^\circ$ . Initially,

control of the secondary orientation was not considered necessary (Gell and Duhl [1986]). However, recent reviews of turbine blade lifetime data have indicated that secondary orientation has a significant impact on high cycle fatigue resistance (Arakere and Swanson [2001; 2002], Arakere et al. [2005]). Single crystal turbine blades have complex internal passages for forced convection air cooling. The air then escapes through an intricate network of cooling holes on the blade surface. These cooling holes are often the site of fatigue crack nucleation. Finite element simulations of turbine blade responses were performed in Hou et al. [2008] to illustrate the effect of deviation of ideal [001] orientation of the blade axis and of secondary orientation on fatigue life.

Crystallographic fatigue crack nucleation is influenced by the resolved shear stress (RSS) on the slip plane and the normal stress on the slip plane with the highest resolved shear stress (Nalla et al. [2002]). Persistent slip band (PSB) formation and accumulated slip are also thought to be important for fatigue crack nucleation (Dunne et al. [2007]). Understanding the localisation and evolution of plasticity in notches, for a fixed [001] primary (load) orientation while the secondary (notch) orientation is varied, is important to characterise crack nucleation in blade cooling holes as a function of blade secondary crystallographic orientation.

Analytical, numerical (two-dimensional) and experimental investigations of slip fields and plastic zones near cracks and notch tips in FCC single crystals have been performed by a number of researchers (See for example Crone and Shield [2001], Crone et al. [2004], Drugan [2001], Rice [1987], Rice and Saeedvafa [1988], Saeedvafa and Rice [1989], Sculson and Xu [1997], Shield [1996], Shield and Kim [1994]). The 2D FE simulations by Rice et al. [1990], Cuitiño and Ortiz [1992], and Mohan et al. [1992] support earlier asymptotic analyses. 3D FE simulations are necessary for determining the stress and strain fields on free surfaces and near notched tensile specimens and fracture mechanics specimens. The first 3D FE simulation of crack tip fields in single crystals was carried out by Cuitiño and Ortiz [1996] and highlights the triaxial nature of the stress and strain fields near the crack tip. Arakere et al. [2009] presented a 3D investigation of evolution of plasticity in FCC superalloy single crystal notched tensile specimens based on 3D elastic anisotropic FE model and identified the activated slip systems using the concept of dominant slip system defined as the single slip system that experiences the highest resolved shear stress (RSS) at a given point near the notch. However, the elastic model used is not capable of accounting for nonlinear effects such as latent hardening and lattice rotation afforded by finite strain crystal plasticity formulations. Flouriot et al. [2003] present comprehensive results from 3D crystal plasticity-based FEA simulation of crack tip fields in a compact tension (CT) fracture mechanics specimen and show that there are strong differences between the crack tip plastic strain fields observed at the free surface and mid-section of CT specimen tested. Mapping of lattice rotation on the free surface in the crack tip zone was also performed using EBSD mapping. These observations revealed the existence of intense slip bands and also kink bands emanating from the crack tip, which was also observed by Kysar and Briant [2002] and Patil et al. [2009], for deformation at low temperature and for specific crystal orientations, as essentially predicted by Rice. Kysar et al. [2007] have studied through-thickness variation of crystal lattice rotation induced by wedge indentation in FCC Copper and Aluminium single crystals. A series of papers by Kysar et al. [2005], Gan et al. [2006] and Borg et al. [2008] have reported detailed analytical (anisotropic slip line theory), numerical (finite deformation strain gradient crystal plasticity simulations) and experimental work, respectively, on the effect of cylindrical voids, their size and distribution on stress and strain fields and void growth in FCC single crystals. The slip field is shown to exhibit angular sectors around the void circumference. Lattice rotation discontinuities

are seen at boundaries between regions of slip around the void. Slip field sector boundaries observed near the notch in this work show similar features. More recent experimental and numerical analyses of slip system activation in single crystal superalloy fracture mechanics specimens include Aluminium edge notched specimens studied by Patil et al. [2008a] and notched specimens studied by Huynh et al. [2010]. Extensions of Rice's initial analysis of crack tip field are proposed by Patil et al. [2008b], and in the review article by Narasimhan et al. [2009]. A multiscale modelling using molecular dynamics to bridge across nano, micro and meso-scales is employed to predict work hardening in FCC aluminium single crystals by Groh et al. [2009]. A novel yield function representing the overall plastic deformation in a single crystal has been presented recently based on the principle of maximum dissipation, where single crystal plasticity is considered as a constrained optimisation problem, in which constraints are yield functions for slip systems (see Zamiri and Pourboghrat [2010]). Horstemeyer and Bammann [2010] present a comprehensive review of internal state variable theory for inelasticity that covers a wide range of applications in multiscale modelling of materials and design optimisation. Such models implemented into a finite element code are useful for simulating large-scale deformation in polycrystalline materials. Rossiter et al. [2010] present a new crystal plasticity scheme with explicit time integration scheme implemented into a finite element code that is capable of utilising EBSD data for crystal orientation and is suitable for large-scale 3D simulation of polycrystalline microstructures.

There exist numerous studies in the literature that show that crystal plasticity is able to capture the strain and lattice orientation fields in large grains or even single crystals for Copper and Aluminium for instance. However, results for slip activity in significantly stronger metals like NBSX do not exist for notched specimens, to our knowledge. Such a validation is of the utmost importance for engineering applications in turbine blades. The behaviour of NBSX materials remains almost elastic-ideally plastic until around 600-700° C, after which elastic-visco-plastic behaviour is observed. The information obtained from tests at room temperature is relevant over a large range of in-service temperature conditions for which strain localisation in the form of intense slip bands can be observed. As such phenomena are known to play a significant role in the initiation of fatigue cracks, the ability of crystal plasticity simulations to accurately capture such phenomena needs to be tested and validated. Keeping these reasons in mind, the experiments described in the following sections were carried out at room temperature.

Fully 3D Crystal Plasticity Finite Element Analysis (CPFEA) of the stress-strain fields near the notch tip in double-notched NBSX tensile specimens for three different orientations are presented. The primary orientation is fixed along the [001] direction while the notch directions are parallel to  $[\bar{1}10]/[1\bar{1}0]$ ,  $[010]/[0\bar{1}0]$  and  $[\bar{3}10]/[3\bar{1}0]$ . The three orientations are presented in Figure 3.7. The specimen geometry definition is shown in Figure 3.4 and the dimensions of the specimens used in the experiments are provided in Table 4.1. The CPFEA model incorporates the effects of hardening and lattice rotation. Experimental results on notched tensile tests at room temperature are then compared with numerical simulations in terms of slip line distributions. Section 4.2 describes the experimental and material procedures and the development of slip traces near the notches recorded using optical microscopy for the three orientations studied. Section 4.3 describes the CPFEA model and the computational tools implemented for the numerical study. Section 4.4 is devoted to numerical results and the comparison with experimental data. Section 4.5 presents a brief discussion of the results and a comparison of CPFEA and Anisotropic Elasticity (AE) simulations. Section 4.6 presents the conclusions of the following study.

## 4.2 Experimental results

### 4.2.1 Material and Experimental Procedure

PWA 1480 single crystal Ni-base superalloy castings in the form of two 25 mm diameter (1 inch) bars, with the cylinder axis along the [001] direction were provided in as-heat-treated condition by Pratt and Whitney. The microstructure of the alloys consisted of cubical primary  $\gamma'$  precipitates in a matrix of solid solution  $\gamma$ . Neither crystal contained any noticeable eutectic pools or pores. Laue X-ray back-reflection technique was employed to identify the crystallographic orientations, based on which the samples' directions were realised. Although this material consists of two phases (*FCC*  $\gamma$ -matrix and *L1<sub>2</sub>*  $\gamma'$ -precipitate), the plastic deformation that occurs at room temperature by precipitate-shearing is geometrically analogous to the plastic deformation observed in a single-phase FCC crystal. The  $\gamma'$  precipitate is an intermetallic. Consequently, these materials have a critical resolved shear stress (CRSS) that is an order of magnitude higher than pure Cu or Al. The advantage of using a superalloy crystal is that it yields at considerably high applied stresses and therefore the applied load levels at small plastic zones can be accurately controlled and measured.

Three double notched specimens were machined from a bar of PWA1480 superalloy. The initial unnotched dog-bone specimens were prepared using Electron-Discharge Machining (EDM), and were then carefully polished to remove any damage caused by EDM. The edge notches were introduced via a slow speed saw with diamond blades. The primary orientation was aligned along the [001] axis in all the specimens. The notch directions were parallel to the  $[\bar{1}10]/[1\bar{1}0]$  (orientation A),  $[010]/[0\bar{1}0]$  (orientation B) and  $[\bar{3}10]/[3\bar{1}0]$  (orientation C) directions. The primary orientation was controlled to within  $8^\circ$ ; this was verified by X-ray analysis). Front and back planes of the specimen are identified separately in Figure 3.4 to facilitate the discussion of slip fields for specimens with an asymmetrical orientation. It should be pointed out that the [001] primary orientation direction in turbine blade castings is also controlled to within  $8^\circ - 10^\circ$ . The notches were introduced using a slow speed saw with a thin diamond blade. A special fixture was designed to achieve co-planar notches with approximately equal lengths on both sides. Consistent notch tips were produced with careful and methodical procedures. The dimensions of the double notch specimens are given in the Table 4.1.

The yield stresses for the considered single crystal superalloy were evaluated by conducting tensile tests along the [001] direction on dog-bone samples with rectangular cross-sections. The analysis of deformation bands on the face and the sides of samples revealed that slip took place along the  $\{111\}$  planes (Ebrahimi et al. [2006], Westbrook [2005], Ebrahimi and Westbrook [2008]). Considering this activation of octahedral slip systems, the average CRSS value was measured to be 324 MPa. In order to investigate the evolution of plasticity near notch tips, samples were loaded to various levels of apparent stress intensity factors calculated based on the sharp crack isotropic assumption. The applied loads were in the range of  $K_I = 20 \text{ MPa}\sqrt{\text{m}}$  to  $50 \text{ MPa}\sqrt{\text{m}}$ . The development of slip traces near the notches was recorded using optical microscopy.

### 4.2.2 Slip field development for orientation A

The experimentally observed slip bands around the notch for orientation A, at load level of 4982 N ( $K_I = 50 \text{ MPa}\sqrt{\text{m}}$ ), are shown in Figure 4.1(b). The slip bands show a slight asymmetry about the notch axis, which can be attributed to the crystallographic deviation

from [001] orientation as well as any misalignment in the loading fixture. Figure 4.1(a) shows the comparison of experimentally observed slip bands with numerical RSS fields generated by anisotropic elastic simulations.

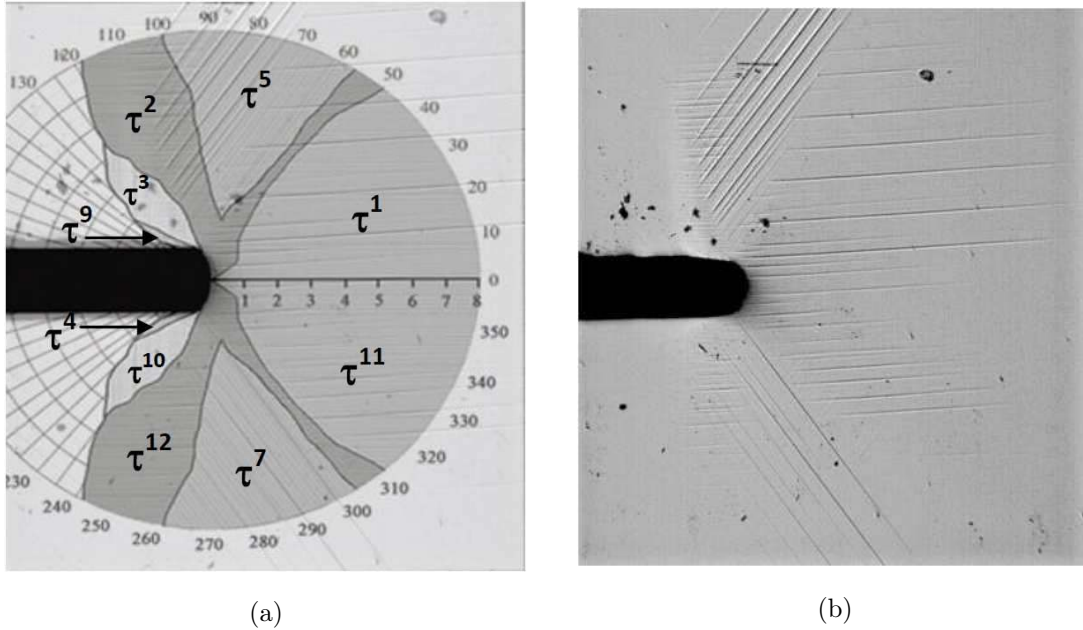


Figure 4.1: Comparison of experimentally observed slip fields near the notch for orientation A at a load of 4982 N with numerical results. (a) Numerical shear stress fields generated by anisotropic elasticity simulations superposed on to the experimentally observed slip lines. (b) Experimentally observed slip lines on the specimen (See Table 4.1 for specimen dimensions)

### 4.2.3 Slip field development for orientation B

The slip fields activated at the surface for this orientation (shown in Figure 4.2) are very different from those observed for orientation A. At a lower load of 1705 N ( $K_I = 20\text{MPa}\sqrt{m}$ ), slip traces along direction  $[01\bar{1}]$  are activated, corresponding to  $(111)$  or  $(11\bar{1})$  slip planes. At the higher load of 3456N ( $K_I = 45\text{MPa}\sqrt{m}$ ), a second set of slip systems becomes activated at a larger distance from the notch tip, with slip traces along  $[011]$  direction, corresponding to  $(111)$  or  $(11\bar{1})$  slip planes.

### 4.2.4 Slip field development for orientation C

Optically observed slip bands around the notch for orientation C, for front plane of left and right notches, are shown in Figure 4.3. Note that “right” and “left” are defined based on looking at the front face. This orientation has mirror symmetry with respect to the notch plane, i.e.  $(001)$  plane, and hence it exhibits symmetrical plastic zone on top and bottom half of the specimen. However, the crystallographic orientations around left and right notches are different and therefore the plastic zones in the vicinity of them are anticipated to be different. Figure 4.3 presents experimental slip fields at the left and right notches for orientation C at a load of 3500N, corresponding to  $K_I = 30\text{MPa}\sqrt{m}$ . Note that the plastic zone sizes observed for the notches at the front and the back planes are different due to crystal asymmetry.

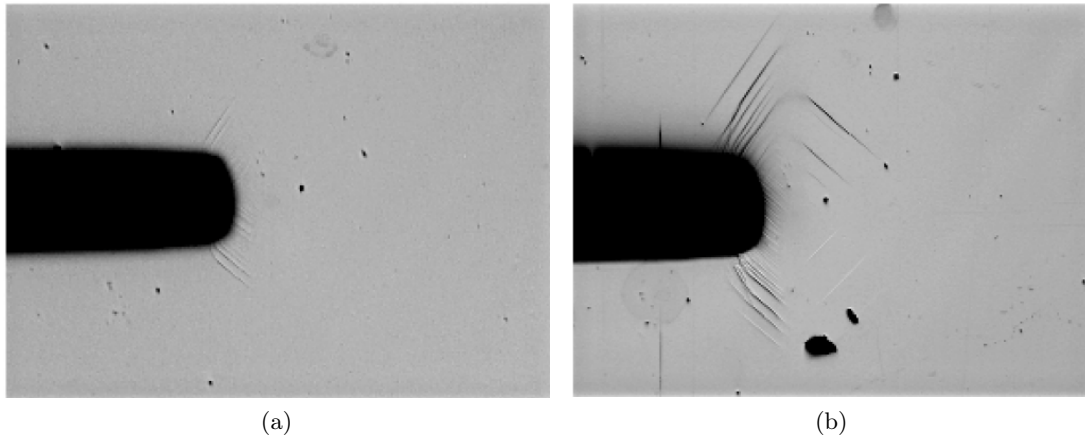


Figure 4.2: Slip fields observed at the specimen surface for orientation B at different loads, (a) at a load of 1705N corresponding to  $K_I = 20\text{MPa}\cdot\sqrt{m}$ , (b) at a load of 3456N corresponding to  $K_I = 45\text{MPa}\cdot\sqrt{m}$ . (See Table 4.1 for specimen dimensions)

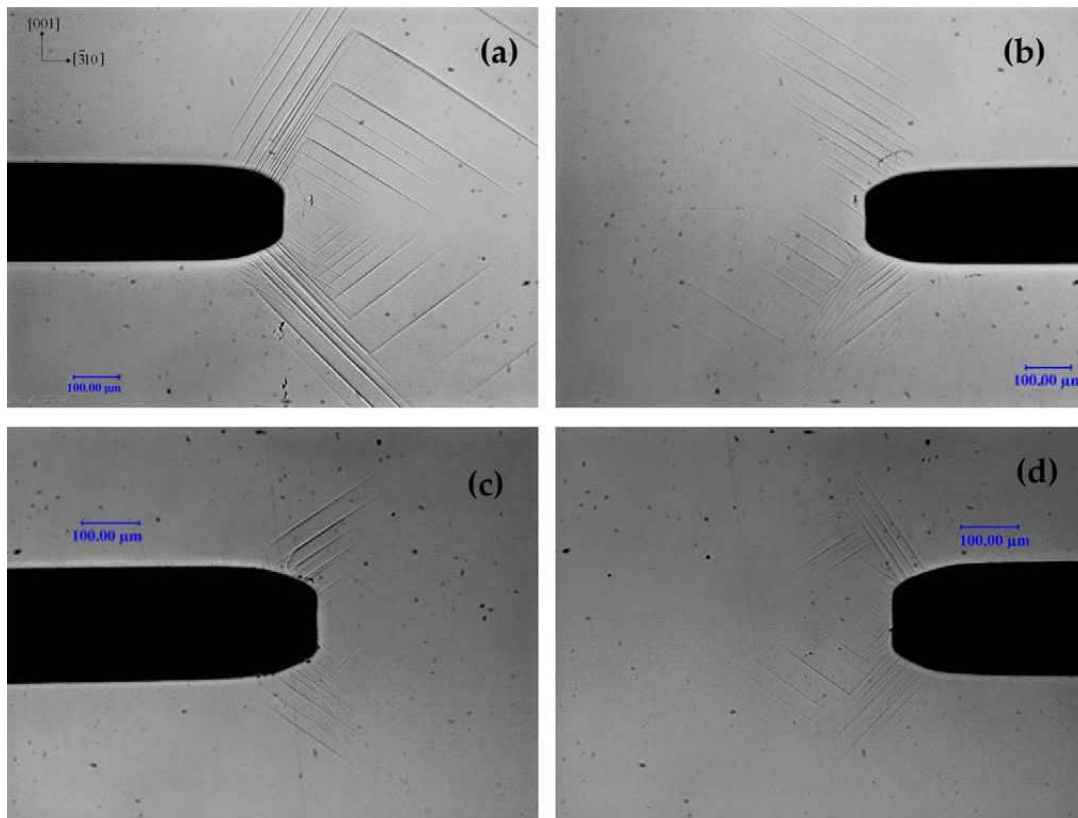


Figure 4.3: Slip fields observed at the specimen surface for orientation C at 3500 N load ( $K_I = 30\text{MPa}\sqrt{m}$ , See Table 4.1 for specimen dimensions). (a) Front plane, left notch. (b) Front plane, right notch. (c) Back plane, right notch. (d) Back plane, left notch

### 4.3 Crystal plasticity finite element model and computational tools

#### 4.3.1 Finite element mesh

The computational modelling of the geometry was carried out using the actual dimensions of the specimens used in the experiments, presented in Table 4.1. The specimen was meshed using 10 layers (along the specimen thickness) of 3D quadratic 20-node brick elements. In the meshing of the specimens, regular mesh domains were used in the vicinity of the notch tips (up to a distance of 450  $\mu\text{m}$  from the notch tips). In the regions away from the notch tips, free meshing was used. Two mesh densities were initially tested. The coarse mesh with 16 nodes along the notch tip yielded plastic slip domain boundaries very similar to the finer mesh with 20 nodes along the notch tip. While the finer mesh gives a better resolution of the boundary of the plastic slip domains, the coarser mesh has been retained in the following simulations as a compromise between computation time and a sufficient description of the slip zones for comparison with experimental results. Since the meshes were tailored to each specimen, there are slight differences in the meshes. Some specific details about each FE mesh are given in Table 4.2. In Figure 3.4 we have defined the coordinate system  $(x, y, z)$  attached to the sample and on the left, the crystal frames associated with the three considered orientations. We call  $z$  the axis normal to the front and back free surfaces of the notched specimens.

#### 4.3.2 Material parameters

The material parameters were calibrated using the tensile curves for a specimen. The curve used for the calibration is shown in Figure 4.4. It displays a typical feature of the mechanical behaviour of NBSX materials at low temperature, namely a high yield stress with a plateau corresponding to the propagation of slip bands filling the gauge length, followed by slight hardening. We have chosen to represent this behaviour by an elastic–quasi–ideally plastic behaviour with a slight linear hardening component. The parameters used for the simulations are given in Table 4.3. The table also includes the cubic elasticity moduli used. The main parameter is the initial critical resolved shear stress  $\tau_c = 324\text{MPa}$ . A small linear hardening component is introduced to limit strain localisation phenomena in perfect plasticity. Viscosity parameters are used only for the selection of slip systems. Their values are such that the material response is practically strain rate independent in the range of strain rates involved in the tests. It does not reflect the plateau stress observed in tension on smooth specimens even though models for simulating the propagation of slip bands do exist (Forest [1997]). However, we do not think this phenomenon to be essential for the material response in the presence of notches.

The curves shown in Figure 4.5 are the load-displacement curves for the notched specimens subject to compact tension loading. The triangles in Figure 4.5 represent the experimental data points obtained for the specimen for orientation A. The tensile loading is imposed on the top face of the specimens while keeping the bottom face rigid. The loads are measured along the top face of the specimen and hence the curves indicate the global loading curves. Thus, the curves shown in Figure 4.5 do not reflect the stresses experienced by the specimen locally at the notch tip. Due to the fact that the loading direction is [001] for all three specimens, the loading curves are still very close. Strong differences will be observed at the local level close to the notches. Some of the differences between the global curves also stem from the slight differences in the geometry of the specimens as shown in

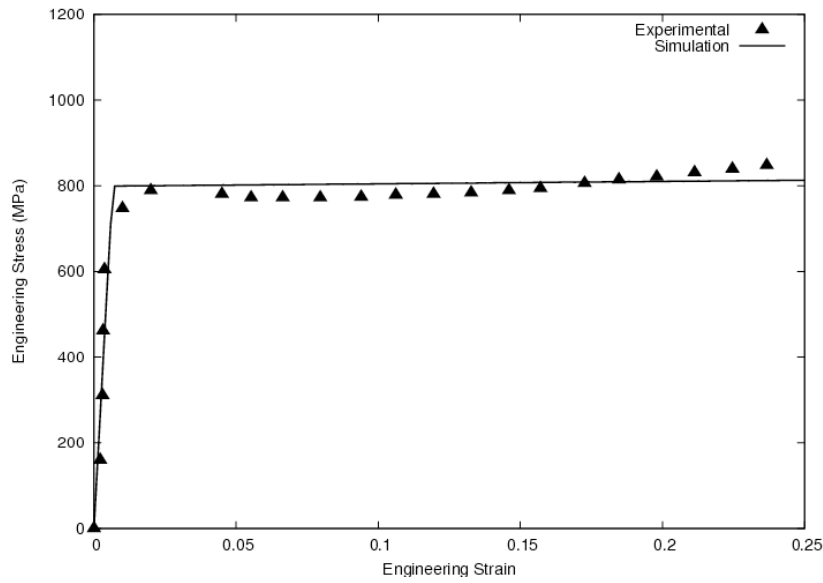


Figure 4.4: Tensile stress strain curve of a smooth specimen along direction [001] used for identification of the material parameters

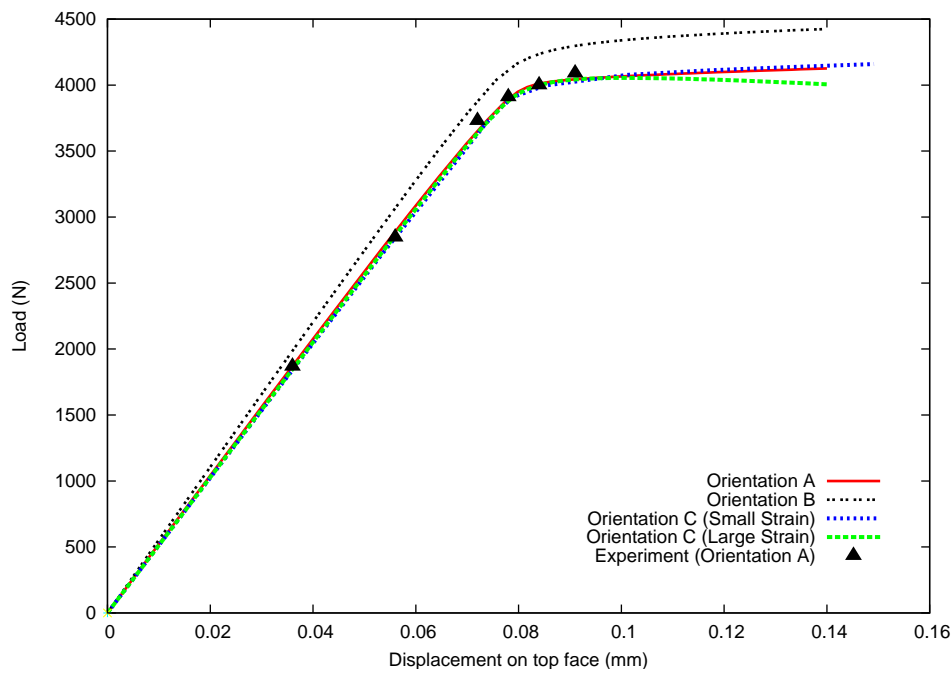


Figure 4.5: Load vs. displacement curves for simulations of compact tension of notched specimens. The displacement is imposed on the top face of the specimen (face normal to the  $y$ -axis in Figure 3.4). The triangles represent the experimental observations for orientation A.

Table 4.1.

For comparison of the experimental results and the crystal plasticity simulations, the  $\gamma$ -maps described earlier were superimposed onto the experimental optical photographs. The visible slip lines were then compared to the contours indicated by the  $\gamma$ -maps. Comparisons of the  $\gamma$ -maps and the RSS contour maps computed from purely elastic computations from the literature are also presented.

Dimension	Orientation A	Orientation B	Orientation C
Width	5.100	5.040	5.100
Height	19.000	17.594	19.000
Thickness	1.800	1.820	1.770
Right Notch Length	1.300	1.394	1.400
Left Notch Length	1.550	1.360	1.390
Right Notch Height	0.113	0.084	0.085
Left Notch Height	0.111	0.084	0.086
a (for both notches)	0.055	0.056	0.055
b (for both notches)	0.226	0.168	0.172

Table 4.1: Dimensions of the specimens used in the computation. All dimensions are in *mm* and correspond to the actual dimensions of the experimental specimens (Arakere et al. [2009])

Orientation	Total number of elements in mesh	Number of elements along the thickness	Number of global DOF
A	24030	10	320484
B	20690	10	276660
C	26940	10	358725

Table 4.2: Main characteristics of the used finite element meshes (DOF : degrees of freedom which are the nodal displacement components)

Parameter	Value
Elastic moduli	
$y_{1111}$	250000 MPa
$y_{1122}$	163000 MPa
$y_{1212}$	129000 MPa
Flow rule parameters	
K	65 MPa.s <sup>1/n</sup>
n	15
Linear isotropic hardening parameters	
H	75 MPa
$R_0$	324 MPa

Table 4.3: Parameters used in the CPFEA simulations.

## 4.4 Results and comparison

### 4.4.1 Prediction of plastic strain field

The evolution of plastic strain in NBSX material and the effect of the secondary orientation on the material's response were studied using crystal plasticity simulations. The simulations are used to quantify the differences in the plastic strain field at notches depending on the secondary crystal orientation. The plastic strain field at the free surface for the three orientations are recorded at loads close to 3500N (3509 N for orientation A, 3510 N for orientation B and 3486N for orientation C). These loads still correspond to a globally linear response of the sample (see Figure 4.5), but confined plasticity has already started at the notches. The equivalent strain is computed using the relation

$$\varepsilon_{eq} = \sqrt{\frac{2}{3} \varepsilon_{ij}^p \varepsilon_{ij}^p} \quad (4.1)$$

where the  $\varepsilon_{ij}^p$  are the plastic strain components at a given time step. It can be observed from Figure 4.6 that the secondary orientation strongly influences the development of plasticity. The plastic zones at the free surfaces exhibit a typical butterfly shape. Plasticity mainly develops at 45° for the three orientations. Significant plasticity is observed at 90° for orientation A. The plastic zone size, defined as the maximum distance from the crack tip at which the equivalent plastic slip becomes less than 0.001, is a strong function of orientation, as evidenced by Figure 4.6. The plastic zone size is about 250  $\mu\text{m}$  for orientations B and C for the considered loads of Figure 4.6 whereas it is about 450  $\mu\text{m}$  for orientation A at the same load. Due to the absence of a vertical symmetry plane, the left and the right plastic zones are strongly asymmetric for orientation C in contrast to the orientations A and B.

As already pointed out in [Flouriot et al. \[2003\]](#), for CT specimens, the plasticity in single crystals is a highly three-dimensional phenomenon so that the observation of the results at the free surface does not give the complete picture of the deformation processes. In Figure 4.7, for illustration we compare the activity of some slip systems at the free surface and along the thickness of the notch. From the Figure 4.7, it is observed that at the same load of 3510 N (for orientation B), the slip systems numbered 1, 2 and 4 are activated on the surface of the specimen. The slip system number 10 however, is not activated on the surface, but is active along the notch tip. It is also observed that the amount of plastic slip due to the slip system number 2 on the surface is very small. However, all the slip systems are active in the core, indicating high amounts of strain localisation along the notch tip of the specimen. Table 4.4 indicates the activated slip systems on the free surface of the specimens as predicted by CPFEA. The fields of activated plastic slips are then used to determine the dominant slip systems depicted in the next section.

Orientation (load)	Activated slip systems on surface (strong activation)	Activated slip systems on surface (Weak activation)	Inactive slip systems
A (3509 N)	1, 2, 5, 7, 11, 12	3, 4, 9, 12	6, 8
B (3510 N)	1, 4, 9, 11	2, 5, 7, 12	3, 10
C (3486 N)	1, 2, 5, 7	3, 10	4, 6, 8, 9

Table 4.4: Activated slip systems on the surface of the 3 orientations as predicted by CPFEA simulations

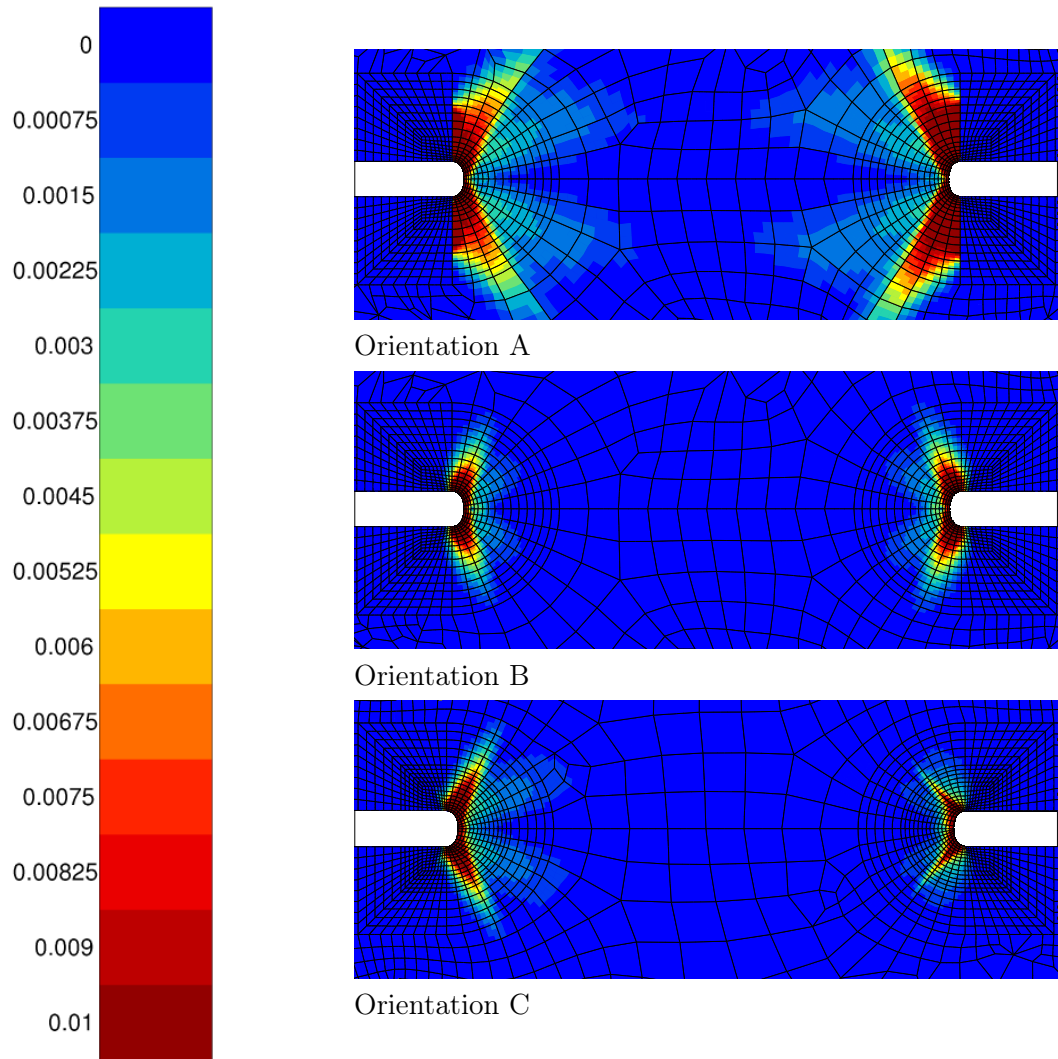


Figure 4.6: Equivalent plastic strain maps for the three orientations at a load close to 3500 N (See table 4.1 for specimen dimensions)

#### 4.4.2 Dominant slip system maps

The “*dominant slip systems*” defined as those slip systems that experience initially the highest RSS at a given location near the notch coincided with the experimentally observed activated slip systems (Arakere et al. [2009]). The plastic strain maps cannot be directly compared to experimental results since no strain field measurements were performed on these samples. Instead, the  $\gamma$ -maps described above are compared to the observation of slip lines.

The experimentally observed slip lines can be associated with the traces of the potential  $\{111\}$  slip planes intersecting with the specimen surface, as shown in Figure 3.8 for orientations A, B and C. As a demonstration of the effectiveness of CPFEA predictions, the  $\gamma$ -maps were superimposed on to the experimentally observed slip field results for orientations B and C shown in Figure 4.8. From the experimental observations alone, it is not possible to identify uniquely the activated slip systems. However, we can compare the slip systems predicted by the CPFEA simulations and identify the activated slip systems among the potential slip systems associated with each slip trace intersecting the

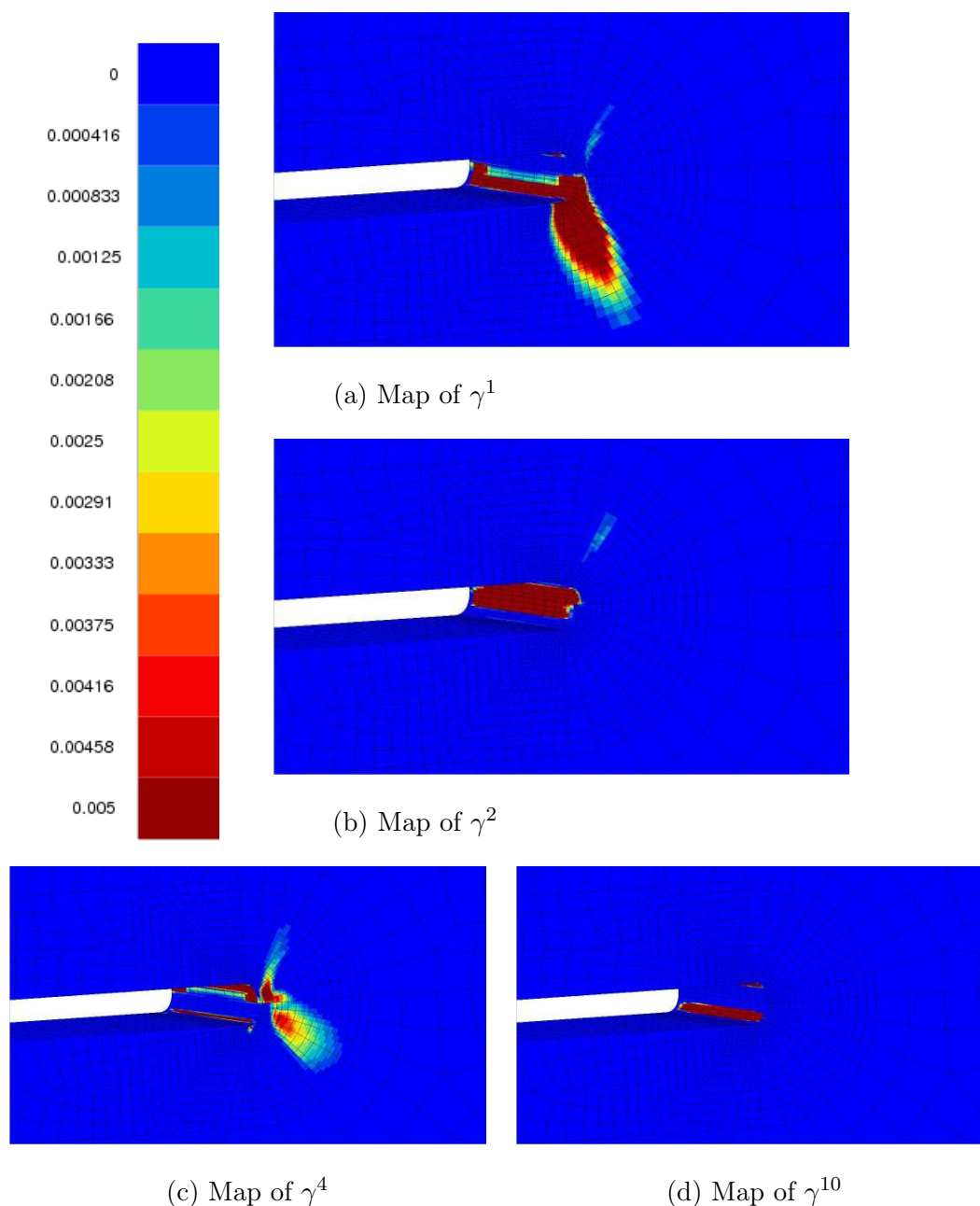
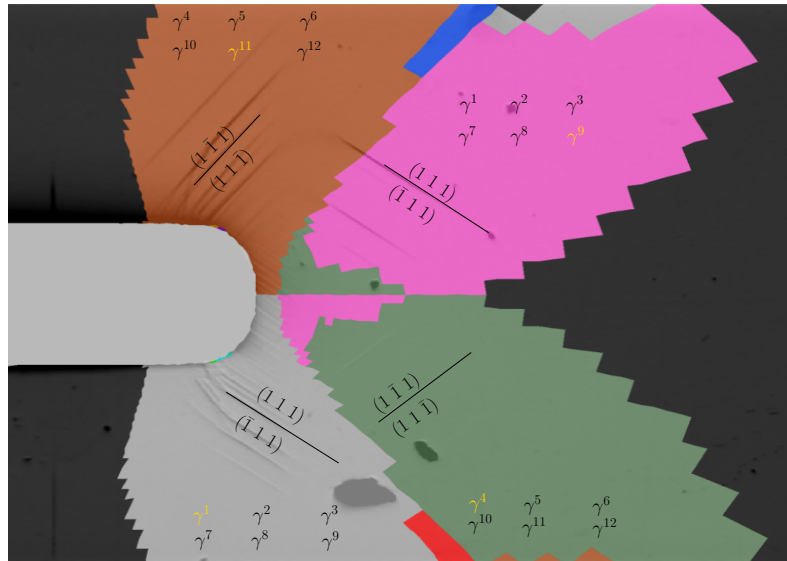


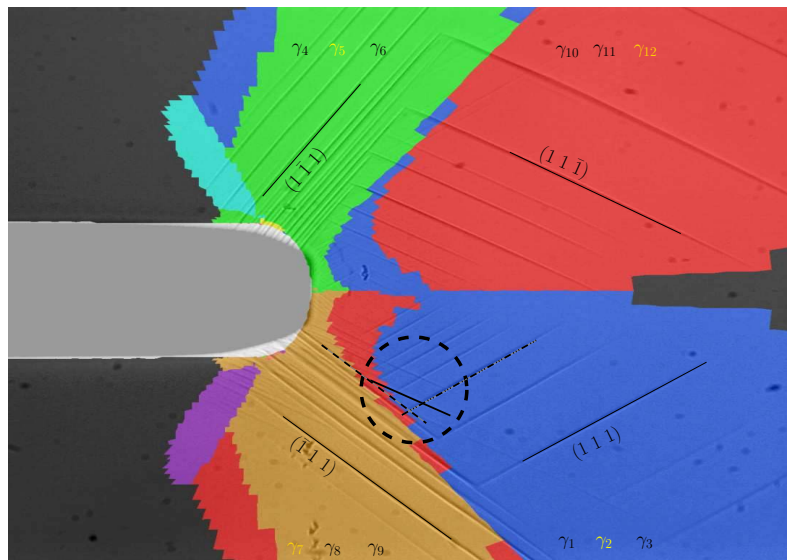
Figure 4.7: Some individual plastic slip maps for orientation B at a load of 3510 N.

surface. Among these potential systems, we can exclude those having a Burgers vector perpendicular to the axis  $z$ , since they would not produce a step on the free surface. Such a comparison is drawn in Figure 4.8. It shows that in most cases, the activated planes are predicted with good accuracy in the proper zones. Indeed, the slip plane corresponding to the predicted dominant slip system (highlighted in Figure 4.8) is in good agreement with observed slip lines. An ambiguity arises for orientation B because of the two potentially observable slip plane traces, but there is no such ambiguity for orientation C. Figures 4.9 and 4.10 respectively show the superposition of the predicted  $\gamma$ -maps on the experimentally observed images for orientations B and C, at different load levels. In general, slip lines are contained in the predicted zones and individual slip lines very often end at the boundaries of the dominant slip domains. In some cases, the slip lines cross boundaries of the predicted

domain showing that there are still limitations in the accuracy of the predictions. This is mainly attributed to the slight deviation in the test specimen from the ideal orientation.



(a) Orientation B at 3510 N

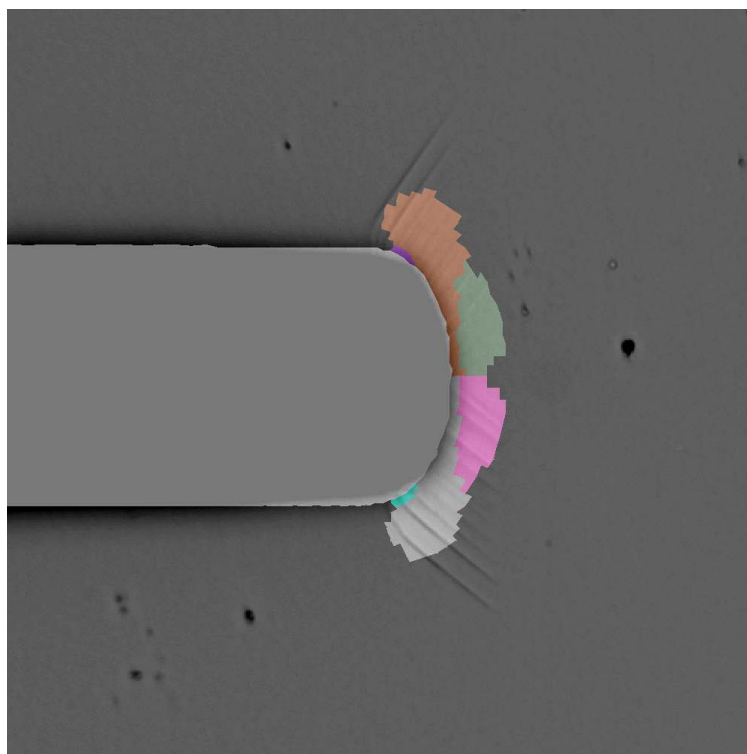


(b) Orientation C at 3486 N

Figure 4.8: Analysis of the superimposed images for orientations B and C. The slip planes potentially activated according to the experiment are indicated, together with the corresponding slip systems and the highlighted dominant slip system from the simulation. The circled region in figure (b) shows one of the zones in which multiple slip lines are observed in the experiment.

### 4.4.3 Core vs. Surface behaviour

Numerical vs. experimental comparisons are possible only at free surfaces. However, full 3D computations are needed since the strain field at the free surface and in the core of the specimens can be shown to differ significantly. Figure 4.11 shows the observations in the mid-plane of the specimen (orientation B) as predicted by CPFEA. It is observed that the dominant active slip patterns in the core of the specimen are significantly different from



(a) superposition for orientation B at 1705 N



(b) superposition for orientation B at 3510 N

Figure 4.9: Superimposed images of experiments and CPFEM results for orientation B

the ones observed on the free surface. In particular, at this load level, the ligament at the core of the sample is entirely plastified whereas an elastic zone remains in the ligament

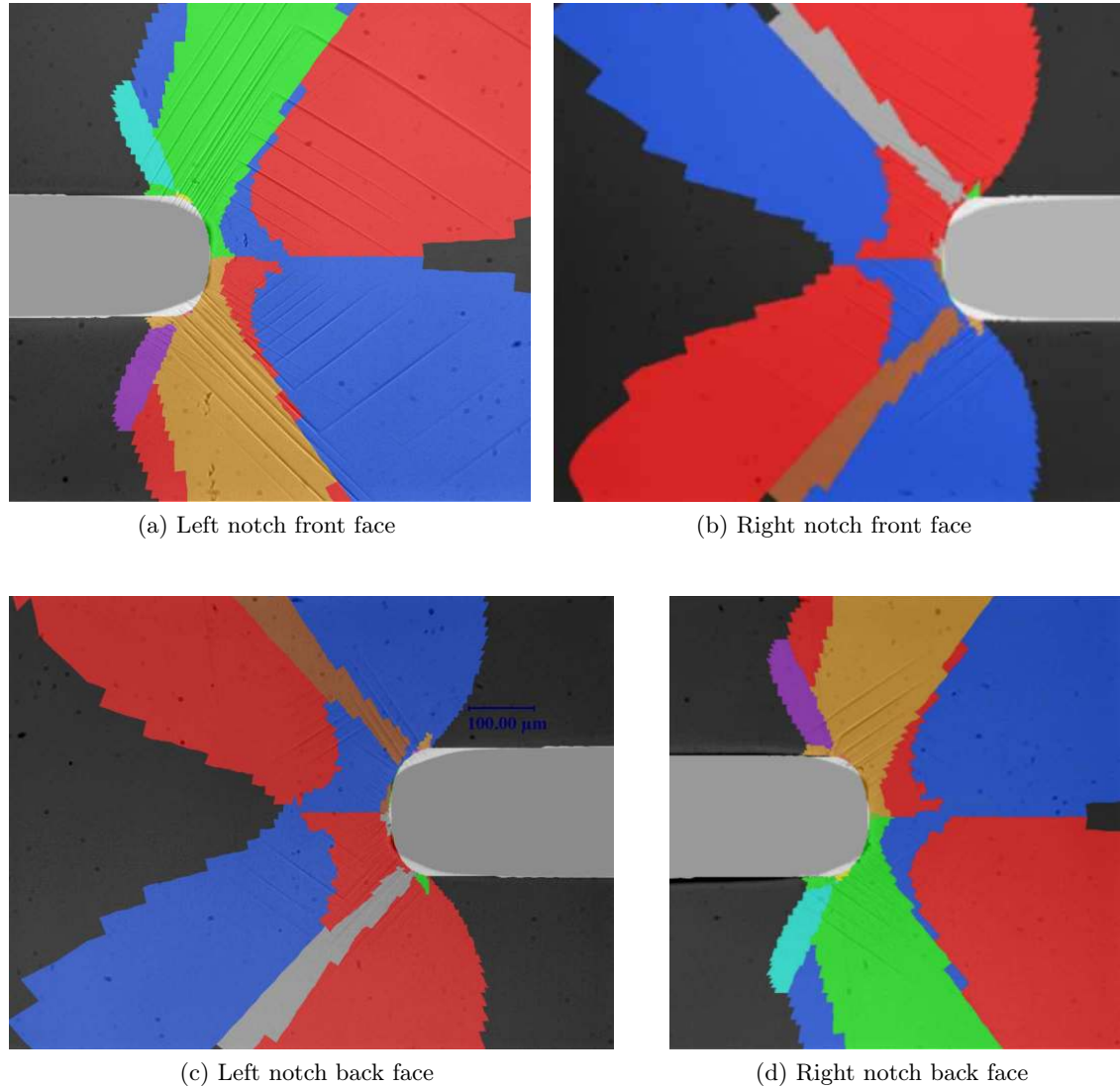


Figure 4.10: Superimposed experimental slip line fields and numerical dominant slip domains for orientation C results at a load of 3486 N. (a) Front face, left notch (b) Front face, right notch (c) Back face, left notch (d) Back face, right notch.

region on the free surface. The  $\gamma$ -maps indicate that the plastic slip systems are more active at the core of the specimen.

Following this observation, stress state plots were generated for orientation A. The stress state plots were then compared to the plane strain analytical yield surface from literature (Rice (1987), Flouriot et al. (2003)). These plots are presented in Figure 4.13. Figure 4.13(a) presents the stress plot for a 2D plane strain simulation. Figure 4.13(b) presents the stress state plot at the core of a 3D simulation, whereas the figure 4.13(c) presents the stress state at the free surface of the 3D specimen. The stress state plots are presented at loads corresponding to an imposed displacement of 0.05 mm and 0.07 mm on the top face. This corresponds approximately to loads of 2600N (globally elastic regime) and 3750N (globally elastic-plastic transition regime) respectively. The triangles represent data set obtained at a distance of 145  $\mu\text{m}$  from the notch tip (red points in Figure 4.12) whereas the squares represent the data set obtained at the notch tip (green points in Figure 4.12). It is observed that for the 2D simulation the stress state remains quite close to the

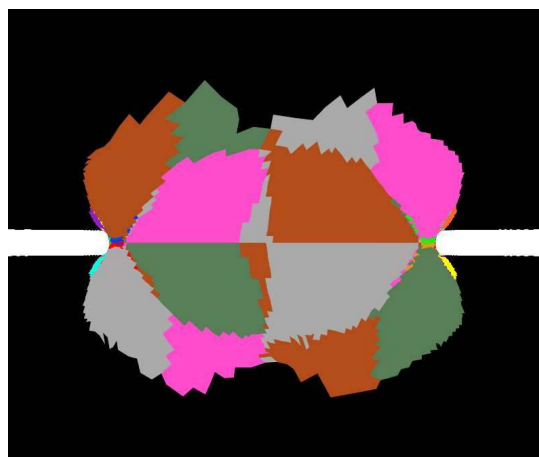
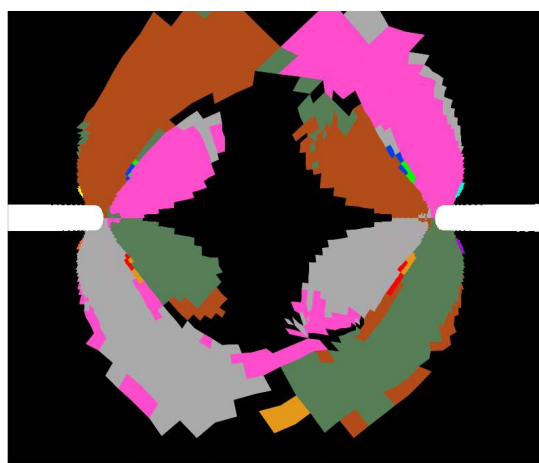
(a)  $\gamma$ -maps in the core(b)  $\gamma$ -maps on the free surface

Figure 4.11: Fields observed at a load of 4039N for orientation B. Figure 4.11a shows the dominant slip system maps at the core of the specimen and figure 4.11b shows the dominant slip system maps at the free surface of the specimen. Observe that the maps are completely different, thus indicating a strong variation in the slip fields along the thickness of the specimen.

analytical yield surface. For the core of the 3D specimen, it is observed that some stress states at the notch tip exceed the analytical initial yield surface, indicating the onset of plastic hardening at the notch. The stress state ahead of the notch tip appears to be close to the analytical yield surface. Note that, contrary to the case of a crack tip in ideally plastic single crystals, the stress states close to the notch are not systematically located at the vertices of the yield surface. This is due to the complex stress field around the notch. From the stress state plot in Figure 4.13, it appears that the stress state plot at the specimen surface is much more complicated than the hexagonal yield surface predicted analytically for the plane strain situation.

For the highly symmetric orientations A and B, one would expect multiple dominant slip systems in the core which exhibits very high amounts of strain localisation. But, the CPFEA results indicate that there is only one dominant slip system at any given time step even at the core, as discussed earlier. It is to be noted that the post-processing procedures here only indicate the slip system with the highest amount of plastic slip at a time step. This does not mean that the slip systems indicated in the  $\gamma$ -maps are the only active slip

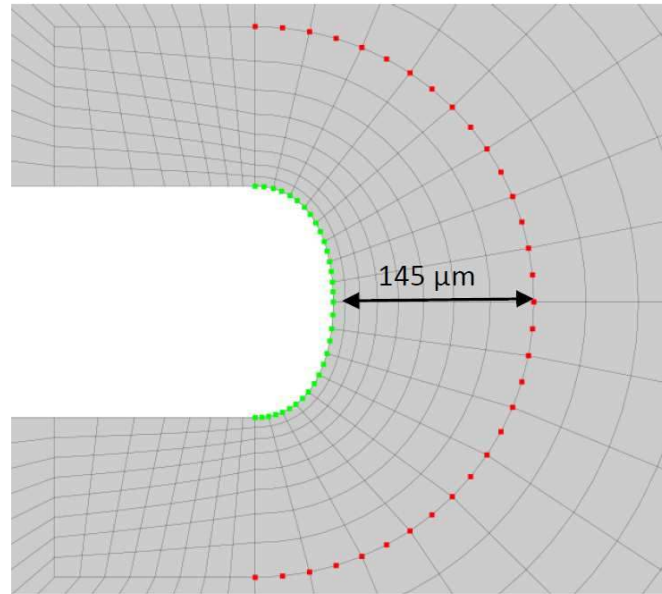


Figure 4.12: The red and green points coincident with FE nodes of the mesh used to generate the plots in Figure 4.13. The red points denote the data set away from notch tip and the green points denote the data set at the notch tip.

systems at the time step. The secondary active slip systems can also be listed to compare with the experimental results. This is discussed further in section 4.5.2.

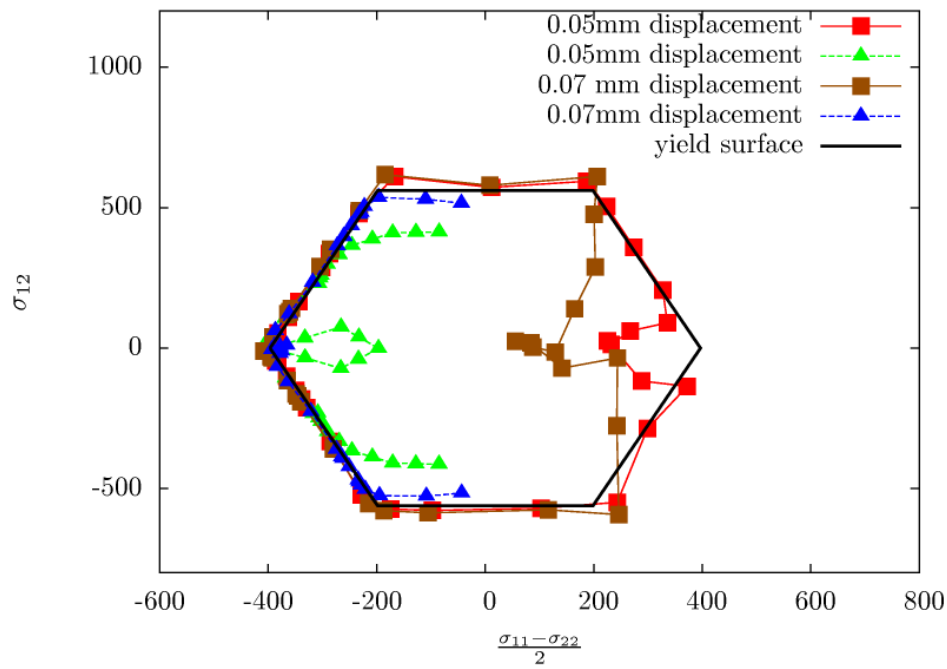
The variations in the dominant slip systems through the thickness can mean that under fatigue loading, the point of crack initiation can be strongly dependent on secondary orientation. Nalla et al. [2002] have indicated that the factors playing an important role in fatigue crack nucleation are the magnitudes of RSS on the slip planes and the normal stress on the slip plane that is initially activated. The variation of activated slip systems through the thickness implies that the load level induces plasticity and its location varies as a function of crystallographic orientation and through thickness location.

#### 4.4.4 Simulations at finite deformations

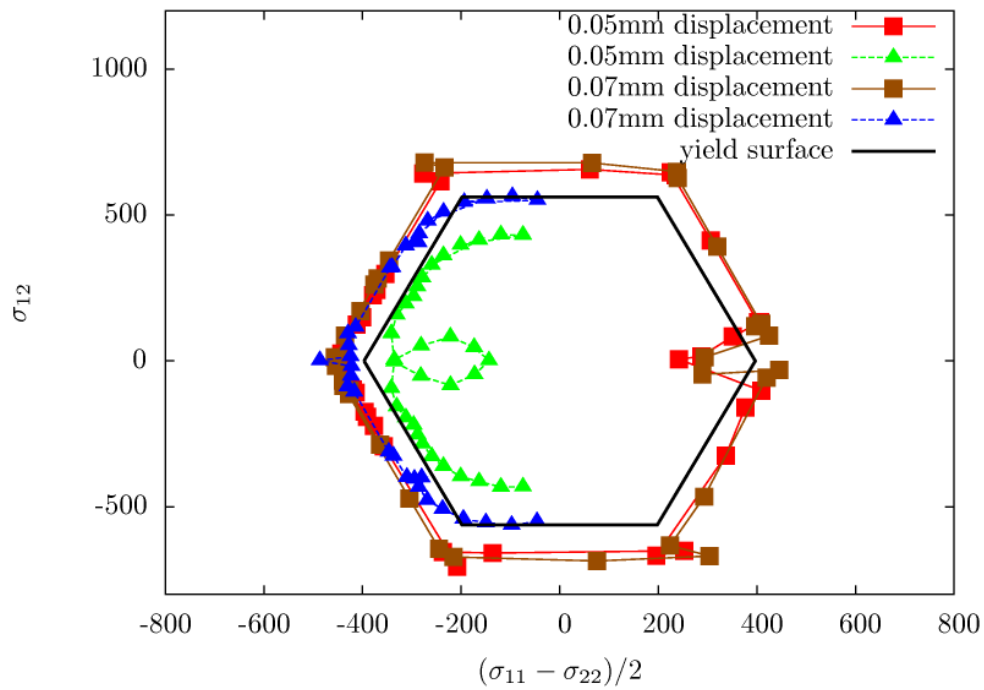
The previous results were obtained from finite element simulations based on the small strain formulation of the single crystal model. It is essential to validate these simulations by comparing them to finite element simulations with the finite deformation model described in section 3.1.

A comparison of the  $\gamma$ -maps obtained from large strain and small strain formulations of the CPFEA simulations indicate that there is no significant difference in the  $\gamma$ -maps generated by the two formulations for the considered load levels. However, the small strain formulation is preferred to the large strain formulation for the problem under consideration here because of its lower computational cost. It is worth noting that small deformation simulations provide the main features of the plastic strain field maps. This may have useful consequences for practical applications in industrial components like computations of single crystal turbine blades.

The finite deformation crystal plasticity model also provides the field of lattice rotation. This is a useful information since it can be directly compared to EBSD measurements. Figure 4.14 shows the lattice rotation angles for orientations A and C at 4037N and 3474N



(a)



(b)

Figure 4.13

respectively. The (positive) rotation angle  $|\phi|$  (in radians) is plotted in these maps. For the intermediate load in specimen C, lattice rotation values up to  $3.5^\circ$  are found. At the

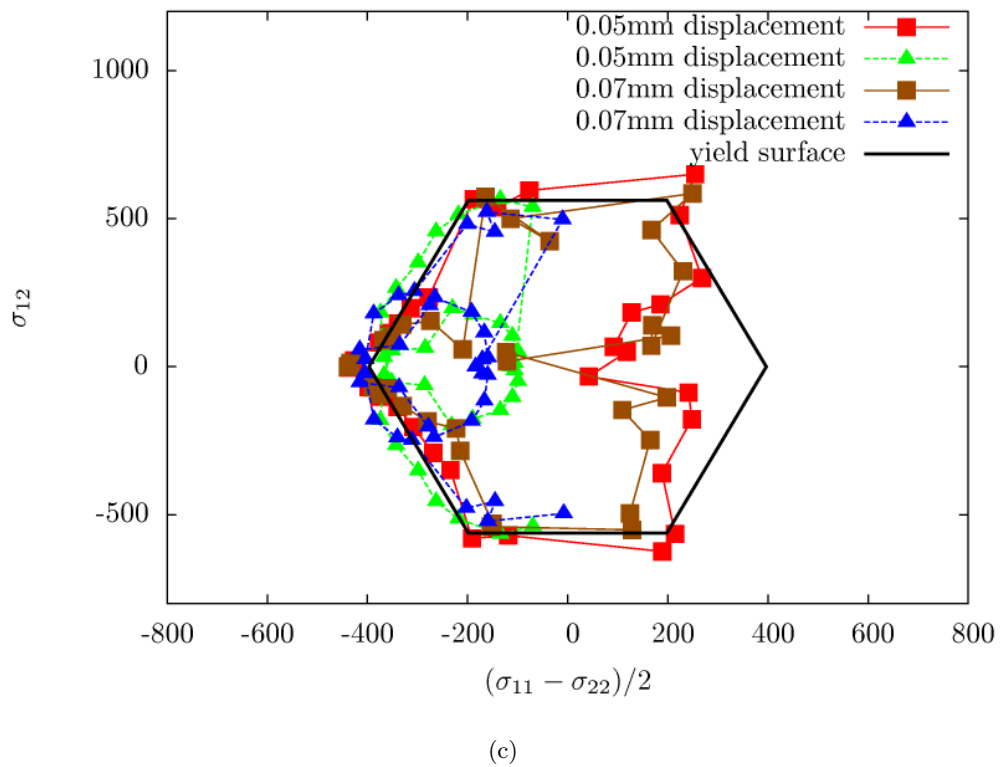
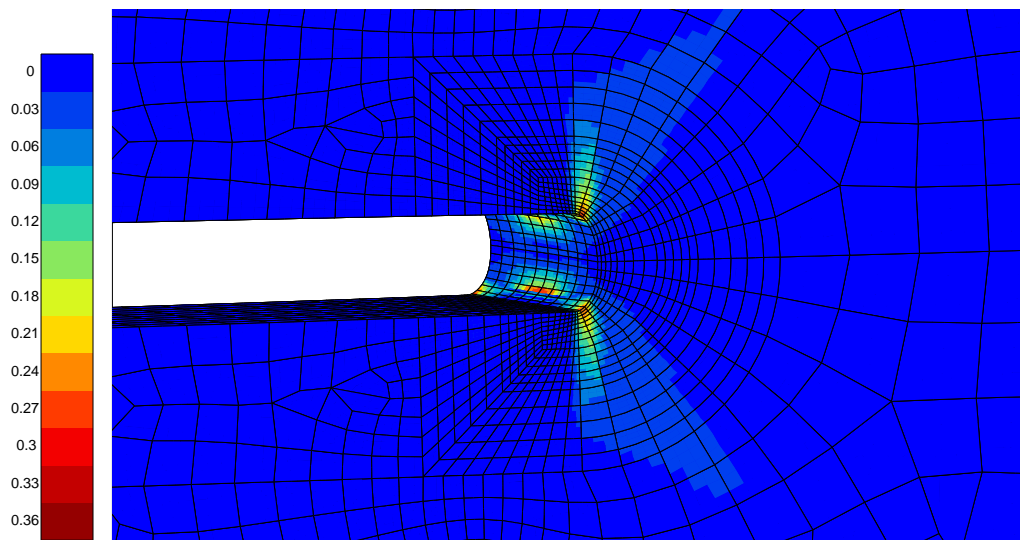
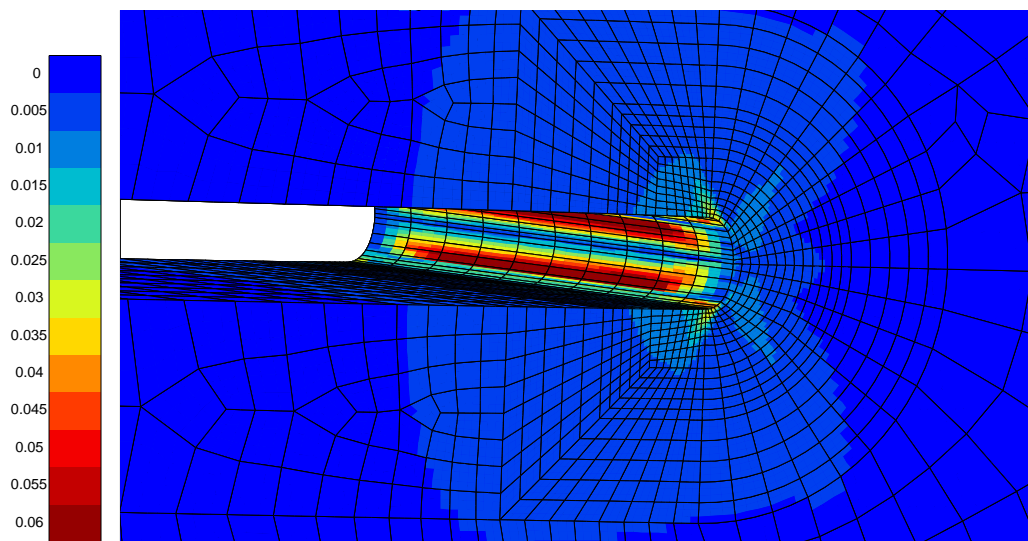


Figure 4.13: Stress state plots along the lines of Figure 4.12 for orientation A at different loads. The squares represent the stress state along the notch-tip; the triangles represent the stress state at a distance of  $145 \mu\text{m}$  from the notch tip. (a) Stress state plot in a 2D specimen (plane strain simulation) (b) Stress state plot at the core of a 3D specimen. (c) Stress state plot at the free surface of a 3D specimen.

higher load considered in specimen A, lattice rotation values of  $20^\circ$  are reached at certain locations. For similar loads, we find higher values of lattice rotations in sample A, which can be related to the fact that this secondary orientation is associated with more plastic strain than the other ones.



(b) Lattice rotation for Orientation A at 4037N



(d) Lattice rotation for Orientation C at 3474N

Figure 4.14: lattice rotations for orientations A and C

## 4.5 Discussion

The previous results are now discussed along the lines of a comparison between predictions based on AE and those based on CPFEA simulations.

### 4.5.1 Comparison of anisotropic elasticity and crystal plasticity

Three-dimensional computations of the single crystal samples based on cubic elastic symmetry (Lekhnitskii [1963]) provide information on possible subsequent slip activity if the results are post-processed to evaluate the RSS on the slip systems. Such simulations have been performed for the samples considered in the present work by Arakere et al. [2009]. The elastic properties of FCC crystals exhibit cubic symmetry and can be described by three independent elastic constants which are defined by either the elastic compliance values ( $S_{11}, S_{12}, S_{44}$ ), the elastic stiffness values ( $C_{11}, C_{12}, C_{44}$ ), or the elastic modulus ( $E$ ), shear modulus ( $G$ ) and Poisson's ratio ( $\nu$ ). The anisotropic elastic constants used are listed in Arakere et al. [2009]. A 3D linear elastic anisotropic FE model with a refined mesh near the notch, using commercial ANSYS Finite element software (version 8.1), was used for computing stress fields. The component stresses at the FE nodal locations were transformed into twelve RSS components ( $\tau^1 - \tau^{12}$ ) (Table 3.1). These RSS values were plotted as a function of radial and angular position about the notch surface and through the thickness and were used to generate polar plots that depict the evolution of activated slip systems as a function of load. The yielding of single crystals is usually evaluated by Schmid's law, which states that plasticity in single crystals takes place when the shear stress resolved on a slip plane and in a slip direction reaches a critical value that is independent of the loading direction. At a given  $(r, \theta)$  location near the notch, the slip systems that experience initially the highest RSS were identified and defined as dominant slip systems and were found to be the activated slip systems observed experimentally on the specimen surface. It was noticed that when plasticity was initiated in a slip system at a given  $(r, \theta)$ , it persisted at higher load levels, i.e. no other slip system became activated at that point except at very large loads. This observation implies that as soon as plasticity is initiated the rate of increase in resolved shear stresses on the other slip systems will be reduced significantly. The persistence of slip can partially be attributed to the softening effect due to  $\gamma'$ -particle shearing in the superalloy studied here (Ebrahimi et al. [2006], Westbrooke [2005]). Therefore, for each point  $(r, \theta)$ , only one dominant slip system can be identified. Clearly, the elastic solution cannot account for nonlinear effects due to plasticity. The high CRSS of these superalloys results in high elastic strains at yield. Therefore it is possible that higher elastic strains will create larger incompatibilities among the different slip systems. However, the evolution of the "dominant slip systems" as evaluated by this work is independent of the value of CRSS. This simple approach is quite effective at identifying which slip system is activated initially at a given  $(r, \theta)$ , and because of persistence of activated slip systems in the superalloy used, we were able to predict slip evolution quite well at higher loads also.

Satisfying agreement was found in Arakere et al. [2009] when comparing the zones of dominant RSS to the observed slip bands. To compare CPFEA and AE simulations, the plastic zones were studied at three main load levels. Around the smaller load of 1705 N in specimen B, the extent of the plastic zone is found to be comparable with the geometric length 'a', as defined in Table 4.1. For an intermediate load of about 3500 N, we find that the plastic zone size is about 2b for orientations B and C and about 4b for orientation A. At the large load levels, i.e. around 4039 N, the plastic zone size becomes comparable with

the specimen thickness for all three orientations. The departure of the elastic prediction from the crystal plasticity results was mainly observed in the latter case. At higher loads, it appears that the AE simulations predict the persistent growth of initially activated slip systems even in the near notch zones for orientation A. It is observed from the figure 4.15 that AE simulations predict persistent growth of certain activated slip systems at higher loads, for example the growth of  $\tau^6$  with increasing load. But, in comparison, CPFEA seems to capture some sort of a competition between the slip systems wherein the zone in which  $\gamma^5$  is dominant is taken over by the dominance of  $\gamma^4$  at a higher load. This effect is not represented by the AE simulations.

#### 4.5.2 Interpretation and discussion of $\gamma$ -maps

The analysis of the dominant slip system maps raises the question of the existence of multiple slip inside each domain. However, the CPFEA results can also be used to predict secondary slip systems, i.e. the existence of a second activated slip system with less intensity, in some domains.

##### $\gamma$ -maps Predictions and activation of multiple slip systems

It can be noted from the figures 4.11(b) and 4.15(c) for example, that no negative value appears, which means that we systematically find one single dominant slip system in each domain even for the highly symmetric orientations A and B. One reason for this symmetry breaking lies in the fact that we look at free surfaces, which operates a selection of slip systems to fulfil the condition of vanishing traction at the surface. On the other hand, a close look at the specimen dimensions presented in Table 4.1 indicates that the specimens are not completely symmetric. These slight differences are unavoidable from an experimental perspective. However, even this slight asymmetry in the test specimens can result in a preferential selection of slip systems in the notch region.

It should be emphasised here again that the term *multiple dominant slip systems* refers to the cases where multiple slip systems take the same values of highest plastic slip due to several simultaneously active slip systems. This is quite different from *multi-slip*, which refers to several simultaneously active slip systems with different amounts of slip. The latter can not be distinguished in experiments.

##### Dominant and secondary slip systems

In Table 3.2, a visibility index 0 indicates that the considered slip system does not have a slip/ displacement component perpendicular to the  $z$ -axis and hence does not create a step on the surface. Also, a greater value of the visibility index indicates a more prominent slip band.

Taking into consideration the values given in Table 3.2 and comparing them to the slip lines in the figure 4.8(b), it is observed that the slip systems predicted by the CPFEA simulations, i.e. the slip systems numbered 2, 5, 7 and 12 have a visibility index of 0.670. The only other slip system which has a higher visibility index of 0.894 is the slip system 8. But since the slip lines seem to be of similar prominence, it can be concluded that the  $\gamma$ -maps predicted by the CPFEA are accurate. Making a closer observation of the results in the area where multiple slip lines are seen (encircled area in Figure 4.8(b)), the  $\gamma$ -maps predict a small amount of slip system 12. Among the slip systems 10, 11 and 12 (all of which have a visibility  $>0$ ) the slip system 12 has maximum amplitude of 0.003. This is

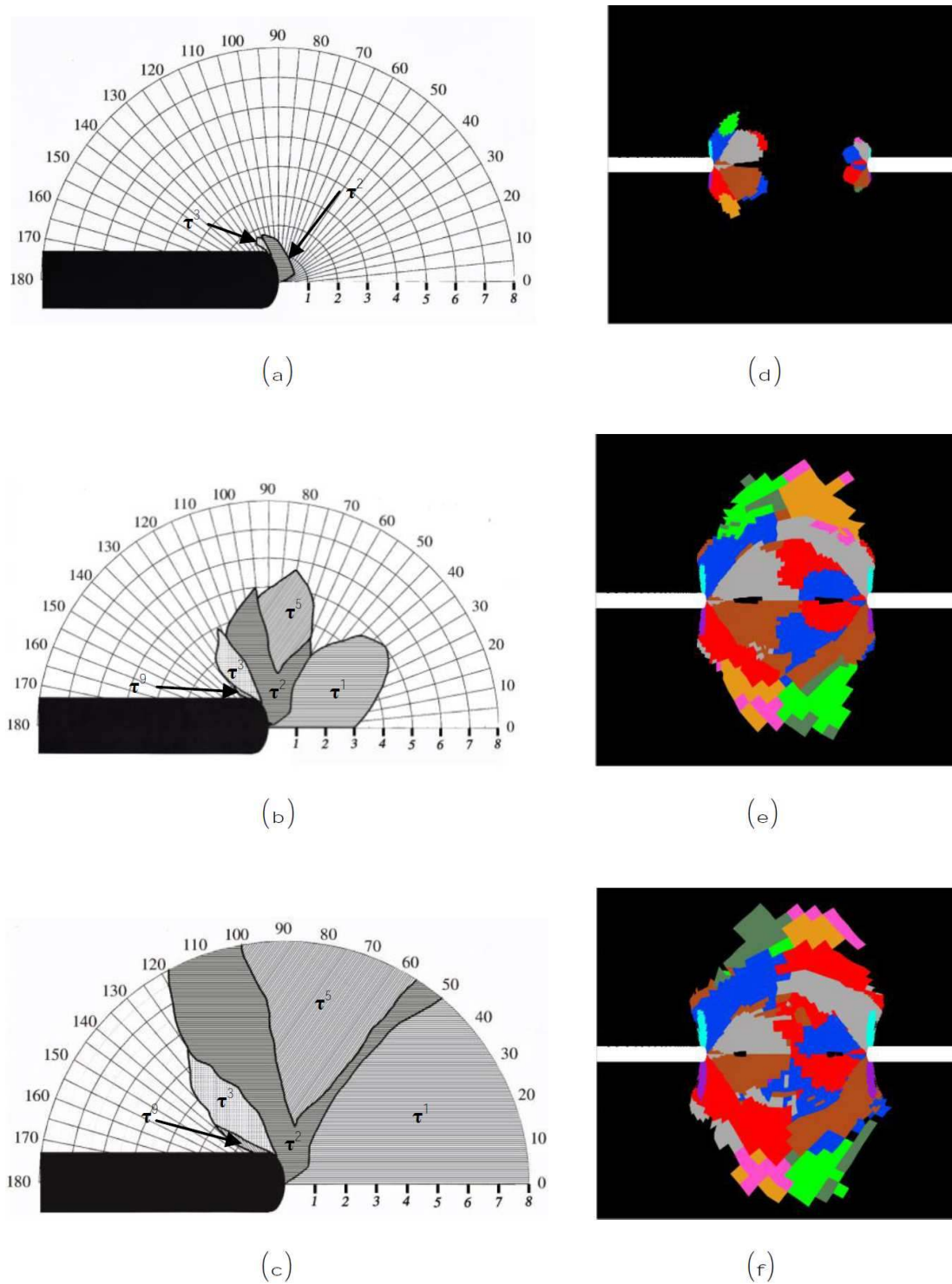


Figure 4.15: (a) Comparison of orientation A for different loads (from Arakere et al. [2009]); (b) CPFEM results for orientation A at 3448N (c) CPFEM results for orientation A at 4037N (d) CPFEM results for orientation A at 4148N

however much smaller than the magnitude of slip system 7 which indicates a slip of 0.11 (0.003 and 0.11 are absolute values of the plastic strain variable at the time step obtained from the program for the slip system under consideration). Thus, the faint appearance of

multiple slip lines can be explained satisfactorily by combining  $\gamma$ -maps with the plastic slips of individual systems.

As a further example, a similar analysis can be carried out with the orientation B (Figure 4.8(a)) and the visibility values for orientation B. The slip lines observed are the ones with equal absolute visibility values. These observations further support the validity of using the  $\gamma$ -maps coupled with CPFEA as a means to predict the evolution of plastic slip in NBSX materials.

## 4.6 Conclusions

The work presented was aimed at comparing the use of AE and CPFEA simulations and their respective suitability in predicting plastic slip evolution in NBSX materials. The simulations were carried out and compared against experimental images of slip line activity for double notched specimens under tension. Post-processing procedures to generate  $\gamma$ -maps were introduced for the CPFEA results. Generally, a good agreement was reached between experiment and simulation for the three considered notch orientations. The results show strong differences in the plastic zone shapes and sizes for the three secondary orientations even though the loading curves for the three orientations are very close. This may have consequences on the subsequent crack initiation and propagation under monotonic or cyclic loading. The FE simulations also reveal the strong differences between the plastic strain fields at the core of the specimen and at the free surface. While this particular aspect was known in the case of cracks, it had not been investigated for notched specimens. The present study indicates the need for extensive non-destructive testing (e.g. acoustic testing) of turbine blades in service to detect crack initiation in such complex triaxial stress-strain fields. AE simulations combined with the use of the Schmid law as a post-processing definitively provide the correct prediction of slip system activity at the early stages of loading. Differences in the slip evolution were observed at subsequent loading stages due to nonlinear effects.

The comparison between FE and experimental results should be extended to other indicators of plastic slip activity, like lattice rotation which can be followed by means of EBSD field measurements close to the notch, as done for wedges and cracks in (Flouriot et al. [2003]), Kysar and Briant [2002]). The next step would be to consider strain field measurements by means of grids or image correlation techniques. The merit of these two techniques is that it allows for truly quantitative comparison between experiment and simulation.

Similar work should be conducted for tests at high temperature due to the use of material in turbine blades. Two-dimensional finite element simulations already exist in Marchal et al. [2006]. Monotonic tests were performed on notched specimens at high temperature by Wen and Yue [2007].

The study of slip line activity at notches and crack tips is of the utmost importance to understand the subsequent mechanisms of crack propagation, that may be responsible for crack propagation on (111) planes, thus leading to complex crack paths. FE simulations of crack propagation in NBSX already exist, at least in 2D, that take into account the crystallographic nature of the active mechanisms (Bouvard et al. [2009], Aslan and Forest [2009], Aslan et al. [2011a]).

## Chapter 5

# Crystal plasticity analysis of cylindrical indentation on Ni-base single crystal superalloy specimens

### Résumé

Les aubes de turbines sont soumises à l'endommagement par frottement et contact au niveau de la liaison entre les aubes et le disque de turbine. Du point de vue de l'initiation et de la propagation des fissures dans les superalliages monocristallins, il est important de comprendre la plasticité qui précède l'endommagement. Des études de l'indentation cylindrique sur des substrats PWA1480 sont présentées. Dans cette optique, ces études passent par des calculs 3D dont les résultats sont traités à l'aide des outils de post-traitement introduits au chapitre 3. Elles montrent une nouvelle fois l'importance de l'orientation cristalline et de simulations 3D. L'analyse montre que les simulations en plasticité cristalline peuvent également être utilisées pour comprendre les effets de désorientation cristalline. Ce type de simulation numérique peut être important dans les cas où les analyses avancées (comme EBSD) ne sont pas disponibles/ possibles.

### 5.1 Introduction

Nickel base single crystal (NBSX) superalloys are used in the fabrication of turbo-machine components such as turbine-blades in aerospace engines. The high-velocity flux of hot gases imposes extreme thermal and mechanical loads on the material. The triaxial, cyclic nature of the mechanical stresses acting on the elements, combined with the thermal stresses due to high operating temperatures causes material deterioration. For example, fretting/contact damage is often observed in the regions where the blade-root is attached into the turbine-disk. The material deterioration usually begins with either crystallographic or non-crystallographic damage initiation, and is often followed by crack propagation along crystallographic planes. Thus, an understanding of the fracture process in NBSX alloys is essential in evaluating the fatigue life of turbine-blades. To foster such an understanding, the study of localised plastic deformation in NBSX superalloys is a necessary step. While there exist many experimental studies addressing the evolution of macro-level-plasticity in this kind of materials, to the authors' knowledge, there are few studies that are aimed at

an analysis of sub-surface behaviour. Many instances of material-damage-initiation and micro-crack-propagation are observed to occur in the sub-surface layers of the material. Consequently, the following chapter presents such a tool to aid in the necessary analysis of localised sub-surface fields in NBSX specimens.

A study of literature related to indentation on NBSX superalloys reveals a few interesting applications of indentation experiments. Xu et al. use experimental indentation to study creep properties of an NBSX material (Xu et al. [2009]), and use Crystal Plasticity Finite Element Analysis (CPFEA) to investigate the effect of varying the primary orientation of the crystal, on the creep surface-morphology (Xu et al. [2008]) in an NBSX material. Eidel [2011] presents an experimental study and a CPFEA investigation of a pyramidal indentation on a CMSX-4 specimen. Brinell-type indentation of CMSX-4 single crystal substrate is considered in Zambaldi et al. [2007] to relate the plastic strain field induced on the indented surface at room temperature and recrystallisation phenomena occurring at higher temperatures. Comparisons between experimental and finite element results are provided regarding the anisotropy of sink-in or pile-up formation on the deformed surface. Arakere et al. [2006] present numerical techniques to investigate subsurface stresses (in 2D and 3D) anisotropic materials, and apply these techniques to simulate cylindrical indentation on a NBSX material. Results from a simulated-contact model are also presented as an interesting alternative to using a numerically-intensive conventional finite-element-method-based contact algorithm. As already stated, the following chapter is aimed at addressing the analysis of sub-surface fields. To this end, numerical simulations were conducted using standard crystal plasticity material models. The details of the material model and the post-processing tools used in the analysis have already been described in Chapter 3.

Blade-roots are often the locations for damage-initiation and crack-propagation due to the presence of stress-concentration features (notches, buffets etc.). A cylindrical indentation experiment on a substrate closely represents the geometry of the section that is in contact with the disk. From a theoretical perspective, two alternative configurations could be considered for the proposed study. The first configuration would use a NBSX cylindrical indent on a hardened-steel substrate. While this configuration represents more closely the setup of a blade attachment, practical considerations concerning the production of an NBSX indent lead to experimentation using the second configuration. The second configuration uses a hardened-steel roller as an indent on an NBSX substrate. A schematic representation of the experiment used in the study is shown in Figure 5.1.

Due to the highly anisotropic nature of this class of materials, the indentation experiments and simulations were carried out for two secondary orientations of the substrate (see Figure 3.7). The present work is structured as follows. Section 5.3 presents some numerical aspects which were not covered in the earlier chapters. The results of the analysis are presented in Section 5.4 in terms of slip system activity. They are then discussed in relation to experimental observations of slip lines on the free lateral surface of the substrate. In particular the CPFEA is used to show the significant differences between slip activation on the free surface and in the bulk, which may have implications for the behaviour of turbine blades.

## 5.2 Experimental study

Micro-indentation tests were conducted on NBSX substrates using a cylindrical hardened steel indent. Figure 5.1 shows a representation of the tests conducted. Figure 5.3 shows

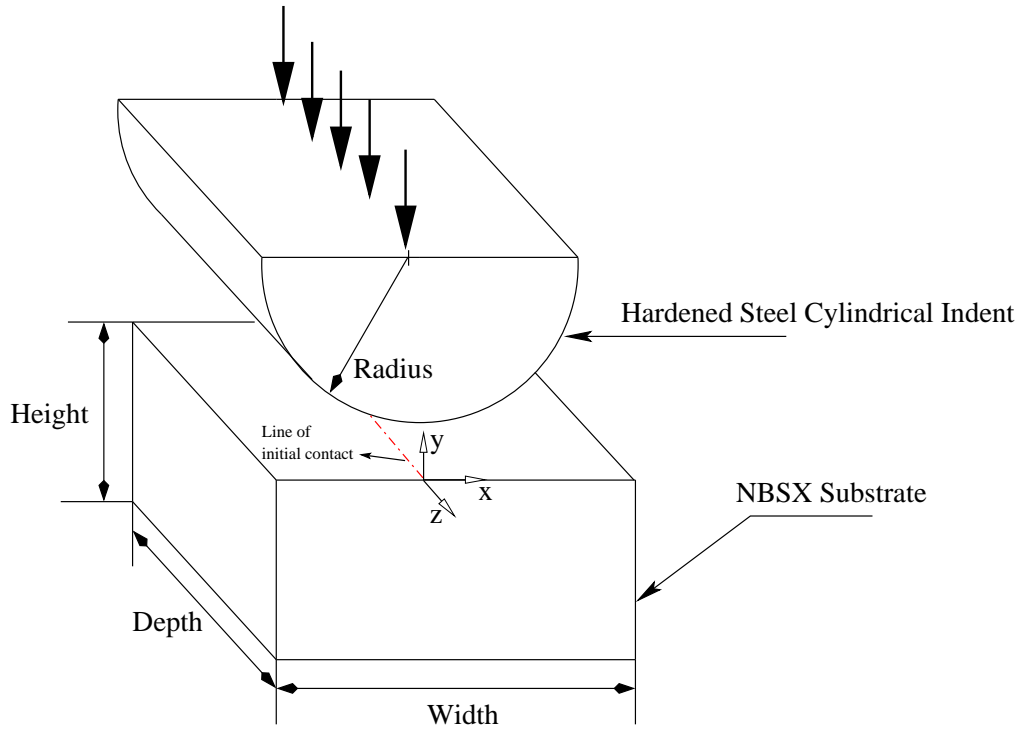


Figure 5.1: Schematic representation of the indentation set-up

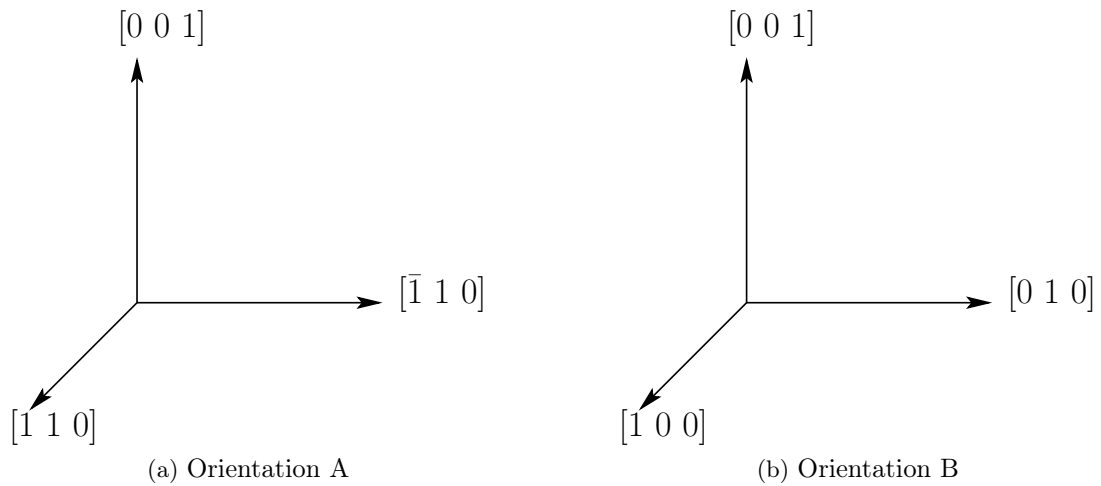


Figure 5.2: The two crystal orientations considered for the substrate materials, with respect to the substrate frame XYZ, Y being the normal direction to the indentation plane.

the slip traces observed on the free surface for the two orientations shown in Figure 5.2, at a contact width of  $250\mu\text{m}$ . For Orientation A, slip traces extend up to a depth of  $\approx 800\mu\text{m}$  from the indentation surface. For Orientation B, the slip traces extend to a depth of  $\approx 300\mu\text{m}$  from the indentation surface. The theoretically expected slip traces for the orientations are shown in Figure 3.8.

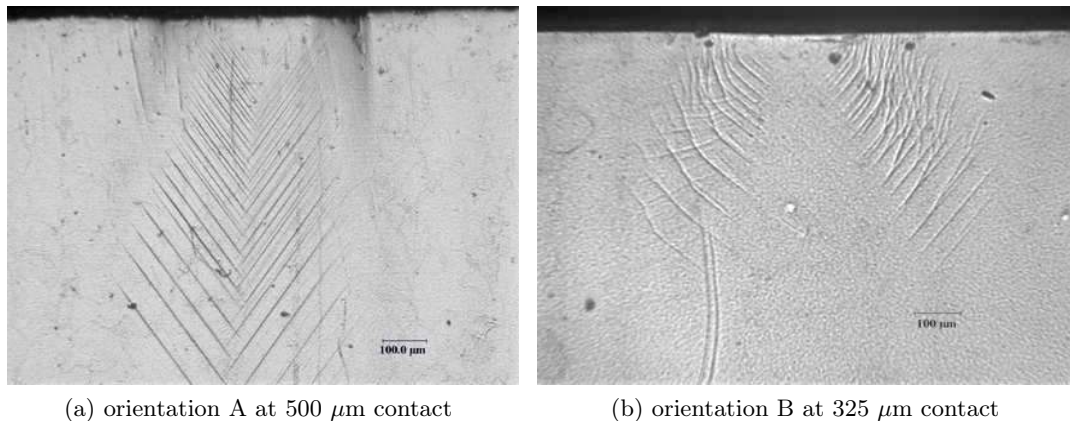


Figure 5.3: Experimental slip traces observed

Specimen dimensions (in <i>mm</i> )	
Width	5.0
Depth	8.5
Height	2.5
Radius of indent	2.25

Table 5.1: Dimensions of the specimens tested

### 5.3 Computational analysis

The phenomena considered in the present study are

- The elastic deformation of the NBSX substrate (represented by a cubic elasticity material model)
- the plastic deformation of the NBSX substrate (represented by a crystal plasticity material model),
- the purely elastic deformation of the cylindrical indent (treated as an isotropic elastic solid with Young's modulus of  $206842.72 \text{ MPa}$ , and Poisson's ratio of 0.3),
- and the actions/reactions of contact forces on the indent/substrate (simulated by a suitable contact algorithm).

They are incorporated in the implicit nonlinear finite element framework Zset (Besson and Foerch [1997]).

#### 5.3.1 Finite element mesh

Two types of meshes are considered in this work. *Mesh 1* represents the full geometry shown in Figure 5.1. It can be used for non symmetric orientations of the single crystal. In particular, it will be used to test the effect of small deviation from ideal crystal orientations. However, the geometry of the system and the main orientations of the single crystal substrate considered in this work allow for reduction of the mesh size due to symmetry

reasons. For the two orientations of Figure 3.7, one quarter of the previous mesh is sufficient to predict the full stress-strain field. This second finite element mesh is called *Mesh 2*.

*Mesh 1* is constructed by the extrusion in the Z-direction of a 2D quadratic-element mesh. The extrusion of the 2D mesh contains 10 layers of elements, with a bias in layering towards the free surface of the specimen. Due to the fulfilment of the traction free surface conditions, high strain gradients are expected near the free surface. This is the reason for the use of a greater number of layers of elements near the free surface. The contact line between the indent and the substrate (corresponding to a contact length of  $500\ \mu\text{m}$  on the top edge of the free surface), was meshed with 40 quadratic elements of equal length with reduced integration.

*Mesh 2* represents one quarter of the NBSX substrate used in experiments, thus requiring symmetry boundary conditions in both X- and Z- directions. It consists of linear elements with reduced integration because, in conjunction with the contact algorithm, it was found to be computationally faster. *Mesh 2* is marginally coarser than *Mesh 1* (31 nodes over a length of  $125\ \mu\text{m}$  in *Mesh 2*, as compared to 41 nodes over a length of  $125\ \mu\text{m}$  in *Mesh 1*). This difference in mesh densities is due to the choice of quadratic elements in *Mesh 1* as compared to linear elements in *Mesh 2*. It is noted that, for the indentation loads considered in this study, there were no remarkable differences in the fields obtained by either of the two meshes.

A greater number of layers along the thickness with the concentration focused towards the free surface is understandably preferable, as it allows for a better estimation of the steep gradients near the free surface. However, increasing the number of elements in the thickness also increases the computational effort required for the resolution of the problem by significant amounts. Computational characteristics such as DOFs, numbers of elements and computational memory required for the resolution of the non-linear problem for some of the meshes used in the simulations are given in Table 5.2. Results from various simulations are presented in the following sections. The results presented contain 10 and 20 layers of elements along the thickness of the specimen (for *Mesh 1* and *Mesh 2* respectively), unless otherwise specified. Both the generated meshes, *Mesh 1* and *Mesh 2*, are shown in Figures 5.4 and 5.5 respectively. The dimensions used for the experimental and numerical specimens are indicated in Table 5.1.

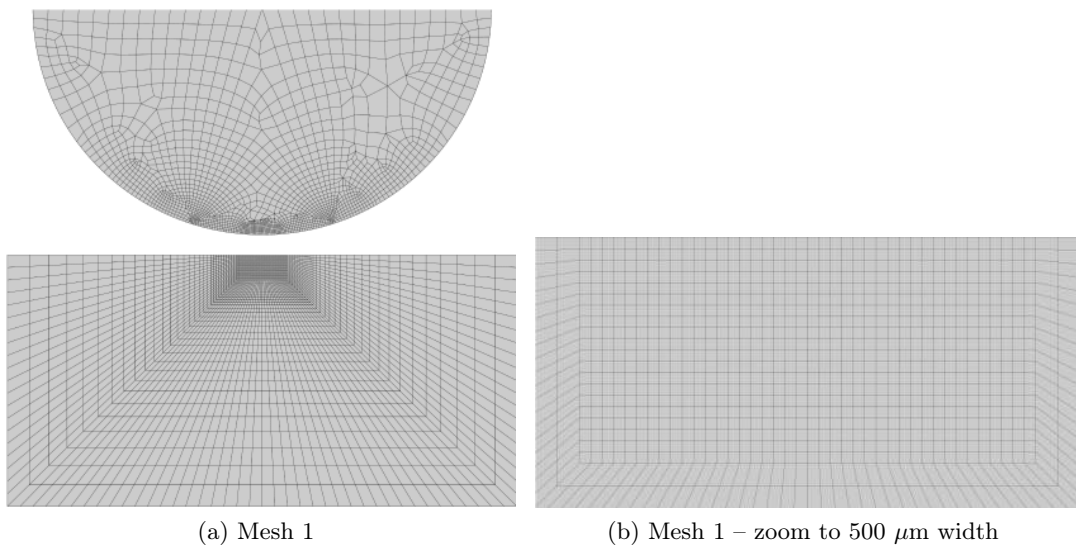


Figure 5.4: Mesh 1 used corresponding to the full indentation setup.

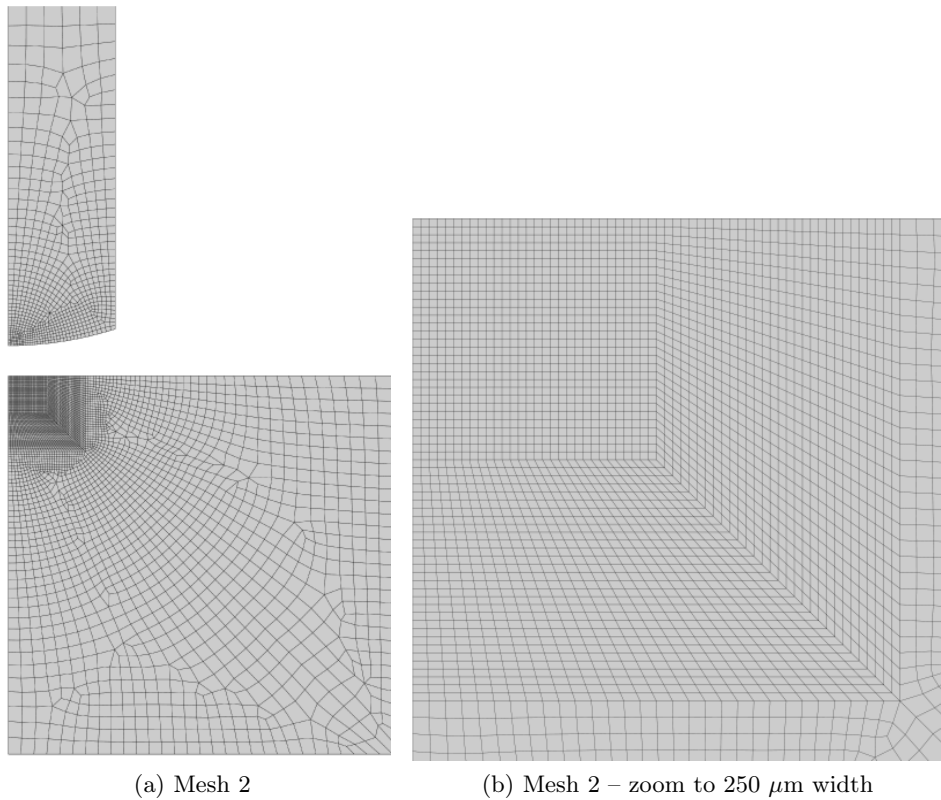


Figure 5.5: Mesh 2 corresponding to one quarter of the indentation setup.

	Number of elements along thickness		
	10 elements	16 elements	20 elements
<b>Mesh 1</b>			
Number of elements in Hardened Steel indent	18207	–	–
Number of elements in NBSX substrate	40003	–	–
Total number of elements in mesh	50210	–	–
Number of DOFs	665499	–	–
Memory required (Mb)	17083	–	–
<b>Mesh 2</b>			
Number of elements in Hardened Steel indent	7640	12224	15280
Number of elements in NBSX substrate	45780	73248	91560
Total number of elements in mesh	53420	85472	106840
Number of DOFs	182688	282336	348768
Memory required (Mb)	2167	4504	6859

Table 5.2: Computational details for symmetric quarter specimen

### 5.3.2 Numerical algorithms

The numerical resolution of the different mathematical problems posed by the finite element analysis of the geometry under consideration necessitates the use of various numerical

algorithms, brief descriptions of which are presented below. The resolution of the global system of equations was carried out by a standard Newton-Raphson implicit solver. The local integration of the constitutive rate equations was carried out by an implicit *theta*-method implementation (Chaboche and Cailletaud [1996]) coupled with an adaptive time-stepping algorithm.

The contact problem was resolved using a stress based contact algorithm incorporated in the finite element software suite Zset (Besson and Foerch [1997]). The frictionless contact (Hertz-Signorini-Moreau) constraints are fulfilled node-wise within the node-to-segment contact discretisation (Wriggers [2006]). The contact constraints are given by the following set of equations

$$\sigma_n \leq 0; \quad g_n \geq 0; \quad g_n \sigma_n = 0,$$

where the contact pressure  $\sigma_n = \vec{n} \cdot \boldsymbol{\sigma} \cdot \vec{n}$  and the normal gap is defined as  $g_n = \vec{n} \cdot (\vec{r} - \vec{\rho})$  where  $\vec{r}$  is the nodal coordinate on the slave surface and  $\vec{\rho}$  is the closest point on the master surface.

We use the contact resolution algorithm proposed in Francavilla and Zienkiewicz [1975], Jean [1995], which can be outlined as follows:

1. The global field (displacement in our case) is made without enforcing contact constraints. This is done by using a standard *Newton-Raphson* scheme. The residual obtained from this step includes the internal reactions obtained from the global equation system, and the contact reactions from the previous iteration.
2. From the stiffness matrix computed in step 1, a *flexibility matrix* for nodes in contact is extracted.
3. The extracted flexibility matrix from step 2 is then used to obtain the displacements and reaction forces that account for the constraints imposed by the contact between the two bodies.
4. As a final step, the newly computed fields and reactions are used to update the global fields, which in turn are used for the computation of the next iteration.

## 5.4 Results & discussion

A direct comparison is drawn between the computational prediction of slip activity at the free surface and the experimentally observed slip lines for two single crystals orientations. This comparison is followed by additional information provided by the Finite Element analysis about the difference between slip activity at the free surface and in the bulk of the specimen. Lattice rotation fields and crystal misorientation effects close the discussion.

### 5.4.1 Comparison of computed $\gamma$ -maps with experimental observations

Cylinder indentation was simulated for substrate single crystal orientations A and B up to a contact length of 500  $\mu\text{m}$  in the plane normal to Z, corresponding to an indentation depth of 20  $\mu\text{m}$  and 16  $\mu\text{m}$  for orientations A and B respectively. The  $\gamma$ -maps were determined at several loading steps. The comparison of FE results with experimental ones is carried out by superimposing the dominant slip maps onto the optical micrographs of the experimental specimens.

For orientation A, slip traces are experimentally observed up to a distance of  $800\ \mu\text{m}$  below the indent for an indentation depth  $\delta = 0.019\ \text{mm}$  at the free surface. The width of the region containing slip lines reaches  $550\ \mu\text{m}$  for a contact length of  $500\ \mu\text{m}$ . In orientation B, slip traces are seen in a region that extends up to  $540\ \mu\text{m}$  below the indent and about  $760\ \mu\text{m}$  wide at a contact length of  $325\ \mu\text{m}$ . An analysis of the  $\gamma$ -maps shows that the plastic slip zones predicted by CPFEA have dimensions close to the experimental ones. This can be clearly seen in Figure 5.6. The CPFEA therefore provides a realistic estimate of the size and shape of the plastic zone below the indent. However, the Figure 5.6 shows that, for the same indentation depth, the width of the plastic zone seems to be somewhat overestimated by the model. In fact the dominant slip systems in the lateral lobes for orientation A have a zero visibility index according to Table 3.1 (slip system 10), so that there is no contradiction between experiment and computation. The situation is different for orientation B where two small lateral lobes are observed according to the simulation in Figure 5.3b in the absence of observed slip traces. The experimental plastic zone is slightly deeper than the predicted one for Orientation A. The reverse is found for orientation B.

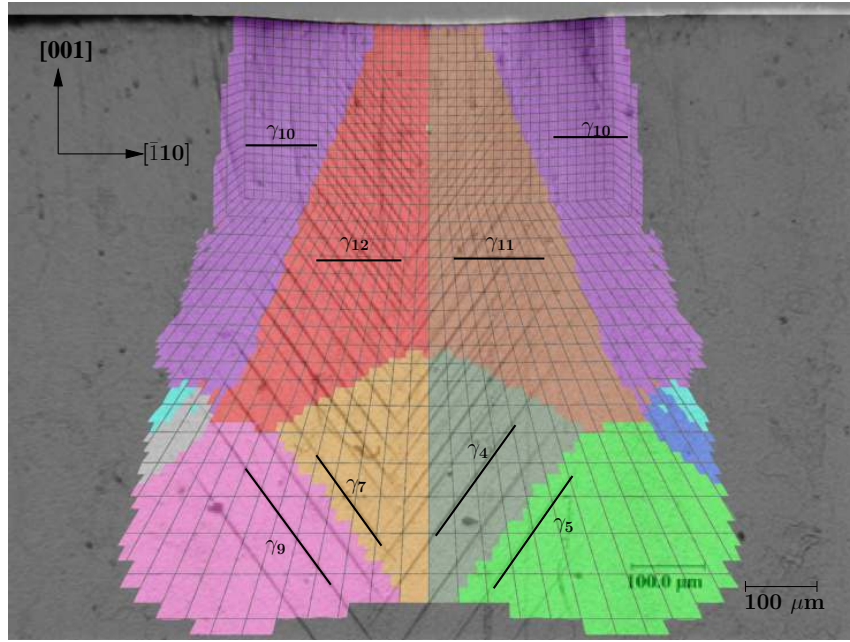
The slip systems predicted by CPFEA are compared in a more systematic way with the slip lines in the optical microscope images, whilst considering the VIs presented in Table 3.1, the angles of the expected slip lines (Figure 3.8) and the magnitude of the individual slip systems predicted by the CPFEA (i.e. the  $\gamma^s$  values stored in the original computation results).

### Orientation A

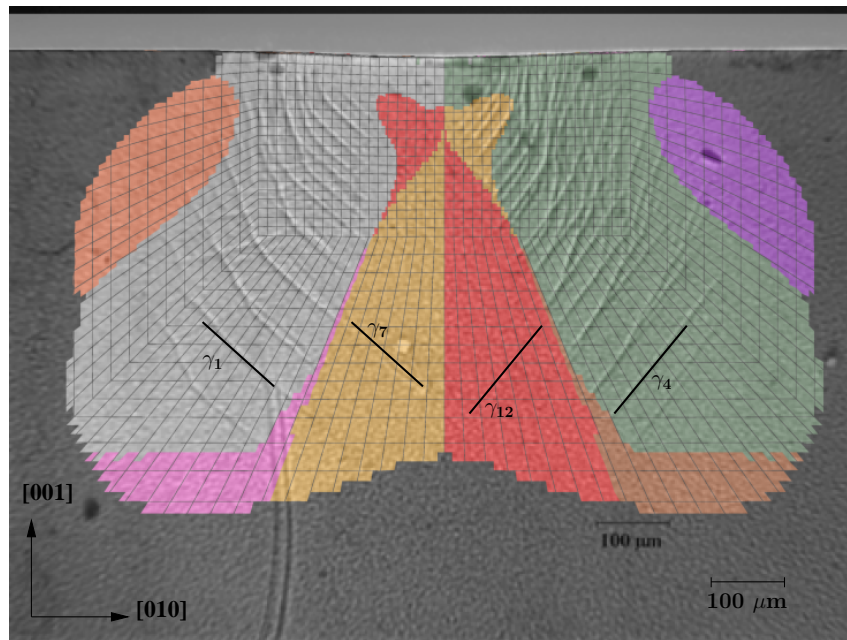
The dominant slip map shown in Figure 5.6a shows an analysis of the  $\gamma$ -map superimposed onto the experimental image. The solid black lines show the theoretically expected slip trace for the dominant slip system identified in the post-processed maps. The zones where the most active-slip systems are identified as systems 4, 5, 7, 9 and 10, are in good agreement with the slip traces observed experimentally. The zones where slip systems 11 and 12 are predicted to be most active do not correspond to the inclined slip traces observed in the experiment. The experimental slip traces hint at the dominance of slip systems 4 and 7 in these regions.

Focusing on the region where system 12 was identified as the dominant slip system, a comparison of Figure 5.3a with the corresponding Figure 3.8 indicates the systems 7, 8 and 9 as the most probable candidates for the position of the “most-active-slip-system” in the region. Upon examination of the plastic slip on each individual system in the CPFEA, systems 8 and 9 are ruled out as they present no activity in the region being considered. Furthermore, the values of slip on system 7 and the system 12 are found to be very close (about 0.027) over a major part of the region in question. Keeping in mind the fact that systems 7 and 12 have the same VI, we conclude these slip systems exhibit similar levels of activity. In this aspect, it is interesting to note that the combination of  $\gamma$ -maps and VI allows one to isolate from a group of slip systems in any given region, a few highly active systems upon which concentrated analysis can be conducted (in the example considered here, 2 out of 12 systems, viz. systems 7 and 12, are isolated as the most probable dominant systems).

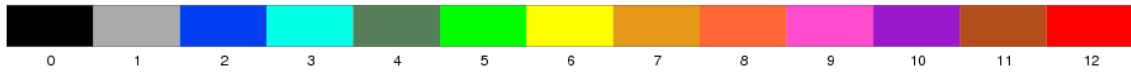
Another feature that is observed in Figure 5.6a, is that the axis of symmetry between the slip lines (which is expected to be in-line with the loading axis for an ideal case) is at an angle of about  $8^\circ$  to the vertical axis. This deviation from the expected slip traces could be due to a misorientation of the primary [001] direction. Although, a confirmation of the



(a) orientation A at 500  $\mu\text{m}$  contact with indent



(b) orientation B at 325  $\mu\text{m}$  contact with indent



(c) Scale indicating the different slip systems represented in the  $\gamma$ -maps

Figure 5.6: Comparison of dominant slip maps ( $\gamma$ -maps) and experimental results for an indentation depth  $\delta = 20 \mu\text{m}$  for fig. (a) and  $\delta = 16 \mu\text{m}$  for fig. (b)

angle of deviation from the ideal orientation by experimental techniques such as EBSD mapping is necessary, such a confirmation of misorientation may shed light on some sort of a bias towards system 7 over system 12 in the experiment. In the absence of such analysis,

further simulations of the experiment are suggested, which account for some misorientation of the material. Such simulations were conducted and are discussed in a later section (see Section 5.4.4).

### Orientation B

Two major lateral plastic zones that are observed in the  $\gamma$ -maps for orientation B match the slip traces observed on the experimental specimens. The  $\gamma$ -maps also indicate two central domains dominated by the slip systems 7 and 12 in the  $\gamma$ -maps, whereas no slip lines are observed in the experiment in these zones. A closer inspection of the VI values for orientation B indicates that the slip systems 7 and 12 are not expected to produce any visible slip traces (i.e. VI=0) for this orientation. Thus, the presence of plasticity on these systems cannot be confirmed by optical examination alone.

It is also noted that some intense rather wavy bands occur in the experimental images. These intense bands are symmetric about the Y-axis and overlap with other slip lines on the surface. To confirm the existence of such more intense deformation zones, the individual amount of plastic slip on each slip plane was examined. The CPFEA simulations indicate a significant strain localisation due to the slip systems 7 and 12, which seems to correspond to the localisation bands observed in the specimen. The computed contours of plastic slip on these two systems are shown in Figure 5.7. However, the simulated results need to be confirmed with further testing such as strain field measurements by microgrid or digital image correlation.

#### 5.4.2 Surface vs. bulk behaviour

The CPFEA reveals a rapid variation of plastic strain along the thickness of the simulated specimen. The plastic strain field observed at the free surface changes drastically 320  $\mu\text{m}$  below the surface. The bulk plastic field then stabilises and becomes invariant along the Z-axis. The  $\gamma$ -maps at the core of the two specimens are shown in Figure 5.8. Comparing these with the  $\gamma$ -maps from Figure 5.6, obvious differences in shape and size of the plastic zone and nature of dominant slip systems, are observed between the core and the free surface. These differences are the consequences of plane stress conditions at the free surface and to plane strain conditions in the core. This indicates that the analysis of such experiments should not be based solely on the observation of the free surface and that complementary destructive analyses are required inside the sample. Such different bulk and free surface behaviours were already noted in the simulation of cracks in single crystal superalloy CT specimens, see [Flouriot et al. \[2003\]](#). In the reference [Kysar and Briant \[2002\]](#), the specimens were cut at the middle section and an EBSD analysis was performed thus revealing parts of the bulk material response.

#### 5.4.3 Small- vs. finite-strain formulation

The results of Finite Element simulations obtained by means of the finite strain and of the small strain versions of the crystal plasticity model (see Chapter 3) were compared for loading conditions encountered in the experiments. The small strain version of the model is less expensive in terms of CPU time, which is an advantage for practical structural computations involving single crystals like in turbine blades. Figure 5.9 shows a comparison between the equivalent plastic strain field predicted by the small- and large-strain formulations, in orientation A at a contact length of 140  $\mu\text{m}$ . Differences can be

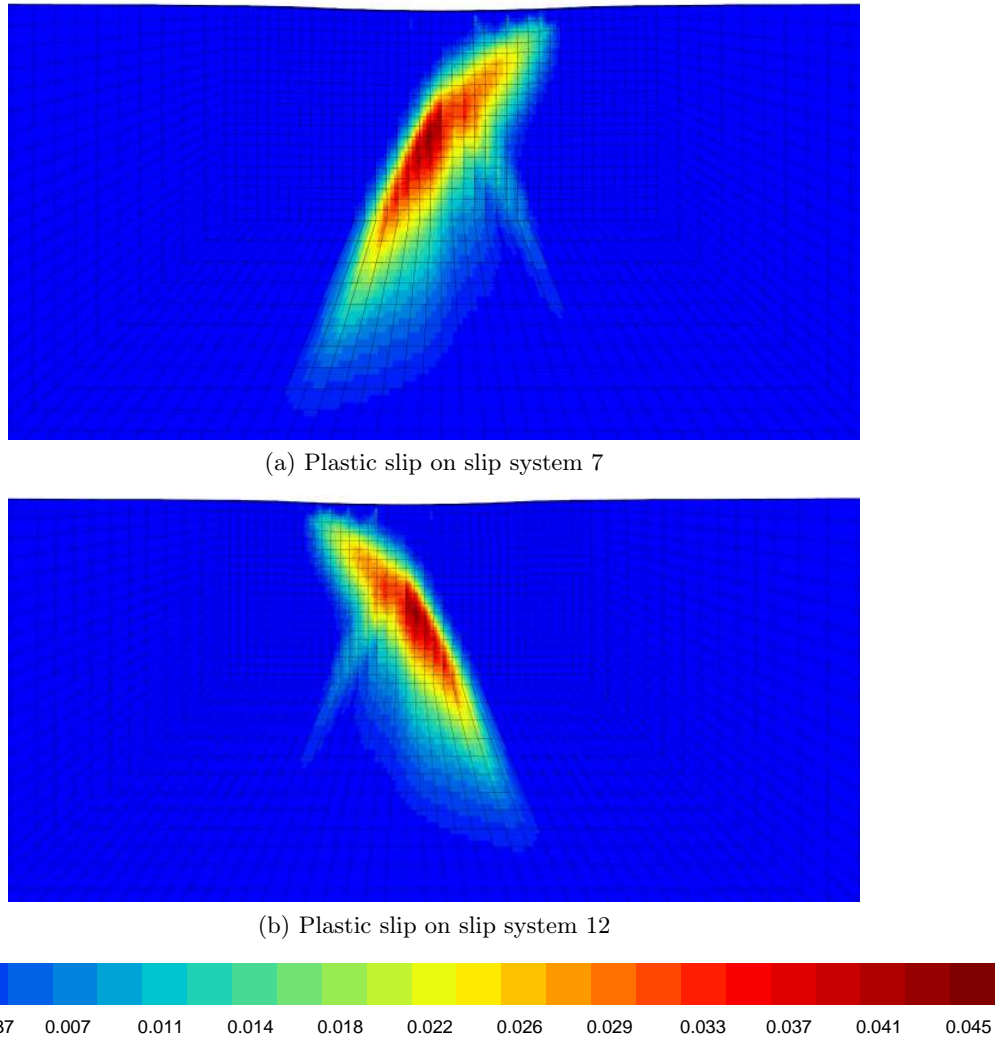
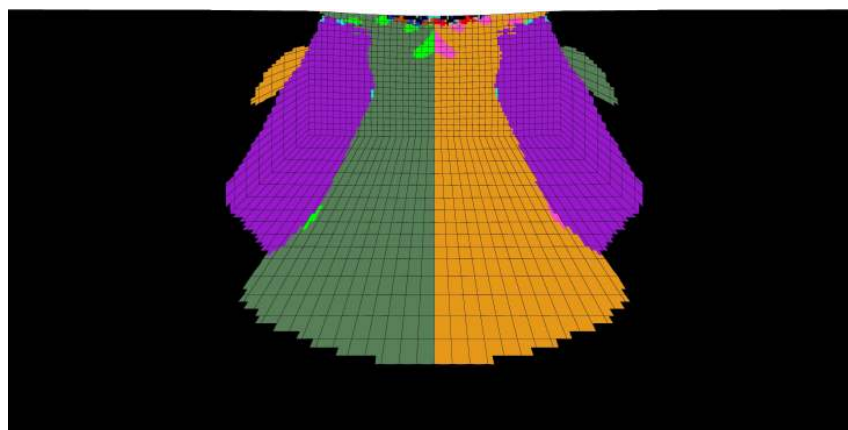
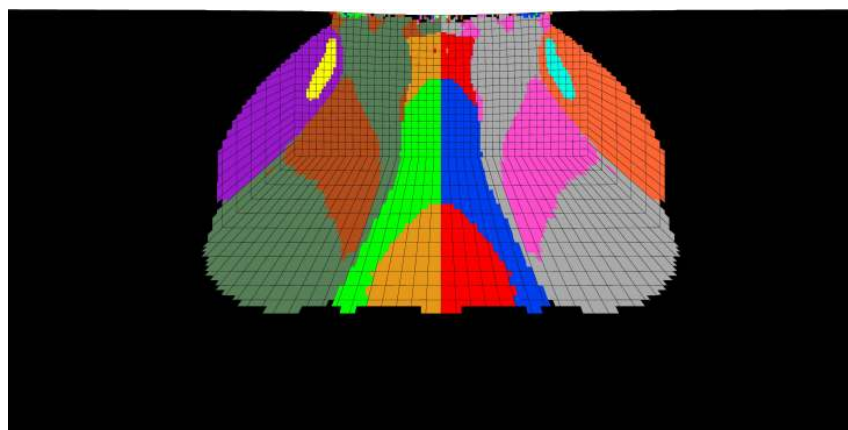
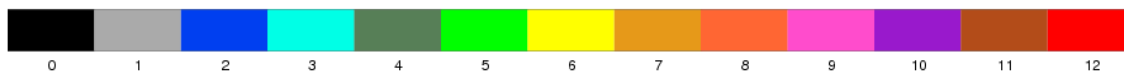


Figure 5.7: Iso-values of plastic slip for systems 7 and 12.

observed but remain insignificant especially with respect to the purpose of comparison with experimental results.

The finite deformation formulation of the model also provides information about lattice rotations in the single crystal material. The Figures 5.10 and 5.11 show the lattice rotations for orientations A and B. At a contact length of  $140 \mu\text{m}$ , orientation A shows a maximum rotation of  $0.077$  radians (i.e. about  $4.5^\circ$ ) and orientation B shows a maximum rotation of  $0.02$  radians (about  $1^\circ$ ). From Figure 5.11, one can observe that the lattice rotation patterns are very different for the two orientations. This indicates that the secondary orientation also affects, in a profound manner, the lattice rotation development in the specimen. On the other hand, Figure 5.10 shows that the rotations are more pronounced toward the free surface and extend up to a depth of about  $320 \mu\text{m}$ .

(a) Orientation A at 500  $\mu\text{m}$  contact length(b) Orientation B at 325  $\mu\text{m}$  contact lengthFigure 5.8: Slip activity at the core of NBSX substrates. To be compared with the  $\gamma$ -maps in Figure 5.6

#### 5.4.4 Effect of a slight misorientation of the crystal with respect to ideal orientation

It was indicated in Section 5.4.1 that the differences between the simulated dominant slip maps and the slip traces observed in experiments could be attributed to misorientation of the crystal. It was also hypothesised that such a misorientation could also cause a bias in the activation of slip systems. To test this hypothesis, simulations using *Mesh 1* were launched. These simulations introduced a  $10^\circ$  misorientation in the crystal. Simulations with clockwise and the anti-clockwise misorientation were tested. It was found that the simulation with the  $10^\circ$  misorientation in the clockwise direction yielded  $\gamma$ -maps closest to the experimentally observed slip traces. This  $\gamma$ -maps is shown in Figure 5.12.

The  $\gamma$ -maps in Figure 5.12 shows that the activated slip systems are no longer symmetric, but are divided by a ‘median’ at an angle of about 11.5 degrees to the axis of loading. It is also observed that the dominant slip regions differ significantly from those observed in Figure 5.6a. The regions in which system 12 was indicated as the dominant slip system are almost completely replaced by regions with system 7 as dominant slip, which is in agreement with the slip traces observed experimentally. This proves that any deviation

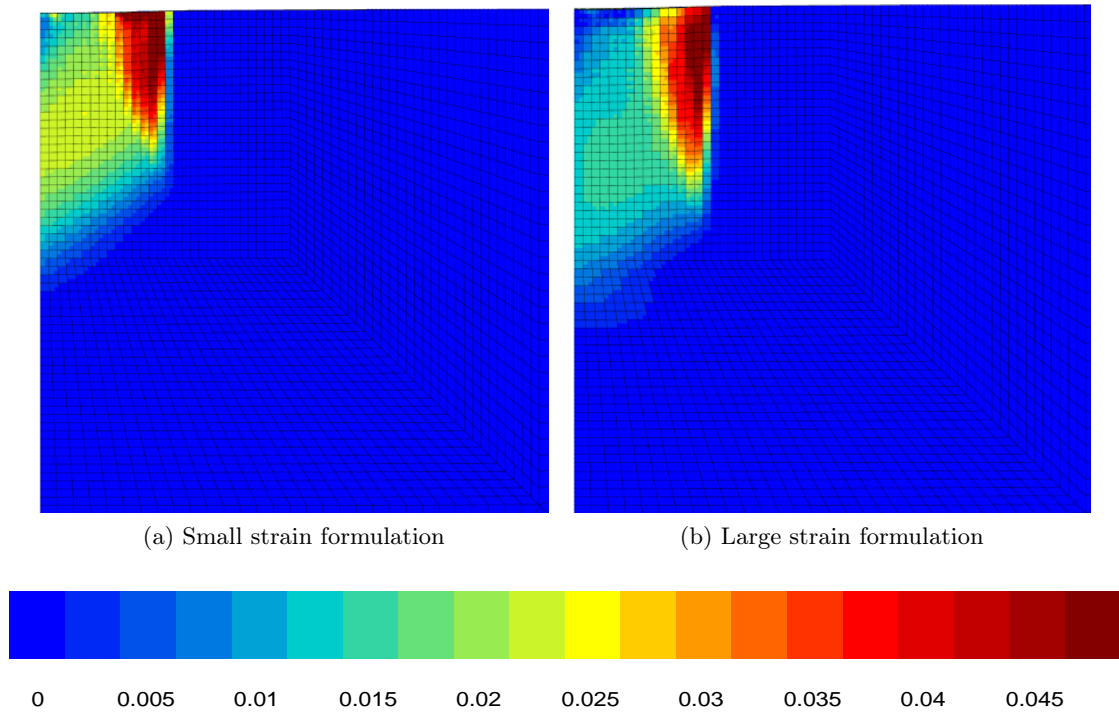


Figure 5.9: Equivalent plastic strain field for FE computations using the small strain formulation of the model (b) and the finite deformation model (a), for orientation A at a contact length of  $140 \mu\text{m}$

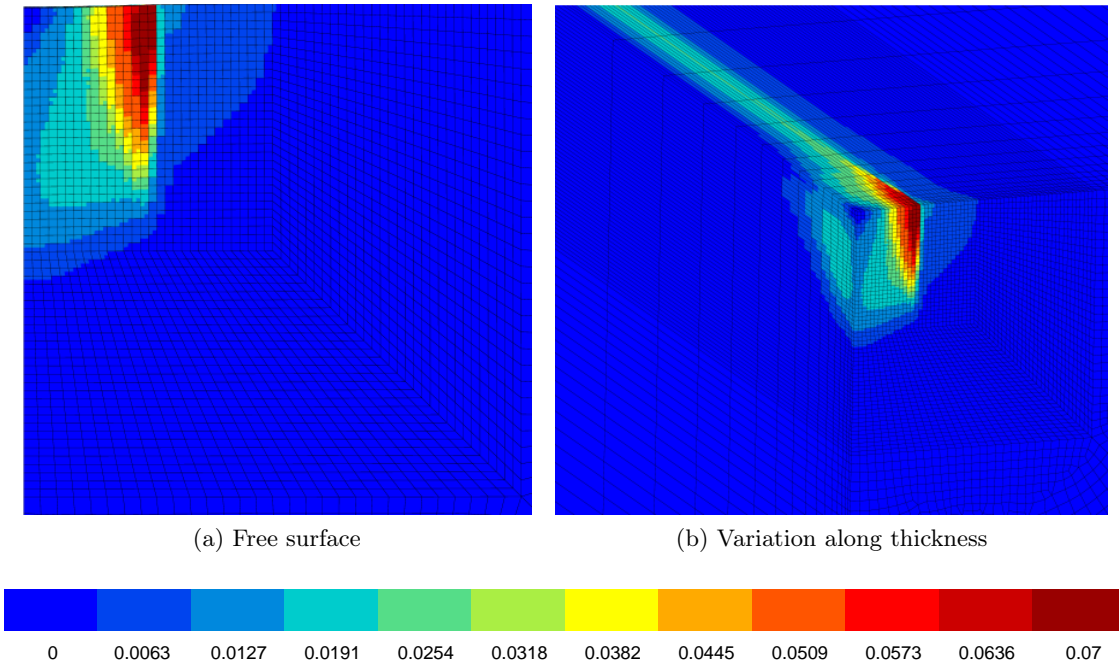


Figure 5.10: Lattice rotation in orientation A at a contact length of  $140 \mu\text{m}$  (in radians)

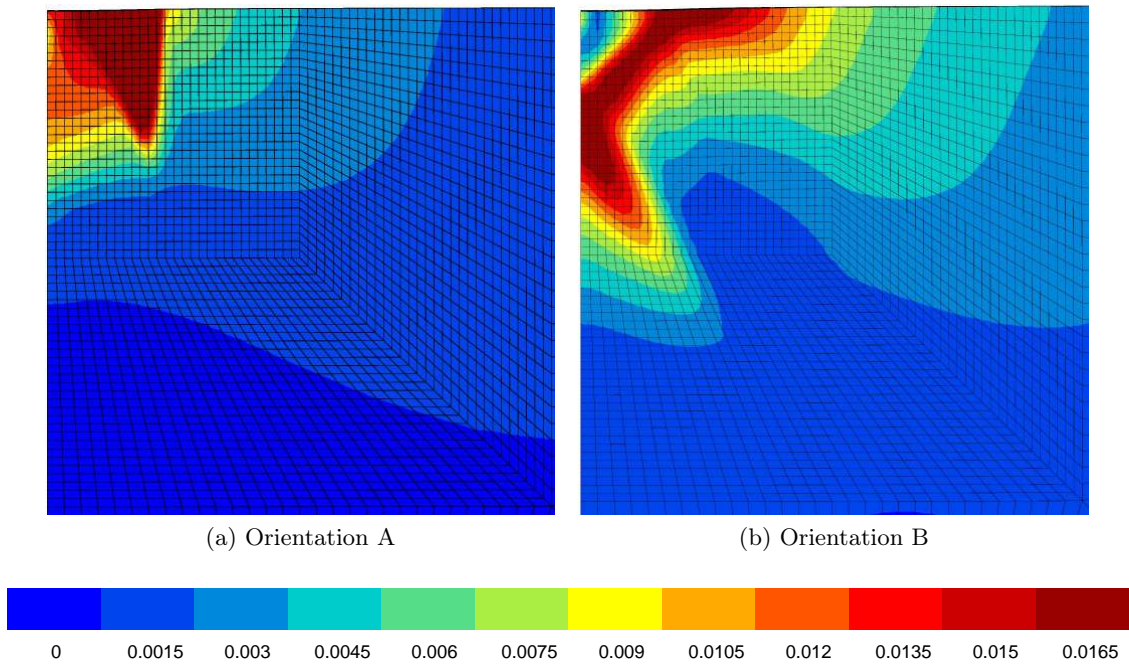


Figure 5.11: Comparison between the lattice rotations in the two secondary orientations at a contact length of  $140 \mu\text{m}$  (in radians)

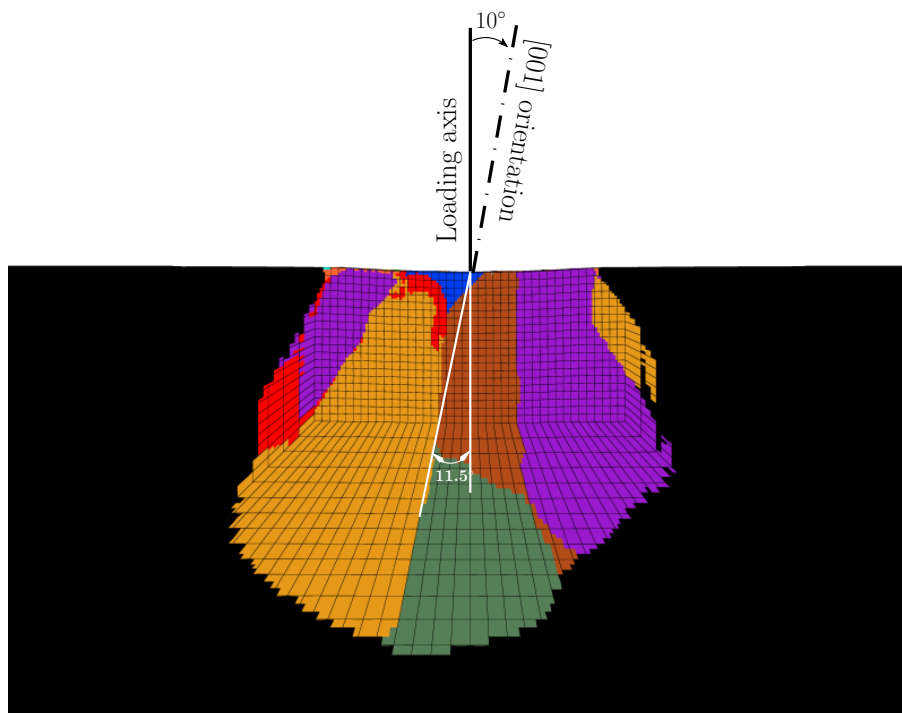


Figure 5.12: Dominant slip map in specimen with  $10^\circ$  misorientation

from intended crystallographic axes can cause biased activation of slip systems.

### 5.4.5 Stress fields and triaxiality

Figure 5.13 presents the stress maps in the specimen with the 10 degree misorientation. It is observed that the stress distribution is asymmetric, and also that the highest stress level is found not at the line of contact between the indent and the substrate, but at a distance of about  $260 \mu\text{m}$  below the indentation surface (Figure 5.13b). The analysis of such zones could be useful in the identification of the locations of damage initiation. It is also clear that the stresses differ rather starkly from the surface to the core.

Another measure which can be used to characterise the complex nature of the stress state in a specimen is the *Stress Triaxiality*, which is defined as the ratio of the mean stress to the Von-Mises equivalent stress. The triaxiality was computed for the substrate used in the simulations. Figure 5.14 shows the absolute values of the triaxiality at the core of the specimen (The actual computed values are negative due to compressive loading, hence the absolute values are shown). It was observed that the core of the specimen experiences substantial triaxiality in comparison with the free surface of the specimen, where the triaxiality is almost zero. This observation is in agreement with the reported observation in a previous publication Sabnis et al. [2012], that the stress state at the core of an NBSX specimen is significantly different in comparison with the free surface, thereby justifying a thorough 3D computational analysis of any NBSX specimen being considered.

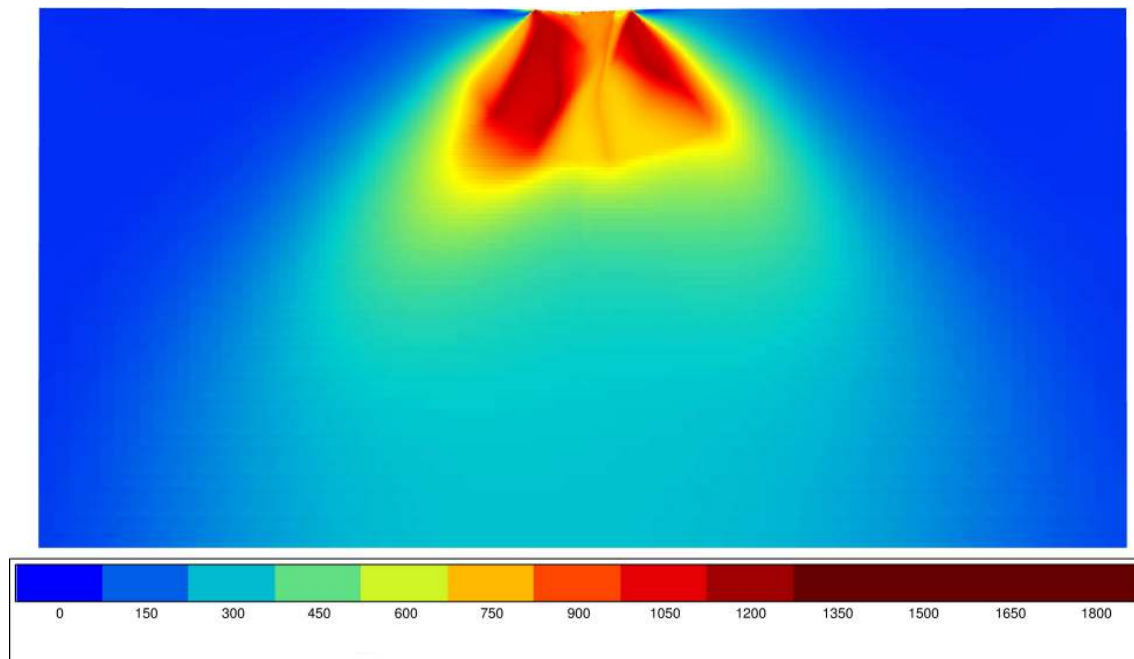
## 5.5 Conclusions

The work presented here was aimed at a numerical analysis of cylindrical indentation tests using crystal plasticity, with the purpose of studying the applicability of crystal plasticity simulations to study sub-surface fields in NBSX materials. The simulations were compared with experimental observations of slip lines. The predicted plastic zone sizes were found to be in good agreement with plastic slip traces found on the surface of the specimen. The secondary orientation of the crystal was found to have a profound impact on the individual slip system activity and the plastic zone shape. Such activity further emphasises the necessity to study the effect of crystal plasticity on damage initiation and crack propagation in NBSX materials.

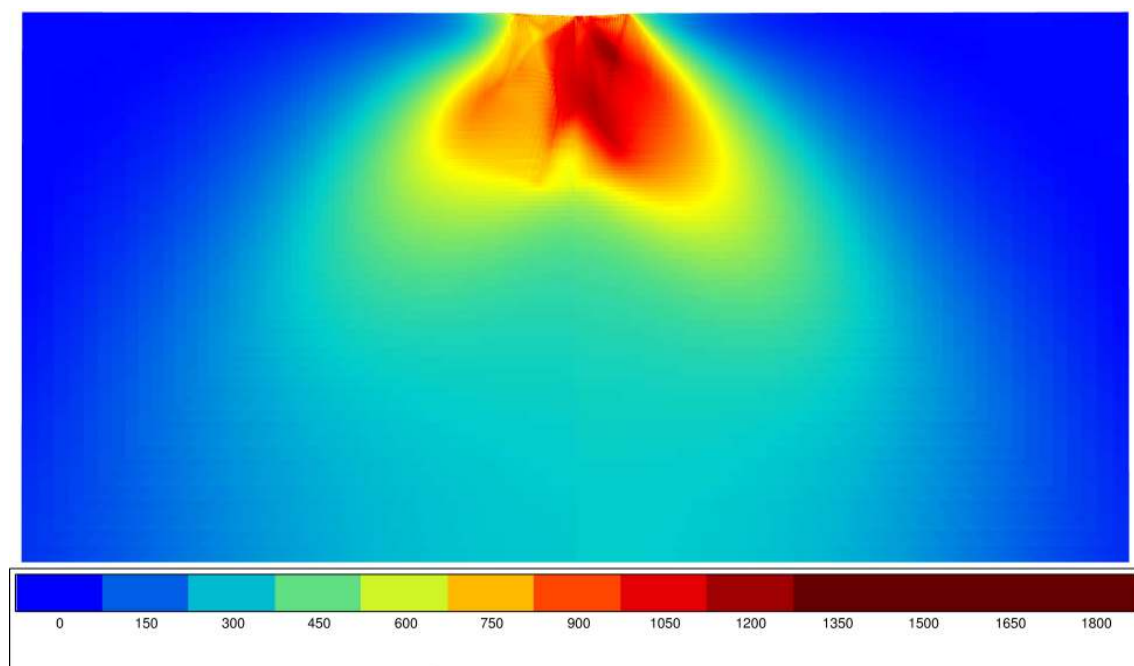
The simulations show that the strain fields and the lattice rotation fields predicted by CPFEA strongly differ on the lateral free surface and in the bulk. The transition zone is a boundary layer close to the surface having a thickness of about  $320 \mu\text{m}$ . An analysis of the stress states at the core and the surface of the specimen also indicated that the peak stresses are found not at the indentation surface, but about  $260 \mu\text{m}$  below the indentation surface. These observations demonstrate the importance of detailed 3D simulations of components for comparison with surface experimental observations.

Pile-up formations were reported in the indentation study discussed in Zambaldi et al. [2007]. In contrast to these reports, only sink-in was predicted by the numerical simulations presented here.

In this work the computational and experimental analyses were limited to the determination of slip activity including dominant slip systems. Additional complementary experimental observations are required for more quantitative comparisons. They include roughness measurements at the indented surface to identify sink-in or pile-up situations, EBSD lattice rotation field measurements and strain field measurements on the lateral free surface.



(a) Specimen core



(b) Specimen free surface

Figure 5.13: Von Mises stress in specimen with  $10^\circ$  misorientation

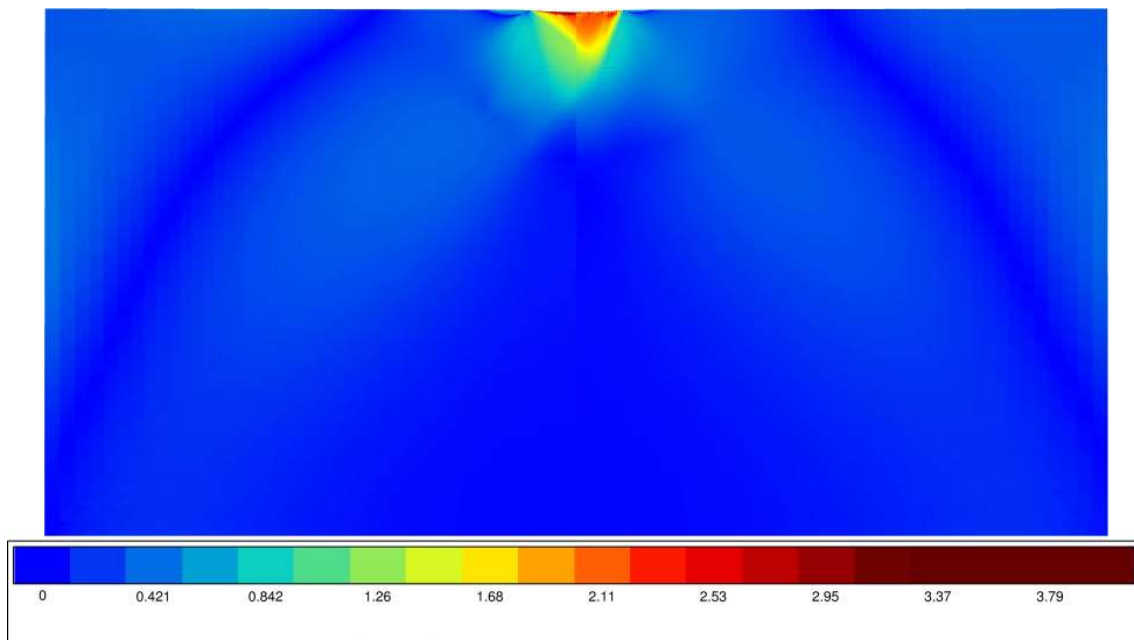


Figure 5.14: Stress triaxiality at the core in the specimen with  $10^\circ$  misorientation



---

Part III

Damage Modelling



## Chapter 6

# Gradient Based Damage Modelling

### Résumé

Le chapitre 6 présente une brève revue de la modélisation d'endommagement. En commençant avec une revue de la littérature, le problème de la dépendance des résultats par rapport maillage est identifié. Ensuite, le modèle «Microdamage», qui a été développé dans la thèse [Aslan \[2010\]](#) est présenté. Ce modèle servira de base pour le développement d'un modèle plus fortement couplé. Enfin, la modélisation des chemins des fissures par la méthode du microdamage et par la méthode des champs de phase sont comparées.

The following chapter introduces the subject of gradient-based damage modelling. The *Microdamage Model*, which was developed in [Aslan et al. \[2011a\]](#) is introduced as the base model for the development of a coupled plasticity-damage material model in the following chapters. A few similar approaches are also presented for a theoretical comparison of distinct models. Some aspects of the microdamage model are also identified as providing room for improvement.

### 6.1 Numerical models for cracks and damaged zones

The main challenge faced in the numerical modelling of fracture/damage mechanics concerns the handling of the singular nature of a cracked structure/material. Many numerical approaches such as the eXtended Finite Element Method (XFEM) and the Cohesive Zone Modelling (CZM) approach have been developed. An example of CZM applied to single crystal superalloys can be found in [Bouvard \[2006\]](#), [Bouvard et al. \[2009\]](#). However, these approaches pose other difficulties. CZM, for example, requires a layer of cohesive/interface elements, which in turn implies that the expected crack path is already known. While such an approach is practical for materials such as composites due to the presence of clearly defined macroscopic interfaces, the practicality of its application to the simulation of plasticity-driven damaging of materials such as single crystals is questionable. It is well known that the inelastic deformation fields ahead of the crack tip usually extend over a “plastic zone”, which means that a relatively high number of interface elements would be required if one were to consider the entire zone as being susceptible to damage. While adaptive remeshing is an option for larger structures, the use of adaptive remeshing in concert with CZM would require not only the remeshing of a region, but the insertion of interface elements in a desired sub-zone within the area being remeshed. This amounts

to a significant increase in the computational power required to efficiently use CZM in single crystals. The XFEM approach on the other hand, is based on the introduction of a local enrichment of the spatial discretisation provided by the finite element method. The local enrichment is usually implemented by an application of the numerical concept of “Partition of Unity” (Melenk and Babuska [1996]). Although the XFEM method, first introduced in Moës et al. [1999], has been gaining popularity in the fracture mechanics community due to its ability to handle arbitrary cracks (see for example Belytschko et al. [2001]), to the author’s knowledge, there are no studies that use XFEM to simulate crack growth in elastic-visco-plastic single crystals. The lack of such study could possibly be attributed to the yet-open-questions that concern the use of XFEM to simulate crack growth that follows extensive plasticity. Some of the difficulties encountered in using XFEM to simulate crack growth in the presence of plasticity are discussed in Seabra et al. [2012]. The robust XFEM, which uses the principle of superposition to introduce local enrichment, approaches the simulation of cracks from the perspective of a convergence problem. Hence, the solutions accorded by the method are a solution obtained by the enhancement of the spatial discretisation that is usually handled by the traditional finite element method. It is in this setting, that the concepts offered by the “Local approach to fracture” and Continuum Damage Models (CDM) are interesting. CDM treat the cracks from the perspective of material responses, thus allowing for a physically accurate modelling of discontinuities such as cracks. Furthermore, the material-response origins of CDM allows for easier inclusion of coupled processes, as will be seen in later chapters.

CDM such as the ones proposed in Lemaitre and Chaboche [1994], Lemaitre and Desmorat [2005], Lemaitre et al. [2000], Sermage et al. [2000], Saanouni [2012] etc. are usually modelled numerically by introducing a scalar/tensorial internal variable that describes the evolution of damage/void growth in the material. These internal variables are then controlled by evolution relations obtained either empirically or by the consideration of a dissipation potential in a thermodynamic framework (as described in Chapter 2). When CDM are used in combination with FEM to simulate softening behaviour of materials, the differential equations controlling the material response may lose their ellipticity, which in turn manifests itself in the form of mesh dependency of the results. Such a dependency has been addressed in many studies (e.g. Marchal [2006], de Borst et al. [1993], Schreyer and Chen [1986], Kuhl and Ramm [1999]). This loss of ellipticity is attributed to the violation of the stability criterion which occurs in the presence of phenomena such as strain-softening, with the condition for stability being given by (as presented in de Borst et al. [1993])

$$\dot{\boldsymbol{\epsilon}} : \dot{\boldsymbol{\sigma}} \geq 0 \tag{6.1}$$

Various numerical solutions to this problem have been proposed. While some authors propose the inclusion of the “non-local” models (e.g. Bažant and Pijaudier-Cabot [1988], Bažant et al. [1984]), others propose the use of a modified form of non-local models (e.g. Poh and Swaddiwudhipong [2009] proposes the so-called “over-non-local model”). A third popular modelling option is found in gradient models which take into consideration, in some form, the gradient of the variable causing the mesh dependency. Many different approaches have been proposed to model strain-softening plasticity or damage. Aifantis [1999; 2003], Forest et al. [2002] for example consider the gradient of plastic strain, Peerlings et al. [1996; 2000] consider gradient enhanced model and Engelen et al. [2003] consider a non-local implicit gradient model. Aslan and Forest [2009] presented a regularised damage model based on the micromorphic approach. Forest [2009] presented a thermodynamic generalised methodology for deriving the non-local models based on micromorphic continua, and showed that the models derived from the

micromorphic approach represent the various non-local/gradient approaches under suitable circumstances. A more complete explanation of the generalised methodology for deriving higher order gradient models in a thermodynamically consistent manner can be found in Saanouni [2012].

In the following chapter, the “Microdamage model” developed in Aslan [2010] is introduced as a reference model. Then, a comparison between this microdamage model and the Phase Field approach (Bourdin et al. [2008]) is presented.

## 6.2 Microdamage model

The microdamage model provides a continuum approach to handling the damage/fracture phenomenon. This is achieved by the introduction of a two-way split of the total strain tensor. Restricting our considerations to the small-strain formulation framework, the symmetric deformation gradient tensor  $\underline{\underline{\xi}}$  is split in an additive manner into two contributions, viz. *elastic* and *damage* contributions, represented by  $\underline{\underline{\xi}}^e$ , and  $\underline{\underline{\xi}}^d$  respectively. The strain rate can then be written as

$$\dot{\underline{\underline{\xi}}} = \dot{\underline{\underline{\xi}}}^e + \dot{\underline{\underline{\xi}}}^d \quad (6.2)$$

This split introduces a “damage-strain”, which in turn paves the way for the introduction of a strain-like degree of freedom (DOF), which represents in some vague sense, a normalised dimension-less indicator of damage. The nature of this variable is such that the lower end is bound at 0 and the upper end is boundless. This means that the “broken” element can deform in an unlimited manner. This added variable–  $d_\mu$  – is referred to as *Microdamage*. The extended DOF set and the extended gradient space can then be represented by

$$\text{DOF} = \{\underline{\mathbf{u}}, d_\mu\} \quad (6.3)$$

$$\text{Grad} = \{\underline{\underline{\xi}}, \nabla d_\mu\} \quad (6.4)$$

Introducing the generalised stresses,  $\underline{\mathbf{b}}$  and  $a$ , which are conjugates of  $\nabla d_\mu$  and  $d_\mu$  respectively, an enhanced form of the principle of virtual power can be considered (see Forest [2009]). Thus, for the static case, the enhanced principle of virtual power is given by the relation

$$\int_{\Omega} \left( \underline{\underline{\boldsymbol{\sigma}}} : \dot{\underline{\underline{\xi}}} + \underline{\mathbf{b}} \cdot \nabla \dot{d}_\mu + a \dot{d}_\mu \right) dV = \int_{\partial\Omega} \left( \underline{\mathbf{t}} \cdot \dot{\underline{\mathbf{u}}} + a_c \dot{d}_\mu \right) dS \quad (6.5)$$

where  $\underline{\mathbf{t}}$  is the traction vector and  $a_c$  represents a generalised traction. In the above relation, integration over the domain  $\Omega$  represents the volume integral for the entire structure/specimen under consideration, and the integration over the domain  $\partial\Omega$  represents the surface integral for boundaries of the specimen. Upon application of the divergence theorem in the absence of volume forces, one arrives at the following set of balance and boundary relations,

$$\text{div } \underline{\underline{\boldsymbol{\sigma}}} = 0 \quad (6.6)$$

$$\text{div } \underline{\mathbf{b}} = a \quad (6.7)$$

$$\underline{\underline{\boldsymbol{\sigma}}} \cdot \underline{\mathbf{n}} = \underline{\mathbf{t}} \quad (6.8)$$

$$\underline{\mathbf{b}} \cdot \underline{\mathbf{n}} = a_c \quad (6.9)$$

where  $\underline{n}$  is the unit vector normal to the free surface at the material point under consideration.

The Equations 6.6 and 6.7 represent balance relations for the stress and the microdamage continuum, while the relations 6.8 and 6.9 provide the conditions at the boundaries of the problem being considered. With the necessary balance relations in place, one proceeds to obtain thermodynamically consistent constitutive relations for the stresses and the internal variables.

As a basis for the thermodynamically consistent derivation of the constitutive relations, a free energy density functional of the following form is considered

$$\rho\Psi: = \Psi^{el} + \frac{Hd^2}{2} + \frac{H_\mu(d - d_\mu)^2}{2} + \frac{A}{2}\nabla d_\mu \cdot \nabla d_\mu \quad (6.10)$$

where  $\Psi^{el}$  denotes the conventional elastic energy, and is given as

$$\Psi^{el}: = \frac{1}{2}\underline{\underline{\xi}}^e: \underline{\underline{\mathcal{C}}}: \underline{\underline{\xi}}^e \quad (6.11)$$

The free energy density functional shown in Equation 6.10 contains the energetic contribution of the elastic deformation, represented by  $\Psi^{el}$ . The functional also contains two additional contributions. First, a term containing the softening material parameter  $H < 0$  (in *MPa*) and the internal variable for damage  $d$  representing the energetic contribution of damage to the free energy change in the system. As damage in a material grows, the stress carrying capacity of the material is reduced. The second additional term in Equation 6.10 is the term containing  $H_\mu$ ,  $d$  and  $d_\mu$ . The material parameter  $H_\mu$  (in *MPa*) can be considered to be a penalty parameter which ensures that the values of  $d$  and  $d_\mu$  remain close; i.e. the penalty term ensures that the value of the computed internal variable and the computed value of the microdamage are close. The impact of the second additional term with the material parameter  $A > 0$  (in *MPa.mm<sup>2</sup>*) is that it ensures effective regularisation of numerical discontinuity associated with damage.

Considering the free energy density functional described previously, one proceeds to determine the constitutive relations for the various stresses and strains. The following state laws are postulated:

$$\begin{aligned} \underline{\underline{\sigma}} &= \rho \frac{\partial \psi}{\partial \underline{\underline{\xi}}^e} \\ \underline{\underline{b}} &= \rho \frac{\partial \psi}{\partial \nabla d_\mu} \\ a &= \rho \frac{\partial \psi}{\partial d_\mu} \end{aligned} \quad (6.12)$$

These can be written more specifically for our case as:

$$\underline{\underline{\sigma}} = \underline{\underline{\mathcal{C}}}: \underline{\underline{\xi}}^e \quad (6.13)$$

$$\underline{\underline{b}} = A\nabla d_\mu \quad (6.14)$$

$$a = -H_\mu(d - d_\mu) \quad (6.15)$$

In addition to the stresses, relations are also obtained for the driving forces, which are the thermodynamic conjugates of the internal variables. The internal variables of interest in the present formulation are the damage  $d$  and elastic strain  $\underline{\underline{\xi}}^e$ . Due to the additive split of the total strain, the latter internal variable does not need a separate evolution relation.

However, an evolution relation for the internal damage variable  $d$  is necessary. To meet this need, a damage potential is defined

$$\Omega_d(\underline{\sigma}, Y) \quad : = \quad \frac{K_d}{n_d + 1} \sum_r \left\langle \frac{f_d^r}{K_d} \right\rangle^{n_d+1} \quad (6.16)$$

where  $Y$  represents the “driving force” for the crack, and is given by

$$Y = \rho \frac{\partial \psi}{\partial d} \quad (6.17)$$

In the relation 6.16, the term  $f_d^r$  represents a damage threshold that controls the activation of damage in the material. For every damage plane (indicated by superscript  $r$ ), two criteria need to be defined. The first criterion incorporates the opening/cleavage along the normal to the plane ‘ $\underline{n}_r$ ’. Once the material is completely damaged on a given plane, there is no resistance to flow under shear loading. This is accounted for by the concept of *accommodation* which has been introduced earlier. Thus, one has two different yield criteria for the evolution of damage which are given by

$$f_d^r = f_c^r = |\underline{n}_d^r \cdot \underline{\sigma} \cdot \underline{n}_d^r| - Y \quad (6.18)$$

$$f_d^r = f_{ai}^r = |\underline{n}_d^r \cdot \underline{\sigma} \cdot \underline{l}_{d_i}^r| - Y \quad (6.19)$$

where the Relations 6.18 and 6.19 represent the criteria for opening and accommodation modes respectively. In the relation 6.19,  $\underline{l}_{d_i}^r (i=1,2)$  represents the two orthogonal accommodation directions in the damage plane. It is observed that both criteria are driven by the same force  $Y$ . The driving force is considered to be isotropic in nature for the sake of simplicity. Thus, the constitutive relation for the driving force is derived as

$$Y : = \rho \frac{\partial \psi}{\partial d} = Y_0 + Hd + H_\mu(d - d_\mu) \quad (6.20)$$

The damage criteria presented in Equations 6.18 and 6.19 are introduced on the basis of experimental observations, which indicate that the evolution of damage in NBSX materials occurs on specific crystallographic planes. In the introduced constitutive relation,  $Y_0$  represents a very high initial cleavage stress, which implies that a very high amount of stress is needed to break an undamaged, homogeneous material. In the presence of either plasticity or pre-existing damage,  $Y_0$  reduces with the evolution of plastic strain/damage. Damage initiation in the model occurs when the resolved normal stress on a plane exceeds the damage threshold  $Y$ . Thus, the initial damage is assumed to occur only along the normal to a damage plane. For the evolution of damage in directions along the damage plane, i.e. for Mode II and Mode III shear-driven evolution of damage in the damage plane, the concept of accommodation is used. The concepts of opening and accommodation have been discussed in detail in Chapter 2.

Using the relations 6.20, 6.18, 6.19 and 6.16, the evolution relations for the opening and accommodation along the damage planes are given by

$$\dot{d}_c^r = \left\langle \frac{f_c^r}{K_d} \right\rangle^{n_d} \text{sign} (\underline{n}_d^r \cdot \underline{\sigma} \cdot \underline{n}_d^r) \quad (6.21)$$

$$\dot{d}_{ai}^r = \left\langle \frac{f_a^r}{K_d} \right\rangle^{n_d} \text{sign} (\underline{n}_d^r \cdot \underline{\sigma} \cdot \underline{l}_{d_i}^r) \quad (6.22)$$

The total damage evolution is then given as

$$\dot{d} = \sum_r |\dot{d}_c^r| + \sum_{r,i} |\dot{d}_{ai}^r| \quad (6.23)$$

Once the relation for  $\dot{d}$  is obtained, the relation for the damage strain is given as

$$\tilde{\dot{\epsilon}}^d = \sum_r \left( \dot{d}_c^r (\mathbf{n}_d^r \otimes \mathbf{n}_d^r) + \sum_i \dot{d}_{ai}^r (\mathbf{n}_d^r \otimes \mathbf{l}_{d_i}^{sym}) \right) \quad (6.24)$$

In the above set of equations, it is noted that the opening on the damage plane  $d_c$  can become negative under compressive loading. In the case of a real material, this corresponds to the mechanism of crack closure. To ensure that the simulations of crack closure remain realistic, special attention must be paid to the cases where closure of open cracks can occur. This is ensured in the code by allowing the reduction of crack opening  $d_c$  under compressive loading (compressive relative to the damage plane being considered), provided that  $d_c > 0$ . Once,  $d_c = 0$ , the evolution of the total damage  $d$  is stopped, thus ensuring that no further damaging of the material occurs when a crack is closed. Once this evolution of damage is stopped, the material exhibits elastic or elastoplastic behaviour.

Aslan [2010] also provided an analytical solution for the width of the regularised zone for the simple case of a 1D strip subject to tensile loading (see Figure 6.1). It is assumed that there exists a zone of fixed width where inelastic loading is active. For a rate-independent case, this imposes the condition that  $f_d = 0$  in this zone. Due to this condition, the spatial derivatives of the yield functions in this zone should also be zero. I.e. requiring

$$f_{d,x} = 0 \quad (6.25)$$

From relation 6.25, a relation between the DOF  $d_\mu$  and the internal variable  $d$  is obtained as

$$d_{,x} = \frac{H_\mu}{H + H_\mu} d_{\mu,x} \quad (6.26)$$

The local form of the balance relation 6.7 can be rewritten as

$$A d_{\mu,xx} = -H_\mu (d - d_\mu) \quad (6.27)$$

Considering the derivative of 6.27 w.r.t.  $x$ , and inserting Equation 6.26 into the resultant equation, one obtains

$$d_{\mu,xxx} - \frac{H_\mu H}{A(H + H_\mu)} d_{\mu,x} = 0 \quad (6.28)$$

The Equation 6.28 is in the form of a classical second order homogeneous differential equation. Thus, the equation contains a characteristic length term which is given as

$$l_c = \sqrt{\left| \frac{A(H + H_\mu)}{H H_\mu} \right|} \quad (6.29)$$

where  $l_c$  represents the characteristic length of Equation 6.7. Inserting the relation between  $d$  and  $d_\mu$  obtained from the yield criterion ( Equation 6.18) into Equation 6.7, we have

$$d_\mu - l_c^2 \Delta d_\mu = 0 \quad (6.30)$$

The analytical solution to this relation is in the sinusoidal form, and is given as

$$d_{\mu,x} = P \cos\left(\frac{x}{l_c}\right) + Q \sin\left(\frac{x}{l_c}\right) \quad (6.31)$$

The analytical solution for  $l_c$  presented in Equation 6.29 will be discussed further in Chapter 7. The microdamage model presented in these paragraphs form the basis for the development of a coupled model for plasticity-driven failure, which will be described in Chapter 7. The following section provides a comparison between the microdamage model and a few other gradient type models.

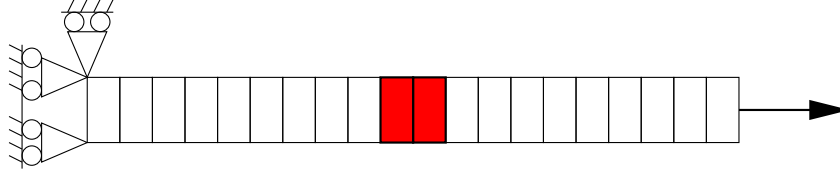


Figure 6.1: Strip test to simulate 1D case for analysis. The red elements represent elements that have been artificially weakened to prompt strain localisation

## 6.3 Regularisation approaches

### 6.3.1 Phase field models for fracture

The use of the so-called “Phase-Field Modelling” (PFM) of fracture has gained popularity in the recent years, mainly due to the simplicity offered by a phase field model. The versatility of this approach to modelling discontinuous phenomena can be seen in the fact that various groups propose models with similar form, while starting from completely different aspects of the problem. For example, [Hakim and Karma \[2008\]](#), [Karma et al. \[2001\]](#) use PFM as a purely mathematical approach to simulating fracture, while [Aranson et al. \[2000\]](#) seem to consider a more physics based approach. They consider the evolution of cracks in a material to be similar to the phenomena of wave propagation in solids. Other groups also introduce different perspectives to the problem. [Eastgate et al. \[2002\]](#) consider the fracture phase to be denoted by a conserved order parameter, thereby using a 4<sup>th</sup> order Cahn-Hilliard type evolution equation. [Kuhn and Müller \[2010\]](#) consider a phase field model based on the variational approach discussed in [Bourdin \[2007\]](#), [Bourdin et al. \[2008\]](#) and in [Francfort and Marigo \[1998\]](#). A physics oriented explanation of the PFM process in the context of elastoplastic behaviour, based on the concept of micro-force balance can be found in [Gurtin \[1996\]](#) and [Ammar et al. \[2009a\]](#), [Ammar et al. \[2009b\]](#). All the above models treat the numerical treatment of fracture on basis of some sort of a variational formulation. A clear description of different aspects involved in the variational modelling of fracture can be found in [Braides \[2002\]](#) and [Welschinger \[2010\]](#).

The result of using these models is rather clear. Irrespective of the physics behind the model or the mathematical starting point, all the models treat cracks by smearing out the sharp interfaces, i.e. the crack surfaces, over a characteristic length  $-\epsilon$ . This smearing out of a sharp boundary is achieved by the introduction of an additional balance relation for the quantity to be smeared. In most models, this additional relation contains a laplacian term, i.e. the second gradient of the localised quantity. Irrespective of the nomenclature used by different groups, this additional equation can be written down as a generalised balance relation in its local form as

$$\begin{aligned} \frac{\delta\psi}{\delta\phi} &= \hat{\phi} \\ \text{with } \frac{\delta\psi}{\delta\phi} &= \frac{\partial\psi}{\partial\phi} - \text{div} \frac{\partial\psi}{\partial\nabla\phi} \end{aligned} \tag{6.32}$$

Here  $\frac{\delta\psi}{\delta\phi}$  is the variational derivative,  $\hat{\phi}$  is a source term. A more descriptive explanation of variational formulation for fracture can be found in [Miehe et al. \[2010\]](#).

In the following sections, a model based on the phase-field approach is considered and is compared to the previously introduced microdamage model. It is shown that under certain conditions, it is possible to retrieve the models obtained from the phase field approach using the micromorphic approach. Both models are considered for their simplicity and their

proven ability to handle complex fracture phenomena such as initiation and bifurcation. A brief discussion is presented on an alternative interpretation of the models.

### 6.3.2 Variational approach based phase field model for fracture

The phase field model presented and discussed in [Kuhn and Müller \[2010\]](#) is considered. The balance relations for the model are given by the equations

$$\operatorname{div} \underset{\sim}{\boldsymbol{\sigma}} = 0 \quad (6.33)$$

$$\dot{\phi} = -M \frac{\delta \psi}{\delta \phi} \quad (6.34)$$

The Equation 6.33 is the standard momentum balance and the Equation 6.34 is the additional balance relation for the evolution of the phase field  $\phi$  that represents damage in the material. The free energy density functional of the model is in the form of a standard Ginzburg-Landau double well potential given by the equation

$$\rho \psi = \left( \frac{\phi^2 + \eta}{2} \right) \Psi^{el} + \frac{G}{2\epsilon} (1 - \phi)^2 + G\epsilon |\nabla \phi|^2 \quad (6.35)$$

with  $\Psi^{el}$  denoting the elastic energy of the material. Under quasi-static considerations, the choice of this particular FEF allows the balance relation in Equation 6.34 to be rewritten as

$$\left( \Psi^{el} + \frac{G}{2\epsilon} \right) \phi - 2G\epsilon \Delta \phi = \frac{G}{2\epsilon} \quad (6.36)$$

The model is constructed such that phase variable  $-\phi$ , which here represents damage, takes a value of  $\phi = 1$  when the material is intact and a value of  $\phi = 0$  when the material is broken. The thickness over which the damage field is regularised is controlled by the parameter  $\epsilon$ (mm).  $G$  indicates the fracture toughness of the material (in terms of  $N/mm$ ) and  $\Psi^{el}$  represents the elastic energy of the system.  $\eta$  is described a residual stiffness added due to reasons of numerical stability. The treatment of damage as a simple scalar field allows for the easy numerical implementation in a standard FE scheme, by the introduction of an additional degree of freedom to a standard element. The authors also report that the path of crack propagation (straight or curved) is controlled principally by the material parameter  $M$  ( $\frac{mm^2}{N \cdot s^2}$ ), which is referred to as a ‘‘mobility parameter’’. Certain properties of this model shall be revisited and discussed further in following sections.

### 6.3.3 Micromorphic continua based models

In order to furnish a comparison between the two models, the balance relations of the microdamage model discussed earlier are rewritten as

$$\operatorname{div} \underset{\sim}{\boldsymbol{\sigma}} = 0 \quad (6.37)$$

$$\frac{\delta \psi}{\delta \phi} = 0 \quad (6.38)$$

where the phase variable,  $\phi$  replaces the microdamage variable  $d_\mu$ . The free energy density functional used in the model (Equation 6.39), allows the balance relation in 6.38 to be rewritten in the form of Equation 6.40.

$$\rho \psi = \Psi^{el} + \frac{1}{2} H \left( \phi^{loc} \right)^2 + \frac{1}{2} H_\mu \left( \phi^{loc} - \phi \right)^2 + \frac{A}{2} \nabla \phi \cdot \nabla \phi \quad (6.39)$$

$$H_\mu \phi - A \Delta \phi = H_\mu \phi^{loc} \quad (6.40)$$

As in the previously discussed model, the term  $\Psi^{el}$  represents the elastic energy of the material. The parameter  $H$  represents the softening of the material caused by the evolution of damage in the material, and the parameter  $A$  is used principally for the control of the regularisation/diffuse-interface thickness. Here,  $\phi^{loc}$  indicates the value of the damage calculated locally via material constitutive equations (i.e.  $\phi^{loc}$  represents an internal variable), whereas  $\phi$  indicates the values computed from the weak form implementation of balance relations. Although the analytical relation for the thickness of the diffuse interface depends on the constitutive relations chosen for damage evolution modelling, it is observed that this thickness –  $\epsilon$  – can be controlled by the relation

$$\epsilon = \sqrt{K \frac{A}{H_\mu}} \quad (6.41)$$

with

$$K = \frac{H + H_\mu}{H}$$

$K$  is a constant factor, which in this particular model is a function of the material parameters  $H$  and  $H_\mu$ .

### 6.3.4 A generalised interpretation of a regularised model for fracture

A brief examination of the models presented so far reveals a strong similarity in the mathematical form of the models. A generalised version of the additional balance relation used in regularisation is already presented in the Equation 6.32. The relation 6.40 is already presented in this form. The Equation 6.34 can be regrouped and written down as

$$\dot{\phi} + M \frac{\delta \psi}{\delta \phi} = 0 \quad (6.42)$$

One difference between the two models is the lack of a “rate”-term in the microdamage model. The variational model treats the evolution of the cracked phase as an additional DOF of the system, thereby allowing a physical control over the evolution of the cracked/damaged zone. While this is practical from a numerical perspective, it is rather improbable in a real material, that one is able to physically control the evolution of damage. In the microdamage model however, the dependency on the rate of damage is included in an implicit manner. With the inclusion of the internal variable  $\phi^{loc}$ , one implies that there are no physical control conditions that can be imposed on the crack growth rate itself. However, the presence of the microdamage variable  $\phi$ , does allow the explicit control of actual damage growth in desired places. For example, it is possible to impose a condition that no damaging is allowed at the points/surfaces of external load application. The penalty term  $H_\mu$  ensures that the effect of such a condition is intrinsically accounted for in the evolution of the internal damage variable  $\phi^{loc}$ .

Following such observation, it is possible to combine the different aspects of the two models to obtain a more complete generalised balance relation for the evolution of damage in a material. Such a generalised relation is given by

$$C_0 \ddot{\phi} + C_1 \dot{\phi} + C_2 \phi + C_3 \Delta \phi = C_4 \phi^{loc} \quad (6.43)$$

The constants  $C_0$ ,  $C_1$ ,  $C_2$ ,  $C_3$  and  $C_4$  are suitable parameters. It is noted that the  $\ddot{\phi}$  term is included for the consideration of problems in dynamics. The particular form of the complete generalised regularisation equation allows for a reduction to simple quasi-static cases by simply setting the constants  $C_0$  and  $C_1$  to 0. It is also observed that the source term in Equation 6.32 is replaced by a functional dependent on the evolution of the internal variable. Thus, the presented generalised relation in Equation 6.43 can be considered as a baseline for multi-scale models, wherein the evolution of a global fracture phase can be driven by a micromechanically based evolution law treating material damage as an internal variable.

## 6.4 Conclusion

Following the description of the microdamage model, a comparison was drawn between the PFM approach and the micromorphic approach to modelling fracture. Based on this comparison a generalised balance relation for fracture/damage in a material was proposed. In what follows, dynamic fracture is not considered. Consequently, the coefficients  $C_0$ ,  $C_1$  are set to zero. It is noted that the reduced equation is then equivalent to the second balance relation of the microdamage model. Thus, the microdamage model is used as a basis for further development of a plasticity-damage coupled numerical model for fracture.

## Chapter 7

# Coupled crystal plasticity and microdamage model

### Résumé

Ce chapitre présente le modèle XMD, qui est basé sur le modèle «microdamage». Ce modèle contient la même régularisation de l'endommagement que son prédécesseur, pour éviter la dépendance des résultats par rapport au maillage. L'amélioration principale apportée par le modèle XMD est le couplage entre la plasticité et l'endommagement, qui est introduit en couplant les seuils de plasticité et d'endommagement.

Ce chapitre présente également le développement du modèle du point de vue de la mécanique des milieux continus. Ensuite quelques essais académiques sont présentés pour mieux exposer des contributions différents de paramètres matériaux. Les essais montrent également que le modèle est capable de simuler les phénomènes d'initiation, de propagation, de bifurcation et de branchement des fissures.

The previous chapter introduced the microdamage model without any links to plasticity and compared the microdamage approach to other similar gradient-based approaches for simulating softening phenomena. The following chapter presents a coupled *Crystal Plasticity and Micro-Damage* (XMD) model in order to address certain aspects that were dealt with inadequately by the previously discussed models. Numerical tests exploring the different features and capabilities of the XMD model are also presented.

In the review of experimental studies related to the micromechanics of crystalline material presented in Chapter 1, four requirements for an efficient material model were identified. These are recalled as

1. Anisotropic elasticity
2. Anisotropic plasticity
3. Anisotropic damage
4. Two-way coupling between the inelastic processes of plasticity and damage evolution.

The first two requirements were shown to be possible by the inclusion of *Cubic Elasticity* and *Crystal Plasticity* (see Part II). In Chapter 2, the concepts of Opening and Accommodation were introduced as an efficient way of modelling anisotropic damage.

The applicability of these concepts was also discussed in depth by [Aslan \[2010\]](#). Finally, following the discussion in Chapter 6, the necessity for *regularisation* of damage was identified.

At this point an observation regarding the identification of damage planes must be made. Although it is theoretically possible to model complex crack paths using a combination of Opening and Accommodation systems only, a choice is made to use multiple damage planes. Experimental observations on the microscopic level indicate that the evolution of damage occurs very often along the  $\{111\}$  family of planes. Hence, the four planes belonging to this family are used as the damage planes. This implies that the damage predicted at a material point, and the macroscopic crack paths predicted in the simulation of realistic specimens are a combination of incremental damage on each damage-plane.

Returning to the microdamage model developed by [Aslan \[2010\]](#), it is acknowledged that a limited coupling between plasticity and damage was introduced. It was limited in the sense that the coupling was chosen such that plasticity evolution affected the damage threshold, but there was no effect of damage on the threshold of plasticity. This coupling was extended in [Aslan et al. \[2011b\]](#) to include a two way coupling of plasticity and damage. In both versions of the microdamage model, the damage variables for opening and accommodation on a given plane were included as a separate system. This implied that each increment in the number of damage planes considered in the simulation required two additional variables that had to be integrated. When combined with the mesh sizes used in realistic specimens, this resulted in a significant increase in the required computational power. In order to address this increase in the required computational power, a slight modification is proposed in the XMD model. Under consideration that the damage often occurs along the crystallographic octahedral planes, it is proposed that the mechanism of Accommodation, introduced in Chapter 2, be included in the manner of plastic slip. This is achieved by reducing the plastic threshold down to a value of zero at those material points which are considered to be completely broken. The incremental values at these points are accounted for by the damage strain  $\tilde{\boldsymbol{\varepsilon}}^d$  and the plastic strain  $\tilde{\boldsymbol{\varepsilon}}^p$ . Thus, in the case of the XMD model, any predicted crack path is obtained by a combination of damage on the damage-planes and shear on the plasticity planes.

Another note concerning the use of multiple damage planes is also justified. Theoretically, it is possible to take into consideration, interaction between the different damage planes. This is analogous to the concept of latent-hardening discussed briefly in Chapter 2. For the simulations presented in this thesis however, no such interaction between damage planes is considered.

## 7.1 Coupled crystal plasticity and microdamage model

The main aim in the development of the model presented in the following section was the practical coupling of the plasticity and damage evolution mechanisms, while retaining the regularisation of damage introduced in the *microdamage* model discussed in chapter 6. To achieve this objective, the additional strain-like DOF representing microdamage  $-d_\mu$  is retained along with the standard displacement vector,  $\underline{\mathbf{u}}$ . Thus, the set of element DOFs and the extended gradient space are retained as

$$\text{DOF} = \{\underline{\mathbf{u}}, d_\mu\} \quad (7.1)$$

$$\text{Grad} = \{\underline{\boldsymbol{\varepsilon}}, \nabla d_\mu\} \quad (7.2)$$

It must be pointed out that the microdamage damage model presented in Chapter 6 was

presented in the context of a purely elastic-damage model. In contrast, the XMD model presented in this chapter is based on a three-way additive split of the strain-rate tensor. The plastic part of the inelastic strains is necessary since it is assumed that damaging of the material occurs in a sequence following plastic slip in the material. As such, the additive split is then given by,

$$\dot{\underline{\underline{\varepsilon}}} = \dot{\underline{\underline{\varepsilon}}}^e + \dot{\underline{\underline{\varepsilon}}}^p + \dot{\underline{\underline{\varepsilon}}}^d \quad (7.3)$$

where  $\dot{\underline{\underline{\varepsilon}}}^e$ ,  $\dot{\underline{\underline{\varepsilon}}}^p$ ,  $\dot{\underline{\underline{\varepsilon}}}^d$  represent the elastic, plastic and damage contributions of the strain-rate tensor respectively.

Using the extended gradient set in the virtual power relation (Equation 6.5), one obtains the set of balance relations for the XMD model. It is seen that the balance laws are also retained from the microdamage model. For reasons of completeness, the balance relations are recalled as

$$\operatorname{div} \underline{\underline{\boldsymbol{\sigma}}} = 0 \quad \forall \underline{\mathbf{x}} \in \Omega \quad (7.4)$$

$$\operatorname{div} \underline{\mathbf{b}} = \underline{\mathbf{a}} \quad \forall \underline{\mathbf{x}} \in \Omega \quad (7.5)$$

$$\underline{\underline{\boldsymbol{\sigma}}} \cdot \underline{\mathbf{n}} = \underline{\mathbf{t}} \quad \forall \underline{\mathbf{x}} \in \partial\Omega \quad (7.6)$$

$$\underline{\mathbf{b}} \cdot \underline{\mathbf{n}} = \underline{\mathbf{a}}_c \quad \forall \underline{\mathbf{x}} \in \Omega \quad (7.7)$$

For a thermodynamically consistent derivation of the constitutive equations, the FEF in Equation 6.10 is modified to include contributions from coupled plasticity/damage mechanisms. The modified FEF is given in the form as

$$\rho\Psi := \rho\Psi^{el} + \rho\Psi^{pl} + r_0\gamma + \frac{h}{2}\gamma^2 + Y_0d + \frac{H}{2}(d + \beta\gamma)^2 + \frac{H_\mu}{2}(d - d_\mu)^2 + \frac{A}{2}\nabla d_\mu \cdot \nabla d_\mu \quad (7.8)$$

The term  $\rho\Psi^{el}$  represents the elastic contribution of the FEF. In the case considered here, a classical form of this elastic contribution is considered and is given as

$$\rho\Psi^{el} = \frac{1}{2}\underline{\underline{\boldsymbol{\varepsilon}}} : \underline{\underline{\boldsymbol{\mathcal{C}}}} : \underline{\underline{\boldsymbol{\varepsilon}}}^e \quad (7.9)$$

$\rho\Psi^{pl}$  represents the classical plasticity contributions such as non-linear isotropic hardening (see [Méric et al. \[1991\]](#)) and kinematic hardening (see [Besson et al. \[2010\]](#)). The advantage of assuming this form for the FEF is that it allows one to easily include plasticity formulations and models that have been developed and validated. The modified form of the FEF presented above also contains additional plasticity contributions in the form of a standard linear isotropic hardening— $\frac{h}{2}\gamma^2$ —and a threshold related contribution  $-r_0\gamma$ . It is pointed out that these terms are added to facilitate the formulation of a simple analytical solution for the model, which will be presented in a later section (see Section 7.2). Also, in the equation (7.8),  $\gamma$  represents the accumulated plastic strain, which in the case of crystal plasticity is given by

$$\dot{\gamma} = \sum_{s=1}^{N_{slip}} |\dot{\gamma}_s| \quad (7.10)$$

From the assumed FEF, the constitutive relations for the generalised stresses  $\underline{\underline{\boldsymbol{\sigma}}}$ ,  $\underline{\mathbf{b}}$  and  $\underline{\mathbf{a}}$

are retained as

$$\underline{\boldsymbol{\sigma}} := \rho \frac{\partial \Psi}{\partial \underline{\boldsymbol{\varepsilon}}^e} = \underline{\boldsymbol{c}} : \underline{\boldsymbol{\varepsilon}}^e \quad (7.11)$$

$$\underline{\boldsymbol{b}} := \rho \frac{\partial \Psi}{\partial \nabla d_\mu} = A \nabla d_\mu \quad (7.12)$$

$$a := \rho \frac{\partial \Psi}{\partial d_\mu} = -H_\mu (d - d_\mu) \quad (7.13)$$

It is pointed out that an isotropic form of the  $\nabla d_\mu$  contribution is adopted for the sake of simplicity. To obtain the equations for the evolution of the internal variables related to plasticity and damage, the following potentials were considered

$$\Omega_p(\underline{\boldsymbol{\sigma}}, R^s) := \sum_s \left( \frac{K_p}{n_p + 1} \left\langle \frac{f_p^s}{K_p} \right\rangle^{n_p + 1} \right) \quad (7.14)$$

$$\Omega_d(\underline{\boldsymbol{\sigma}}, Y^r) := \sum_r \left( \frac{K_d}{n_d + 1} \left\langle \frac{f_d^r}{K_d} \right\rangle^{n_d + 1} \right) \quad (7.15)$$

where,  $f_p^s$  and  $f_d^r$  denote the plastic yield and damage initiation criteria respectively. The plastic yield criterion considered in the XMD model presented here corresponds to the classical *Schmid* criterion for plasticity. For the simulation of the damage evolution, the criterion introduced in the *microdamage* model (Equation 6.18) is retained. The equations for the criteria are recalled as

$$f_p^s = |\underline{\boldsymbol{m}}^s \cdot \underline{\boldsymbol{\sigma}} \cdot \underline{\boldsymbol{l}}_i^s| - R^s, \quad i = 1, 2, 3 \quad (7.16)$$

$$f_d^r = |\underline{\boldsymbol{n}}_d^r \cdot \underline{\boldsymbol{\sigma}} \cdot \underline{\boldsymbol{n}}_d^r| - Y^r \quad (7.17)$$

where  $\underline{\boldsymbol{m}}^s$  is the normal to the  $s^{\text{th}}$  slip plane and  $\underline{\boldsymbol{l}}_i^s$  is the  $i^{\text{th}}$  slip direction on slip plane  $s$ . The unit vector  $\underline{\boldsymbol{n}}_d^r$  is the normal to the damage plane  $r$ .

The differentiation of the considered ‘Dissipation’ potentials for plasticity and damage (equations 7.14 and 7.15) w.r.t the Cauchy stress  $\underline{\boldsymbol{\sigma}}$  yields the constitutive equations for the inelastic strains as of slip and damage on each plane as

$$\underline{\boldsymbol{\varepsilon}}^p := \frac{\partial \Omega_p}{\partial \underline{\boldsymbol{\sigma}}} = \sum_s \dot{\gamma}_s \underline{\boldsymbol{M}}_s \text{sign}(\underline{\boldsymbol{m}}^s \cdot \underline{\boldsymbol{\sigma}} \cdot \underline{\boldsymbol{l}}_i^s) \quad (7.18)$$

$$\underline{\boldsymbol{\varepsilon}}^d := \frac{\partial \Omega_d}{\partial \underline{\boldsymbol{\sigma}}} = \sum_r \dot{d}_{open}^r \underline{\boldsymbol{N}}_r \text{sign}(\underline{\boldsymbol{n}}_d^r \cdot \underline{\boldsymbol{\sigma}} \cdot \underline{\boldsymbol{n}}_d^r) \quad (7.19)$$

and the evolution relations for the plastic slip and the damage on the plastic and damage planes are given as

$$\dot{\gamma}^s = \left\langle \frac{f_p^s}{K_p} \right\rangle^{n_p} \quad (7.20)$$

$$\dot{d}_{open}^r = \left\langle \frac{f_d^r}{K_d} \right\rangle^{n_d} \quad (7.21)$$

with the tensors  $\underline{\boldsymbol{M}}$  and  $\underline{\boldsymbol{N}}$  being given by

$$\underline{\boldsymbol{M}}_s = \underline{\boldsymbol{m}}^s \overset{sym}{\otimes} \underline{\boldsymbol{l}}_i^s \quad (7.22)$$

$$\underline{\boldsymbol{N}}_r = \underline{\boldsymbol{n}}_d^r \otimes \underline{\boldsymbol{n}}_d^r \quad (7.23)$$

Lastly, the constitutive relations for the thermodynamic conjugates of plastic slip  $\gamma_s$  and the total damage  $d$  are needed. Ideally, every  $\gamma_s$  has a corresponding conjugate  $R_s$ . Thus, for the FEF considered for the XMD model, we have the relation for  $R^s$  as

$$R^s = R_{pl}^s + R \quad (7.24)$$

where  $R_{pl}^s$  is the contribution from the conventional crystal plasticity part of the FEF  $\rho\Psi^{pl}$  (see Equation 7.8) and  $R$  is the contribution of the XMD part of the FEF. In what follows, we assume that this contribution  $R$  emerging from the XMD model contribution is the same for all the slip systems, and is given by

$$R := \rho \frac{\partial \Psi}{\partial \gamma} = r_0 + h\gamma + H\beta^2\gamma + H\beta d \quad (7.25)$$

$$Y := \rho \frac{\partial \Psi}{\partial d} = Y_0 + Hd + H\beta\gamma + H_\mu(d - d_\mu) \quad (7.26)$$

It is also pointed out that the construction of the XMD model is such that the crack driving force  $Y$  is a thermodynamic conjugate of the total damage  $d$  at the material point under consideration. Thus, the relation for  $Y$  is given by the Equation 7.26. The total damage is given in the rate form as the summation of all the opening rates. This relation is shown in Equation 7.27.

$$\dot{d} = \sum_r \dot{d}_{open}^r \quad (7.27)$$

The total damage is chosen in the rate form to facilitate the extension of XMD model to cases of cyclic loading. It is also noted that typically, the values for the introduced material parameters are chosen such that  $h > 0$ ,  $H < 0$ ,  $H_\mu > 0$  and  $A > 0$ .

### Implementation of accommodation systems

It has been indicated before that the system of accommodation (discussed in Chapter 2) is needed in the cracked zone, to include the effects of shear loads on the damage plane. This is accounted for in the XMD model by the slip systems in the cracked zone. To implement this system of accommodation of Mode II and Mode III damaging in the plastic-slip systems, particular attention had to be paid to the numerical implementation. Firstly, it is necessary to determine, whether or not the material is completely broken at a given material point. The confirmation that a material point is entirely broken is obtained by ensuring that the value of the crack driving force  $Y$  is less than a chosen ultimate stress  $\sigma_{ult}$ . Once this is ensured, the plasticity threshold  $R$  is artificially dropped to zero. This ensures that there is no resistance to shear deformation on any of the slip systems at that material point. This allows for a free shearing motion on the planes, which in turn represents Mode II and Mode III crack growth.

## 7.2 Analytical Solution for a simple case

As stated earlier, the XMD model aims at an efficient coupling between plasticity and damage mechanisms, while retaining the regularisation provided by the *microdamage* model. It is observed that setting the material parameter  $\beta = 0$  decouples the plasticity and damage processes completely, and setting  $\beta = 1$  indicates that the thresholds of plasticity and damage are reduced identically with the evolution of damage and plasticity respectively. For practical cases, the values of  $\beta$  are expected to be typically between 0

and 1 as the damage-driven reduction of plastic threshold is expected to be significantly stronger than the plasticity-driven lowering of damage threshold. The following section presents an analytical solution for the XMD model in the simple case of a strip with a defect. For the purpose of this analysis, it is assumed that the contribution  $\rho\Psi^{pl} = 0$ .

To present a theoretical analysis of the model, the example of a strip representing a 1D bar in tension is considered (see Figure 7.1). It is assumed that there exists a zone of fixed width where inelastic loading is active. For a rate-independent case, this imposes the conditions  $f_p = 0$  and  $f_d = 0$  in this zone. Due to these imposed conditions, the spatial derivatives of the yield functions in this zone should also be zero. I.e. requiring

$$f_{p,x} = 0 \quad (7.28)$$

$$f_{d,x} = 0 \quad (7.29)$$

Introducing Relations 7.16 and 7.17 in 7.28 and 7.29, we obtain a relation between the gradients of plastic slip and damage. This relation is given as

$$\gamma_{,x} = \frac{-H\beta}{H\beta^2 + h} d_{,x} \quad (7.30)$$

Inserting this relation into 7.29, a relation between the DOF  $d_\mu$  and the internal variable  $d$  is obtained as

$$d_{,x} = \frac{H_\mu H\beta^2 + H_\mu h}{Hh + H_\mu h + H_\mu H\beta^2} d_{\mu,x} \quad (7.31)$$

The local form of the balance relation 7.5 can be rewritten as

$$Ad_{\mu,xx} = -H_\mu(d - d_\mu) \quad (7.32)$$

Considering the derivative of 7.32 w.r.t.  $x$ , and inserting Equation 7.31 into the resultant equation, one obtains

$$d_{\mu,xxx} = \frac{H_\mu Hh}{A(Hh + H_\mu h + H_\mu H\beta^2)} d_{\mu,x} = 0 \quad (7.33)$$

The Equation 7.33 is in the form of a classical second order homogeneous differential equation. Thus, the equation contains a characteristic length term which is given as

$$l_c = \sqrt{\left| \frac{A(H + H_\mu)}{HH_\mu} + \frac{A\beta^2}{h} \right|} \quad (7.34)$$

In Equation 7.34, two types of solutions are possible. In the first case, when

$$\frac{A(H + H_\mu)}{HH_\mu} + \frac{A\beta^2}{h} < 0$$

the solution is of the form

$$d_{\mu,x} = P \cos\left(\frac{x}{l_c}\right) + Q \sin\left(\frac{x}{l_c}\right) \quad (7.35)$$

In the second case, when

$$\frac{A(H + H_\mu)}{HH_\mu} + \frac{A\beta^2}{h} > 0$$

the solution is of the form

$$d_{\mu,x} = P \exp\left(\frac{x}{l_c}\right) + Q \exp\left(-\frac{x}{l_c}\right) \quad (7.36)$$

with the constants  $P$  and  $Q$  being settled for the boundary conditions. Since the material parameter  $A > 0$ , it follows that the choice of the parameters  $H$ ,  $H_\mu$  and  $\beta$  will decide which of the two solution forms are applicable.

### 7.3 Characteristic response of the XMD model

It has been indicated earlier that setting  $\beta = 0$  reduces the model to the microdamage model discussed in Chapter 6. To test this case, a sequence of tests were conducted with the setting of  $\beta = 0$  and with a plastic threshold much higher than the damage threshold. This ensured that the material response was purely elastic-damage.

#### Regularisation of damage

To test for regularisation, the strip test shown in Figure 7.1 was simulated using different mesh densities along the length of the strip. The values of  $A$ ,  $H$  and  $H_\mu$  remained unchanged for all the tests. Figure 7.2 shows three different mesh densities that were tested. It is seen clearly that the size of the regularisation zone remains unchanged, irrespective of the mesh size. Another key point to ensure, was that the regularisation actually matched the analytical solution, which is in the form of a sinusoidal function. To test this case, the damage along the strip was plotted. The plot is shown in Figure 7.3. The figure shows clearly that the regularised microdamage variable corresponds to the analytical solution. The values used for the simulation in Figure 7.3 were  $A = 33333.3 \text{ MPa.mm}^2$ ,  $H = -26000.0 \text{ MPa}$  and  $H_\mu = 100000.0 \text{ MPa}$ . Figure 7.4 shows the plot of the damage variable  $d$  and the microdamage variable  $d_\mu$  along the length of the bar at various stages of damage evolution.

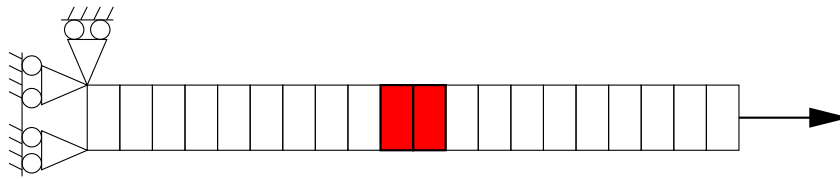


Figure 7.1: Strip test to simulate 1D case for analysis. The red elements represent elements that have been artificially weakened to prompt strain localisation

#### Effect of softening parameter $H$

The effect of varying the softening parameter  $H$ , while the values of  $A$  and  $H_\mu$  remain unchanged is shown clearly in Figure 7.5. As expected, the greater the value of  $|H|$ , the steeper is the softening curve.

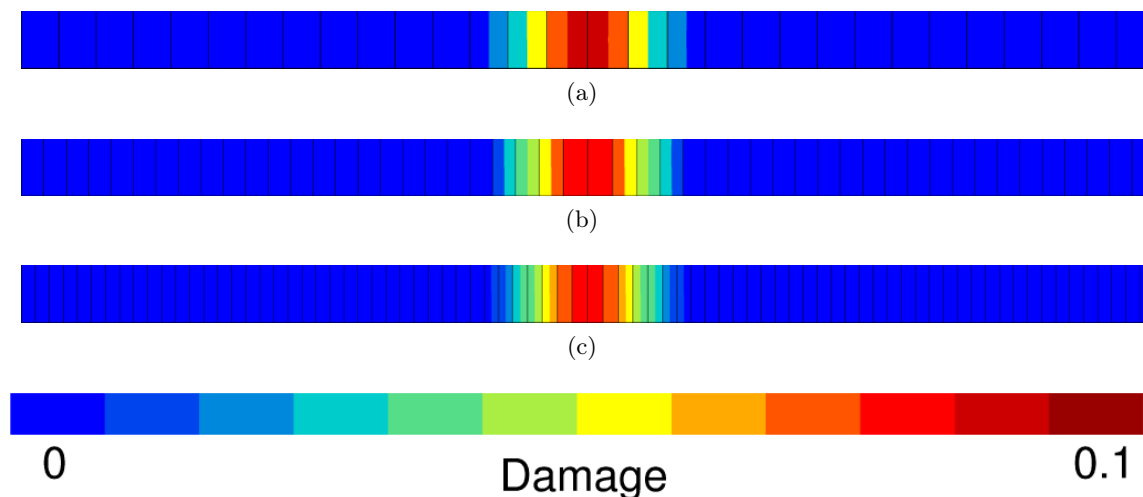


Figure 7.2: Regularised damage in a strip

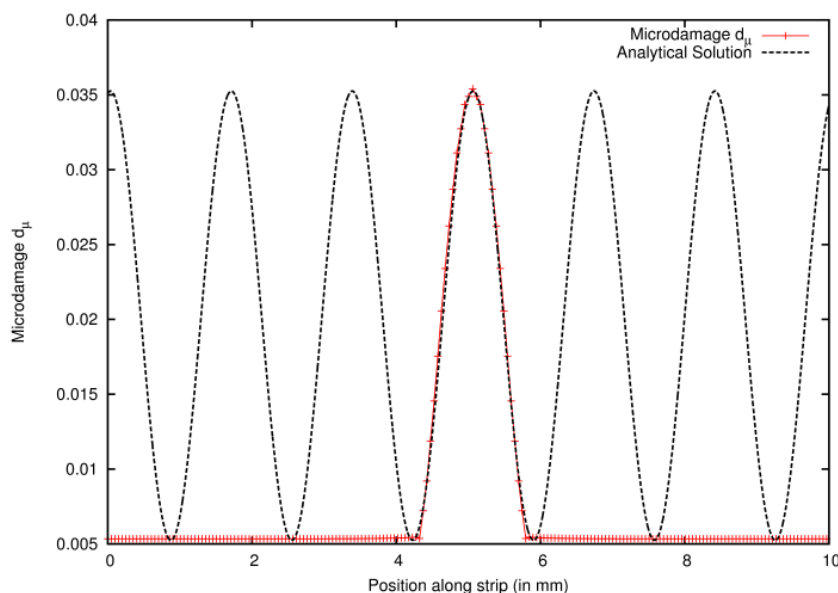


Figure 7.3: Comparison of the the regularised simulation and the analytical solution for a 1D strip with a 100 element discretisation

### Evolution of damage threshold $Y$

Figure 7.6 shows the stress-strain response for a material point subject to simple tensile loading conditions. The material mechanisms considered in the shown example are isotropic elasticity, non-linear isotropic hardening and damage. The plot shows the evolution of stress and damage threshold with respect to strain for two different values of the coupling parameter  $\beta$ . The evolution of  $Y$  is such that it remains constant during the elastic loading stage. Once plasticity is initiated, the reduction of the damage threshold commences (provided  $\beta \neq 0$ ) and continues until the damage threshold reaches the stress levels at the material point under consideration. This point is seen as the intersection of the damage threshold vs. strain and the stress-strain plots, and represents a change in the rate of change of damage threshold. In the event that  $\beta = 0$ , the damage threshold remains unchanged until the stress level crosses the threshold, beyond which it starts to diminish. Figure 7.7a shows clearly the evolution of stress, damage and plasticity thresholds w.r.t.

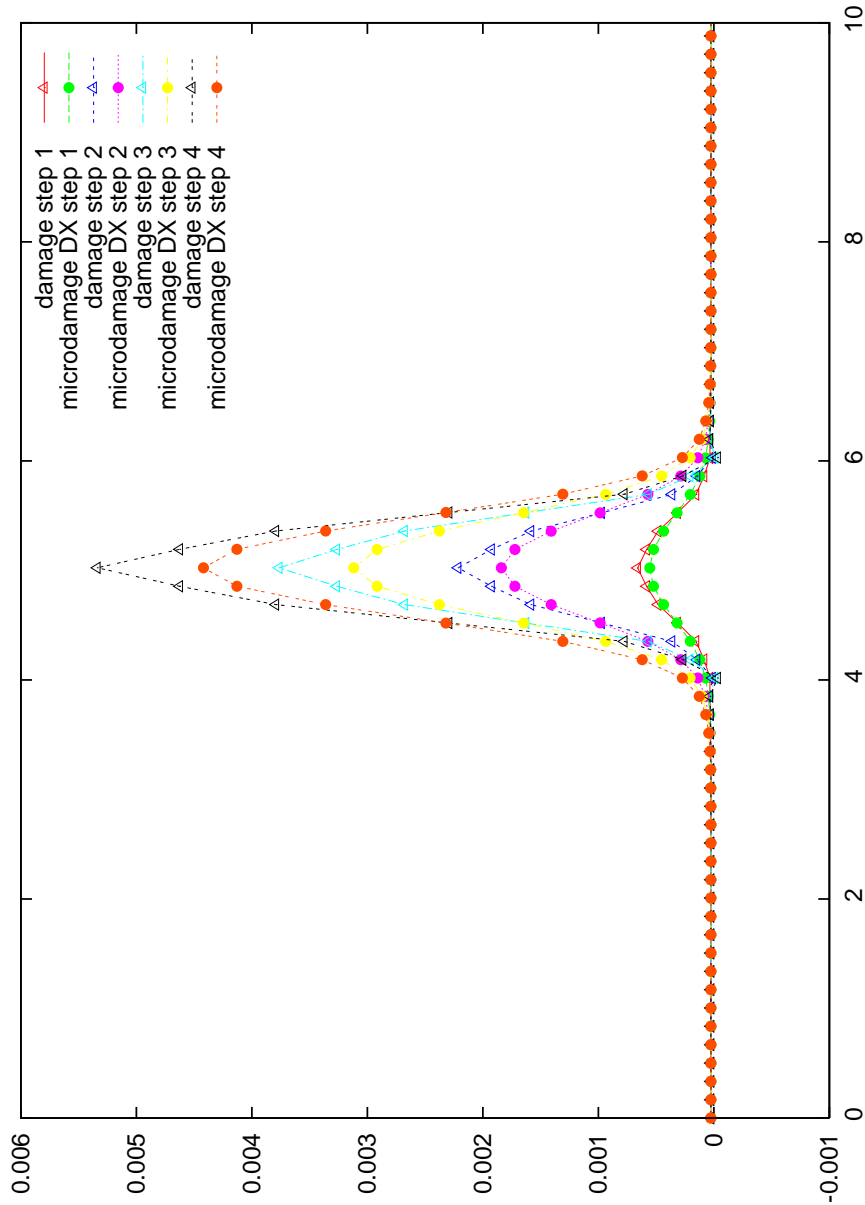


Figure 7.4: Plot showing the evolution of damage  $d$  and microdamage  $d_\mu$  along the length of the strip ( $x$ -axis).  $A = 33333.0 \text{ MPa.mm}^2$ ,  $H = -26000.0 \text{ MPa}$ ,  $H_\mu = 100000 \text{ MPa}$

displacement. It is seen that the damage commences when the curves for stress and damage threshold  $Y$  intersect. Due to the particular choice of  $H$  it is seen that the material softens extremely quickly. Also seen is the increase in plastic threshold  $R$  along with increasing strain. When the material begins to damage, the value of  $R$  also starts reducing. Figure 7.7b shows the evolution of  $Y$  w.r.t. plastic strain. It is observed that the rate at which  $Y$  evolves is initially dictated only by plasticity, but then changes due to the influence of evolving damage.

### 7.3. Characteristic response of the XMD model

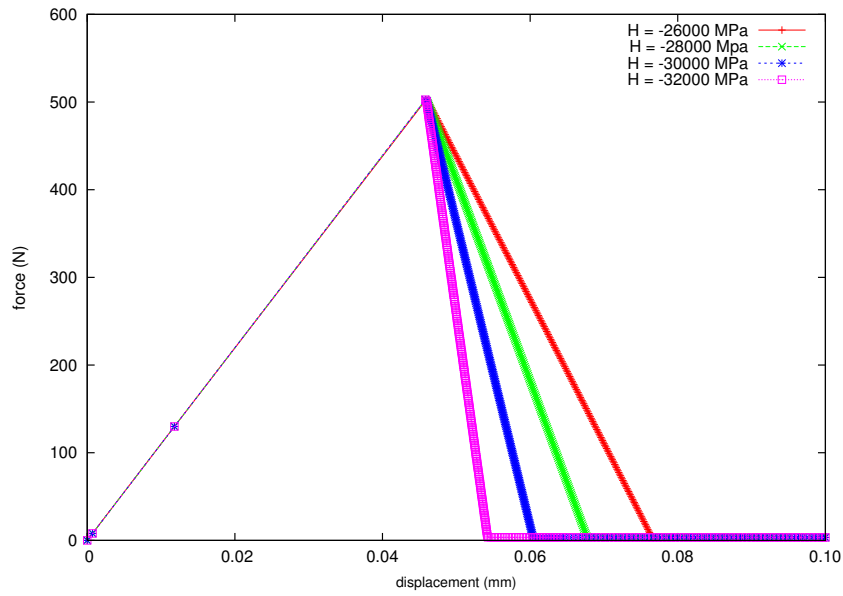


Figure 7.5: Effect of softening parameter  $H$  on the load displacement curve (Length of the bar is 10 mm).

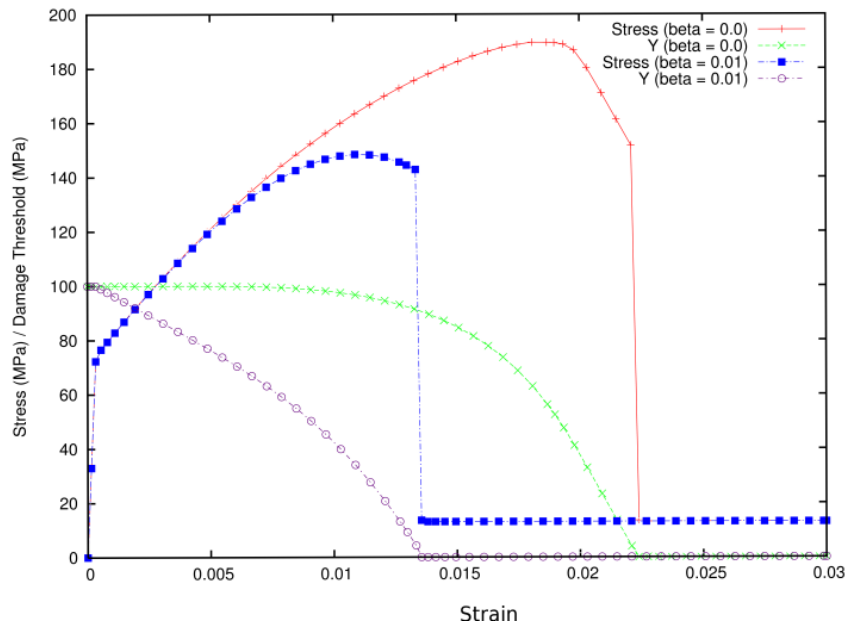
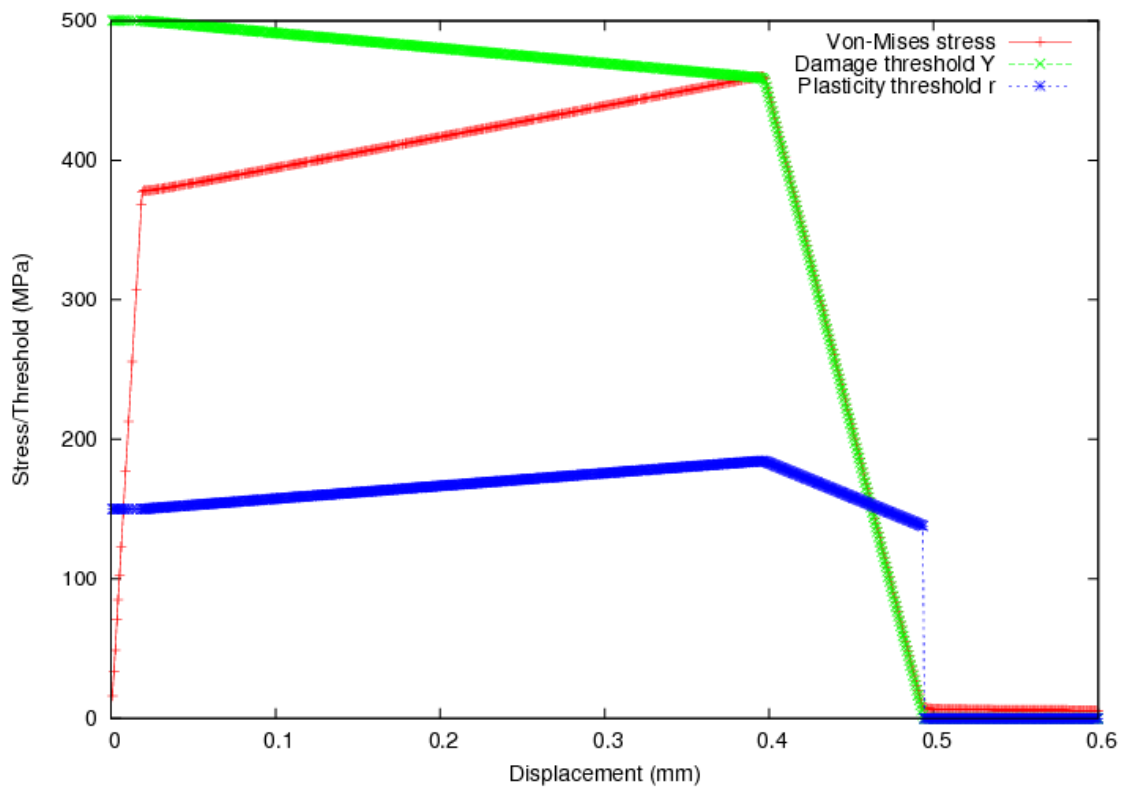
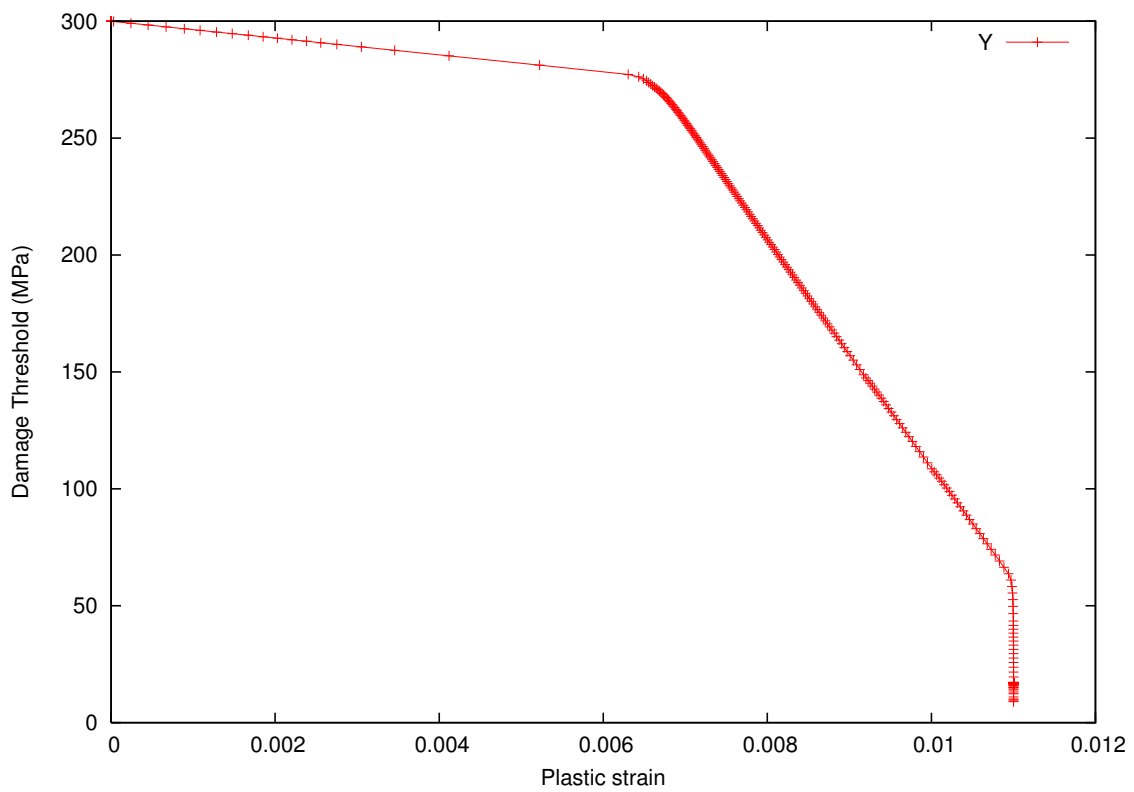


Figure 7.6: Plot showing the evolution of stress  $\tilde{\sigma}$  and  $Y$  w.r.t. total strain  $\varepsilon$



(a) Evolution of Stress  $\sigma$ , damage threshold  $Y$ , plastic threshold  $R$  w.r.t. displacement



(b) Evolution of damage threshold  $Y$  w.r.t. evolving plastic strain

Figure 7.7: Evolution of damage threshold  $Y$  w.r.t. other parameters

### Effect of coupling parameter $\beta$

A closer inspection of Equation 7.34 indicates a few noteworthy aspects regarding the use of the XMD model. It is observed that by setting  $\beta = 0$  one retrieves the analytical characteristic length relation obtained for the microdamage model, which is given by Aslan [2010] as

$$l_c = \sqrt{\left| \frac{H + H_\mu}{HH_\mu} \right|} \quad (7.37)$$

Thus, in the case of  $\beta = 0$ , the regularisation remains unchanged as compared to the regularisation obtained in the *microdamage* model (see Section 7.3). Secondly, the typical values of the parameters  $\beta$  ( $0 \leq \beta \leq 1$ ) and  $h$  (strain hardening coefficient) are such that the second term in Equation 7.34 ( $A\beta^2/h$ ) does not significantly change the size of the regularisation zone as compared to the regularisation obtained in the *microdamage* model.

Setting  $\beta = 0$  in the Equation 7.34, the values of  $H_\mu$ ,  $H$  and  $A$  can be regulated to obtain the desired regularisation length. For a finite-element implementation,  $l_c$  in Equation 7.34 is equal to the  $N\epsilon$ , where  $N$  represents the number of finite elements over which damage is regularised, and  $\epsilon$  represents the length of an individual element edge (in the direction along which regularisation occurs).

To better understand the effect of the parameter  $\beta$ , a series of numerical tests were conducted on a strip (see Figure 7.1 for a description of the strip test). The material parameters, given in table 7.1, were kept constant and only the value of the parameter  $\beta$  was varied between 0 & 1. The force displacement plot, shown in Figure 7.8, shows that the time of initiation of softening and the time to complete failure decrease along with the increase of the coupling strength between plasticity and damage, as expected theoretically. However, the trend does not continue for all values of  $\beta$ . It is observed from Figure 7.9 that the strain hardening in the material decreases as the strength of the coupling parameter is increased. Then, between the values of  $\beta = 0.6$  and  $\beta = 0.7$ , there is a sharp transition in the material behaviour. The material response changes from the expected response of strain-hardening plasticity followed by damage induced softening, to a response that represents pure softening. This change in material behaviour indicates that the choice of the material parameter  $\beta$  is crucial in depicting the appropriate material response.

For the simple case considered, there exists a critical value  $\beta_c$  for the coupling parameter  $\beta$ , corresponding to a change in the type of solution to the PDE (see Equations 7.35 and 7.36). This relation is given as

$$\beta_c^2 = -\frac{h(H + H_\mu)}{HH_\mu} \quad (7.38)$$

A value of  $\beta^2 > \beta_c^2$  leads to a hyperbolic solution, and a value of  $\beta^2 < \beta_c^2$  leads to a harmonic (sinusoidal) solution. The effects of this transition from a harmonic to a hyperbolic solution on the predicted crack paths are yet to be investigated.

### Response under cyclic loading

NBSX components are used in applications that are subject to continued cyclic loading. This leads to fatigue damage in the material. Simulation of cyclic loading needs particular attention to the crack closure aspects. The model incorporates a condition to handle unilateral damage and contact. To ensure this, the value of the opening  $d^r$  on each damage plane  $r$  is checked at the beginning of each iteration. The case of  $d^r < 0$  indicates closure

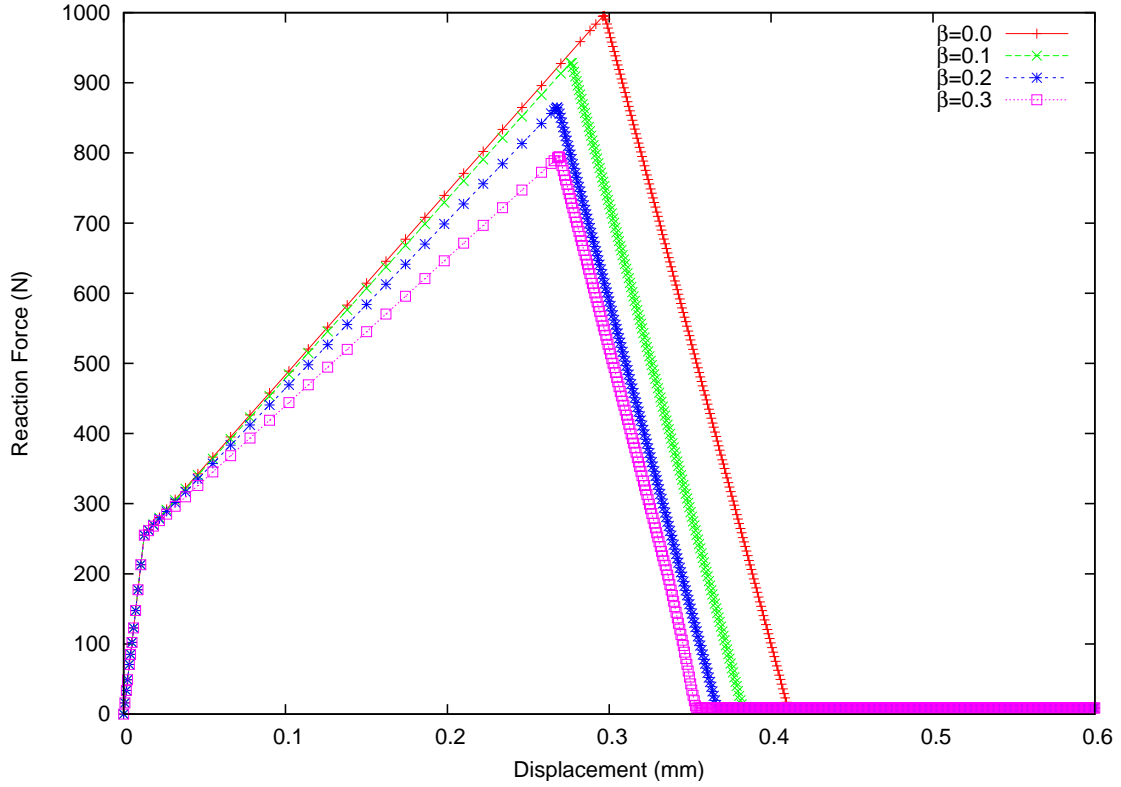


Figure 7.8: Load-displacement diagram showing the effect of the coupling parameter for values,  $0 < \beta \leq 0.3$

Material Parameter	Value
Young's modulus $E$	200000.0 MPa
Poisson's ratio $\nu$	0.3
Regularisation parameter $A$	1500.0 MPa.mm <sup>2</sup>
Plasticity threshold $R_0$	100.0 MPa
Linear isotropic hardening coefficient $h$	5000.0 MPa
Viscoplasticity coefficient $n_{plast}$	10.0
Viscoplasticity coefficient $K_{plast}$	10.0 MPa.s <sup>1/<math>n_{plast}</math></sup>
Damage threshold $Y_0$	1000.0 MPa
Damage coefficient $n_{dam}$	10.0
Damage coefficient $K_{dam}$	4.0 MPa.s <sup>1/<math>n_{dam}</math></sup>
Softening coefficient $H$	-12000.0 MPa
Penalty parameter $H_\mu$	50000.0 MPa

Table 7.1: Material parameters used in the strip test exploring effects of  $\beta$

of the crack. In the case of  $d^r \leq 0$  and  $\text{sign}(\sigma_n) < 0$ , the condition  $d^r$  is enforced. In other cases, evolution of damage is possible, provided that the yield condition  $f_d^r > 0$ .

To exhibit this implementation, cyclic loading was imposed on the strip example considered earlier. The results of these tests are shown in Figures 7.10 and 7.11. The material parameters are chosen such that the plastic threshold is sufficiently above the damage threshold, so that an elastic-damage response is achieved in tension. The application of shear loading after the central elements are completely cracked shows that

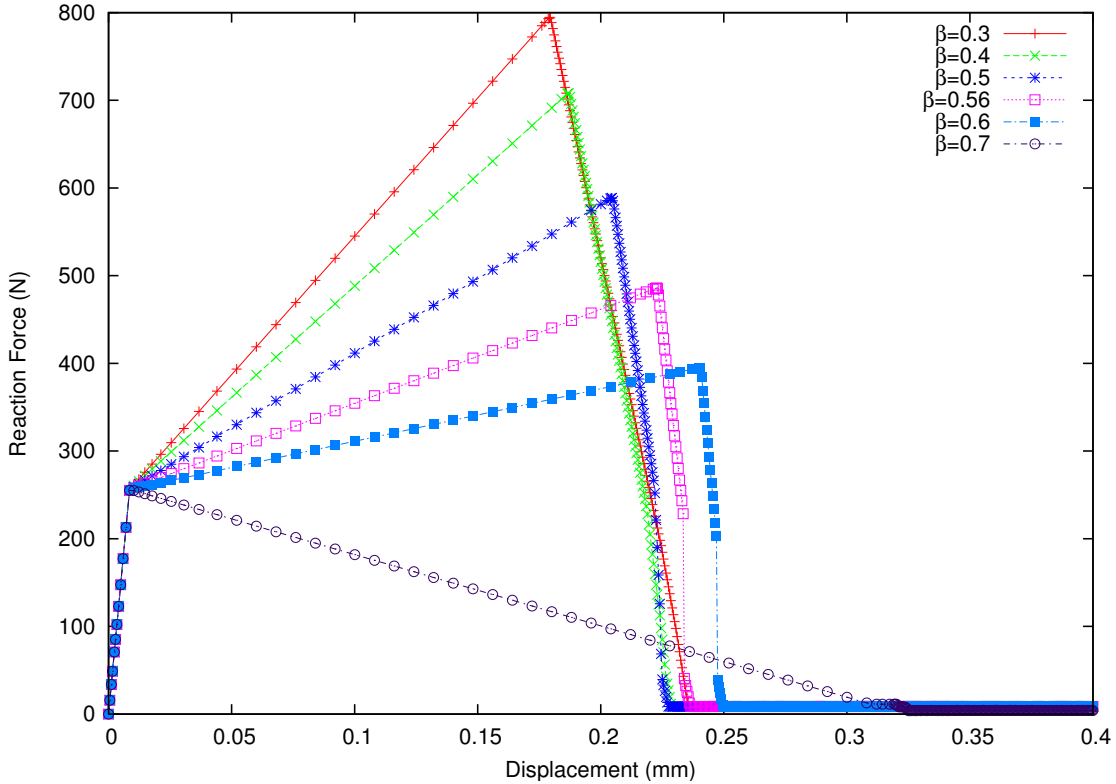


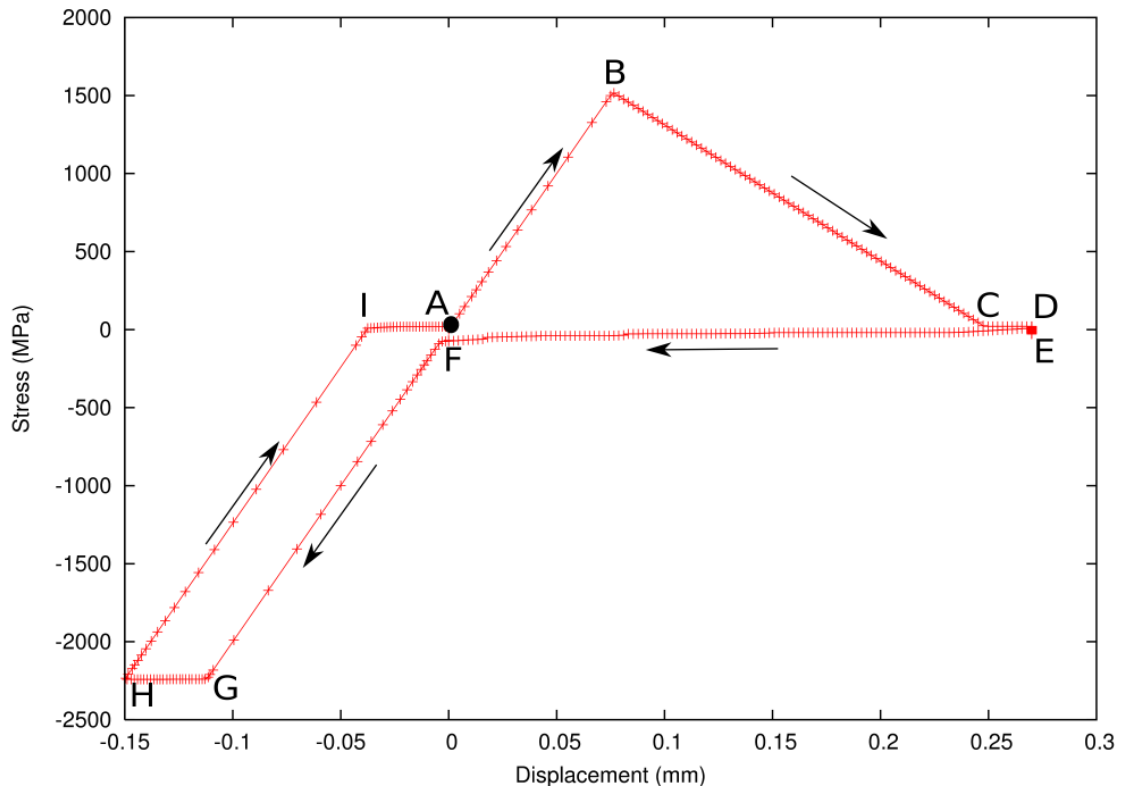
Figure 7.9: Load-displacement diagram showing the effect of the coupling parameter for values  $0.3 \leq \beta \leq 0.7$ ; Note the transition in material response between  $\beta = 0.6$  and  $\beta = 0.7$

there is effectively no resistance to shear deformation after the specimen is cracked. It is also noted that the little amount of residual stress in the damaged zone arises from the use of a viscous type power law for evolution of damage/plasticity. When the loading is reversed, there is again no stress until the opening is completely closed. Once, the “opening” is closed, we retrieve the elastic response in compression, which continues until the plastic yield limit. Once the compressive stresses exceed the plastic yield limit in compression, plastic deformation is observed in the strip. Thus, it is seen that the XMD model is capable of simulating fracture under cyclic loading conditions.

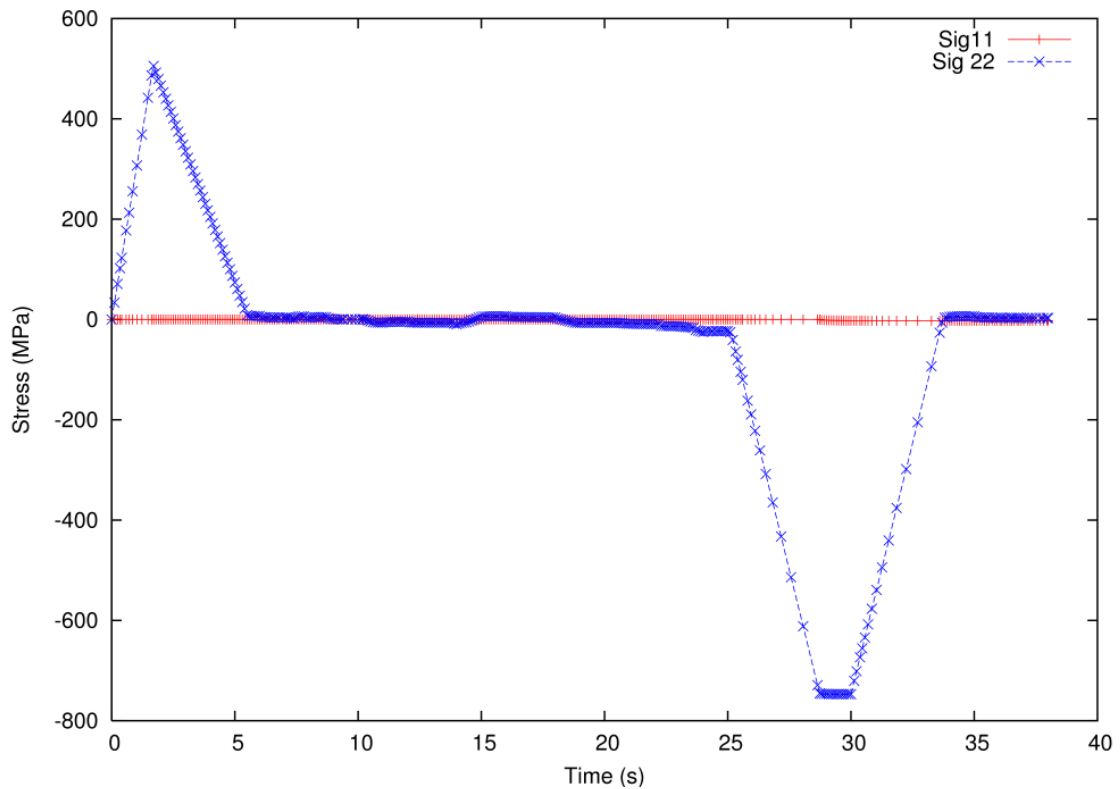
Figure 7.11 shows the strip at various points of the loading cycle. Starting from point A on the curve (Figure 7.10), the strip is loaded under monotonic tension until damage induced softening begins at Point B. The softening continues until failure at point C. At this point shear loading is introduced, the response corresponds to the images (c)-(g) in the Figure 7.11. It has been checked that these lateral displacements are possible with negligible shear load. Figure h corresponds to the compression imposed on the broken strip, which in turn corresponds to the regime FG on the plot. The last figure corresponds to the plastic evolution in the reverse direction, thereby leading to a final strip which is still completely broken. This shows that the XMD model can also be used under instances of complex cyclic loading.

### Damage planes and branching

The XMD model uses an anisotropic damage formulation, which allows the simulation of varying crack paths via the combination of damage planes and slip planes. It also allows the description of multiple damage planes, thereby allowing the simulation of crystallographic



(a) Stress evolution in the damaged elements w.r.t. vertical loading



(b) Reaction loads measured along the top edge of the strip

Figure 7.10: Response of strip test under cyclic loading

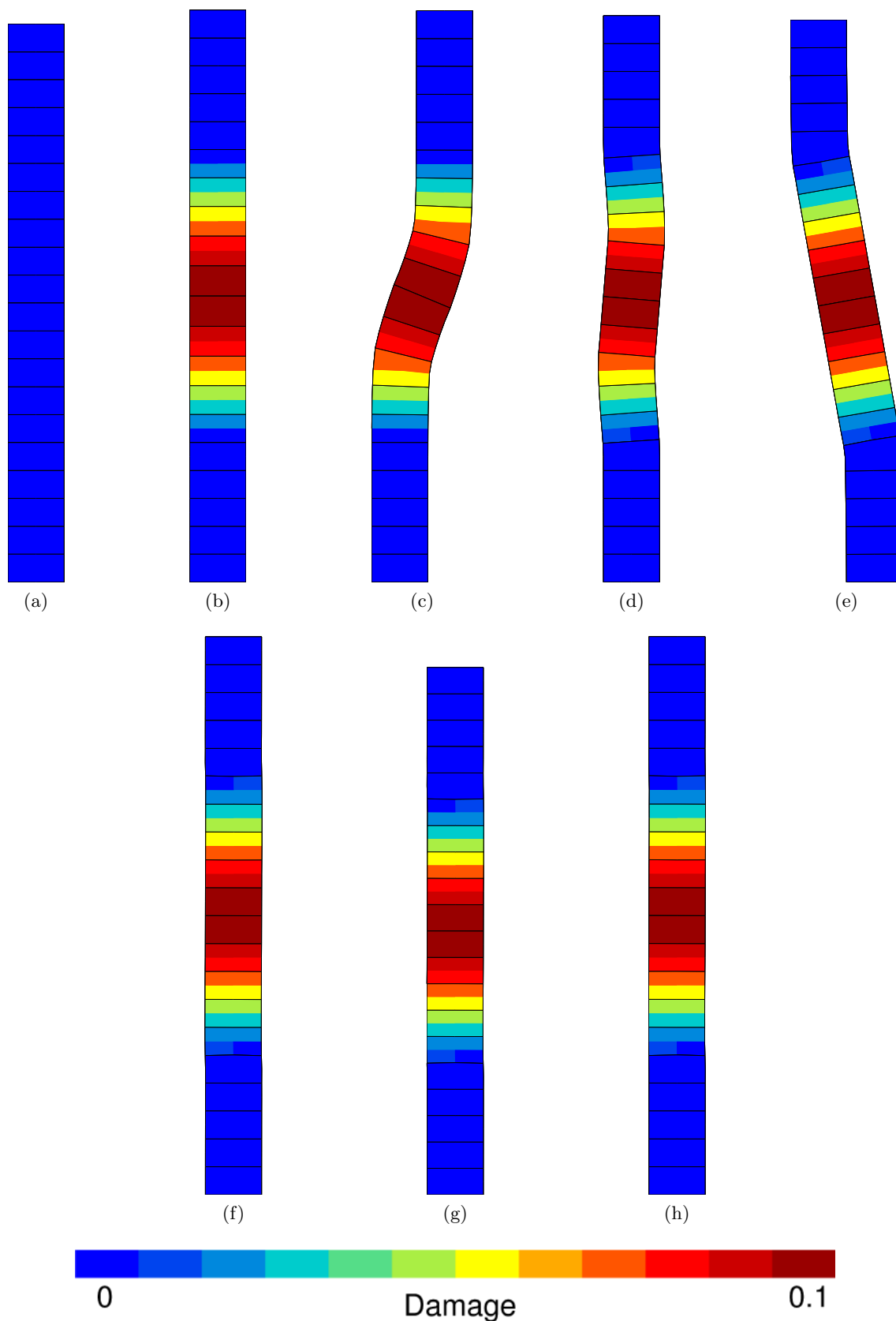


Figure 7.11: Results of strip test for the cyclic load shown in Figure 7.10. Figure (d) shows residual deformation despite shear load being reduced to zero; this is due to accommodation on plasticity planes. Figure (f) shows that plastic slip in the reverse direction cancels out most of the residual slip from Figure (d). Figures (g) and (h) shows that even in compression, the broken elements remain broken.

damage as a result of combined damage and slip processes on multiple planes. To test the influence of the choice of damage planes on the propagation of the crack, several tests were conducted on a block specimen with a wedge-shaped notch. Tensile loading was applied as shown in Figure 7.12. As seen in Figures 7.13a and 7.13b, the evolution of the crack depends on the defined crystallographic damage planes. For Figure 7.13a, where the normal to the damage plane lies along the direction of loading, the crack develops perpendicular to the direction of the loading as expected. In the latter case (Figure 7.13b), the choice of a damage plane with the normal at an angle of  $18^\circ$  to the loading direction leads to crack along the chosen damage plane.

In order to test whether the model is capable of handling phenomena such as branching, the block test was repeated with multiple damage planes. The material was considered to exhibit isotropic elasticity, thereby ensuring that there was no biased evolution of stresses at the beginning of the calculation. The plasticity planes were once again chosen to be the octahedral slip systems. Three damage planes were chosen such that the normals to these damage planes lay at angles of  $45^\circ$ ,  $90^\circ$ ,  $135^\circ$  w.r.t. to the loading  $[010]$  axis. Figure 7.14 shows one example of crack branching achieved by the use of 3 damage planes under monotonic loading. From the crack branches predicted it is seen that the combination of multiple damage mechanisms can be used to predict complex crystallographic/non-crystallographic crack paths.

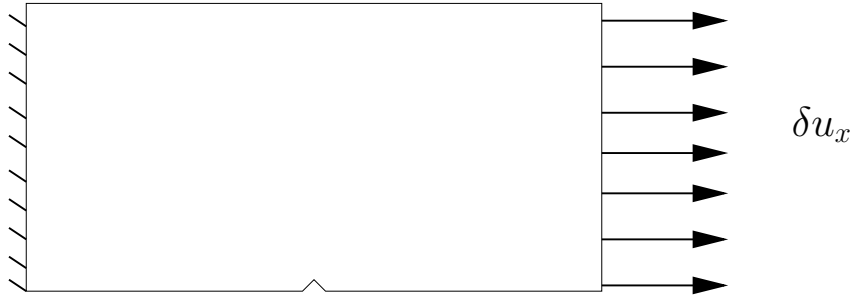


Figure 7.12: The block test used to test damage anisotropy in the XMD model

## 7.4 Conclusion

The chapter presented a fully coupled XMD model as an improvement over the original microdamage model. A number of tests were conducted to study the characteristic responses of the model. The test cases show that the model can capture the basic mechanisms of damage required for a realistic simulation of cracking processes. The presented XMD model was also used to simulate a few experimental observations, in order to test the relevance of the results predicted by the model to the actual experimental observations. The details of the numerical implementation and the results of the simulated experiments are discussed in the following chapter.

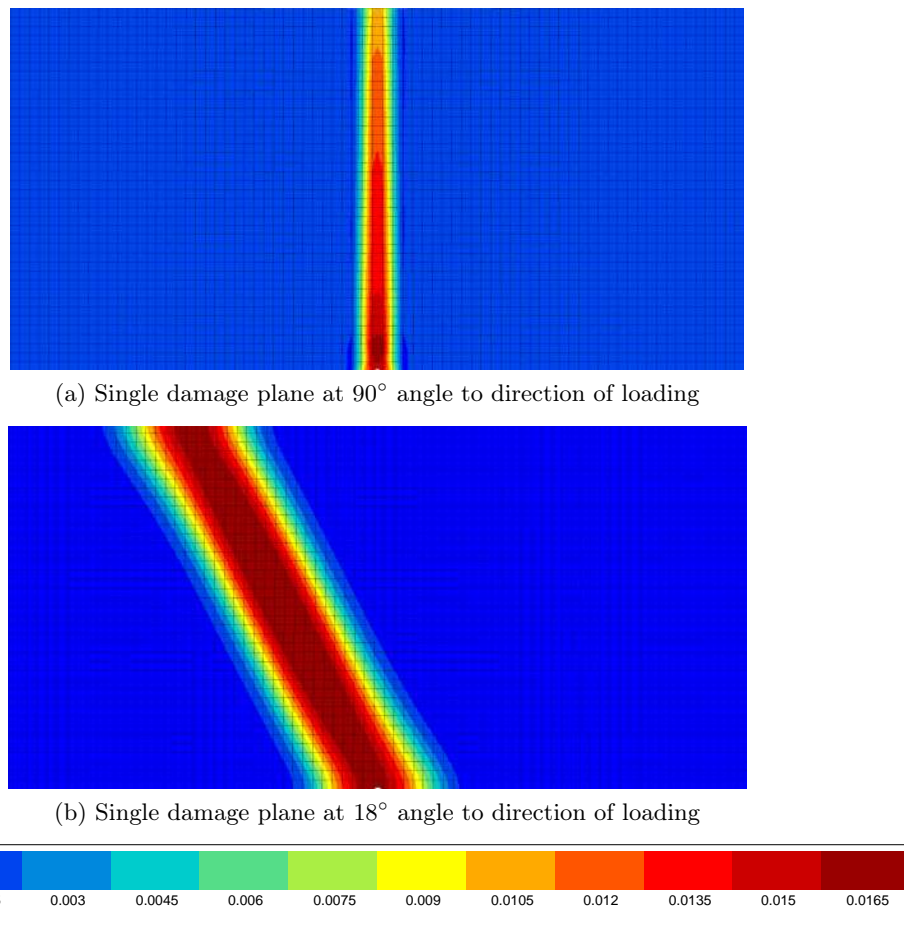


Figure 7.13: Examples showing the dependency of the crack direction on the damage plane chosen. Total damage  $d$  is shown.

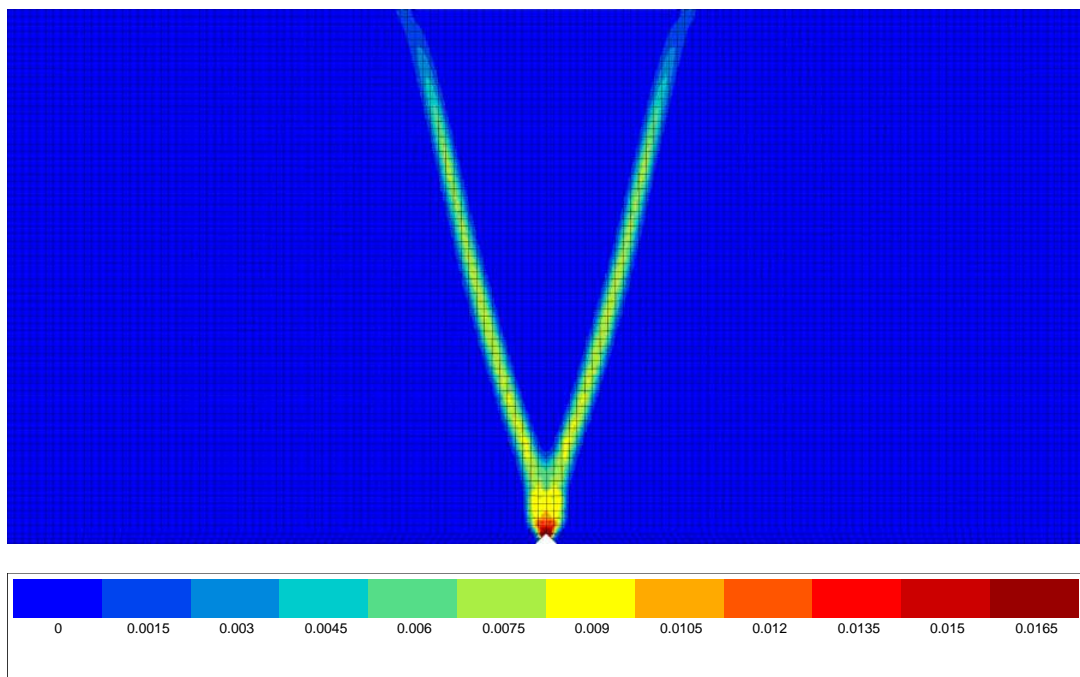


Figure 7.14: Example of branching in quasi-static fracture simulated by XMD model. 3 planes needed to be defined with plane normals at  $45^\circ$ ,  $90^\circ$  and  $135^\circ$  to the direction of loading. Total damage  $d$  is shown.



## Chapter 8

# Numerical Experiments

### Résumé

Avec la formulation en petite déformations, présentées dans le dernier chapitre, les questions concernant les chemins de fissuration prévus par le modèle doivent être testés et validés. Afin de pouvoir permettre une étude qualitative de la fissuration, plusieurs simulations numériques ont été lancées. Les résultats des trois types d'essais (CT, cisaillement et fluage) sont présentés dans ce chapitre. Pour rester plus proche que possible des essais expérimentaux, les éprouvettes réelles ont été maillées avec des éléments finis.

Les essais de CT permettent la comparaison des chemins des fissurations qui dépendent de l'orientation de la fissure dans le monocristal. Les essais de cisaillement pur permettent d'analyser le comportement du modèle XMD sous chargement en mode II. Finalement, les essais du fluage permettent d'analyser une éprouvette simple et de la comparer avec une éprouvette expérimentale. En considérant les types d'essais différents, une identification des paramètres matériaux est aussi proposée.

It has already been pointed out that the use of a standard damage model, like the model proposed in [Marchal \[2006\]](#) leads to a localisation of the numerical damage-zone such that, the zone stays confined to the width of a single finite element. This in turn results in the mesh dependency of the predicted crack paths. In other words, the crack paths vary as a function of not only the finite element size, but also the patterns observed in finite element meshes such as those generated by free-meshing algorithms. While this problem can be addressed to a certain extent by using a very high-density mesh, such a solution is not practical as far as real components with complex geometries are concerned.

A second solution to this problem is to use some form of numerical regularisation, where the key field variable which leads to an ill-conditioned problem set is “regularised”. In a most common form this is achieved by a smearing of this sharp discontinuity over a finite distance. Many types of regularised models have been proposed in literature, some of which have been discussed and/or referred to in the previous chapter. Some models (see for example [Lorentz and Godard \[2011\]](#)), propose a regularised damage model, which is derived in a systematic manner, similar to the methods discussed in Chapters 2 and 6. However, few models (e.g. [Abdul-Latif and Saanouni \[1996\]](#), [Saanouni and Abdul-Latif \[1996\]](#)) available in literature present a thorough coupling between the essential phenomena of crystallographic plasticity and crystallographic damage. It is in order to address this need that the XMD model was introduced and described in Chapter 7.

While the observation that non-regularised models yield damage predictions that remain confined to the size of a single element is an important one, this is but one of the difficulties observed in the numerical simulation of damage/fracture. The problems of convergence that arise in numerical simulations of fracture are also well known. Another problem that has been identified and addressed in literature is the presence of spurious hydrostatic stresses in the finite elements (see [Bargellini et al. \[2009\]](#)). According to [Bargellini et al. \[2009\]](#), there are two typical solutions to this problem; (i) the use of enhanced finite elements, which entails the use of additional DOFs at the elemental nodes, (ii) the use of reduced order integration in the elements. Following these suggestions, the simulations presented in this dissertation are carried out using an enhanced finite element with either quadratic or linear interpolation of all fields at the element nodes. The element is considered an *enhanced element* due to the introduction of the microdamage variable as an additional DOF. Furthermore, reduced order integration is used to avoid locking effects. It is acknowledged that the use of such an element typically leads to the fluctuation of hydrostatic stresses in the damaged zone, as pointed out in [Bargellini et al. \[2009\]](#). A solution was proposed in the form of a mixed element, which introduces an additional pressure variable. The development and implementation of a mixed-formulation element for the XMD model is reserved as future work. The effects of these stress fluctuations on the crack paths have not yet been investigated.

## 8.1 Element formulation and integration schemes

The variational formulation of the element is presented in the following section. The principle of virtual power is recalled from Equation 6.5 as

$$\int_{\Omega} \left( \underline{\boldsymbol{\sigma}} : \underline{\dot{\boldsymbol{\varepsilon}}} + \underline{\mathbf{b}} \cdot \nabla \dot{d}_{\mu} + a \dot{d}_{\mu} \right) dV = \int_{\partial\Omega} \left( \underline{\mathbf{t}} \cdot \underline{\dot{\mathbf{u}}} + a_c \dot{d}_{\mu} \right) dS \quad (8.1)$$

The spatial discretisation of the displacement and microdamage fields can then be written in terms of shape functions  $N_u$  and  $N_{d_{\mu}}$  as,

$$\underline{\mathbf{u}} = N_u D_u \quad ; \quad d_{\mu} = N_{d_{\mu}} D_{d_{\mu}} \quad (8.2)$$

thereby allowing for the derivatives of the fields as,

$$\nabla \underline{\mathbf{u}} = B_u D_u \quad ; \quad \nabla d_{\mu} = B_{d_{\mu}} D_{d_{\mu}} \quad (8.3)$$

where  $D_u$  and  $D_{d_{\mu}}$  represent the nodal DOFs and correspond to the fields  $\underline{\mathbf{u}}$  and  $d_{\mu}$ .  $B_u$  and  $B_{d_{\mu}}$  denote the partial derivatives of the shape functions w.r.t. the spatial coordinates and are used to obtain the gradient fields  $\underline{\boldsymbol{\varepsilon}}$  (total strain) and  $\nabla d_{\mu}$  (microdamage gradient). The shape functions  $N_u$  and  $N_{d_{\mu}}$  are chosen to be either linear or quadratic functions in the simulations presented in this thesis. However, in some cases, a mixed choice of shape functions is possible. [Aslan \[2010\]](#) for example uses quadratic interpolation for the displacement and a linear interpolation function for the microdamage. The introduction of Equations 8.2 and 8.3 into Equation 8.1 leads to the discretised balance relations, given as

$$\int_{\Omega} B_u^T \underline{\boldsymbol{\sigma}} dV = \int_{\partial\Omega} N_u^T \underline{\mathbf{t}} dS \quad (8.4)$$

$$\int_{\Omega} \left( B_{d_{\mu}}^T \underline{\mathbf{b}} + N_{d_{\mu}}^T a \right) dV = \int_{\partial\Omega} N_{d_{\mu}}^T a_c dS \quad (8.5)$$

The integration of the internal variables at the Gauss points is carried out, for the simulations presented in this thesis, using the second order explicit Runge-Kutta integration coupled with adaptive time-stepping scheme. A generalised description of the integration scheme implemented in the software suite *Z-set* can be found in [Besson et al. \[2010\]](#). The linearised numerical forms of the evolution relations used in the integration are given as,

$$\gamma(t + \Delta t) = \gamma(t) + \Delta t \dot{\gamma}(t + \Delta t) \quad (8.6)$$

$$d_{open}^s(t + \Delta t) = d_{open}^s(t) + \Delta t \dot{d}_{open}^s(t + \Delta t) \quad (8.7)$$

$$\underline{\varepsilon}^e(t + \Delta t) = \underline{\varepsilon}^e(t) + \Delta t \left( \underline{\dot{\varepsilon}}(t + \Delta t) - \underline{\dot{\varepsilon}}^p(t + \Delta t) - \underline{\dot{\varepsilon}}^d(t + \Delta t) \right) \quad (8.8)$$

$$d(t + \Delta t) = d(t) + \Delta t \sum_r \left| \dot{d}_{open}^s(t + \Delta t) \right| \quad (8.9)$$

Again, it is pointed out that the relations above hold for a case of the XMD model with linear isotropic hardening plasticity. For a case of non-linear isotropic hardening, the evolution relation for  $v$  (see Equation 3.30) is integrated in place of  $\gamma$  (Equation 8.6). The terms for the inclusion of kinematic hardening can be found in [Chaboche and Cailletaud \[1996\]](#).

The global system of equations is solved using a Newton-Raphson solver, with the convergence criterion being defined as below

$$res \leq tol$$

with  $res$  being the residual of the global set of equations and  $tol$  being a user-defined maximum acceptable global residual. The residual  $res$  can be computed using either of the two following relations:

$$res = \frac{|R^{ext} - R^{int}|}{|R^{ext}|} \quad (8.10)$$

$$res = |R^{ext} - R^{int}| \quad (8.11)$$

In the above relations  $R^{ext}$  and  $R^{int}$  are the external and internal reactions computed from the global equation system. Equation 8.10 represents a normalised convergence condition, where the equation 8.11 represents a non-normalised convergence condition. In the simulations presented in this thesis, the latter criterion has been used because the external loads go to zero at fracture. Further comments on the choice of the convergence criterion are provided in the following section.

## 8.2 Compact tension specimens

The simulation of mode I crack growth is theoretically rather simple, in the sense that a monotonically increasing load applied to a specimen leads to a crack propagation that is similar to the opening of the specimen. As far as the experimental testing of mode I fracture is concerned, the use of Compact Tension (CT) specimens has pervaded practice. Many experimental studies can be found in literature, that explore the propagation of a crack along a straight line perpendicular to the direction of loading. In many cases, these studies are restricted to isotropic brittle damage and are used as validation experiments for fracture/damage models. However, in the particular case of NBSX specimens, [Wen and Yue \[2007\]](#) have presented experimental observations that indicate that the crack propagation

Dimension	Value (in $mm$ )
Width 'w'	25.0
Height 'h'	24.0
Notch height 'b'	1.0
Pre-crack length 'a'	0.8
Diameter 'D'	5.0

Table 8.1: Dimensions of the CT specimen used in the simulations

path is not determined by the loading direction alone. Some of their observations indicate rather clearly that, despite the imposition of Mode I tensile loading on the specimen, crack paths could well occur along the loading direction and not necessarily perpendicular to the direction of loading. Furthermore, such observations hint at a very complex stress state at the tips of cracks, notches and other stress concentration features. This implies that the traditional classification of different modes of fracture may not apply if one were to consider the combined effects of plasticity and damage.

To study the above mentioned observations numerically, the complete CT specimen was modelled in 2D. The geometry of the CT specimen is shown in Figure 8.1. The red part in the figure shows the NBSX specimen and the grey part shows the rigid holders used to introduce displacement controlled loading,  $u$ , on the specimen. The geometric dimensions of the specimen are indicated in Table 8.1. Two different meshes were generated to test the mesh-independence of the model. The first mesh contained a regular distribution of elements in the region of interest (near the crack tip). This mesh is shown in Figures 8.3a and 8.3b. The element size near the crack tip is  $30\ \mu m \times 55\ \mu m$ . A second irregular mesh was generated using the mesh generator in ABAQUS. The mesh was imported in to Z-set for simulations. The average element size ahead of the pre-crack tip in this mesh was  $100\ \mu m \times 100\ \mu m$ . This second mesh is shown in Figures 8.4a and 8.4b. Henceforth, these meshes are referred to as *Mesh A* and *Mesh B* respectively.

*Note: The pair of regular and irregular meshes were considered for the tests as they allow the verification of the dependency of results on the element size, and on the element arrangement patterns.*

Numerical simulations were conducted using both, the standard CP model from Chapter 3 and the XMD model from Chapter 7. Furthermore, the three different orientations considered in Wen and Yue [2007] were simulated. The orientations simulated are shown in Figures 8.2a, 8.2b and 8.2c. These orientations will henceforth be referred to as *Orientation 1*, *Orientation 2* and *Orientation 3* respectively. The orientations are chosen to explore the crack growth conditions under different primary loading directions. The property of NBSX materials to retain room-temperature-like behaviour up to about  $700^\circ C$  has been mentioned earlier. Consequently material parameters obtained at room temperatures were used in the simulations.

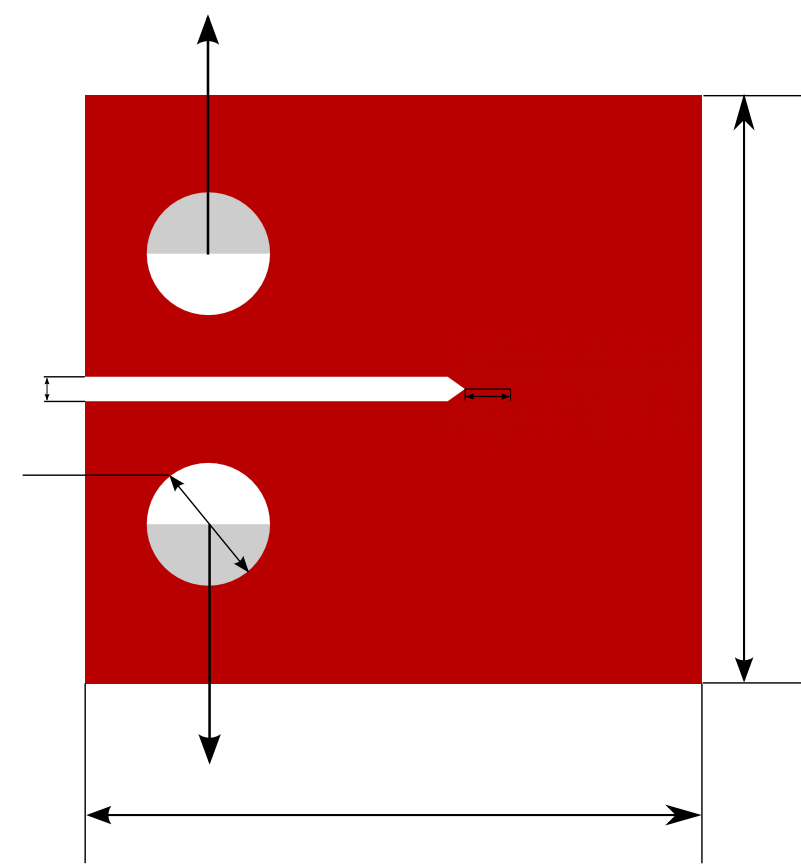


Figure 8.1: Geometry used in CT study

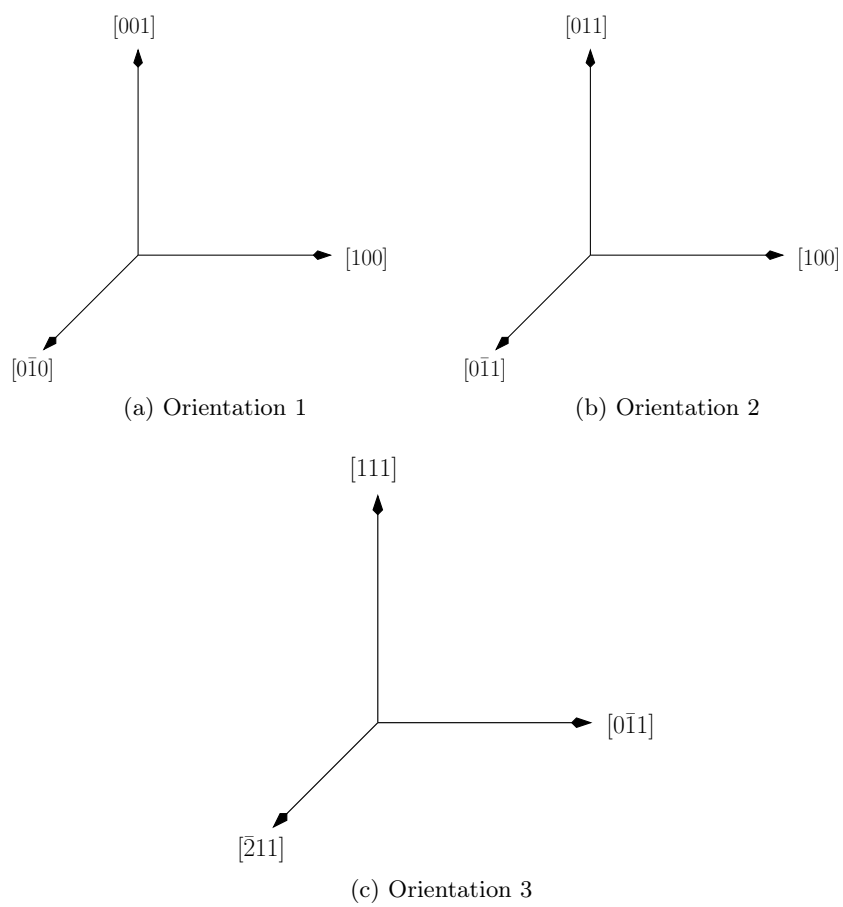
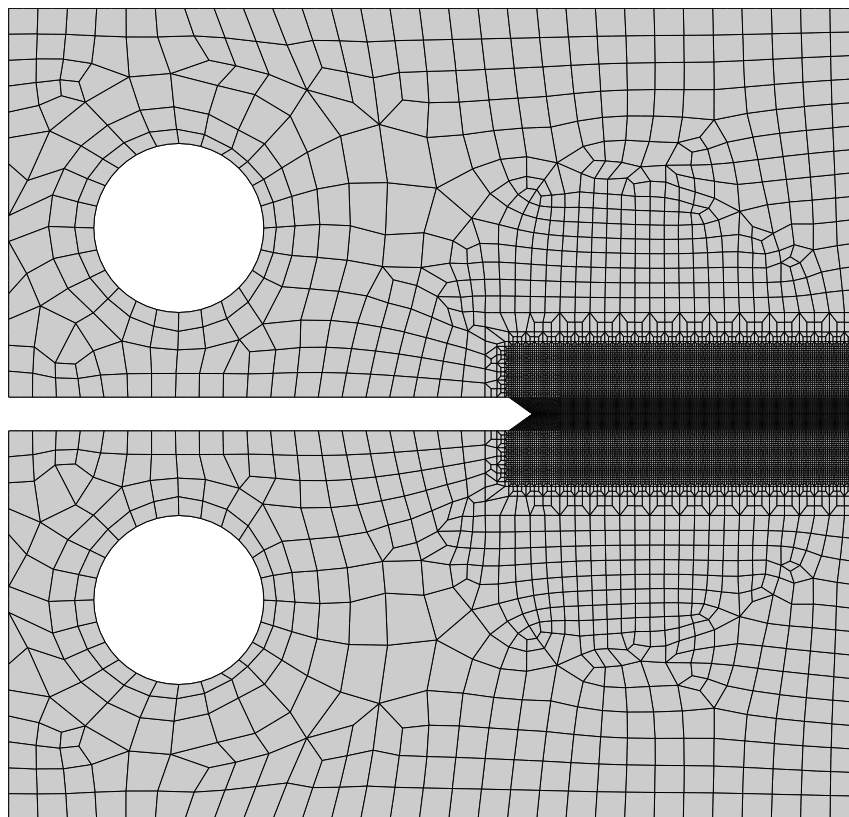
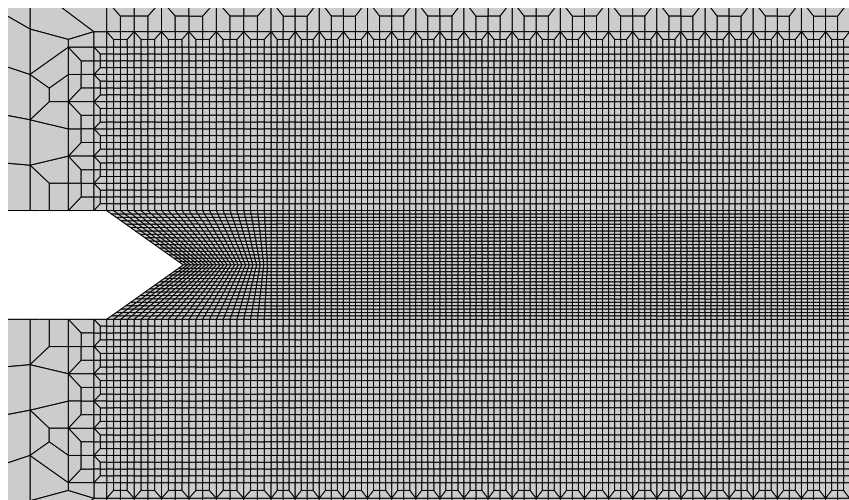


Figure 8.2: Orientations used in the Compact Tension study

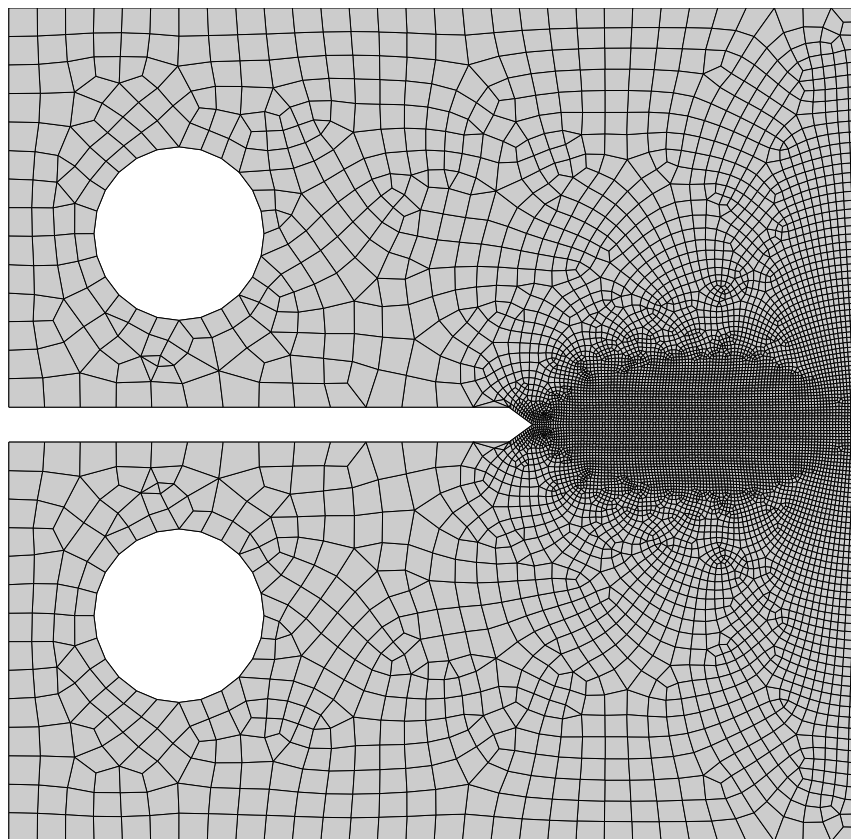


(a) Mesh with regular meshing ahead of pre-crack (Holders used to apply load are not shown)

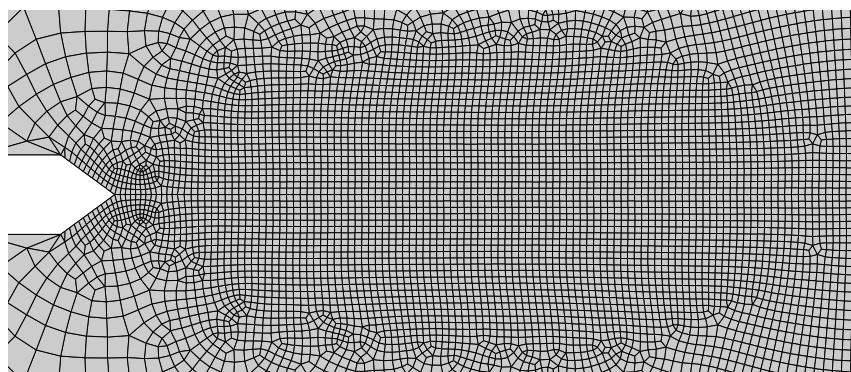


(b) Close-up view of mesh near crack tip. Element size in the vicinity of the crack tip is  $30\mu\text{m} \times 50\mu\text{m}$  (*width x height*)

Figure 8.3: *Mesh A* used in the simulation of Compact tension experiments



(a) Mesh with free meshing for the complete specimen (Holders used to apply load are not shown)



(b) Close-up view of the mesh near the crack tip. Element size in the vicinity of the crack tip is about  $100\mu\text{m} \times 100\mu\text{m}$  (*width x height*)

Figure 8.4: *Mesh B* used in the simulation of Compact tension experiments

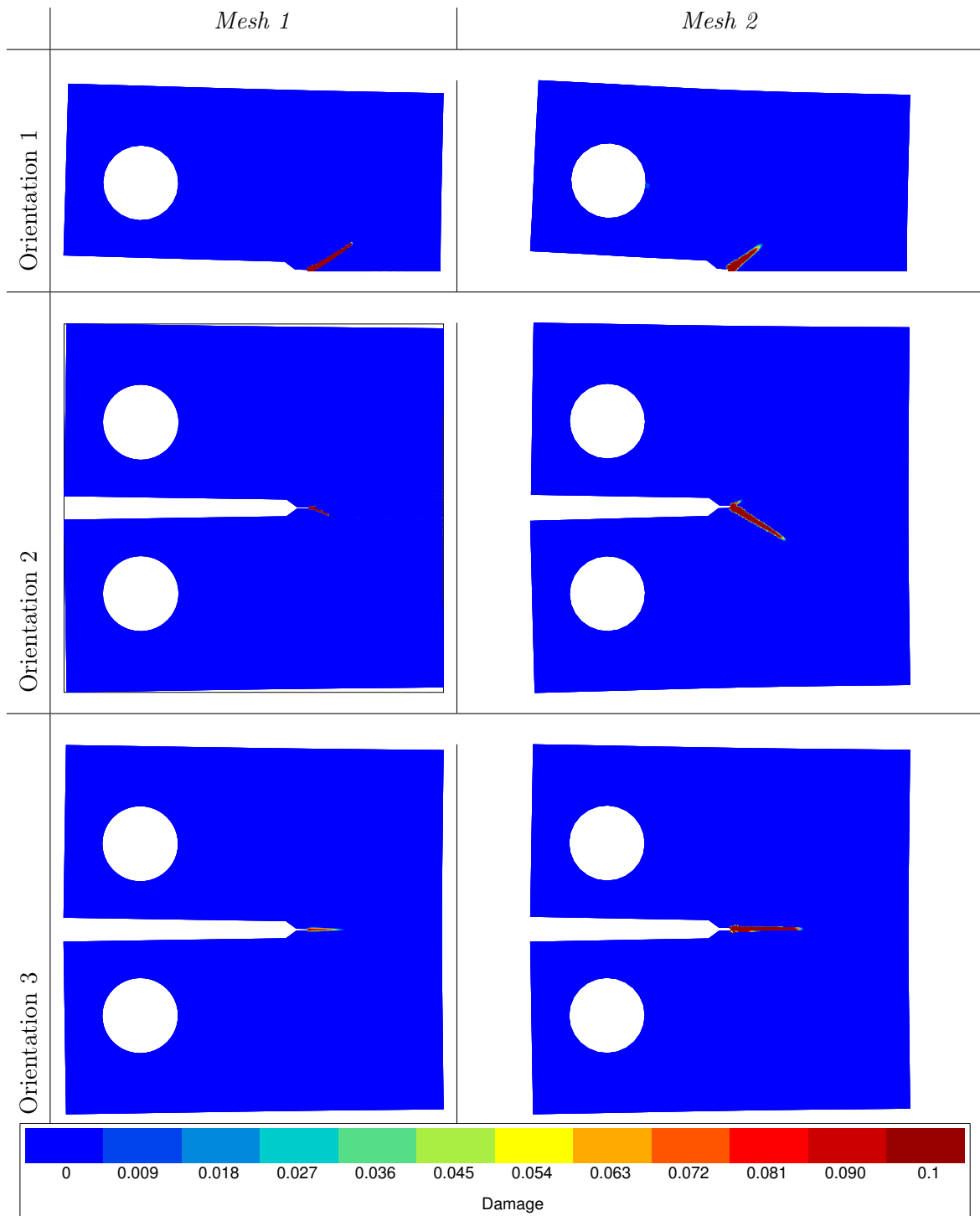


Table 8.2: Simulations showing the mesh independence of crack growth predicted by the XMD model for the various orientations tested

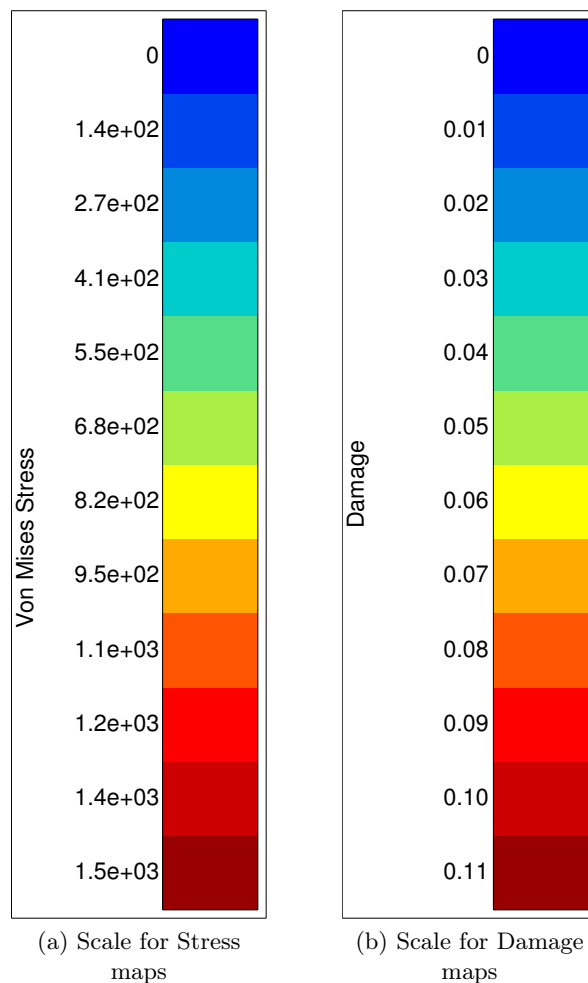


Figure 8.5: Scale for Stress and Damage maps in Tables 8.3 and 8.4

### 8.2.1 Discussion

The simulations of compact tension tests indicate several aspects of the XMD model. Table 8.2 shows the predicted crack paths for both *Meshes A and B*. Simulated crack paths are shown for all three orientations. It is seen that the crack paths are independent of the mesh. The maps shown are “convergent” in the sense that smaller values of  $tol$  lead to the same results. However, very small values of  $tol$  lead to the divergence of the Newton-Raphson algorithm, and we are unable to simulate subsequent crack propagation. It has been pointed out that the non-normalised convergence criterion has been chosen for the presented simulations. Various simulations were conducted using different tolerance values ranging between  $tol = 0.01N$  to  $tol = 100N$  (see Equation 8.11). For all the tests, it was found that the computation times taken for the simulations to diverge was directly proportional to the tolerance value chosen. For the rest of the simulations, discussed in the chapter a tolerance value of  $tol = 1N$  was used.

Tables 8.3 and 8.4 show different stages of crack propagation for the Orientations 2 and 3. These simulations show that the orientation dependency of the crack paths can be simulated using the XMD model. Following the verification of the mesh independence, further tests regarding different loading conditions are presented in the following sections.

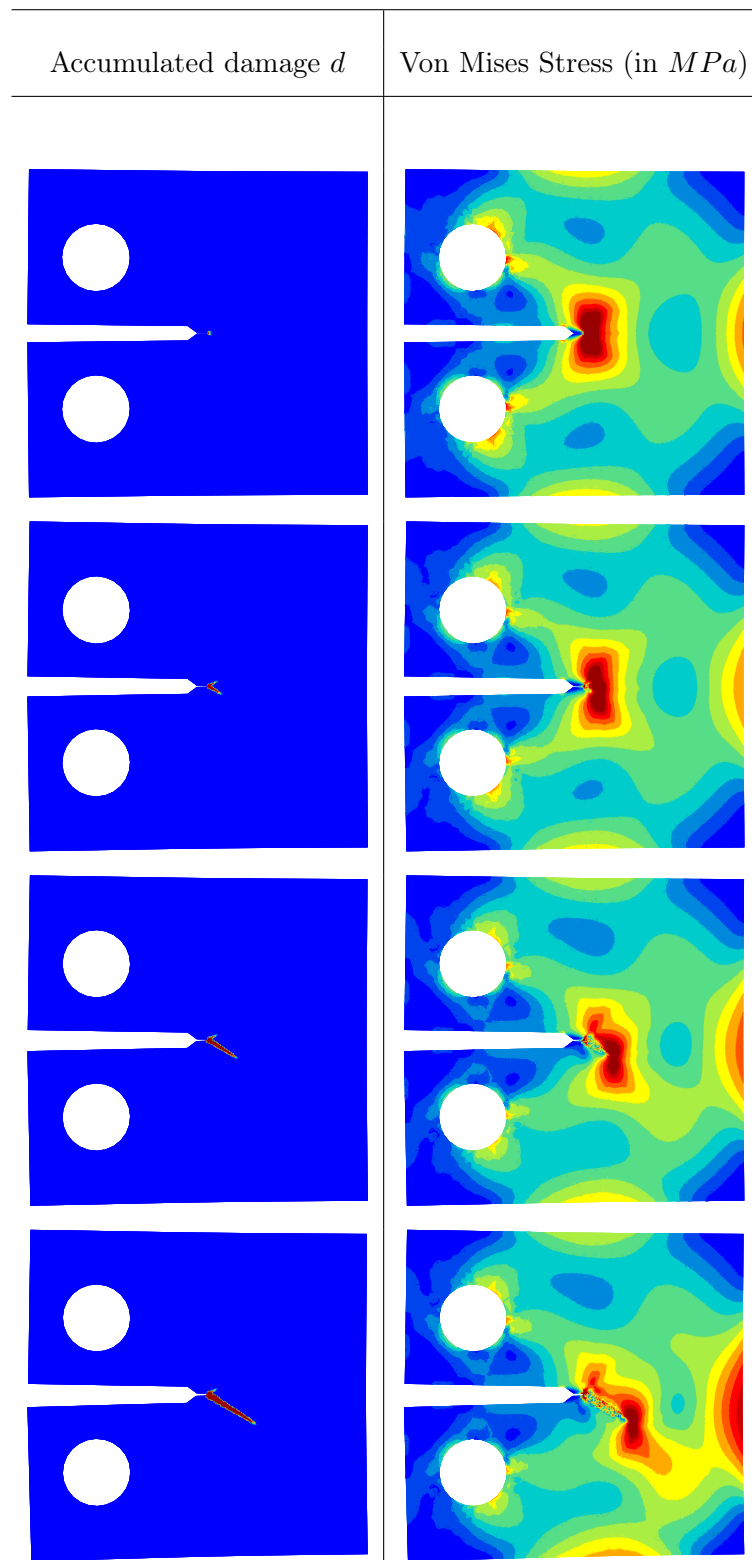


Table 8.3: Table showing different stages of crack propagation in the CT specimen for Orientation 2. The column on the left shows the propagation of the crack in terms of the accumulated damage variable  $d$ . The column on the right shows the advance of the stress field at each corresponding step of crack propagation.

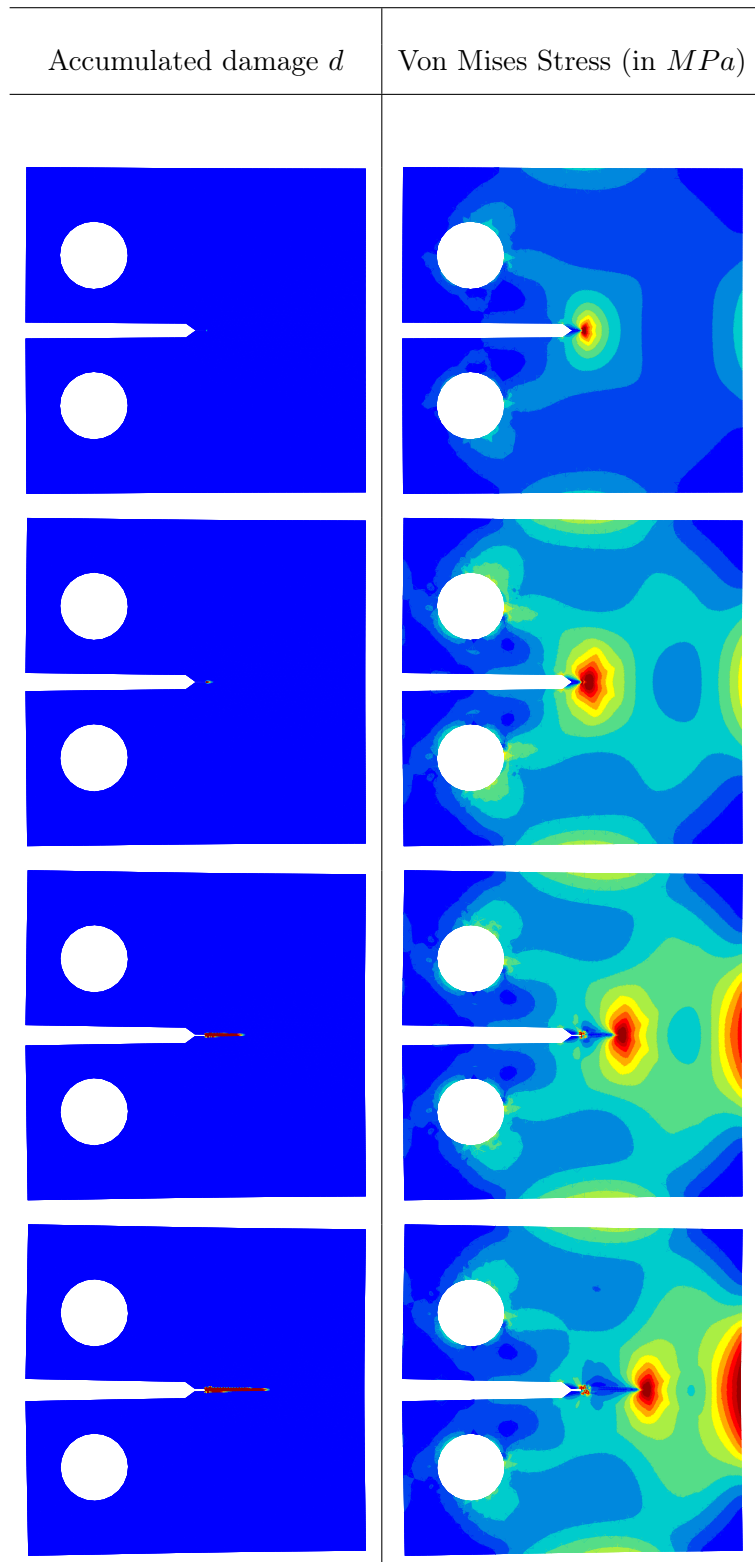


Table 8.4: Table showing different stages of crack propagation in the CT specimen for Orientation 3. The column on the left shows the propagation of the crack in terms of the accumulated damage variable  $d$ . The column on the right shows the advance of the stress field at each corresponding step of crack propagation.

### 8.3 Mode II test

In the numerical results presented up to this point, the imposed loads have been restricted to Mode I loading applied to various numerical test specimens. However, no test has been presented so far to address the performance of the XMD model under pure Mode II loading conditions. To the author's knowledge, very few experimental studies are available in literature as regards the propagation of cracks in NBSX specimens subject to Mode II loading. The following section presents a case study of Mode II loading. The few Mode II crack propagation studies in literature are presented in the context of isotropic material experiencing brittle fracture (e.g. [Welschinger \[2010\]](#)). It has been pointed out many times in earlier sections that models applicable to such behaviour cannot be used in realistic simulation of NBSX. To ensure that the simulations presented in the following section resemble real NBSX specimens as closely as possible, the material parameters relating to elasticity and plasticity have been chosen from earlier material-characterisation experiments. The additional parameters introduced in the XMD model present certain challenges. Since the parameters related to the damage aspect of the model are yet to be identified for the materials, the results presented in the following section can only be considered as sample studies showing the effects of the choice of material parameters on the simulations.

To study the crack growth under Mode II loading, experimental studies were conducted as part of the SOCRAX project. The project dealt principally with the propagation of short cracks in NBSX specimens. For a more detailed description of the SOCRAX project, see [Marchal \[2006\]](#), [Marchal et al. \[2002\]](#). One of the experiments conducted within the scope of this project at IMM (Athens, GREECE), was chosen to study the behaviour of the XMD model under Mode II loading. The specimen used for the study is shown in [Figure 8.6](#). In the figure, the red regions show the rigid holders used to impose displacement controlled loading on the specimen. It is noted that the imposed load  $U_2 > U_1$ . The mesh used for the simulations is shown in [Figure 8.7](#). The average size of the elements in the central zone (zone of stress concentration) is around  $100 \mu m$ , and the elements near the tip of the pre-crack are around  $20 \mu m$  in size. Loading was imposed in the vertical direction, which was aligned with the  $[001]$  direction. The horizontal axis was aligned along the  $[010]/[0\bar{1}0]$  direction. A study of the stresses in the specimen reported in [Gallerneau and Sanson \[2004\]](#), showed that the shear stresses were dominant in the regions between the two stress concentrators. It follows that the crack growth observed in this region is driven primarily by in-plane shear and hence, represents a Mode II propagation of cracks in NBSX.

Before proceeding further, a few key differences between the experiment and the numerical simulations must be pointed out. The experimental observations were conducted under fatigue loading conditions. However, due to the complicated nature of fatigue testing, numerical simulations were carried out under purely monotonic loading. Also, in the experimental specimens, a pre-crack was introduced to localise crack initiation. However, due to the complex geometry of the specimen, the pre-crack was simulated by the introduction of a smaller second round-tip notch. The details of the geometric dimensions of the specimen are given in [Table 8.5](#). The material parameters used for the simulation are presented in [Table A.2](#) (see [Appendix A](#)).

[Figure 8.8](#) shows a few experimental observations of short crack propagation and a few contour plots of crack path development (contour map of accumulated damage variable,  $d$ ). A comparison of the simulated crack paths from [Figures 8.8a](#), [8.8b](#), [8.8c](#) and [8.8d](#) indicate that the crack paths simulated are reasonably accurate. Similar crack paths were

Dimension	Value (in <i>mm</i> )
Width 'w'	80.0
Height 'h'	20.0
Radius 'R'	3.0
Notch height 's'	5.0
Pre-crack length 'a'	1.15
Diameter of holder 'D'	6.0
Distance between inner holders 's1'	24.0
Distance between outer holders 's2'	68.0

Table 8.5: Dimensions of specimen for Mode II test

observed while varying the softening parameter  $H$  (see Figures 8.8e, 8.8f and 8.8g). The closeness of the simulated crack paths to the experimentally observed crack patterns seem to indicate that the propagation of short cracks can be simulated using monotonic loading in lieu of computationally expensive fatigue simulations. However, such indicators need to be verified by actual fatigue simulations which incorporate accurate kinematic hardening. These are the key features which are lacking in the simulations presented here.

Figures 8.8e, 8.8f and 8.8g show the effect of varying the parameter  $H$  on prolonged crack propagation simulation. Different crack paths are observed after the crack advances beyond half the specimen height. Table 8.6 shows different stages of crack propagation in the test specimen and the corresponding Von-Mises stress contour maps. The various stress maps show the advance of the stress field with a corresponding advance of the crack. The stress maps are particularly useful in the final stages, where the development of crack branches are hard to distinguish. In these stages, two separate stress fields are seen, indicating the branching of the main crack. In the final stages, in addition to the already propagating crack, the initiation of two other small cracks are observed. In the last figure, it is observed that one of the newer cracks, which is located closer to the existing longer crack, becomes the dominant crack and propagates, while the new cracks further away from the longer crack do not propagate. Finally, the two propagating cracks meet, thereby resulting in complete material failure. At the point of failure, there are two additional

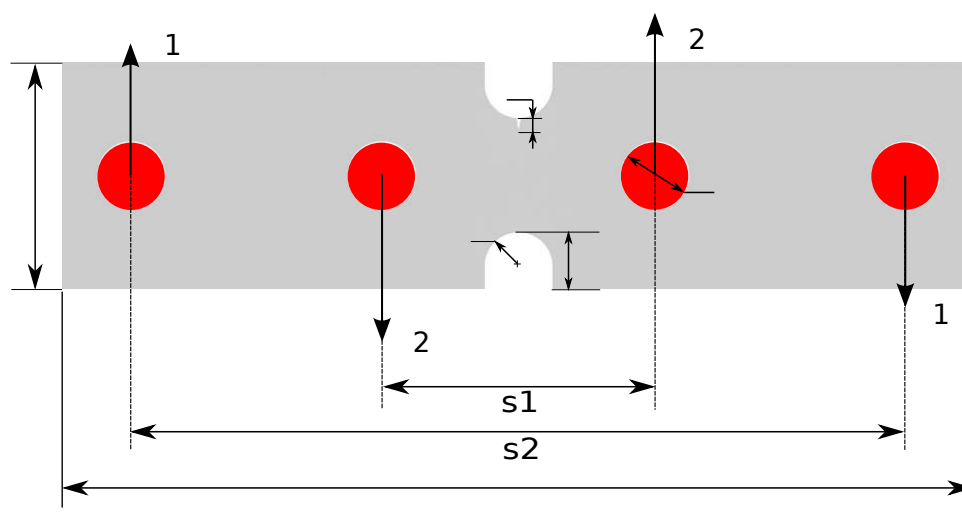
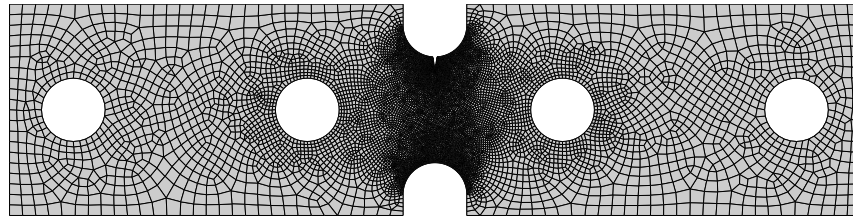
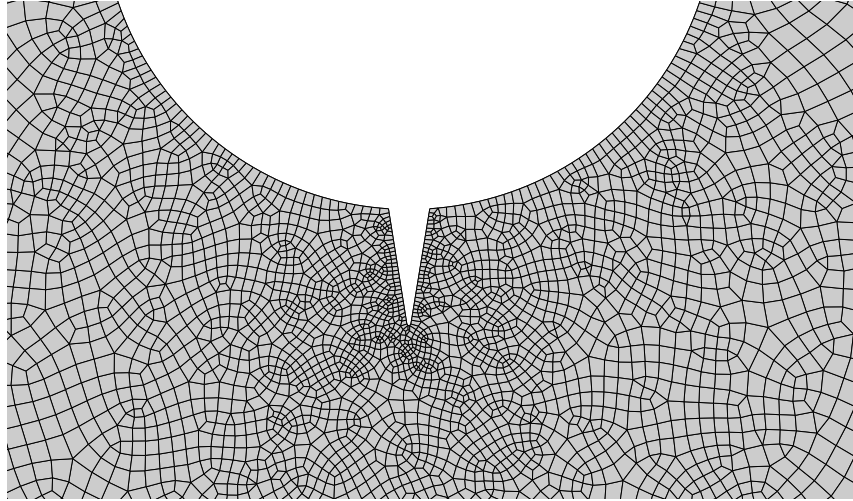


Figure 8.6: Geometry of the specimen used for testing crack propagation under Mode II loading



(a) Mesh for complete specimen



(b) Close-up view of mesh around notch

Figure 8.7: Mesh used in the simulation of Mode II crack propagation (Holders not shown)

features that develop in the longer crack. It is seen that the tip of the original crack deflects to meet the newly propagating crack. Also, a second branch is seen developing from the original crack. This branching of the longer crack occurs in the vicinity of the tip of the second propagating crack. These observations highlight the capability of the XMD model to handle the initiation and propagation of multiple cracks, in addition to the capability of handling complex crack phenomena such as branching and bifurcation. The results show that the XMD model is capable of simulating sustained crack growth under pure shear loading. Attention is also drawn to the final stages of crack propagation shown in Table 8.6. Despite the prediction of these cracks, the various crack paths observed in Figure 8.8 emphasise the importance of identifying appropriate material parameters.

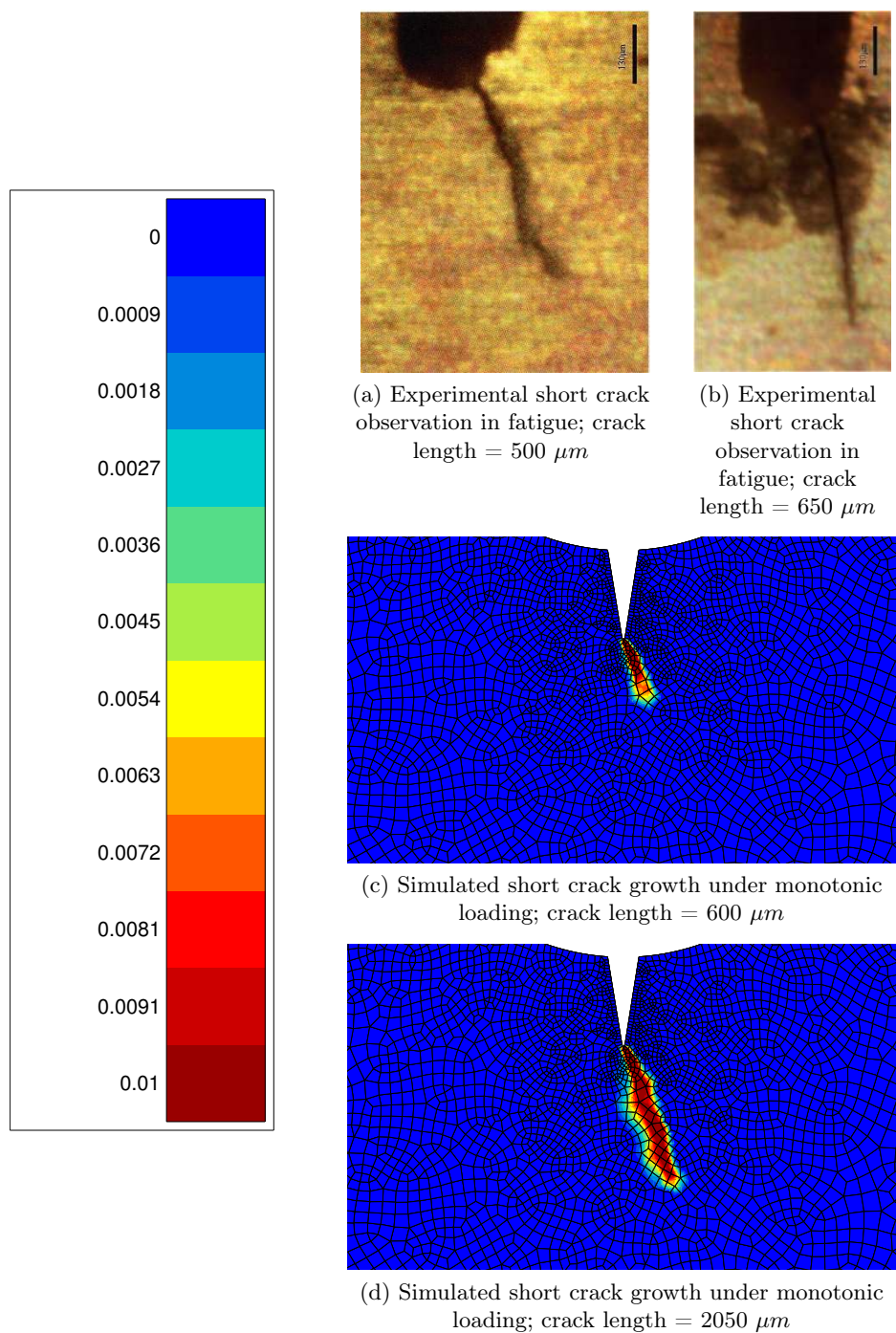
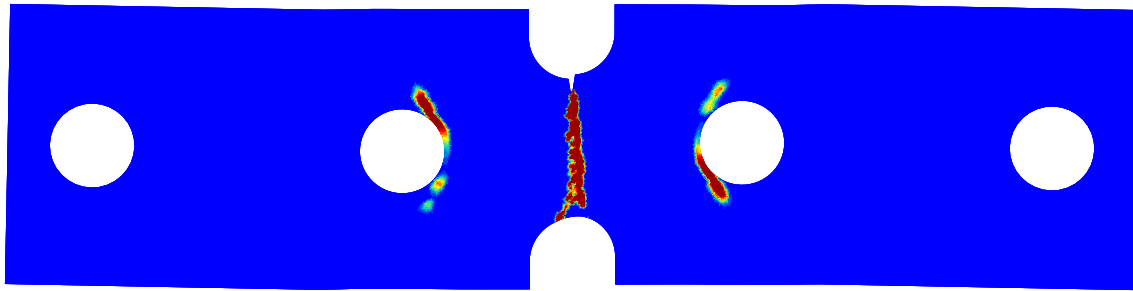
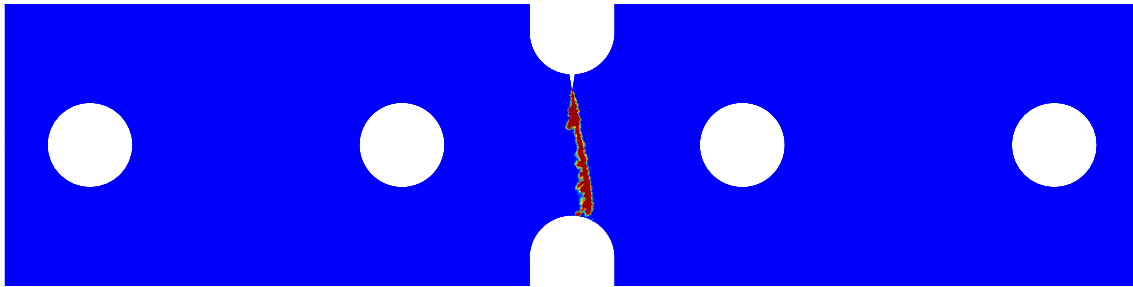


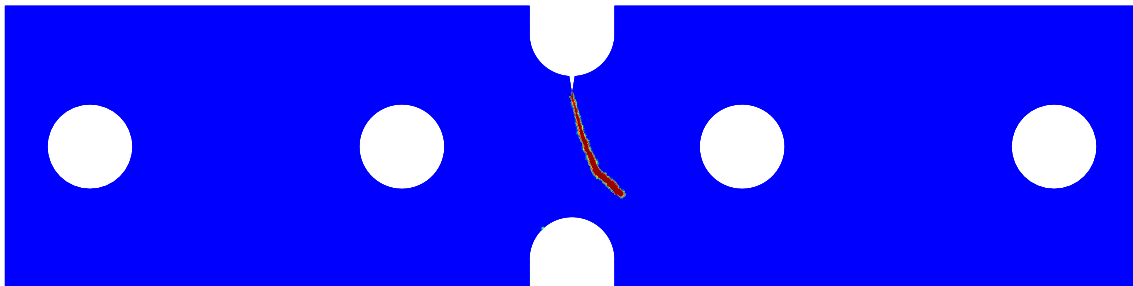
Figure 8.8: *Continued on next page ...*



(e) Crack propagation with softening parameter  $H = -15000MPa$

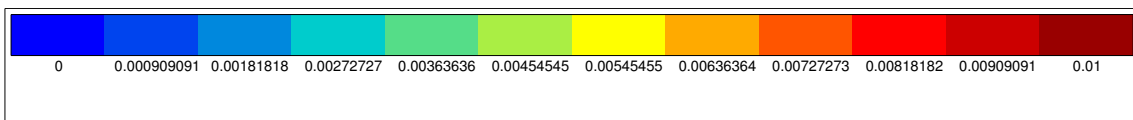


(f) Crack propagation with softening parameter  $H = -30000MPa$

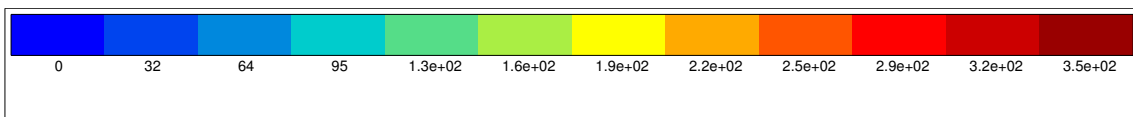


(g) Crack propagation with softening parameter  $H = -45000MPa$

Figure 8.8: Results from Mode II crack growth tests; Simulated crack paths are presented in the form of contour plots of the accumulated damage variable ‘d’. Figures (a) and (b) are taken from [Marchal et al. \[2002\]](#).

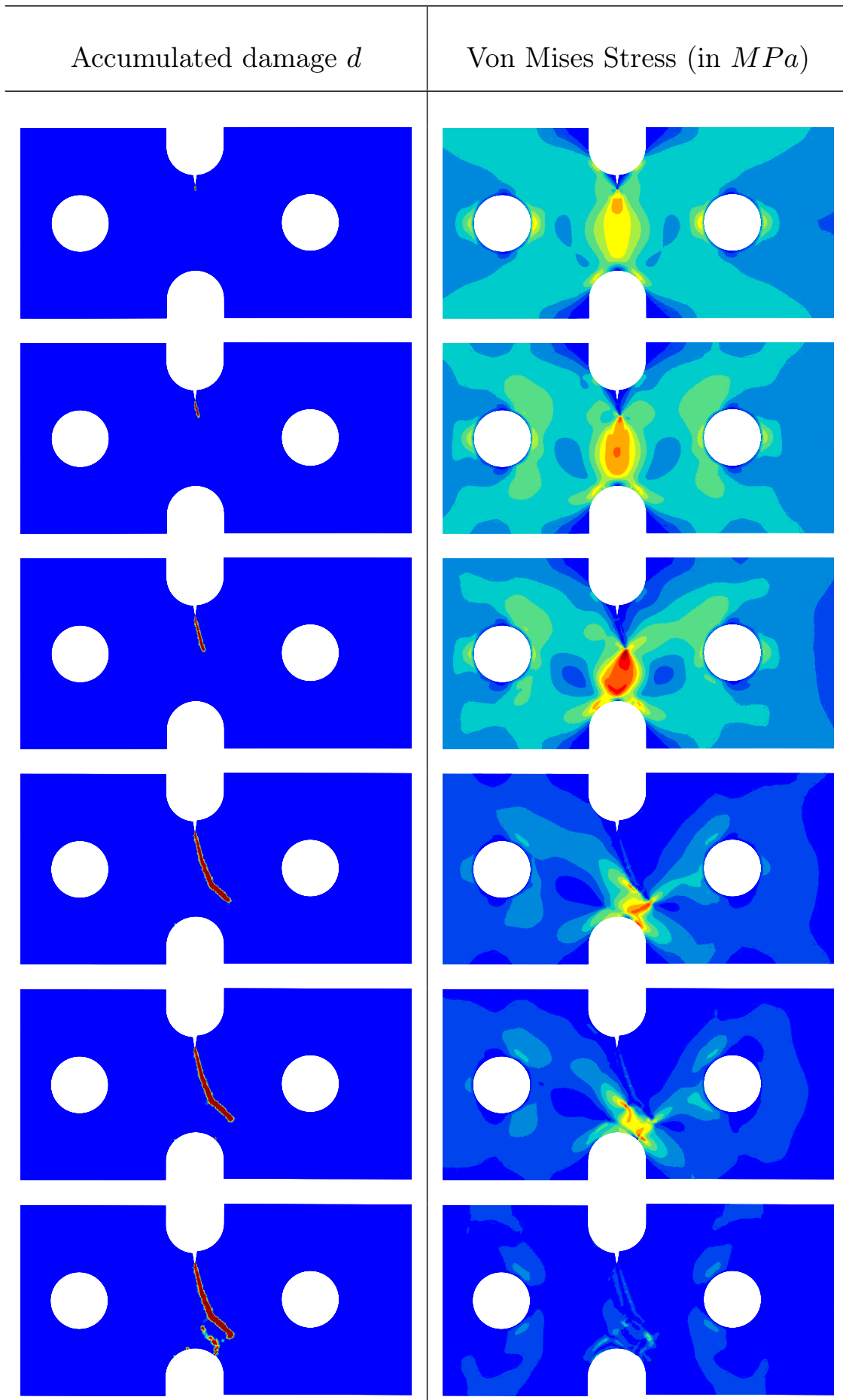


(a) Damage Scale



(b) Stress Scale

Figure 8.9: Stress and Damage scales for Table 8.6



138 Table 8.6: Table showing different stages of crack propagation in the Mode II test specimen for  $H = -45000MPa$ .

## 8.4 Creep tests

Throughout the discussion of the XMD model presented in Chapter 7, the importance of the parameters introduced in the model has been stressed upon. This applies even more so to the parameters  $\beta$  and  $H$ , which are the two key parameters to control the mechanics of damage in the material. The effect of varying  $H$  and  $\beta$  will be addressed in the following paragraphs. The parameters  $A$  and  $H_\mu$  are also important. Once the values of  $H$ ,  $H_\mu$  and  $\beta$  are settled upon, the value of  $A$  can be varied relatively freely. However, it must be ensured that the size of the smallest element is smaller than the regularisation thickness (at the very least, in the immediate vicinity of a crack/notch. Despite these guiding points, the identification of parameters  $\beta$  and  $H$  is quite tricky. The first difficulty arises due to the fully coupled nature of the material parameters. Assuming that the numerical parameters  $A$  and  $H_\mu$  are constant, it is possible to obtain similar crack paths with multiple combinations of  $H$  and  $\beta$ . Thus, the identification of the correct combination of parameters from a set of valid parameters requires a time consuming process of trial-and-error simulations and the comparison of simulated results with available experimental data. The problem of parameter identification is compounded by the added difficulty of quantifying the nature of coupling between damage and plasticity. To the author's knowledge, there are no studies available addressing the quantification of the mutual coupling between plasticity and damage. In other words, many studies identify that plasticity precedes fracture (e.g. [Flouriot \[2004\]](#)) and there are studies that identify the localisation of plasticity bands between voids and other damage related features (e.g. [Scheyvaerts and Pardoen \[2010\]](#)). However there is no quantification available, regarding the effect of one process on the other. The following section proposes a methodology to address these issues.

It is found that the simulation of crack propagation observed in creep tests can be useful in identifying these parameters, particularly the coupling parameter  $\beta$ . Creep phenomenon is fairly common in NBSX components. Sustained loads at extremely high temperatures, combined with processes such as oxidation cause the superalloys to deform and tear at loads well below the ultimate strength of the material. Thus, creep phenomenon in NBSX are a point of focus in many studies (see for example [Chatterjee et al. \[2010\]](#), [Staroselsky and Cassenti \[2011\]](#), [Yu et al. \[2009\]](#), [Yeh et al. \[2008\]](#) and [Tinga et al. \[2009\]](#)). The numerical simulation of creep (using FEA) is usually conducted by introducing a force  $F$  on a particular face of the specimen, which is then combined with a multipoint constraint that specifies that the displacement of the nodes on that particular face remains equal to that of the node on which the load is imposed. The specimens and the load imposed on the specimens are chosen such that the stresses in the material are well below the fracture stresses obtained from characterisation experiments such as the CT specimen, but are slightly above the plastic threshold. The consequence of such a test is that the failure of the material is purely driven by the sustained growth of plasticity in the material. Thus, simulating a creep test, could allow for the estimation of the strength of the coupling between plasticity and damage  $\beta$ , and to a lesser certain extent, the value of softening parameter  $H$ . These points are discussed further following the presentation of simulation results.

### 8.4.1 Creep simulations

To determine an approximate value for  $\beta$ , a creep test was simulated using the XMD model. Of the many creep experiments available in literature ([Cormier et al. \[2008\]](#), [Sugui](#)

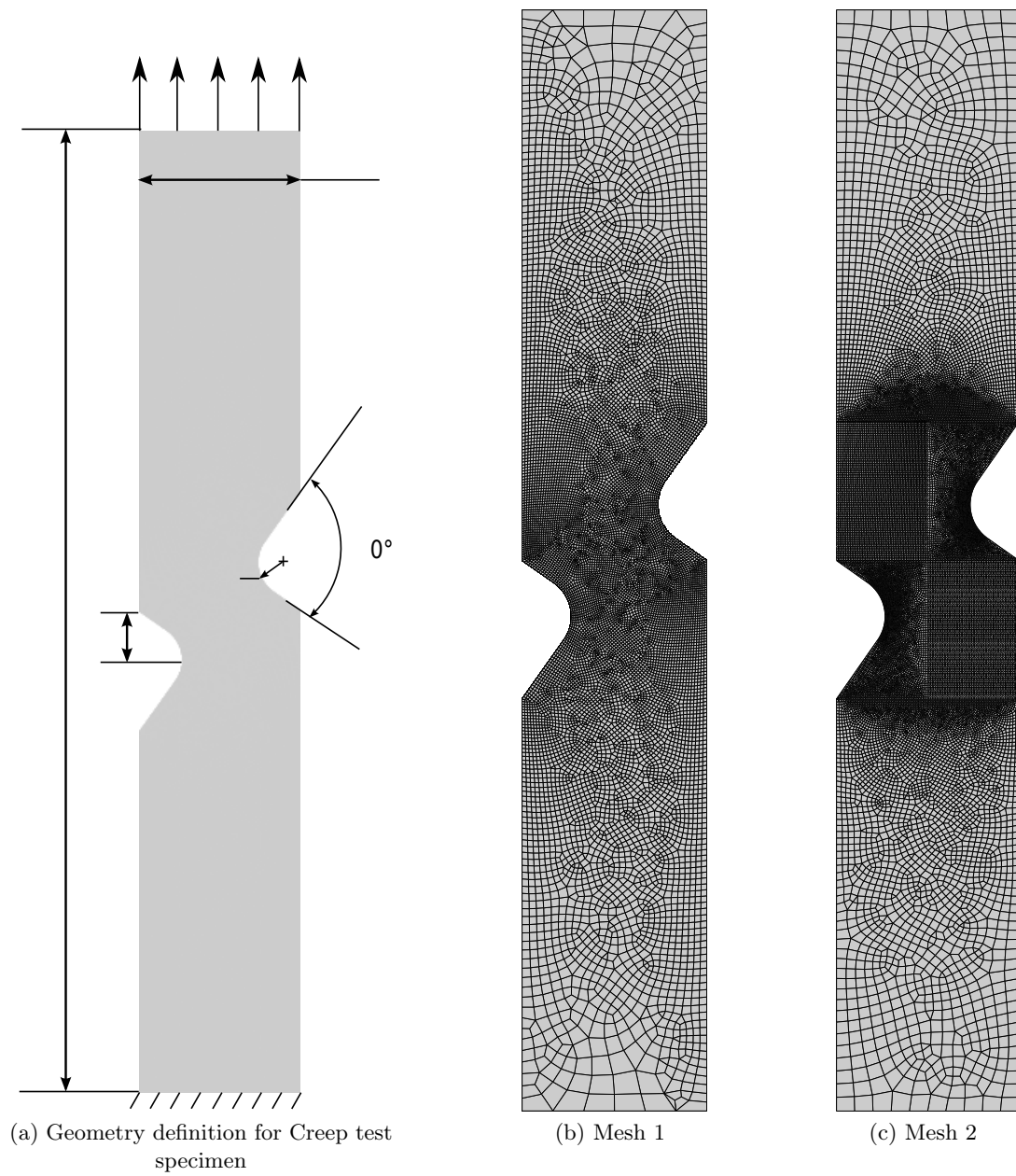
Dimension	Value (in <i>mm</i> )
Width 'w'	4.0
Height 'h'	24.0
Fillet Radius 'R'	0.9
Notch height 's'	1.0

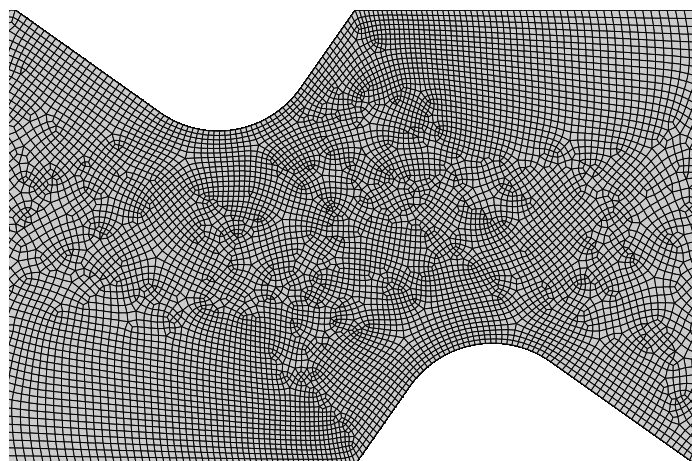
Table 8.7: Dimensions of specimen for Creep test

et al. [1999], Seetharaman and Cetel [2004] etc.), the experiment reported in Pragassam and Helstroffer [2010-2011] was chosen for the tests. The asymmetric specimen that was used in the test is shown in Figure 8.10a and the dimensions are given Table 8.7. The specimen was loaded up to  $440N$  of force. Two different meshes were used for the creep simulations. Initially, the coarser mesh of the two (*Mesh 1*; see Figures 8.10b and 8.10d) was used to obtain the material parameters which provided an acceptably accurate strain-field development. Following the identification of creep test parameters, the simulation was relaunched with the finer mesh (*Mesh 2*; see Figures 8.10c and 8.10e). The crack path obtained from the fine mesh simulation was then used for the analysis in Figure 8.13. It must be pointed out that the average element-size in the region of interest between the two stress concentration features varies between  $50\ \mu m$  and  $75\ \mu m$ . However, the key difference between the two meshes lies in the number of elements at the location of crack initiation. It is also pointed out that the elements used in all the simulations were linear elements with reduced integration. The integration of the evolution equations was carried out using a second order Runge-Kutta integration scheme, coupled with a time stepping algorithm and that the global system of equations were solved using a Newton-Raphson solver.

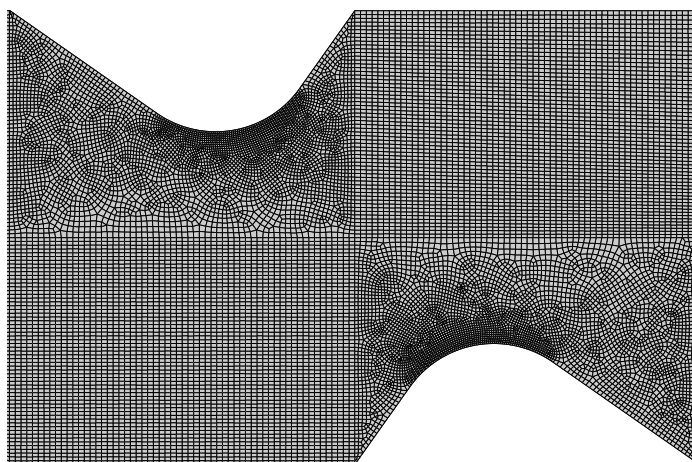
Crystal Plasticity simulations were conducted to identify the material parameters relating to the evolution of plasticity. The results obtained from the calibration simulations are shown in Figure 8.11. The values obtained by the calibration simulation show that the strain hardening in the material is almost nil. The simulations show that the plastic strain localises between the stress concentrators (Figure 8.12). Since the damage initiation in the model is plasticity driven, the growth of a crack is expected to occur in this band of localised plastic strain.

Since creep tests are usually conducted at high temperatures, the initial opening/cleavage stress was chosen to be  $Y_0 = 1000\ MPa$ , which is a relatively low value for a typical NBSX superalloy. Various combinations of  $\beta$ ,  $H$  and  $H_\mu$  were tested. Figure 8.13 shows a comparison of the simulated crack path with the experimentally observed crack path. The simulated creep curves are shown in Figure 8.14.

Figure 8.10: *Continued ...*



(d) Close-up view of mesh 1 for Creep specimen



(e) Close-up view of mesh 2 for Creep specimen

Figure 8.10: Creep test simulated using XMD model

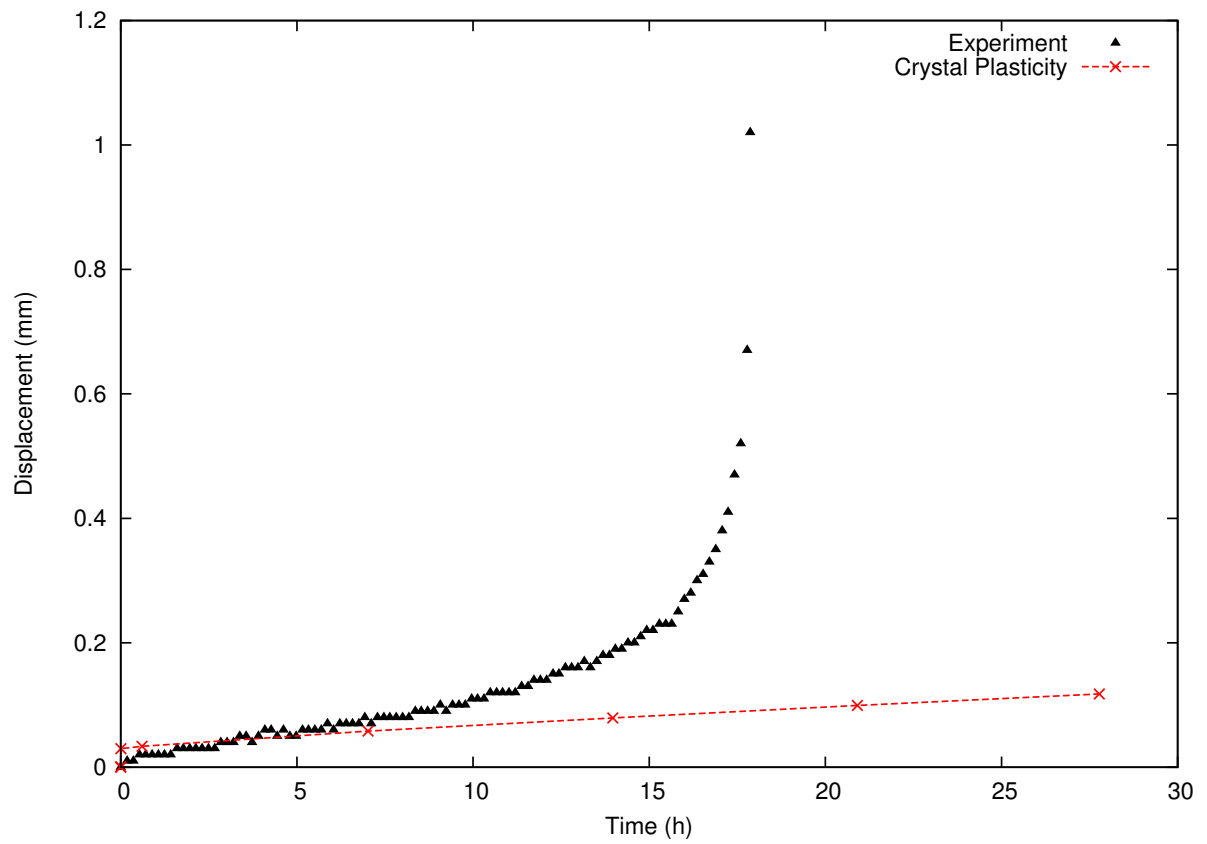


Figure 8.11: Calibration of crystal plasticity parameters

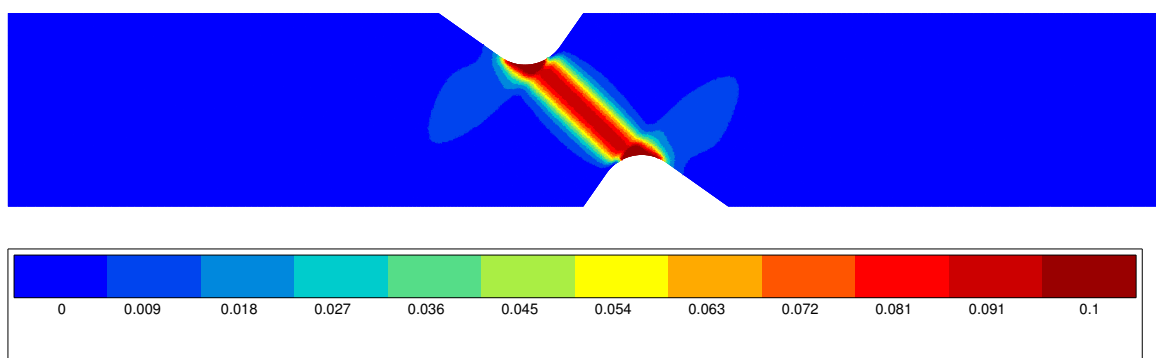
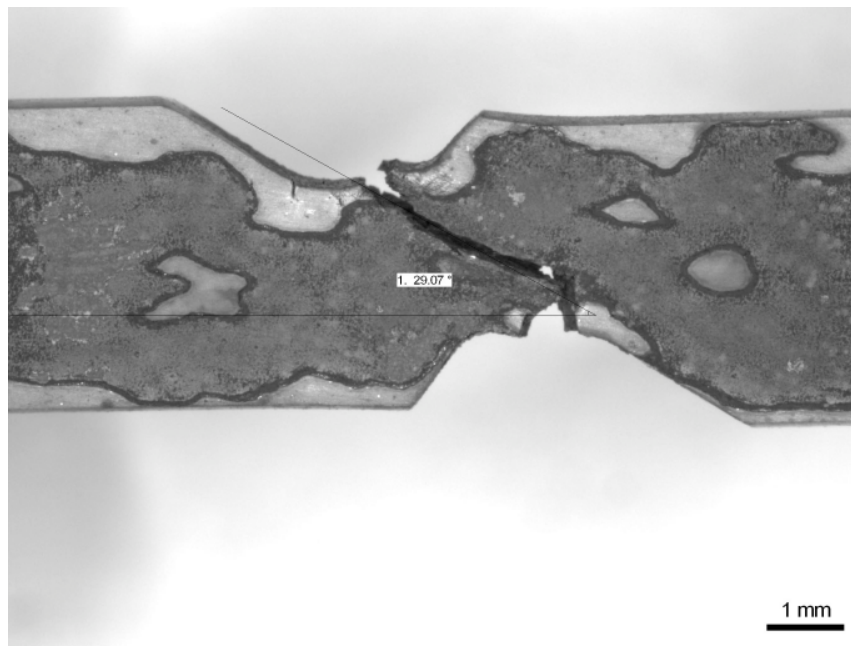
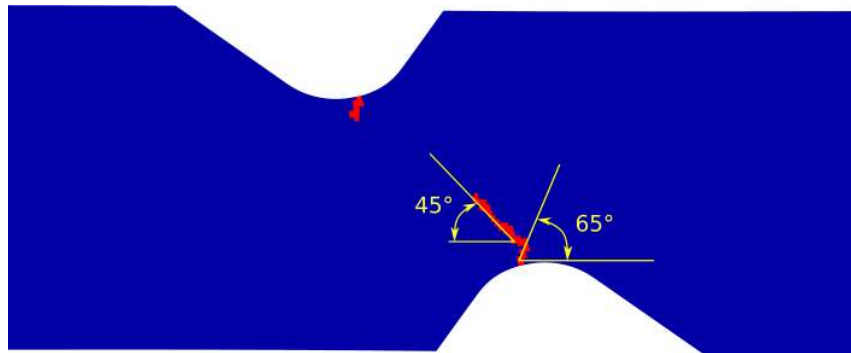


Figure 8.12: Plastic slip predicted by CPFEA after 27 hours



(a) Experimental crack growth observation



(b) Crack growth predicted by XMD model

Figure 8.13: Comparison of experiment and simulation for Creep test

### 8.4.2 Discussion

The experimental specimen shows an initial crack propagation at an angle of approximately  $70^\circ$ . Following the propagation of this initial crack, a sharp bifurcation is observed. Once the abrupt crack deviation has occurred, the crack propagates at an angle of about  $30^\circ$  with respect to the loading axis. In comparison to these observations, the simulated crack propagation is found to occur at an angle of  $65^\circ$ . The sharp deviation from the original crack path that is observed in the experiment is also observed in the simulation. In the regime after the crack bifurcation has occurred, it is observed that the simulated crack propagates at an angle of about  $45^\circ$  (w.r.t. loading axis; See Figure 8.13).

The experimentally observed post-bifurcation-crack-propagation occurs at an angle of  $30^\circ$  to the loading  $[001]$  axis. However, the simulated post-bifurcation-crack-growth-angle is about  $45^\circ$ . In order to understand this deviation from the experimental observation, further analysis was needed. Figure 8.15 (*EBSD image courtesy: ENSMA*) shows an EBSD mapping of the experimental specimen. The mapping was carried out at the Institute  $p'$  (Futuroscope Chausseuil, FRANCE). It is observed that there is extensive

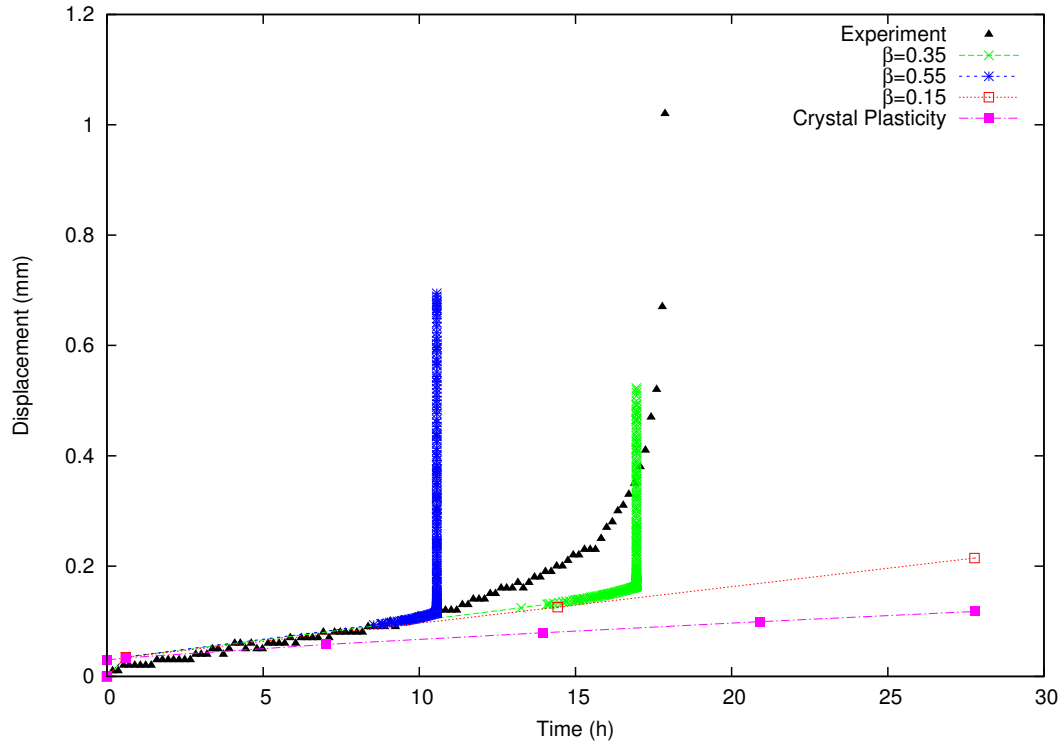
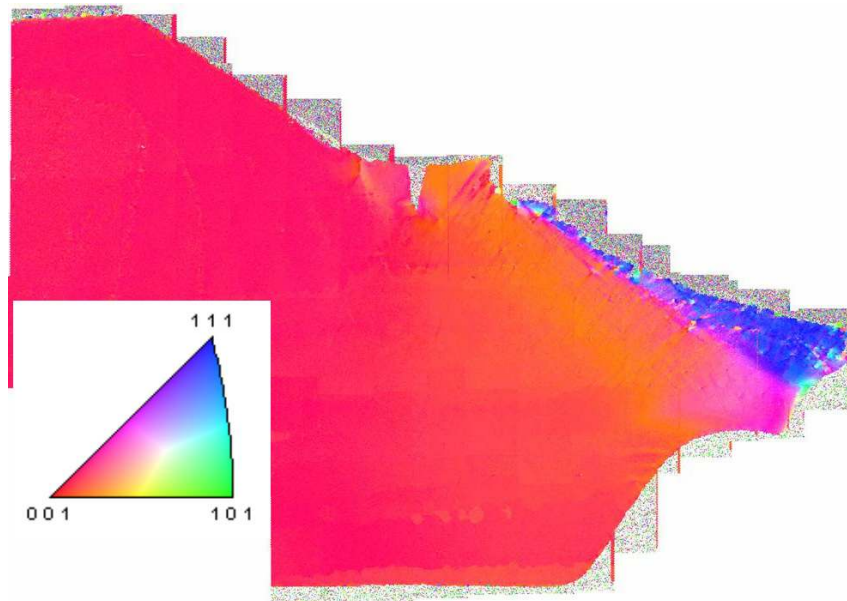


Figure 8.14: Experimental and Simulated Creep curves

lattice rotation near the zone of crack bifurcation. The EBSD map indicates that the microstructure in the entire region reorients itself along the  $\{111\}$  orientation. At this point it is pointed out that neither lattice rotation nor microstructure evolution are accounted for explicitly in the XMD model. Given these considerations, the crack evolution simulated by the XMD model are considered to be reasonably accurate. It is noteworthy that the vast amounts of lattice rotation predicted by the EBSD map highlight the need for a finite-deformation formulation of the XMD model.

Figure 8.15: EBSD map of the experimental specimen. *Images courtesy: Institute P', ENSMA*

## 8.5 Conclusion

Various numerical examples have been presented and discussed in order to analyse the effectiveness of using the XMD model for simulation of crack propagation. The numerical examples presented in this chapter are the simulations of real experiments, conducted according to the experimental data available. The crack paths observed justify the principles used in the XMD model, viz. a thoroughly coupled, plasticity driven evolution of anisotropic damage along selected crack planes. While the crack paths predicted by the model are not 100% accurate, they are realistic. The crack paths however, are found to be a function of the choice of material parameters.

The importance of choosing the appropriate material parameters has been mentioned earlier. This point is more obvious from Figure 8.16, which shows a few other crack paths that were simulated by choosing extreme values for material parameters.

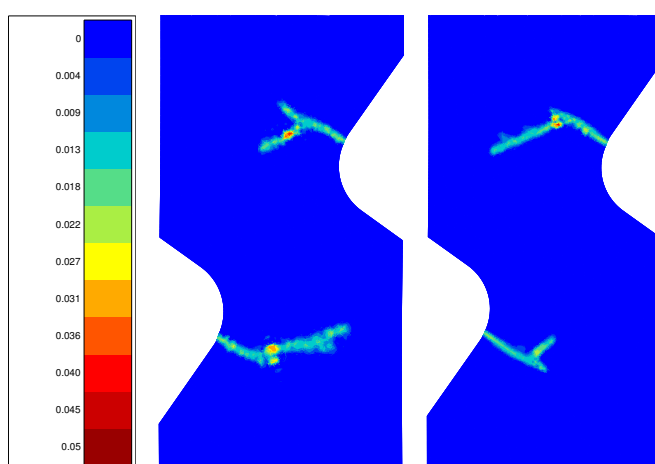


Figure 8.16: Different crack paths for the creep test predicted by the XMD model (Mesh 1 from Figure 8.10 was used for the simulations)

The choice of the appropriate material parameters is the one aspect of the XMD model, which at the present is the most time-consuming. The model introduces two previously uncharacterised material parameters,  $H$  and  $\beta$ , which are in turn coupled with the numerical parameters  $A$  and  $H_\mu$ . The analytical solution presented in Chapter 7 only provides a ball-park value, which can be used to reduce the time spent on parameter identification. Keeping this idea in mind the following steps are suggested for the parameter-identification process:

- ▶ Identify the classical parameters related to the Elasticity and Crystal Plasticity components of the model.
- ▶ Select the required crack thickness. Mesh the subject such that the average element size in the zone of interest is smaller ( $\approx 4$  times smaller is suggested, 2 times smaller is the bare minimum) than the desired crack thickness.
- ▶ Fix a value of  $H_\mu$  such that the value is sufficiently high to ensure the closeness of  $d$  and  $d_\mu$ .
- ▶ Calibrate the values of the parameters  $H$ ,  $A$  and  $\beta$  such that the simulated crack thickness, crack path and the crack growth rate are in agreement with the experimental observations.

- Validate the parameter choice by simulation of supplementary simulations.

The chapter presented simulations of various experiments and in some cases, comparisons with experimental observations. It was mentioned towards the beginning of the chapter, that the integration of the evolution equations was carried out using a second order Runge-Kutta integration scheme, coupled with a time stepping algorithm and that the global system of equations were solved using a Newton-Raphson solver. The simulations show that the XMD model can be considered to be a robust and accurate model. However, there is yet room for improvement in terms of element performance, inclusion of finite strains and in terms of coupling with other phenomena such as oxidation and diffusion. These are reserved for future projects.



# Conclusions and Perspectives

## Résumé

Le but de ce travail était de développer un modèle en incluant un couplage fort entre les phénomènes de plasticité et d'endommagement afin d'être capable de simuler les branchements et bifurcations des fissures. Dans ce but, le modèle XMD a été développé. L'application de cette modélisation aux éprouvettes expérimentales sous des chargements différents a montré que ce modèle généralisé est capable de simuler les chemins complexes des fissures sans démarches numériques spéciales. Avec l'implémentation de ce modèle matériau plusieurs perspectives d'avancements étaient identifiés, qui sont listées ci-dessous :

- Développements d'une formulation en grandes déformations
- Amélioration des démarches numériques utilisées pour l'intégration des équations d'évolution
- Couplage avec des algorithmes avancés (par exemple remaillage mis à jour de la géométrie d'éprouvette, insertion d'une fissure dans les zones cassées, contact etc.)
- Couplage avec d'autres modèles liés à des phénomènes comme l'oxydation et la mise en radeaux
- Application aux éprouvettes perforées et aux polycristaux.

The present thesis was concerned with the development of a completely coupled model which is capable of simulating complex crack-propagation-related phenomena such as crack bifurcation and crack branching in Nickel base single crystal superalloys. To ensure that the most essential aspects of NBSX crack development formed the basis of the model, a literature review of the deformation mechanisms in superalloys was conducted. A brief review of the formation of superalloys, and the various phenomena that affect the evolution of strains in single-crystal superalloys were considered. Following a review of the material aspects of NBSX, the essential concepts in the numerical modelling of fracture were revisited. In particular, the rational-mechanics based approach to constitutive modelling of materials was introduced.

Following the consideration of the fundamentals in the first part, the classical crystal plasticity model was introduced in the second part. The crystal plasticity model was used to simulate tension tests on double-edge-notch specimens. It was also used to simulate indentation specimens. A set of post processing tools was introduced to facilitate the analysis of plasticity fields predicted by the crystal plasticity finite element model. The

---

predicted plasticity fields were then compared to the experimentally observed slip lines in the experimental specimens. The tests were conducted on different orientations of the crystal. The experimental observations indicated that the secondary orientation of the single crystals can also affect the development of strain fields in a strong manner. This was an important observation since the secondary orientation is usually neglected during the manufacturing of these superalloys. The plasticity simulations confirmed that the crystal plasticity model can be used to obtain accurate strain-field predictions, which in turn can be used to analyse accurately the expected deformation of components during the design phase.

The third part then presented the need for regularised models for simulating crack growth using numerical models. A literature review of various regularised numerical models was carried out and a detailed presentation of the Microdamage model, developed in Aslan [2010] was presented as a base model. An improved version of this model, which includes a complete two-way coupling of plasticity and damage was developed and presented in Chapter 7. The model was developed using the methodology presented in Forest [2009]. Chapter 7 also presented various numerical tests aimed at exhibition of the various capabilities of the XMD model. Chapter 8 presented the details behind the numerical implementation of the XMD model, and presented the numerical simulations of experimental observations. The numerical simulations were found to be in good agreement with most of the experimental observations. Based on these comparisons, the XMD model can be said to be a robust model that can be used to effectively simulate different crack growth patterns. However, certain avenues for further development were also identified.

Principal among these possibilities are the improvements in element performance and in numerical integration. It has been pointed out that the problem of fluctuation of hydrostatic stresses can be addressed by the development of a mixed finite-element, which includes an additional pressure type variable to account for these fluctuations. Also, elements with mixed interpolation functions could present an interesting alternative. The development of an adaptive remeshing scheme could significantly reduce the number of elements used for simulations. This in turn would cut down the number of integration points and consequently lead to reduced computation times. Finally, another aspect that can be considered is the introduction of a crack in the geometry via element removal. This strategy could be useful in addressing the problem of hydrostatic-stress-fluctuation. Since the fluctuations are mainly observed in the cracked/broken zone, a removal of elements in these regions would eliminate the possibility of any stresses in the region. Examples of crack insertion algorithms can be found in works by Feld-Payet [2010] and Cuvilliez [2012].

In terms of numerical integration, difficulties with regards to the use of standard implicit scheme are observed. At present, the material model contains multiple checking conditions to ensure the accommodation of post-failure shear in the slip systems. This abrupt shifting of pure shear to post-failure-shear causes the Jacobian of the residual to become ill-conditioned (see Appendix B for the development of the standard implicit scheme), which in turn results in divergence. To resolve this problem, the development of alternative numerical schemes is suggested. Considering the prevalent use of explicit integration in commercial/industrial packages, it could be interesting to develop a fully explicit scheme with a higher-order accuracy. Alternatively, a new algorithm to better implement the XMD model could also be developed.

Another major development possibility in the short-term is found in the finite-strain formulation of the model. It was pointed out towards the end of Chapter 8 that there were differences of a few degrees between the simulated crack paths and the experimentally observed crack paths. The presence of vast amounts of localised plasticity at the crack-tip

leads to significant lattice rotations. The comparison of the simulated results with the EBSD analysis shown towards the end of Chapter 8 supports the presence of extensive lattice rotations in the vicinity of the fractured zone. This implies that the inclusion of these rotations in the numerical model is important for accurate simulation. Furthermore, a comparison between the lattice rotations obtained from finite-strain simulations can be used with EBSD observations, to allow a more accurate quantitative analysis of crack-related features such as crack-fronts and crack-surfaces. Such quantitative analysis is considered indispensable in the final validation of the model.

In a number of simulations conducted with the XMD model, some non-zero-stresses were observed in the damaged zone. It is not yet clear if and how the presence of these non-zero stresses affects the crack path predictions in the XMD model. However, it was observed that these stresses could be caused by a number of sources. For example, in some simulations, it was observed that choosing the values of the parameters  $K_d$  and  $n_d$  such that they resemble rate independent damage evolution, led to reduced fluctuation of stresses in the cracked zone. Furthermore, these fluctuations of stresses were more prevalent in the tests with crack bifurcations. Thus, the analysis and if possible the elimination of these spurious stresses should be counted among the list of possible short term improvements. Also, the damage induced softening is included in a linear format in the XMD model. The development of a non-linear version of this softening could lead to better prediction of crack paths.

The long-term perspectives of the model are rather extensive. It has been indicated in the sections dealing with creep experiments that the current model does not include the effects of phenomena such as microstructure evolution and oxidation of the material. Thus, the inclusion of such effects could prove to be an interesting possibility for development. Also, the numerical simulations presented in this thesis are carried out under isothermal assumptions. Following the approach to development of constitutive relations presented here and in Forest [2009] and Aslan [2010], it should be possible to develop a thermo-mechanically coupled elastic-viscoplastic-damage model. Once such possibility would be to couple the obvious dependence of the initial plastic and damage thresholds, and the viscosity parameters to temperatures. Such extensively coupled models would require extremely efficient numerical solvers to ensure good convergence and accurate results. Simulations of polycrystalline aggregates would provide another interesting avenue for the extension of the XMD model. Some preliminary examples of this nature are presented in Appendix C.

The work presented in this thesis indicates that many aspects of numerical fracture remain open questions. Some of these can be addressed effectively by the development of thermodynamically consistent, thoroughly coupled models, a simple example of which is provided by the XMD model developed in this thesis.



# Appendices



## Appendix A

# Material Parameters used in simulations

The material parameters used in the simulation of experimental specimens (discussed in Chapter 8) are presented here. It is noted that all the simulations considered only octahedral slip. Neither cubic slip nor kinematic hardening were accounted for. Table A.2 shows the material parameters, Table A.1 shows the slip and cleavage plane definitions used in the simulations.

System No.	System type	Plane normals			In-plane directions		
		N1	N2	N3	L1	L2	L3
1	Octahedral Slip	1	1	1	$\bar{1}$	0	1
2	Octahedral Slip	1	1	1	0	$\bar{1}$	1
3	Octahedral Slip	1	1	1	$\bar{1}$	1	0
4	Octahedral Slip	1	$\bar{1}$	1	$\bar{1}$	0	1
5	Octahedral Slip	1	$\bar{1}$	1	0	1	1
6	Octahedral Slip	1	$\bar{1}$	1	1	1	0
7	Octahedral Slip	$\bar{1}$	1	1	0	$\bar{1}$	1
8	Octahedral Slip	$\bar{1}$	1	1	1	1	0
9	Octahedral Slip	$\bar{1}$	1	1	1	0	1
10	Octahedral Slip	1	1	$\bar{1}$	$\bar{1}$	1	0
11	Octahedral Slip	1	1	$\bar{1}$	1	0	1
12	Octahedral Slip	1	1	$\bar{1}$	0	1	1
1	Damage	1	1	1	-	-	-
2	Damage	1	1	$\bar{1}$	-	-	-
3	Damage	$\bar{1}$	1	1	-	-	-
4	Damage	1	$\bar{1}$	1	-	-	-

Table A.1: Material parameters used in different simulations discussed in Chapter 8

Material	Fig. no.	y1111 (MPa)	y1212 (MPa)	y1122 (MPa)	$R_0$ (MPa)	$K_{plast}$ (MPa.s <sup>1/n<sub>plast</sub></sup> )	$n_{plast}$	$Q$ (MPa)	$b$ (MPa.s <sup>1/n<sub>dam</sub></sup> )	$h$ (MPa)	$Y_0$ (MPa)	$K_{dam}$	$n_{dam}$	$H$ (MPa)	$H_\mu$ (MPa)	$\beta$
DD3	Table 8.3	192614.17	127000.0	94869.72	300.0	10.0	10.0	5000.0	10.0	0	2500.0	10.0	2.0	-12000.0	50000.0	0.4
DD3	Table 8.4	192614.17	127000.0	94869.72	300.0	10.0	10.0	5000.0	10.0	0	2500.0	10.0	2.0	-12000.0	50000.0	0.4
AM1	8.8g	261000.0	93000.0	198000.0	69.0	517.0	5.0	0.0	0.0	1000.0	1500.0	20.0	2.0	-15000.0	100000.0	0.5
AM1	8.8f	261000.0	93000.0	198000.0	69.0	517.0	5.0	0.0	0.0	1.0	1500.0	10.0	2.0	-35000.0	100000.0	0.5
AM1	8.8e	261000.0	93000.0	198000.0	69.0	517.0	5.0	0.0	0.0	1.0	1500.0	10.0	2.0	-45000.0	100000.0	0.5
MC2	8.13	170042.0	111745.0	97418.0	3.0	899.99	6.3	0.0	15.0	9.0	1000.0	20.0	2.0	-12000.0	50000.0	0.55
MC2	8.16b	170042.0	111745.0	97418.0	18.0	899.99	5.1	10.0	15.0	1.0	1000.0	10.0	2.0	-1000.0	50000.0	0.35
MC2	8.16c	170042.0	111745.0	97418.0	18.0	899.99	5.1	10.0	15.0	1.0	1000.0	10.0	2.0	-1000.0	50000.0	0.35

Table A.2: Material parameters used in different simulations discussed in Chapter 8

## Appendix B

# Numerical aspects

### B.1 Finite elements

In the simulations presented in this thesis, different element formulations were considered. The quadrilateral elements with linear and quadratic interpolation functions are shown in Figure B.1. The positions of the Gauss points are also shown.

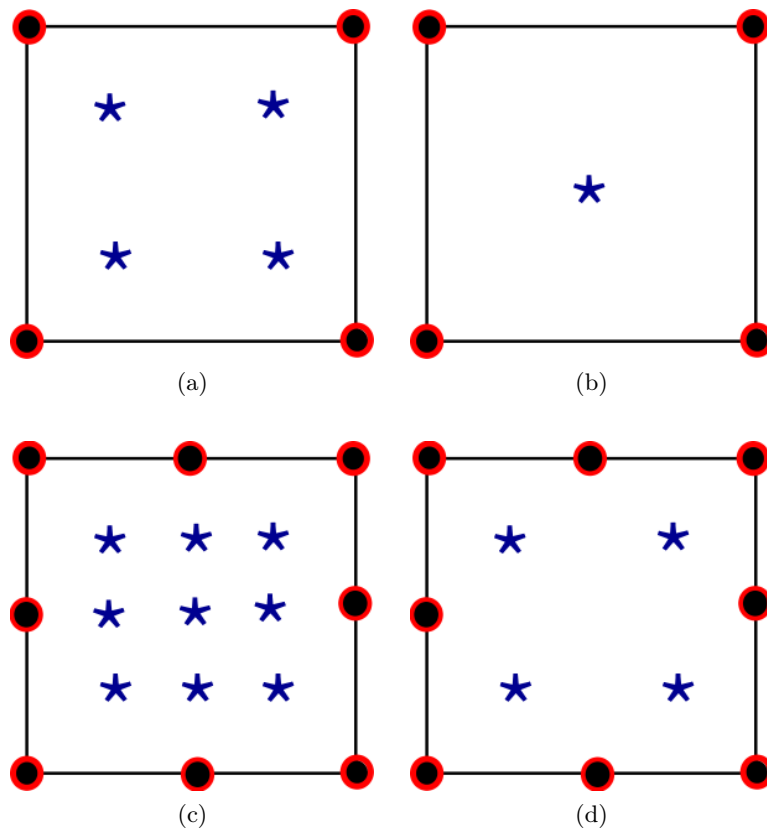


Figure B.1: (a) Linear interpolation, full integration (b) Linear interpolation, reduced integration (c) Quadratic interpolation, full integration (d) Quadratic interpolation, reduced integration. Blue stars indicate integration points (Gauss points). Red circles represent the DOF microdamage  $d_\mu$ , and the black solid circles represent displacement DOFs.

## B.2 Numerical algorithm for XMD model (local integration at Gauss point)

The following algorithm describes the implementation of the XMD model used in the simulations presented:

1. Beginning with the imposed load for the initial time step, compute the stress,  $\boldsymbol{\sigma}$ .
2. If plasticity or damage already exists in the structure, update the plastic threshold  $r$  and the damage threshold  $Y$  by including the effects of strain hardening and of coupled plasticity/damage induced strain softening. Then check if  $Y \leq 0$ . If yes set  $r = 0$  and  $Y = 0$  (*thereby indicating that the material is completely “broken”*). If there is no plasticity/damage (as in most cases of early stage loading), set  $r = r_0$ ,  $Y = Y_0$ .
3. Check if RSS  $\tau^s$  exceeds  $r$ . If yes, compute the plastic strain increment  $\gamma^s$  for slip system  $s$ . the plastic and elastic components of the strain tensors ( $\boldsymbol{\varepsilon}_p$  and  $\boldsymbol{\varepsilon}_e$ ) by numerical integration of the evolution equations for plastic slip and plastic strain.
4. Check if the stress acting normal to the damage plane,  $\sigma_n \geq Y$ . If yes, compute  $d_{open}^r$  and total damage  $d$  by numerical integration of evolution equations for the damage variables.
5. Obtain the updated values for displacements and microdamage by resolving the global system of equations for the next loading increment.

Additional steps are needed to handle “crack-closure” as explained in section 7.3.

## B.3 Implicit $\theta$ -integration for constitutive equations

It has been indicated that the implementation of the XMD model leads to certain convergence related difficulties in the implementation of an implicit integration scheme. The formulation of the generalised implicit scheme is provided in the following paragraphs.

We begin by recalling the numerical relations for the integration of internal variables (from Equations 8.6...8.9) as

$$\gamma(t + \Delta t) = \gamma(t) + \Delta t \dot{\gamma}(t + \Delta t) \quad (\text{B.1})$$

$$d_{open}^r(t + \Delta t) = d_{open}^r(t) + \Delta t \dot{d}_{open}^r(t + \Delta t) \quad (\text{B.2})$$

$$\boldsymbol{\varepsilon}^e(t + \Delta t) = \boldsymbol{\varepsilon}^e(t) + \Delta t \left( \dot{\boldsymbol{\varepsilon}}(t + \Delta t) - \dot{\boldsymbol{\varepsilon}}^p(t + \Delta t) - \dot{\boldsymbol{\varepsilon}}^d(t + \Delta t) \right) \quad (\text{B.3})$$

$$d(t + \Delta t) = d(t) + \Delta t \sum_r |\Delta d_{open}^r(t + \Delta t)| \quad (\text{B.4})$$

To ensure the inclusion of a non-linear isotropic hardening, the relation B.1 is replaced by the relation

$$v^s(t + \Delta t) = v^s(t) + \Delta t \dot{v}^s(t + \Delta t), \quad (\text{B.5})$$

and the relation for the plastic threshold is modified as

$$r = r_0 + h \sum_s v^s + H \beta^2 \sum_s v^s + Q \sum_{s,r} h^{sr} (1 - e^{-bv^r}) \quad (\text{B.6})$$

From the above given relations, it is possible to obtain the residuals for each of the integration equations, after substituting the rate terms in Equation B.3 by the equations 7.18 and 7.19, as

$$\mathcal{R}_{\varepsilon^e} = \Delta \tilde{\varepsilon}^e - \Delta \tilde{\varepsilon} + \Delta t \left[ \sum_{s=1}^{N_{slip}} \left\langle \frac{|\mathbf{C}_{\tilde{\varepsilon}}^e : \tilde{\mathbf{M}}^s| - r^s}{\tilde{K}_p} \right\rangle^{n_p} \tilde{\mathbf{M}}^s \text{sign}(\tau^s) \right] + \Delta t \left[ \sum_{r=1}^{N_{dam}} \left\langle \frac{|\mathbf{C}_{\tilde{\varepsilon}}^e : \tilde{\mathbf{N}}_d^r| - Y}{\tilde{K}_d} \right\rangle^{n_d} \tilde{\mathbf{N}}_d^r \right] \quad (\text{B.7})$$

$$\mathcal{R}_{v^s} = \Delta v^s - \Delta t \left\langle \frac{|\mathbf{C}_{\tilde{\varepsilon}}^e : \tilde{\mathbf{M}}^s| - r^s}{\tilde{K}_p} \right\rangle^{n_p} \quad (\text{B.8})$$

$$\mathcal{R}_{d^r} = \Delta d_{open}^r - \Delta t \left\langle \frac{|\mathbf{C}_{\tilde{\varepsilon}}^e : \tilde{\mathbf{N}}_d^r| - Y}{\tilde{K}_d} \right\rangle^{n_d} \text{sign}(\mathbf{C}_{\tilde{\varepsilon}}^e : \tilde{\mathbf{N}}_d^r) \quad (\text{B.9})$$

$$\mathcal{R}_d = \Delta d + \sum_{r=1}^{N_{dam}} |\Delta d_{open}^r| \quad (\text{B.10})$$

Based on this set of residuals, the Jacobian matrix  $\mathcal{J}$  can be calculated as

$$\mathcal{J} = \begin{bmatrix} \frac{\partial \mathcal{R}_{\varepsilon^e}}{\partial \Delta \tilde{\varepsilon}^e} & \frac{\partial \mathcal{R}_{\varepsilon^e}}{\partial \Delta v^s} & \frac{\partial \mathcal{R}_{\varepsilon^e}}{\partial \Delta d_{open}^r} & \frac{\partial \mathcal{R}_{\varepsilon^e}}{\partial \Delta d} \\ \frac{\partial \mathcal{R}_{v^s}}{\partial \Delta \tilde{\varepsilon}^e} & \frac{\partial \mathcal{R}_{v^s}}{\partial \Delta v^s} & \frac{\partial \mathcal{R}_{v^s}}{\partial \Delta d_{open}^r} & \frac{\partial \mathcal{R}_{v^s}}{\partial \Delta d} \\ \frac{\partial \mathcal{R}_{d_{open}^r}}{\partial \Delta \tilde{\varepsilon}^e} & \frac{\partial \mathcal{R}_{d_{open}^r}}{\partial \Delta v^s} & \frac{\partial \mathcal{R}_{d_{open}^r}}{\partial \Delta d_{open}^r} & \frac{\partial \mathcal{R}_{d_{open}^r}}{\partial \Delta d} \\ \frac{\partial \mathcal{R}_d}{\partial \Delta \tilde{\varepsilon}^e} & \frac{\partial \mathcal{R}_d}{\partial \Delta v^s} & \frac{\partial \mathcal{R}_d}{\partial \Delta d_{open}^r} & \frac{\partial \mathcal{R}_d}{\partial \Delta d} \end{bmatrix} \quad (\text{B.11})$$

The individual terms for the jacobian  $\mathcal{J}$  are given as

$$\frac{\partial \mathcal{R}_{\varepsilon^e}}{\partial \Delta \tilde{\varepsilon}^e} = \underline{\mathbf{1}} \quad (\text{B.12})$$

$$\frac{\partial \mathcal{R}_{\varepsilon^e}}{\partial \Delta v^s} = \underline{\mathbf{M}}^s \text{sign}(\tau^s) \quad (\text{B.13})$$

$$\frac{\partial \mathcal{R}_{\varepsilon^e}}{\partial \Delta d_{open}^r} = \underline{\mathbf{N}}_d^r \quad (\text{B.14})$$

$$\frac{\partial \mathcal{R}_{\varepsilon^e}}{\partial \Delta d} = \underline{\mathbf{0}} \quad (\text{B.15})$$

$$\frac{\partial \mathcal{R}_{v^s}}{\partial \Delta \tilde{\varepsilon}^e} = -\Delta t \frac{n_p}{K_p} \left\langle \frac{|\tau^s| - r}{K_p} \right\rangle^{n_p-1} \underline{\mathbf{C}} : \underline{\mathbf{M}}^s \text{sign}(\tau^s) \quad (\text{B.16})$$

$$\frac{\partial \mathcal{R}_{v^s}}{\partial \Delta v^s} = \underline{\mathbf{1}} + (h + H\beta^2 + Qb \sum_{s,r} h^{sr} e^{-bv^r}) \Delta t \frac{n_p}{K_p} \left\langle \frac{|\tau^s| - r}{K_p} \right\rangle^{n_p-1} \quad (\text{B.17})$$

$$\frac{\partial \mathcal{R}_{v^s}}{\partial \Delta d_{open}^r} = \underline{\mathbf{0}} \quad (\text{B.18})$$

$$\frac{\partial \mathcal{R}_{v^s}}{\partial \Delta d} = H\beta \Delta t \left\langle \frac{|\tau^s| - r}{K_p} \right\rangle^{n_p-1} \quad (\text{B.19})$$

$$\frac{\partial \mathcal{R}_{d_{open}^r}}{\partial \Delta \tilde{\varepsilon}^e} = \Delta t \frac{n_d}{K_d} \frac{n_d}{K_d} \left\langle \frac{|\underline{\boldsymbol{\sigma}} : \underline{\mathbf{N}}_d^r| - Y}{K_d} \right\rangle^{n_d-1} (\underline{\mathbf{C}} : \underline{\mathbf{N}}_d^r) \quad (\text{B.20})$$

$$\frac{\partial \mathcal{R}_{d_{open}^r}}{\partial \Delta v^s} = \beta H \Delta t \frac{n_d}{K_d} \left\langle \frac{|\underline{\boldsymbol{\sigma}} : \underline{\mathbf{N}}_d^r| - Y}{K_d} \right\rangle^{n_d-1} \text{sign}(\underline{\boldsymbol{\sigma}} : \underline{\mathbf{N}}_d^r) \quad (\text{B.21})$$

$$\frac{\partial \mathcal{R}_{d_{open}^r}}{\partial \Delta d_{open}^r} = \underline{\mathbf{1}} \quad (\text{B.22})$$

$$\frac{\partial \mathcal{R}_{d_{open}^r}}{\partial \Delta d} = (H + H_\mu) \Delta t \frac{n_d}{K_d} \left\langle \frac{|\underline{\boldsymbol{\sigma}} : \underline{\mathbf{N}}_d^r| - Y}{K_d} \right\rangle^{n_d-1} \text{sign}(\underline{\boldsymbol{\sigma}} : \underline{\mathbf{N}}_d^r) \quad (\text{B.23})$$

$$\frac{\partial \mathcal{R}_d}{\partial \Delta \tilde{\varepsilon}^e} = \underline{\mathbf{0}} \quad (\text{B.24})$$

$$\frac{\partial \mathcal{R}_d}{\partial \Delta v^s} = \underline{\mathbf{0}} \quad (\text{B.25})$$

$$\frac{\partial \mathcal{R}_d}{\partial \Delta d_{open}^r} = - \text{sign}(\underline{\boldsymbol{\sigma}} : \underline{\mathbf{N}}_d^r) \quad (\text{B.26})$$

$$\frac{\partial \mathcal{R}_d}{\partial \Delta d} = 1 \quad (\text{B.27})$$

The Jacobian is then used in the Newton method used to solve the set of Equations B.7...B.10

$$\mathcal{J} = 1 - \theta \Delta t \left. \frac{\partial \dot{\Theta}}{\partial \Delta \Theta} \right|_{t_{\Delta t}} \quad (\text{B.28})$$

## Appendix C

# Polycrystal simulations

It has been shown that the XMD model is capable of handling crack growth under different crystal orientations. Since polycrystalline materials are an agglomeration of single crystals, it should be possible to extend the XMD model to simulate crack growth in polycrystals in a realistic manner. To test this hypothesis, 2D polycrystals with 25 grains were simulated. Figures C.1 and C.2 show the grain distribution and the finite element mesh used for the simulations. The grains were defined in terms of Euler angle rotations. Two different grain distributions were tested. The first distribution consisted of grain orientations varying between  $0^\circ$  and  $250^\circ$ . The rotations were assigned sequentially in steps of  $10^\circ$ , starting with the grain on the top-left corner of the block (see Figure C.1). The second grain distribution consisted of a random distribution of Euler angles, varying between  $0^\circ$  and  $100^\circ$ . Figure C.3 show the crack paths predicted for the two orientations.

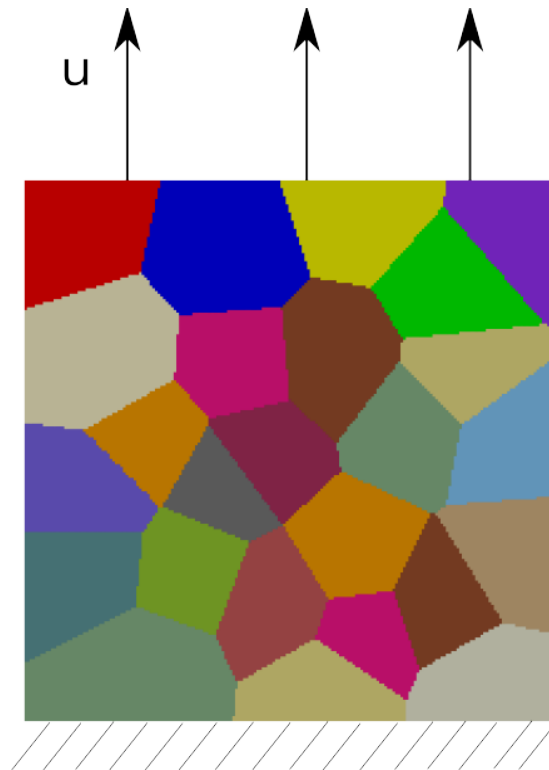


Figure C.1: Grain distribution and loading conditions used in the polycrystal simulations.

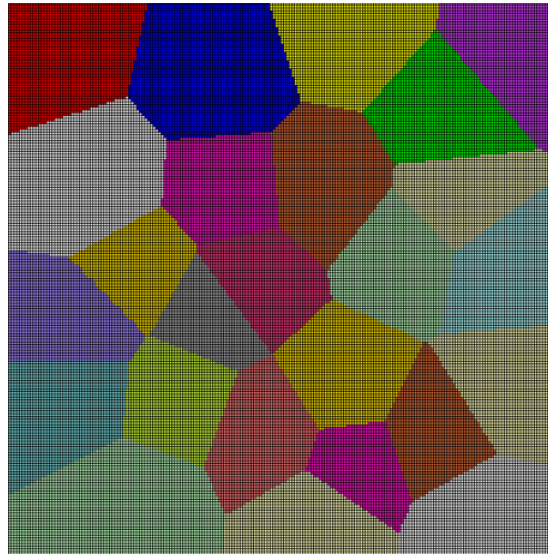


Figure C.2: Mesh used in the polycrystal simulations. Linear elements with full integration were used in the simulations. An uniform mesh was used; element size =  $50 \mu\text{m}$ .

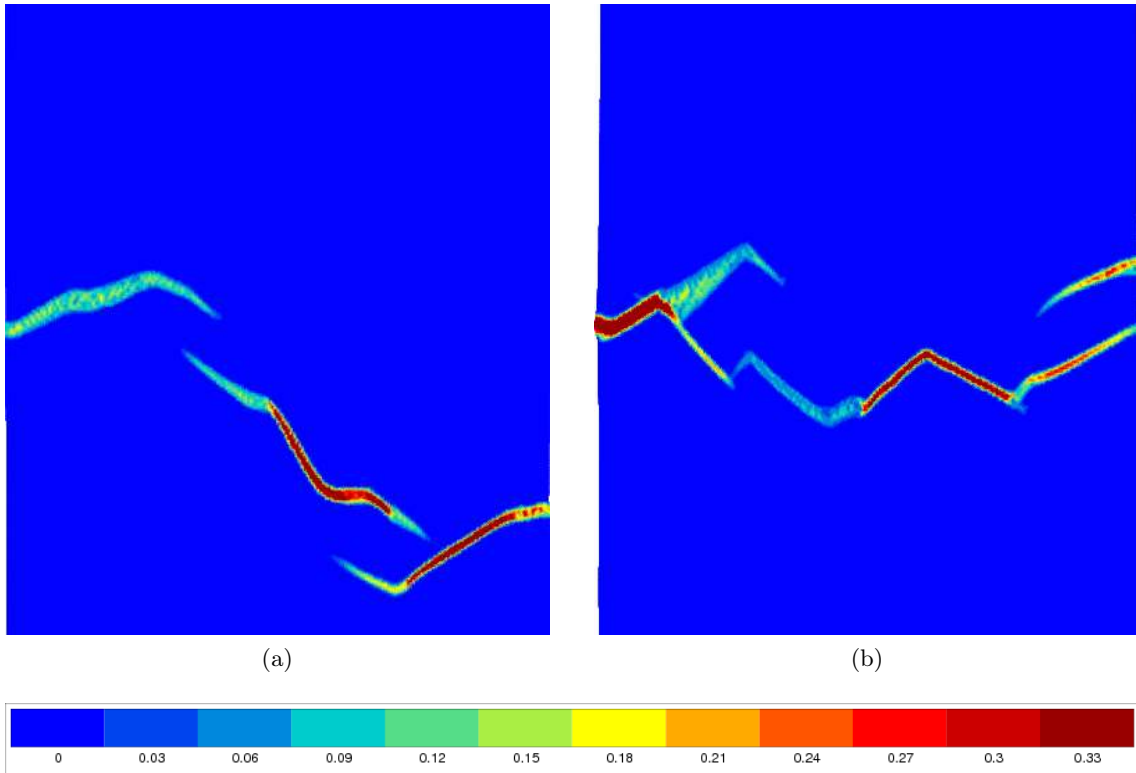


Figure C.3: A comparison of the crack paths predicted by the XMD model for the two grain distributions. (a) Grain distribution 1: Sequential variation of Euler angles in steps of  $10^\circ$ . (b) Random grain orientations varying between  $0^\circ$  and  $100^\circ$ .

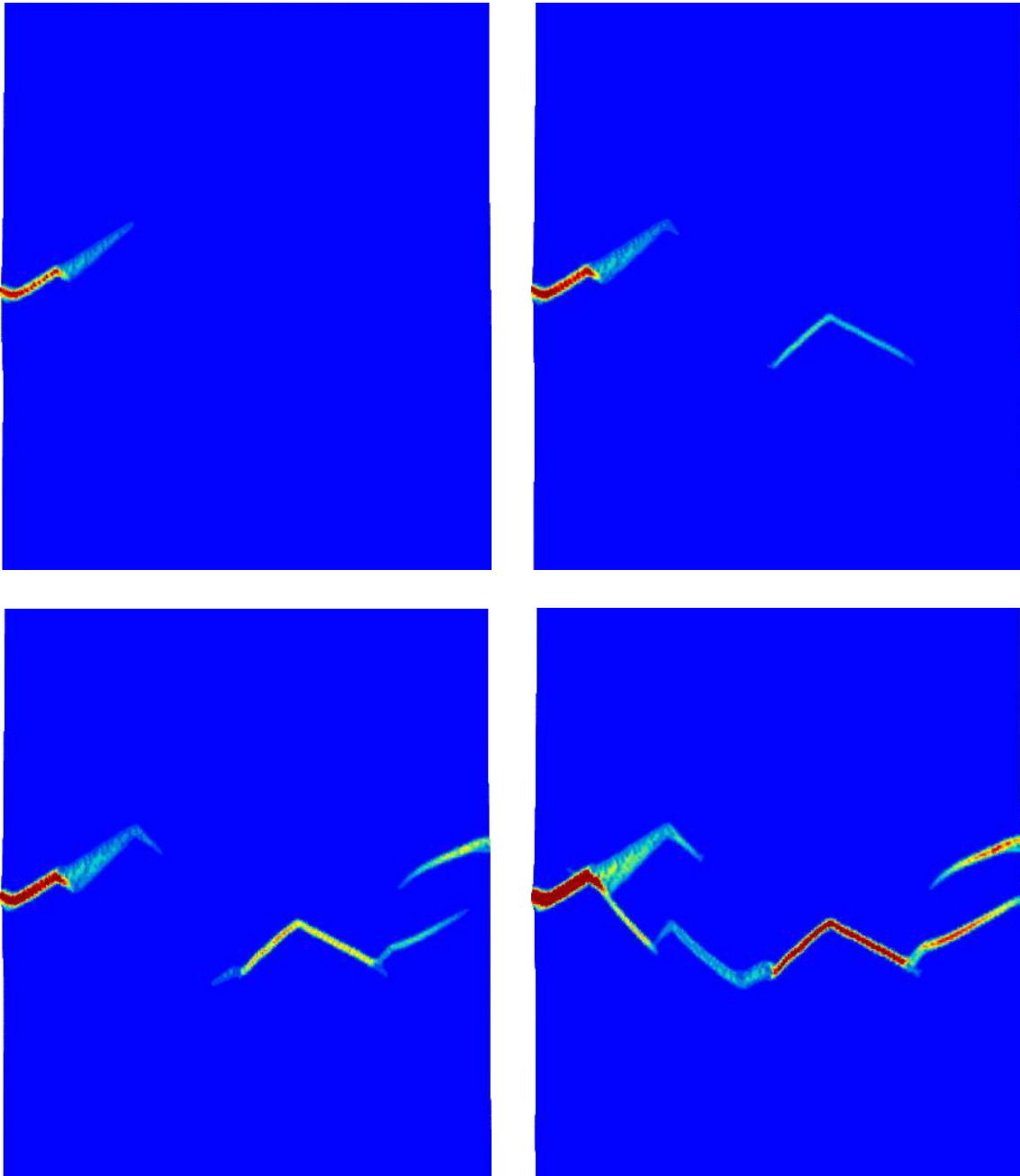


Figure C.4: Various stages of crack evolution for the the second grain distribution. Comparing with Figures C.1 and C.5, it is observed that the initial crack is an intra-granular crack, whereas the subsequent cracks are inter-granular.

Figures C.4 and C.5 show the evolution of multiple cracks as predicted by the XMD model for the second grain distribution. In these preliminary tests, it is observed that the XMD model exhibits the capability to simulate intra-granular and inter-granular crack evolutions.

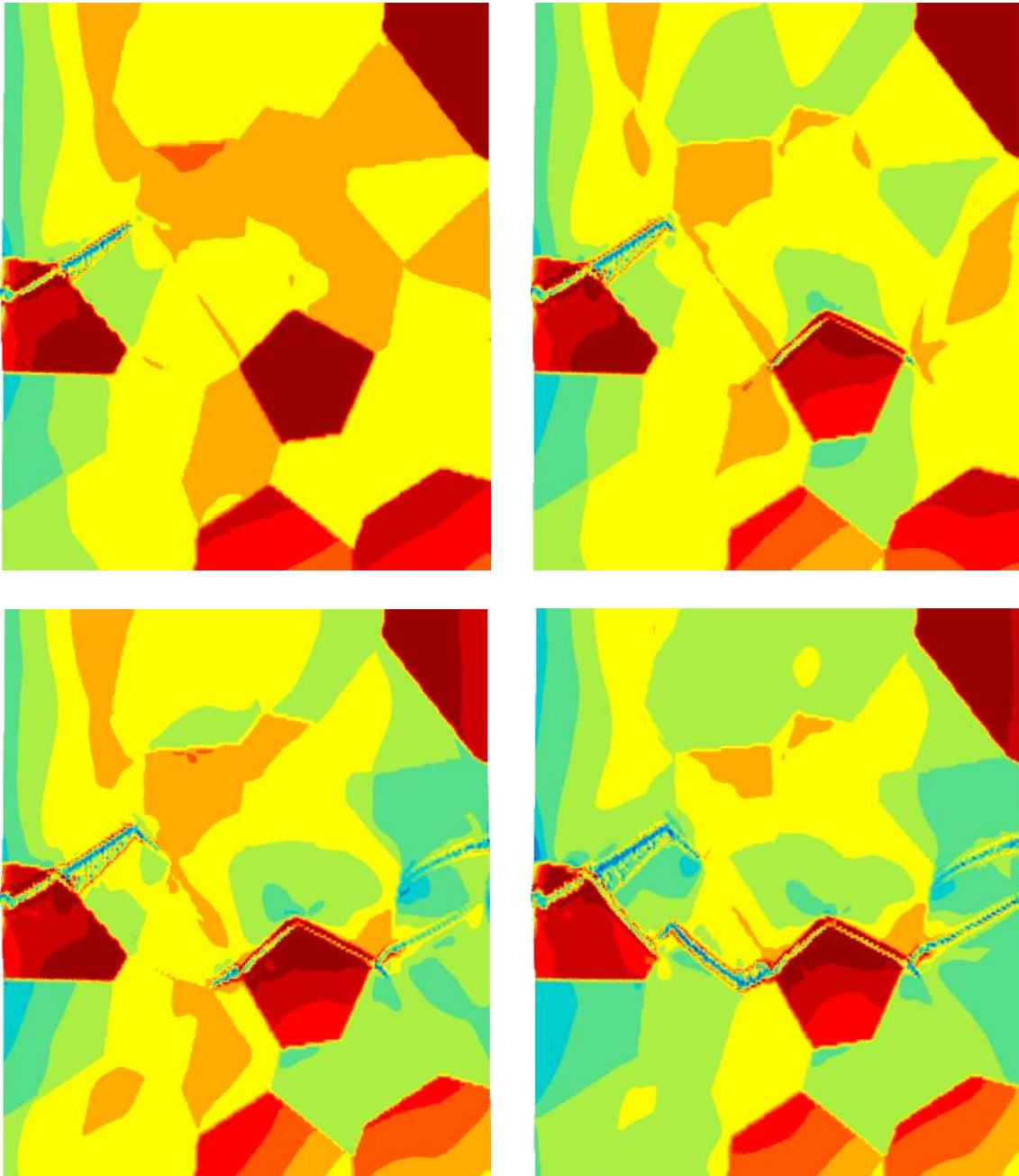


Figure C.5: Various stages of stress evolution in one of the polycrystal simulations. Intra-granular and inter-granular crack path evolution is observed.





---

# References

- A. Abdul-Latif and K. Saanouni, “Micromechanical Modeling of low cycle fatigue under complex loadings - Part II.Applications,” *International Journal of Plasticity*, vol. 12, no. 9, pp. 1123–1149, 1996.
- E. C. Aifantis, “Gradient Deformation Models at Nano, Micro, and Macro Scales,” *Journal of Engineering Materials and Technology*, vol. 121, pp. 189–202, 1999.
- E. C. Aifantis, “Update on a class of gradient theories,” *Mechanics of Materials*, vol. 35, pp. 259–280, 2003.
- K. Ammar, B. Appolaire, G. Cailletaud, F. Feyel, and S. Forest, “Finite element formulation of a phase field model based on the concept of generalized stresses,” *Computational Materials Science*, vol. 45, pp. 800–805, 2009.
- K. Ammar, B. Appolaire, G. Cailletaud, and S. Forest, “Combining phase field approach and homogenization methods for modelling phase transformation in elastoplastic media,” *European Journal of Computational Mechanics*, vol. 18, pp. 485–523, 2009.
- T. Anderson, *Fracture Mechanics – Fundamentals and Applications*. CRC Press, 2005.
- B. F. Antolovich, A. Saxena, and S. D. Antolovich, “Single crystal CMSX-2 at elevated temperature,” *Superalloys*, pp. 727–736, 1992.
- S. D. Antolovich, E. Rosa, and A. Pineau, “Low cycle fatigue of René 77 at elevated temperatures,” *Materials Science and Engineering*, vol. 47, pp. 47–57, 1981.
- N. K. Arakere and G. R. Swanson, “Analysis of fretting stresses in single crystal Ni-base turbine blade attachment regions,” *ASME Journal of Tribology*, vol. 123, pp. 413–423, 2001.
- N. K. Arakere and G. R. Swanson, “Effect of crystal orientation on fatigue failure of single crystal Nickel base turbine blade superalloys,” *ASME Journal of Gas Turbines and Power*, vol. 124, pp. 161–176, 2002.
- N. K. Arakere, S. Siddiqui, F. Ebrahimi, and L. Forero, “Investigation of three dimensional stress fields and slip systems for FCC single crystal superalloy notched specimens,” *ASME Journal of Tribology*, vol. 127, pp. 629–637, 2005.
- N. K. Arakere, G. R. Swanson, G. Duke, and G. Ham-Battista, “Subsurface stress fields in Face-Centred-Cubic single-crystal anisotropic contacts,” *Journal of Engineering for Gas Turbines and Power*, vol. 128, no. 4, pp. 879–888, July 2006.
- N. K. Arakere, S. Siddiqui, and F. Ebrahimi, “Evolution of plasticity in notched Ni-base superalloy single crystals,” *International Journal of Solids and Structures*, vol. 46, pp. 3027–3044, 2009.

## REFERENCES

---

- I. S. Aranson, V. A. Kalatsky, and V. M. Vinokur, “Continuum Field Description of Crack Propagation,” *Physical Review Letters*, vol. 85, p. 118, 2000.
- G. Arfken, H. J. Weber, and F. E. Harris, *Mathematical Methods for Physicists*, 7th ed. Elsevier, 2012.
- R. J. Asaro and V. A. Lubarda, *Mechanics of solids and materials*. Cambridge, 2006.
- O. Aslan, “Numerical modeling of thermomechanical fatigue crack growth in single crystal nickel superalloys,” Ph.D. dissertation, l’Ecole Nationale Supérieure des Mines de Paris, March 2010.
- O. Aslan and S. Forest, “Crack growth modelling in single crystals based on higher order continua,” *Computational Materials Science*, vol. 45, pp. 756–761, 2009.
- O. Aslan, N. M. Cordero, A. Gaubert, and S. Forest, “Micromorphic approach to single crystal plasticity and damage,” *International Journal of Engineering Sciences*, vol. 49, pp. 1311–1325, 2011.
- O. Aslan, S. Quilici, and S. Forest, “Numerical modeling of fatigue crack growth in single crystals based on microdamage theory,” *International Journal of Damage Mechanics*, vol. 20, pp. 681–705, July 2011.
- H. Badreddine, K. Saanouni, and A. Dogui, “On non-associative anisotropic finite plasticity fully coupled with isotropic ductile damage for metal forming,” *International Journal of Plasticity*, vol. 26, pp. 1541–1575, 2010.
- R. Bargellini, J. Besson, E. Lorentz, and S. Michelle-Ponnelle, “A non-local finite element based on volumetric strain gradient: Application to ductile fracture,” *Computational Materials Science*, vol. 45, pp. 762–767, 2009.
- Z. P. Bažant and G. Pijaudier-Cabot, “Nonlocal continuum damage, localization instability and convergence,” *Journal of Applied Mechanics*, vol. 55, pp. 287–293, 1988.
- Z. P. Bažant, T. Belytschko, and T. P. Chang, “Continuum theory for strain-softening,” *Journal of Engineering Mechanics*, vol. 110, pp. 1666–1692, 1984.
- T. Belytschko, N. Moës, S. Usui, and C. Parimi, “Arbitrary discontinuities in finite elements,” *International Journal For Numerical Methods In Engineering*, vol. 50, pp. 993–1013, 2001.
- J. Besson and R. Foerch, “Large scale Object-Oriented Finite Element code design,” *Computer Methods in Applied Mechanics and Engineering*, vol. 142, pp. 165–187, 1997.
- J. Besson, C. Berdin, S. Bugat, F. Feyel, S. Forest, E. Lorentz, E. Maire, T. Pardoen, A. Pineau, and B. Tanguy, *Local approach to fracture*. Presses des Mines, 2004.
- J. Besson, G. Cailletaud, J. L. Chaboche, and S. Forest, *Non-linear mechanics of materials*. Springer, 2010.
- D. Bettge and W. Österle, ““Cube slip” in near-[111] oriented specimens of a single-crystal nickel-base superalloy,” *Scripta Materialia*, vol. 40, no. 4, pp. 389–395, 1999.
- U. Borg, C. F. Niordson, and J. W. Kysar, “Size effects on void growth in single crystals with distributed voids,” *International Journal of Plasticity*, vol. 24, no. 4, pp. 688–701, 2008.

- B. Bourdin, "Numerical implementation of the variational formulation of brittle fracture," *Interfaces Free Bound*, vol. 9, pp. 411–430, 2007.
- B. Bourdin, G. A. Francfort, and J. J. Marigo, "The Variational Approach to Fracture," *Journal of Elasticity*, vol. 91, no. 1-3, pp. 5–148, 2008.
- J. L. Bouvard, "Modélisation de la propagation de fissure dans les aubes de turbines monocristallines," Ph.D. dissertation, l'Ecole Nationale Supérieure des Mines de Paris, 2006.
- J. L. Bouvard, J. L. Chaboche, F. Feyel, and F. Gallerneau, "A cohesive zone model for fatigue and creep-fatigue crack growth in single crystal superalloys," *International Journal of Fatigue*, vol. 31, pp. 868–879, 2009.
- A. Braides,  *$\Gamma$ -convergence for beginners*. Oxford University Press, 2002.
- M. Brünig, "Numerical analysis of anisotropic ductile continuum damage," *Computer Methods in Applied Mechanics and Engineering*, vol. 192, pp. 2949–2976, 2003.
- J. L. Chaboche and G. Cailletaud, "Integration methods for complex constitutive equations," *Computer Methods in Applied Mechanics and Engineering*, vol. 133, pp. 125–155, 1996.
- P. Chadwick, *Continuum Mechanics - Concise Theory and Problems*. Dover, 1999.
- G. Chalant and L. Rémy, "Plastic strain distribution at the tip of a fatigue crack application to fatigue crack closure in the threshold regime," *Engineering Fracture Mechanics*, vol. 16, no. 5, pp. 707–720, 1982.
- D. Chatterjee, N. Hazari, and R. Mitra, "Microstructure and creep behavior of DMS4-type nickel based superalloy single crystals with orientations near  $\langle 001 \rangle$  and  $\langle 011 \rangle$ ," *Materials Science and Engineering A*, vol. 528, pp. 604–613, 2010.
- N. Clément, A. Couret, and D. Caillard, "An in situ study of cube glide in the gamma prime phase of a superalloy : I. the controlling mechanism," *Philosophical Magazine*, vol. 64, pp. 669–695, 1991.
- N. Clément, A. Couret, and D. Caillard, "An in situ study of cube glide in the gamma prime phase of a superalloy : II. the anomalous stress-temperature dependence," *Philosophical Magazine*, vol. 64, pp. 697–708, 1991.
- B. D. Coleman and W. Noll, "The thermodynamics of elastic materials with heat conduction and viscosity," *Archive for Rational Mechanics and Analysis*, vol. 13, no. 1, pp. 167–178, 1963.
- S. M. Copley and B. H. Kear, "A dynamic theory of coherent precipitation hardening with application to nickel-base superalloys," *Transactions of the AIME Metallurgical society*, vol. 239, pp. 977–983, 1967.
- J. Cormier, X. Milhet, and J. Mendez, "Anisothermal creep behavior at very high temperature of a Ni-based superalloy single crystal," *Materials Science and Engineering A*, vol. 483-484, pp. 594–597, 2008.
- W. C. Crone and T. W. Shield, "Experimental study of the deformation near a notch tip in Copper and Copper-Beryllium single crystals," *Journal of the Mechanics and Physics of Solids*, vol. 49, pp. 2819–2838, 2001.

## REFERENCES

---

- W. C. Crone, T. W. Shield, A. Creuzigera, and B. Hennemanb, "Orientation dependence of the plastic slip near notches in ductile FCC single crystals," *Journal of the Mechanics and Physics of Solids*, vol. 52, pp. 85–112, 2004.
- A. Cuitiño and M. Ortiz, "Computational modeling of single crystals," *Modelling and Simulation in Materials Science Engineering*, vol. 1, pp. 225–263, 1992.
- A. Cuitiño and M. Ortiz, "Three-Dimensional crack tip fields in four point bending Copper single crystal specimens," *Journal of the Mechanics and Physics of Solids*, vol. 44, pp. 863–904, 1996.
- S. Cuvilliez, "Passage dun modèle dendommagement continu régularisé à un modèle de fissuration cohésive dans le cadre de la rupture quasi-fragile," Ph.D. dissertation, l'Ecole Nationale Supérieure des Mines de Paris, 2012.
- R. de Borst, L. J. Sluys, H. B. Mühlhaus, and J. Pamin, "Fundamental issues in Finite-Element analyses of localization of deformation," *Engineering Computations*, vol. 10, no. 2, pp. 99–121, 1993.
- D. Deluca and C. Annis, "Fatigue in Single Crystal Superalloys," Office of Naval Research, Tech. Rep. FR23800, 1995.
- M. J. Donachie and S. J. Donachie, *Superalloys: A technical guide*, 2nd ed. ASM International, 2002.
- G. L. Drew, R. C. Reed, K. Kakehi, and C. M. F. Rae, "Single crystal superalloys: the transition from primary to secondary creep," in *Superalloys 2004*. TMS, 2004.
- W. J. Drugan, "Asymptotic solutions for tensile crack tip fields without kink-type shear bands in elastic-ideally plastic single crystals," *Journal of the Mechanics and Physics of Solids*, vol. 49, pp. 2155–2176, 2001.
- F. Dunne and N. Petrinic, *Introduction to Computational Plasticity*. Oxford University Press, 2006.
- F. P. E. Dunne, A. J. Wilkinson, and R. Allen, "Experimental and computational studies of low cycle fatigue crack nucleation in a polycrystal," *International Journal of Plasticity*, vol. 23, pp. 273–295, 2007.
- M. Durand-Charre, *The microstructure of superalloys*. Gordon and Breach Science Publishers, 1997.
- L. O. Eastgate, J. P. Sethna, M. Rauscher, T. Cretegnny, C. S. Chen, and C. R. Myers, "Fracture in mode I using a conserved phase field model," *Physical Review E*, vol. 65, p. 036117, 2002.
- F. Ebrahimi and E. F. Westbrooke, "Effect of HIP'ping on deformation anisotropy in a single crystal Ni-based superalloy," *Acta Materialia*, vol. 56, no. 16, pp. 4349–4357, 2008.
- F. Ebrahimi, L. E. Forero, S. Siddiqui, and N. K. Arakere, "Effect of notch orientation on the evolution of plasticity in superalloy single crystals," *Materials Science and Engineering: A*, vol. 426, pp. 214–220, 2006.
- B. Eidel, "Crystal plasticity finite-element analysis versus experimental results of pyramidal indentation into (0 0 1) fcc single crystal," *Acta Materialia*, vol. 59, pp. 1761–1771, 2011.

- M. Ekh, R. Lillbacka, and K. Runesson, "A model framework for anisotropic damage coupled to crystal (visco)plasticity," *International Journal of Plasticity*, vol. 20, pp. 2143–2159, 2004.
- R. A. B. Engelen, M. G. D. Geers, and F. P. T. Baaijens, "Nonlocal implicit gradient-enhanced elasto-plasticity for the modelling of softening behaviour," *International Journal of Plasticity*, vol. 19, pp. 403–433, 2003.
- S. Feld-Payet, "Amorçage et propagation de fissures dans les milieux ductiles non locaux," Ph.D. dissertation, l'Ecole Nationale Supérieure des Mines de Paris, 2010.
- L. Feng, K. S. Zhang, G. Zhang, and H. D. Yu, "Anisotropic damage model under continuum slip crystal plasticity theory for single crystals," *International Journal of Solids and Structures*, vol. 39, pp. 5279–5293, 2002.
- E. Fleury and L. Rémy, "Behavior of Nickel-base superalloy single crystals under thermal-mechanical fatigue," *Metallurgical and Materials Transactions A*, vol. 25A, pp. 99–109, 1994.
- S. Flouriot, "Détermination expérimentale et simulation numérique des phénomènes de localisation de la déformation en pointe de fissure dans un monocristal c.f.c." Ph.D. dissertation, l'Ecole Nationale Supérieure des Mines de Paris, June 2004.
- S. Flouriot, S. Forest, G. Cailletaud, A. Köster, L. Rémy, B. Burgardt, V. Gros, S. Mosset, and J. Delautre, "Strain localization at the crack tip in single crystal CT specimens under monotonous loading: 3D Finite Element analyses and application to Nickel-base superalloys," *International Journal of Fracture*, vol. 124, pp. 43–77, 2003.
- S. Forest, "The micromorphic approach for gradient elasticity, viscoplasticity and damage," *ASCE Journal of Engineering Mechanics*, vol. 135, pp. 117–131, 2009.
- S. Forest, "Strain localization phenomena in generalized single crystal plasticity," *Journal of the Mechanical Behavior of Materials*, vol. 11, pp. 45–50, 1997.
- S. Forest, R. Sievert, and E. C. Aifantis, "Strain gradient crystal plasticity : Thermomechanical formulations and applications," *Journal of the Mechanical Behavior of Materials*, vol. 13, pp. 219–232, 2002.
- A. Francavilla and O. C. Zienkiewicz, "A note on numerical computation of elastic contact problems," *International Journal For Numerical Methods In Engineering*, vol. 9, pp. 913–924, 1975.
- G. A. Francfort and J. J. Marigo, "Revisiting brittle fracture as an energy minimization problem," *Journal of the Mechanics and Physics of Solids*, vol. 46, no. 8, pp. 1319–1342, 1998.
- F. Gallerneau and A. Sanson, "Socrax - expanding the limits of single crystal superalloys through short crack fracture mechanics analysis. deliverable no. d5.1 - report - application of the socrax methods to aeronautical components and tests cases," ONERA, Tech. Rep., 2004.
- Y. X. Gan, J. W. Kysar, and T. L. Morse, "Cylindrical void in a rigid-ideally plastic single crystal II: Experiments and simulations," *International Journal of Plasticity*, vol. 22, no. 1, pp. 39–72, 2006.

## REFERENCES

---

- M. Gell and D. N. Duhl, “The development of single crystal superalloy turbine blades, Processing and properties of advanced high temperature materials,” in *ASM*, Metals Park, Ohio, 1986, p. 41.
- A. A. Griffith, “The phenomena of rupture and flow in solids,” *Philosophical Transactions of the Royal Society of London, Series A*, vol. 221, pp. 163–198, 1921.
- S. Groh, E. B. Marin, M. F. Horstemeyer, and H. M. Zbib, “Multiscale modeling of the plasticity in an aluminum single crystal,” *International Journal of Plasticity*, vol. 25, no. 8, pp. 1456–1473, 2009.
- D. Gross and T. Seelig, *Fracture Mechanics*. Springer, 2006.
- M. E. Gurtin, “Generalized Ginzburg-Landau and Cahn-Hilliard equations based on a microforce balance,” *Physica D*, vol. 92, pp. 178–192, 1996.
- V. Hakim and A. Karma, “Laws of crack motion and phase field models of fracture,” *Journal of Mechanics and Physics of Solids*, vol. 57, no. 2, pp. 342–368, 2008.
- M. F. Horstemeyer and D. J. Bammann, “Historical review of internal state variable theory for inelasticity,” *International Journal of Plasticity*, vol. 26, no. 9, pp. 1310–1334, 2010.
- N. X. Hou, W. X. Gou, Z. X. Wen, and Z. F. Yue, “The influence of crystal orientations on fatigue life of single crystal cooled turbine blade,” *Materials Science and Engineering A*, vol. 492, pp. 413–418, 2008.
- N. H. Huynh, C. Lu, G. Michal, and K. Tieu, “A modelling of tensile deformation around the notch tip in single crystal aluminium,” *Computational Materials Science*, vol. 48, pp. 179–186, 2010.
- G. R. Irwin, “Analysis of stresses and strains near end of a crack,” *Journal of Applied Mechanics*, vol. 24, pp. 361–364, 1957.
- M. Jean, “Frictional contact in collections of rigid or deformable bodies: numerical simulation of geomaterial motions,” *Studies in applied mechanics*, vol. 42, pp. 463–486, 1995.
- M. Kaminski, “Modelisation de l’endommagement en fatigues des superalliages monocristallins pour aubes de turbines en zone de concentration de contrainte,” Ph.D. dissertation, l’Ecole Nationale Supérieure des Mines de Paris, November 2007.
- A. Karma, D. A. Kessler, and H. Levine, “Phase field model of mode III dynamic fracture,” *Physical Review Letters*, vol. 87, p. 045501, 2001.
- E. Kreyszig, *Advanced Engineering Mathematics*, 9th ed. John Wiley & Sons, 2006.
- E. Kuhl and E. Ramm, “Simulation of strain localization with gradient enhanced damage models,” *Computational Materials Science*, vol. 16, pp. 176–185, 1999.
- C. Kuhn and R. Müller, “A continuum phase field model for fracture,” *Engineering Fracture Mechanics*, vol. 77, pp. 3625–3634, 2010.
- J. W. Kysar and C. L. Briant, “Crack tip deformation in ductile single crystals,” *Acta Materialia*, vol. 50, pp. 2367–2380, 2002.

- J. W. Kysar, Y. X. Gan, and G. Mendez-Arzuza, "Cylindrical void in a rigid-ideally plastic single crystal. Part I: Anisotropic slip line theory solution for face-centered cubic crystals," *International Journal of Plasticity*, vol. 21, no. 8, pp. 1481–1520, 2005.
- J. W. Kysar, Y. X. Gan, T. L. Morse, X. Chen, and M. E. Jones, "High strain gradient plasticity associated with wedge indentation into face-centered cubic single crystals: Geometrically necessary dislocation densities," *Journal of Mechanics and Physics of Solids*, vol. 55, no. 7, 2007.
- S. Lekhnitskii, *Theory of Elasticity of an Anisotropic Elastic Body*. San Francisco: Holden-Day, 1963.
- J. Lemaitre and J. L. Chaboche, *Mechanics of solid materials*. Cambridge University Press, 1994.
- J. Lemaitre and R. Desmorat, *Engineering Damage Mechanics – Ductile, Creep, Fatigue and Brittle Failures*. Springer, 2005.
- J. Lemaitre, R. Desmorat, and M. Sauzay, "Anisotropic damage law of evolution," *European Journal of Mechanics A/Solids*, vol. 19, pp. 187–208, 2000.
- E. Lorentz and V. Godard, "Gradient damage models: Toward full-scale computations," *Computer Methods in Applied Mechanics and Engineering*, vol. 200, pp. 1927–1944, 2011.
- V. A. Lubarda, *Elastoplasticity Theory*. CRC Press, 2002.
- S. Magnan, "Three-Dimensional Stress Fields and Slip Systems in Single Crystal Superalloy Notched Specimens," Master's thesis, Department of Mechanical & Aerospace Engineering, University of Florida, Gainesville, Florida, 2002.
- J. Mandel, "Equations constitutives et directeurs dans les milieux plastiques et viscoplastiques," *International Journal of Solids and Structures*, vol. 9, pp. 725–740, 1973.
- J. Mandel, *Thermodynamics and Plasticity*. Wiley, 1974, vol. Foundations of Continuum Thermodynamics, ch. 15.
- N. Marchal, "Propagation de fissure en fatigue-fluage à haute température de superalliages monocristallins à base de nickel," Ph.D. dissertation, l'Ecole Nationale Supérieure des Mines de Paris, June 2006.
- N. Marchal, S. Forest, L. Remy *et al.*, "Socrax - expanding the limits of single crystal superalloys through short crack fracture mechanics analysis. deliverable no. d2.4.2 - report - the characterisation of the short/long crack growth behaviour of the single crystal superalloys am1 and pwa1487," ONERA, Tech. Rep., 2002.
- N. Marchal, S. Flouriot, S. Forest, and L. Rémy, "Crack-tip stress-strain fields in single crystal nickel-base superalloys at high temperature under cyclic loading," *Computational Materials Science*, vol. 37, pp. 42–50, 2006.
- B. Markert, "Weak or strong on coupled problems in continuum mechanics," 2010, habilitation Thesis, *Universität Stuttgart*.
- J. M. Melenk and I. Babuska, "The partition of unity finite element method: Basic theory and applications," *Computer Methods in Applied Mechanics and Engineering*, vol. 139, pp. 289–314, 1996.

- L. Méric, P. Poubanne, and G. Cailletaud, “Single crystal modeling for structural calculations. Part 1: Model presentation,” *Journal of Engineering Materials and Technology*, vol. 113, pp. 162–170, 1991.
- C. Miehe, F. Welschinger, and M. Hofacker, “Thermodynamically consistent phase-field models of fracture: Variational principles and multi-field FE implementations,” *International Journal For Numerical Methods In Engineering*, vol. 83, pp. 1273–1311, 2010.
- W. W. Milligan and S. D. Antolovich, “Yielding and Deformation Behaviour of the Single Crystal Superalloy PWA 1480,” *Metallurgical Transactions*, vol. 18, no. 1, p. 85, 1987.
- N. Moës, J. Dolbow, and T. Belytschko, “A finite element method for crack growth without remeshing,” *International Journal For Numerical Methods In Engineering*, vol. 46, pp. 131–150, 1999.
- R. Mohan, M. Ortiz, and C. Shih, “An analysis of cracks in ductile single crystals 2. Mode I loading,” *Journal of the Mechanics and Physics of Solids*, vol. 40, no. 2, pp. 315–337, 1992.
- R. K. Nalla, J. P. Campbell, and R. O. Ritchie, “Mixed-mode, high-cycle fatigue-crack growth thresholds in Ti-6Al-4V: Role of small cracks,” *International Journal of Fatigue*, vol. 24, no. 10, p. 1047, 2002.
- R. Narasimhan, H. Y. Subramanya, S. D. Patil, P. Tandaiya, and U. Ramamurty, “Stationary crack tip fields in elastic–plastic solids: an overview of recent numerical simulations,” *Journal of Physics D: Applied Physics*, vol. 42, no. 21, 2009.
- D. Nouailhas and G. Cailletaud, “Tension-torsion behavior of single-crystal superalloys – experiment and finite-element analysis,” *International Journal of Plasticity*, vol. 11, pp. 451–470, 1995.
- D. Nouailhas, J. P. Culie, G. Cailletaud, and L. Méric, “Finite-element analysis of the stress-strain behavior of single-crystal tubes,” *European Journal of Mechanics A: Solids*, vol. 14, no. 1, pp. 137–154, 1995.
- S. D. Patil, P. Biswas, R. K. Mishra, and R. Narasimhan, “Crack Tip Fields in a Single Edge Notched Aluminum Single Crystal Specimen,” *Journal of Engineering Materials and Technology*, vol. 130, no. 2, pp. 1–11, 2008.
- S. D. Patil, R. Narasimhan, and R. K. Mishra, “A numerical study of crack tip constraint in ductile single crystals,” *Journal of Mechanics and Physics of Solids*, vol. 56, no. 6, pp. 2265–2286, 2008.
- S. D. Patil, R. Narasimhan, and R. K. Mishra, “Observation of kink shear bands in an aluminium single crystal fracture specimen,” *Scripta Materialia*, vol. 61, no. 5, pp. 465–468, 2009.
- R. H. J. Peerlings, R. de Borst, W. A. M. Brekelmans, and J. H. P. Vree, “Gradient enhanced damage for quasi-brittle materials,” *International Journal For Numerical Methods In Engineering*, vol. 39, pp. 3391–3403, 1996.
- R. H. J. Peerlings, W. A. M. Brekelmans, R. de Borst, and M. G. D. Geers, “Gradient-enhanced damage modelling of high-cycle fatigue,” *International Journal For Numerical Methods In Engineering*, vol. 49, pp. 1547–1569, 2000.

- R. H. J. Peerlings, M. G. D. Geers, R. de Borst, and W. A. M. Brekelmans, "A critical comparison of nonlocal and gradient-enhanced softening continua," *International Journal of Solids and Structures*, vol. 38, pp. 7723–7746, 2001.
- A. Pineau and S. D. Antolovich, "High temperature fatigue of nickel-base superalloys – A review with special emphasis on deformation modes and oxidation," *Engineering Failure Analysis*, vol. 16, pp. 2668–2697, 2009.
- L. H. Poh and S. Swaddiwudhipong, "Over-nonlocal gradient enhanced plastic-damage model for concrete," *International Journal of Solids and Structures*, vol. 46, pp. 4369–4378, 2009.
- C. Pragassam and A. Helstroffer, "Analyse des micro-mécanismes d'endommagement en fluage," ENSMA, Tech. Rep., 2010-2011.
- W. H. Press, S. A. Teukolsky, W. T. Vetterling, and B. P. Flannery, *Numerical Recipes: The Art of Scientific Computing*, 3rd ed. Cambridge University Press, 2007.
- W. Qi and A. Bertram, "Anisotropic continuum damage modeling for single crystals at high temperatures," *International Journal of Plasticity*, vol. 15, pp. 1197–1215, 1999.
- R. C. Reed, *the Superalloys: Fundamentals and Applications*. Cambridge University Press, 2006.
- L. Rémy and A. Defresne, "Fatigue behaviour of CMSX 2 superalloy [001] single crystals at high temperature II: Fatigue crack growth," *Materials Science and Engineering*, vol. A129, pp. 55–64, 1990.
- J. R. Rice, "Tensile crack tip fields in elastic-ideally plastic crystals," *Mechanics of Materials*, vol. 6, no. 4, pp. 317–335, 1987.
- J. R. Rice, "A path independent integral and the approximate analysis of strain concentration by notches and cracks," Brown University, Tech. Rep., 1967.
- J. R. Rice and M. Saeedvafa, "Crack tip singular fields in ductile crystals with taylor power-law hardening 1. Anti-plane shear," *Journal of the Mechanics and Physics of Solids*, vol. 36, no. 2, pp. 189–214, 1988.
- J. R. Rice, D. Hawk, and R. Asaro, "Crack tip fields in ductile single crystals," *International Journal of Fracture*, vol. 42, no. 4, pp. 301–321, 1990.
- J. Rossiter, A. Brahme, M. H. Simha, K. Inal, and R. Mishra, "A new crystal plasticity scheme for explicit time integration codes to simulate deformation in 3D microstructures: Effects of strain path, strain rate and thermal softening on localized deformation in the aluminum alloy 5754 during simple shear," *International Journal of Plasticity*, vol. 26, no. 12, pp. 1702–1725, 2010.
- F. Roters, P. Eisenlohr, L. Hantcherli, D. D. Tjahjanto, T. R. Bieler, and D. Raabe, "Overview of constitutive laws, kinematics, homogenization and multiscale methods in crystal plasticity finite-element modeling: Theory, experiments, applications," *Acta Materialia*, vol. 58, pp. 1152–1211, 2010.
- K. Saanouni, *Damage mechanics in metal forming – Advanced modeling and Numerical simulation*. ISTE Ltd. and John Wiley & Sons, 2012.

## REFERENCES

---

- K. Saanouni and A. Abdul-Latif, "Micromechanical Modeling of low cycle fatigue under complex loadings - Part I. Theoretical Formulation," *International Journal of Plasticity*, vol. 12, no. 9, pp. 1111–1121, 1996.
- P. A. Sabnis, M. Mazière, S. Forest, N. K. Arakere, and F. Ebrahimi, "Effect of secondary orientation on notch-tip plasticity in superalloy single crystals," *International Journal of Plasticity*, vol. 28, pp. 102–123, 2012.
- M. Saeedvafa and J. R. Rice, "Crack tip singular fields in ductile crystals with Taylor power-law hardening 2. Plane-Strain," *Journal of the Mechanics and Physics of Solids*, vol. 37, no. 6, pp. 673–691, 1989.
- F. Scheyvaerts and T. Pardoen, "A new model for void coalescence by internal necking," *International Journal of Damage Mechanics*, vol. 19, pp. 95–126, 2010.
- E. Schmid, "Yield point of crystals, critical shear stress law," *Proceedings of I International Congress Applied Mechanics (Delft)*, p. 342, 1924.
- H. L. Schreyer and Z. Chen, "One-dimensional softening with localization," *Journal of Applied Mechanics*, vol. 53, pp. 791–797, 1986.
- E. M. Sculson and Y. Xu, "Notch-tip deformation of Ni3Al single crystals," in *MRS proceedings*, vol. 460, 1997, pp. 550–560.
- M. R. R. Seabra, M. A. Jose, C. de Sa, P. Šuštaric, and T. Rodič, "Some numerical issues on the use of XFEM for ductile fracture," *Computational Mechanics*, 2012.
- V. Seetharaman and A. D. Cetel, "Thickness debit in creep properties of PWA 1484," in *Superalloys 2004*. TMS, 2004.
- J. P. Sermage, J. Lemaitre, and R. Desmorat, "Multiaxial creep-fatigue under anisothermal conditions," *Fatigue & Fracture of Engineering Materials & Structures*, vol. 23, pp. 241–252, 2000.
- D. M. Shah, S. Vega, S. A. Woodard, and A. D. Cetel, "Primary creep in nickel-base superalloys," in *Superalloys 2004*. TMS, 2004.
- T. W. Shield, "Experimental study of the plastic strain fields near a notch tip in a copper single crystal during loading," *Acta Materialia*, vol. 44, pp. 1547–1561, 1996.
- T. W. Shield and K. S. Kim, "Experimental measurement of near tip strain field in an Iron-Silicon single crystal," *Journal of the Mechanics and Physics of Solids*, vol. 42, pp. 845–873, 1994.
- G. C. Sih and B. MacDonald, "Fracture mechanics applied to engineering problems-strain energy density fracture criterion," *Engineering Fracture Mechanics*, vol. 6, no. 2, pp. 361–386, 1974.
- C. T. Sims, N. S. Stoloff, and W. C. Hagel, Eds., *Superalloys II*. John Wiley & Sons, 1987.
- A. Staroselsky and B. N. Cassenti, "Creep, plasticity, and fatigue of single crystal superalloy," *International Journal of Solids and Structures*, vol. 48, pp. 2060–2075, 2011.
- T. Sugui, Z. Jinghua, Z. Huihua, Y. Hongcai, X. Yongbo, and H. Zhuangqi, "Aspects of primary creep of a single crystal nickel-base superalloy," *Materials Science and Engineering A*, vol. 262, pp. 271–278, 1999.

- M. Sujata, M. Madan, K. Raghavendra, M. A. Venkataswamy, and S. K. Bhaumik, "Identification of failure mechanisms in nickel base superalloy turbine blades through microstructural study," *Engineering Failure Analysis*, vol. 17, pp. 1436–1446, 2010.
- S. Suresh, *Fatigue of materials*. Cambridge University Press, 1991.
- S. Suresh, "Fatigue crack growth," 2003, MIT OpenCourseWare study material.
- T. Tinga, W. A. M. Brekelmans, and M. G. D. Geers, "Time-incremental creep-fatigue damage rule for single crystal Ni-base superalloys," *Materials Science and Engineering A*, vol. 508, pp. 200–208, 2009.
- T. Tinga, W. A. M. Brekelmans, and M. G. D. Geers, "Cube slip and non-Schmid effects in single crystal Ni-base superalloys," *Modelling and Simulation in Materials Science Engineering*, vol. 18, p. 015005, 2010.
- C. Truesdell, *Rational Thermodynamics*. McGraw-Hill, 1969.
- F. L. VerSnyder and R. W. Guard, "Directional grain structure for high temperature strength," *Transactions of the American Society of Metals*, vol. 52, p. 485, 1960.
- F. R. Welschinger, "A variational framework for gradient-extended dissipative continua. application to damage mechanics, fracture, and plasticity," Ph.D. dissertation, Universität Stuttgart, 2010.
- Z. X. Wen and Z. F. Yue, "Fracture behaviour of the compact tension specimens of Nickel-based single crystal superalloys at high temperatures," *Materials Science and Engineering A*, vol. 456, no. 1-2, pp. 189–201, 2007.
- E. F. Westbrooke, "Effect of crystallographic orientation on plastic deformation of single crystal nickel-base superalloys," Ph.D. dissertation, University of Florida, Gainesville, Florida, 2005.
- K. Wintrich, "Schädigungsverhalten der einkristallinen superlegierung CMSX-4 bei hochtemperaturbelastung," Ph.D. dissertation, Technische Universität Darmstadt, 2004.
- P. Wriggers, *Computational contact mechanics*, 2nd ed. Springer Verlag, 2006.
- B. Xu, A. Yonezu, Z. F. Yue, and X. Chen, "Indentation creep surface morphology of nickel-based single crystal superalloys," *Computational Materials Science*, vol. 46, pp. 275–285, 2009.
- B. X. Xu, X. M. Wang, B. Zhao, and Z. F. Yue, "Study of crystallographic creep parameters of nickel-based single crystal superalloys by indentation method," *Materials Science and Engineering A*, vol. 478, pp. 187–194, 2008.
- A. C. Yeh, A. Sato, T. Kobayashi, and H. Harada, "On the creep and phase stability of advanced Ni-base single crystal superalloys," *Materials Science and Engineering A*, vol. 490, pp. 445–451, 2008.
- Q. M. Yu, Y. Wang, Z. X. Wen, and Z. F. Yue, "Notch effect and its mechanism during creep rupture of nickel-base single crystal superalloys," *Materials Science and Engineering A*, vol. 520, pp. 1–10, 2009.
- C. Zambaldi, F. Roters, D. Raabe, and U. Glatzel, "Modeling and experiments on the indentation deformation and recrystallization of a single-crystal nickel-base superalloy," *Materials Science and Engineering A*, vol. 454-455, pp. 433–440, 2007.

## REFERENCES

---

- A. R. Zamiri and F. Pourboghraat, “A novel yield function for single crystals based on combined constraints optimization,” *International Journal of Plasticity*, vol. 26, pp. 731–746, 2010.
- J. X. Zhang, T. Murakumo, H. Harada, Y. Koizumi, and T. Kobayashi, “Creep deformation mechanisms in some modern single-crystal superalloys,” in *Superalloys 2004*. TMS, 2004.

## Modélisation numérique de la propagation et de la bifurcation des fissures dans les superalliages monocristallins à base de nickel

**Résumé :** Le but principal de cette thèse est de développer un modèle numérique pour modéliser les phénomènes de bifurcation et du branchement des fissures. Pour réaliser cet objectif, il était indispensable de posséder un modèle permettant un couplage fort entre le modèle de Plasticité cristalline et celui de l'Endommagement régularisé. Dans un premier temps, quelques outils de post-traitement ont été développés pour analyser les systèmes de glissement actifs. Ces outils ont été utilisés sur des simulations d'éprouvettes réelles, et comparés à des résultats expérimentaux. Par ces comparaisons, l'application du modèle de Plasticité cristalline aux superalliages monocristallins a été validée. Ce modèle a ensuite été couplé avec le modèle d'endommagement régularisé. Le couplage a été réalisé dans les deux sens, c'est-à-dire que l'évolution de la plasticité a une influence sur l'endommagement et vice-versa. Le nouveau modèle peut être implémenté simplement, avec la méthode traditionnelle des Éléments Finis. Des expériences étudiant la propagation de fissure sous des chargements de types différents ont été simulées à l'aide de ce nouveau modèle : éprouvettes CT, fissuration en Mode II et rupture en fluage. Une méthode pour l'identification des paramètres matériaux a également été proposée.

**Mots clés :** Nickel, Monocristal, Superalliages, Plasticité Cristalline, Propagation de fissure, Bifurcation de fissure, Couplage, Régularisation, Évolution de l'endommagement, Micro-endommagement, Essais de Fluage, Essais de cisaillement, Epreuve CT, Méthode des Éléments Finis, Approche micromorphe

## Modelling the propagation and bifurcation of plasticity induced cracks in Nickel base single crystal superalloys

**Abstract:** The main goal of this dissertation was to develop a model to simulate the processes of crack bifurcation and crack branching in anisotropic materials. To achieve this goal, a thorough coupling of crystal plasticity and regularised damage models was deemed necessary. Firstly, post-processing tools were developed to better analyse the results obtained from standard Crystal Plasticity simulations. These were then compared with experiments, thereby validating the use of Crystal Plasticity models for Nickel base single crystal superalloys. The validated Crystal plasticity model was then coupled with a regularised microdamage model such that the evolution of plasticity influenced damage and vice versa. The newly developed model allows for the simulation of cracks using the standard Finite Element Approach. Experiments studying crack propagation under different types of loads were simulated using the newly developed model, including CT, shear and creep specimens. A methodology was also proposed for the identification of the newly introduced material parameters.

**Keywords:** Nickel base, Single Crystal, Superalloys, Crystal Plasticity, Crack Propagation, Crack Bifurcation, Two-way Coupling, Damage Evolution, Microdamage, Regularisation, Creep tests, Shear tests, CT tests, Finite Element Method, Micromorphic approach

